UNIVERSITA' DEGLI STUDI DI PADOVA

Scuola di Dottorato di Ricerca in

Scienza ed Ingegneria dei Materiali

CICLO XXI

Sede Amministrativa: Università degli Studi di Padova

Dipartimento di Scienze Chimiche

Tesi di Dottorato:

Optical Active Thin Films for Micro-Cavity Lasers

Direttore della Scuola : Ch.mo Prof. Gaetano Granozzi

Supervisore :Ch.mo Prof. Renato Bozio

Dottorando : Samuele Gardin

Anno: 2008

Il Presente

Credo sia giunto il momento di parlarvi del presente.
Per i filosofi il presente non esiste, si sa. E forse hanno ragione perché sicuramente c'è il passato e c'è il futuro. E il presente sarebbe fatto da un po' di passato e da un po' di futuro. Fatto sta che quando uno dice: "Ora"... è già dopo, o prima! Chiaro! Mica tanto, insomma.
Volevo dire 'prima' si stava male, 'ora' siamo messi male.
Alcuni degli amici più cari sono un po' scoppiati, altri si illanguidiscono in sane ginnastiche corporali. In Parlamento c'è n'è uno, tutti gli altri sono in galera!
E allora? Non c'è più l'interlocutore? No signori. Dimenticavo i più geniali, siamo qui, noi, i migliori. Intendo dire tutti coloro che sono riusciti a togliersi di dosso la pesantezza di qualcosa che ingombra per dedicarsi allo smitizzante.
Sì, perché di fronte all'idiozia dei vecchi moralisti preferisco vedere l'uomo di cultura che si fa fotografare nudo su un divano a fiori. Eh sì, per questa sua capacità di saper vivere il gioco. Sto parlando insomma di quelli veramente colti che con sottile ironia hanno riscoperto l'effimero.
Ecco che cos'è il presente: l'effimero. E devo dire che per della gente come noi che non crede più a niente è perfetto.
Basta lamentarsi! La cosa più intelligente da fare è quella di giocare d'astuzia con i segnali del tempo.
Ma attenzione, eh. Perché tra l'avere la sensazione che il mondo sia una cosa poco seria e il muoversi dentro perfettamente a proprio agio esiste la stessa differenza che c'è tra l'avere il senso del comico e essere ridicoli.

Il Futuro

Come... come conclusione mi sarebbe molto piaciuto un bel discorso sul futuro. Solo che io sul futuro c'ho ben poco da dire. So solo che un tempo, non so se vi ricordate, si cercava di creare delle prefigurazioni di cose, di... di immagini a cui tendere, sì, quasi dei punti d'arrivo, eh? Erano come delle bellissime fotografie di una società che noi avremmo dovuto... Sì, poi queste immagini invecchiavano, si irrancidivano ma noi continuavamo ad essere affezionati a queste meravigliose fotografie ingiallite nella speranza magari che con una rispolveratina...
No, ora finalmente io non ho futuro. Ora io preferisco pensare che ciò che mi spinge fuori sia solo una conseguenza o meglio una forza che è alle mie spalle. Davanti c'è soltanto uno spazio vuoto.
L'importante è guardarlo attentamente questo spazio vuoto, come se da un momento all'altro le cose potessero uscire dal silenzio e rivelarsi.

Giorgio Gaber

CONTENTS

ABSTRACT

Optical microcavities can find broad application areas, like tunable and compact sources, dynamic filters for optical communications, biological and chemical sensors, etc.

Optical microcavities are key component allowing one to obtain compact laser devices exhibiting small cavity volume and low threshold. Among the different resonators architectures for microcavities laser, photonic crystal (PC) structures are one of the most promising. These structures feature the periodicity in one or more dimensions, and are resonant for light waves of a specific wavelength.

Two-dimensional PCs are planar dielectric waveguide where photons are vertically confined by the vertical profile of the optical index, while the crystal periodicity acts only in the slab plane.

In photonic crystals the refractive index contrast of the periodic structure is high enough to open a full band gap, and thus to fully confine light at very small scale.

Strong coupling is theoretically feasible, and quality factor of more than 10^6 have been experimentally achieved for small modal volumes.

Substantial additional gains are possible with confinement improvement in microfabrication techniques and with implementation of low loss design.

Photonic crystal whose index contrast is lower can be used as DFB gratings. In a DFB device, the laser modes receive feedback at one specific wavelength, determined by the grating period of the structure. The feedback strength is related to the coupling constant, κ, which in turn depends on the grating index contrast, and to the grating length, L. The κL product must be high enough to ensure the feedback required for lasing.

In an optically pumped laser, an external source supplies the excitation energy necessary to get the population inversion. To do that, it must be on resonance with one of the absorption

transitions of the active medium. When the external source provides enough energy, the active material exhibits gain: more photons are generated than lost.

For intense incoming beams, i.e. intense laser sources, multiple-photon absorption processes become appreciable.

It is thus possible to have absorption also by pumping with sources having photon energies lower than the resonance energy of the active medium.

The two-photon absorption (TPA), described from the 3rd order susceptibility, involves the simultaneous absorption of two photons with energy:

$$E_{exc} - E_{ground} = 2\hbar\omega$$

The absorption of the first photon causes the promotion of the electron to the virtual level. Here the simultaneous absorption of the second photon promotes the electron to the real excited state.

The system can then decay to the ground state emitting an up-converted photon, i.e., a photon having energy higher than that of the exciting ones.

A large part of this work is devoted to the realization and characterization of active microresonators behaving as laser sources.

Two main research subjects will be pursued:

- ✓ An integrated InP semiconductors photonic crystal microcavity laser, operating in the telecommunication wavelength.
- ✓ A distributed feedback laser for two-photon induced IR-to-visible up-conversion lasing.

Within the second subject, particular attention will be devoted to the characterization of the two-photon induced emission properties of organic push-pull dyes and II-VI semiconductors quantum dots (QDs) to evaluate their potentiality as candidates for all-solid-state up-converted laser devices.

The third reported research subject is the exploitation of hybrid silica-titania sol-gel films for UV lithography application, finalized to the production of surface relief gratings.

MICROLASER BASED ON EFFECTIVE INDEX CONFINED, SLOW-LIGHT MODES IN PC WAVEGUIDES

This research regards the study of photonic crystal microcavity having small mode volume *V* and high quality factor *Q*, for the production of low threshold integrated laser devices. The light propagation inside the PC is modified because of its periodicity. In this study we exploit the low-

light guided modes at the high symmetry point of the dispersion curve of a PC-W1 waveguide. The PC-W1 waveguide is a PC having triangular symmetry with a missing row of hole along the *ΓK* direction. The linear defect entails the appearance of defect modes with frequencies localized inside the unperturbed PC band gap, and thus modes that exponentially decay inside the PC. The band associated with the defect mode becomes flat at the *K* point of the band diagram, leading to slow-modes whose group velocity goes to zero. The lateral confinement of low-group velocity modes is controlled by locally changing the refractive index of the two dimensional photonic crystal waveguides. The index modulation is induced by post-processing a dielectric strip on top of the two-dimensional PC waveguide. This results in a photonic heterostructure whose confinement properties are the result of the effective index shift and the local curvature of the band associated with the waveguide mode.

In this thesis the results of the device simulation, experimental realization and characterization will be reported.

Computational tools, such as MPB and 3D-FDTD software have been used for the device design and for the study the electromagnetic field behavior inside the cavity.

The realization of the PC structure has been accomplished through lithography techniques like e-beam lithography and reactive ion etching. Intense clean-room activities have been necessary to reach optimized structure quality.

The characterization of the microcavity laser has been pursued with a proper optical set-up, in such a way to determine its performance.

UP-CONVERTED LASING

The up-converted lasing is an alternative method to convert the emission of a cheap, easily available IR laser into that of a more technological valuable visible laser.

It involves the two photon pumping (TPP) mechanism, i.e., the NLO system is excited through the simultaneously absorption of two photons in the near-IR range.

In this work we report our effort towards the realization of a solid-state visible laser device based on a TPP induced emission.

The starting point of this technology is to find a system able to efficiently convert the IR incoming radiation to a visible one.

We have studied the up-conversion process both in push-pull organic dyes embedded in sol-gel hybrid films and in semiconductor core-shell CdSe-CdS-ZnS quantum dots embedded in zirconia films. The excitation source is an amplified Ti:Sapphire laser at 800 nm.

Concerning the organic compounds, it has been possible to characterize the emission properties only in solution, because of their poor photostability when they are embedded in sol-gel matrices.

On the opposite, quantum dots embedded in zirconia films show promising amplified emission properties, with interesting gain value and extremely long time stability.

We have investigated the possibility to implement this material with a distributed feedback optical resonator for obtaining compact and integrated laser devices.

The grating parameters have been determined with MPB software, and first attempts of e-beam lithography of the pattern have been done.

We have also prepared a devoted optical set-up for the optical characterization of the laser devices.

SILICA-TITANIA SOL-GEL FILM FOR DIRECT PHOTOPATTERNIG APLICATIONS

The possibility to exploit the photocatalytic action of hybrid silica-titania sol-gel film towards the decomposition of their organic component, for the direct patterning of surface structure has been investigated. These films have been characterized to study their microstructural properties, and to confirm the presence of crystalline titanium oxo-clusters. Their photocatalytic efficiency has been measured using stearic acid as reference material.

To test the potentiality of this system for UV-lithography, it has been exposed to a UV-lamp.

The organic component decomposition leads to a film shrinkage of about 60%, accompanied by a refractive index increases of about 0.1

By irradiating the spin-coated films through an UV-mask, structures of different shapes and micrometer dimension have been achieved.

ABSTRACT *(Italiano)*

Lo studio delle microcavità ottiche riveste un grande interesse per applicazioni in svariati campi, quali la ricerca di sorgenti laser tunabili e compatte, filtri per le telecomunicazioni, sensori chimici e biologici, etc.

Le microcavità ottiche sono fondamentali per l'ottenimento di dispositivi laser compatti, aventi bassa soglia di emissione laser, ove il campo elettromagnetico è confinato in volumi estremamente ridotti, con conseguente aumento dell'interazione radiazione-materia,.

Tra le possibili architetture della cavità risonante, per dispositivi pompati otticamente, i cristalli fotonici rappresentano una delle soluzioni più promettenti.

Questi ultimi sfruttano la periodicità in una o più direzioni e sono risonanti con determinate lunghezze d'oda della radiazione elettromagnetica.

In un cristallo fotonico bidimensionale il confinamento verticale è garantito dal profilo verticale dell'indice di rifrazione, mentre il confinamento nel piano del cristallo è opera della strutture periodica.

Nei cristalli fotonici il contrasto di indice di rifrazione della struttura periodica è tale da aprire un intervallo completo di energie proibite per la propagazione della radiazione nel mezzo. Essa può quindi essere confinata in volumi molto piccoli, dell'ordine del cubo della lunghezza d'onda, con fattori di qualità sperimentali superiori a 10^6. Inoltre i valori ottenuti sperimentalmente sono inferiori a quelli previsti teoricamente, e ulteriori passi in avanti saranno possibili con lo sviluppo delle tecniche litografiche e di produzione del materiale attivo.

I cristalli fotonici nei quali il contrasto di indice di rifrazione è insufficiente per aprire un *band-gap* completo si comportano come reticoli *distributed feedback*, DFB. In un dispositivo DFB, i modi risonanti ricevono il *feedback* a lunghezze d'onda specifiche, determinate dal periodo del reticolo. La forza dell'accoppiamento è legata alla costante di accoppiamento κ, la quale, a sua

volta, dipende dal contrasto di indice nel reticolo e all'estensione totale del reticolo. Il prodotto *κL* deve essere sufficiente per garantire il *feedback* richiesto per l'emissione laser.

In un laser a pompaggio ottico, una sorgente esterna fornisce al mezzo attivo l'energia di eccitazione richiesta per raggiungere l'inversione di popolazione, requisito necessario per ottenere il guadagno all'interno del mezzo e quindi l'amplificazione.

Affinché si verifichi assorbimento, l'energia del fascio di pompa deve essere in risonanza con una delle transizioni del mezzo attivo. Per campi incidenti molto intensi, come possono essere quelli legati a fasci laser focalizzati, diventano tuttavia apprezzabili anche fenomeni di assorbimento multi fotonici.

Si può quindi avere assorbimento anche utilizzando sorgenti di pompa aventi energie inferiori all'energia di risonanza del mezzo attivo.

L'assorbimento a due fotoni (TPA), legato alla suscettibilità non lineare al terzo ordine, comporta l'assorbimento simultaneo di due fotoni, con energia:

$$E_{exc} - E_{ground} = 2\hbar\omega$$

L'assorbimento del primo fotone promuove l'elettrone dallo stato fondamentale a uno stato virtuale, dal quale esso passa immediatamente allo stato eccitato attraverso l'assorbimento simultaneo di un secondo fotone incidente. Infine il sistema può tornare allo stato fondamentale, attraverso l'emissione di un fotone a energia superiore rispetto ala pompa.

Gran parte del lavoro di dottorato è incentrato sulla realizzazione e caratterizzazione di microcavità attive per l'ottenimento di sorgenti laser.

All'interno di tale attività sono stati studiati due sistemi differenti:

- ✓ Una microcavità laser a semiconduttore, realizzata sfruttando le proprietà dei cristalli fotonici bi-dimensionali, che emette alla lunghezza d'onda delle telecomunicazioni.
- ✓ Un dispositivo laser DFB, pompato oticamente a due fotoni, per la conversione di emissione laser dall'infrarosso al visibile.

All'interno della seconda tematica, particolare attenzione è stata rivolta alla caratterizzazione delle proprietà di emissione indotta a due fotoni di un cromoforo organico e di *quantum dots* di un semiconduttore II-VI, il CdSe, entrambi inglobati in matrice sol-gel.

Un terzo soggetto è costituito dallo studio delle proprietà foto catalitiche di film sol-gel ibridi a base di silica e titania, in vista di possibili applicazioni per il patterning diretto tramite radiazione UV.

CONFINAMENTO DI MODI LENTI IN GUIDA D'ONDA A CRISTALLO FOTONICO PER L'OTTENIMENTO DI MICROCAVITA' LASER

Questa ricerca riguarda lo studio di cavità, ottenute sfruttando cristalli fotonici bidimensionali, a basso volume modale e alto fattore di qualità Q, finalizzate all'ottenimento di dispositivi laser integrati a bassa soglia. Questo lavoro si basa sull'utilizzo dei modi guidati lenti corrispondenti al punto ad elevata simmetria *K* della curva di dispersione di una guida d'onda *W1-PC*.

Una guida d'onda *W1-PC* si ottiene da un cristallo fotonico a simmetria triangolare, attraverso la rimozione di una fila di buche lungo la direzione *ΓK.* In questo modo si introduce un difetto lineare, il quale si riflette nella comparse di modi del difetto, aventi frequenze localizzate all'interno del *band-gap* del cristallo fotonico, che pertanto decadono esponenzialmente all'interno del cristallo. Le bande associate ai modi del difetto hanno curvatura nulla in corrispondenza dei punti a elevata simmetria, e ciò implica una velocità di gruppo del modo nulla in corrispondenza di tali punti.

L'estensione laterale dei modi lenti viene controllata agendo sull'indice di rifrazione del cristallo fotonico, in modo da creare una etero struttura in grado di confinarli efficacemente. L'indice effettivo della guida viene modificato localmente depositando un film di polimero all'interfaccia superiore della guida. La forza del confinamento dipende dall'entità della variazione dell'indice e dalla curvatura della banda associata al modo lento.

L'attività svolta all'interno di questo progetto consiste nel design della struttura, nella sua realizzazione sperimentale e infine nella caratterizzazione ottica del dispositivo.

Per ottimizzare i parametri del dispositivo e comprendere il comportamento della radiazione elettromagnetica all'interno della cavità, sono stati impiegati strumenti di calcolo computazionale, quali i software MPB e TESSA 3D-FDTD.

I parametri delle simulazioni sono stati poi utilizzati per la realizzazione del cristallo fotonico, effettuata tramite tecniche litografiche, quali la litografia con fascio elettronico e l'*etching* ionico.

La caratterizzazione ottica del dispositivo è stata effettuata con un apposito set-up, al fine di determinarne le prestazioni.

EMISSIONE LASER CON CONVERSIONE DI FREQUENZA

La conversione di frequenza laser fornisce l'interessante possibilità di convertire una sorgente laser economica e di facile reperibilità nell'infrarosso, in una sorgente laser nel visibile di enorme interesse tecnologico.

Essa si basa sull'emissione indotta a seguito di processi di assorbimento a due fotoni nel vicino IR.

In questo lavoro verranno presentati gli sforzi profusi e i risultati preliminari ottenuti nella ricerca di un dispositivo laser allo stato solido per la conversione di frequenza.

A tal fine sono state investigate le proprietà di conversione di un cromoforo push-pull organico disperso in matrici sol-gel ibride, e di *quantum dots* di semiconduttore II-VI, CdSe-CdS-ZnS, dispersi in una matrice inorganica a base di zirconia.

Il composto organico presenta interessanti proprietà di emissione indotta a due fotoni in soluzione. Tuttavia la sua scarsa resistenza al pompaggio ottico in matrice solida preclude un suo possibile impiego e rende estremamente problematica la stessa caratterizzazione ottica.

Al contrario i film di QDs-ZrO_2 mostrano una buona efficienza di conversione di frequenza, con valori di guadagno per l'emissione spontanea amplificata interessanti, e elevata stabilità del segnale emesso nel tempo.

E' stata pertanto studiata la possibilità di implementare i film di QDs-ZrO_2 all'interno di una cavità risonante di tipo *distributed feedback* per ottenere un dispositivo laser compatto e integrabile.

I parametri del reticolo sono stati determinati con il software MPB e sono stati fissati in modo da avere amplificazione in corrispondenza del massimo di emissione dei QDs.

Sono tutt'ora in corso delle prove di realizzazione del reticolo DFB tramite litografia elettronica su film sol-gel appositamente sviluppati per il *patterning* diretto.

Infine è stato messo appunto un set-up dedicato per la caratterizzazione ottica dei dispositivi prodotti.

FILM SOL-GEL IBRIDI A BASE DI SILICA-TITANIA PER IL PATTERNING DIRETTO CON LUCE UV

E' stata studiata l'attività fotocatalitica di film sol-gel ibridi a base di silica-titania, promossa dalla radiazione UV.

I film sono stati caratterizzati a livello micro strutturale tramite spettroscopia infrarossa, e sono stati osservati al microscopio elettronico per confermare la presenza di cluster di titanio cristallino al loro interno.

L'efficienza del processo di fotocatalisi è stata determinata mediante test standard che si avvalgono dell'acido stearico come materiale di riferimento. Quest'ultimo infatti è in grado di simulare efficacemente i comuni inquinanti organici, è può essere depositato facilmente per spin-coating.

Successivamente è stata valutata la possibilità di sfruttare l'attività foto catalitica per il patterning diretto dei film. Tale studio parte dall'osservazione che la fotocatalisi si manifesta anche nei confronti della componente organica dei film sol gel ibridi.. Questo fenomeno è accompagnato da una diminuzione dello spessore del film, fino al 60% sullo spessore iniziale, e può pertanto essere sfruttato per la realizzazione di strutture a rilievo.

Test di *patterning* diretto sono stati effettuati irradiando il film con una lampada UV attraverso una maschera in quarzo, ottenendo strutture di dimensione micrometrica ben definite.

OUTLINE OF THE THESIS

The focus of this thesis lies on the study of laser structures and active species for laser emission. The research project consists in two main subjects:

- integrated InP semiconductors photonic crystal microcavity laser source, operating at the telecommunication wavelength,
- distributed feedback laser, for two-photon induced up-conversion lasing, using IR sources.

Moreover the exploitation of hybrid silica-titania sol-gel films for UV lithography applications, finalized to the production of surface relief gratings, has been explored.

Chapter 1 reports a review of the theoretical basis of semiconductors laser. The absorption and stimulated emission mechanisms in bulk and in quantum confined structures, and the basic principles beyond semiconductors microcavities are described.

In Chapter 2 the basic physical concepts of photonic crystal are introduced, in order to aid understanding and interpreting the design rules.

Chapter 3 presents an overview of the computational methods and modeling tools applicable to the analysis and design of photonic crystals. The emphasis is put on the strengths and weakness of each method. The calculation results and the design roles derived are presented in chapter 5.

Chapter 4 describes the employed technologies: e-beam lithography and reactive ion etching, while chapter 5 deals with the description of the fabrication results obtained using these technologies. It reports also the results of the optical characterization.

Chapter 6 introduces the fundamental principles governing non-linear optics, with particular attention to the two-photon absorption processes.

Chapter 7 is devoted to the description of the experimental techniques used for the optical characterization of materials and samples.

Chapter 8 gives an overview of the optical properties of the two classes of materials studied for TPA: organic push-pull chromophores and II-VI core-shell quantum dots.

In Chapter 9 the sol-gel technique and the benefits of using this synthesis for obtaining solid matrices for photonics application are introduced.

Chapter 10 contains the study of the active materials investigated for up-conversion lasing. The emission properties have been characterized to evaluate the potentiality as active medium of a DFB laser system.

In Chapter 11 the design and the realization of a DFB structure are presented; preliminary results of gratings lithography and device characterization are also given.

Chapter 12 is devoted to the exposition of the results from the study of silica-titania photo-sensible films for direct patterning applications.

CHAPTER 1

Basic principles of semiconductor lasers

Semiconductor lasers are lasers based on a semiconductor gain medium. The optical gain is usually achieved by stimulated emission at an interband transition under conditions of a high carrier density in the conduction band.[1] The physical origin of gain in a semiconductor is illustrated in figure 1.1 for the usual case of an interband transition. For semiconductors at room temperature, most of the electrons are in the valence band. A pump beam with photon energy slightly above the band gap energy can excite electrons into a higher state in the conduction band, from where they quickly decay to states near to the bottom of the conduction band. At the same time, the holes generated in the valence band move to the top of the valence band. Electrons in the conduction band can then recombine with these holes, releasing photons with energy near the band gap energy (spontaneous emission). This process can also be stimulated by incoming photons with suitable flux density (stimulated emission). A quantitative description can be based on the Fermi–Dirac distributions for electrons in both bands.

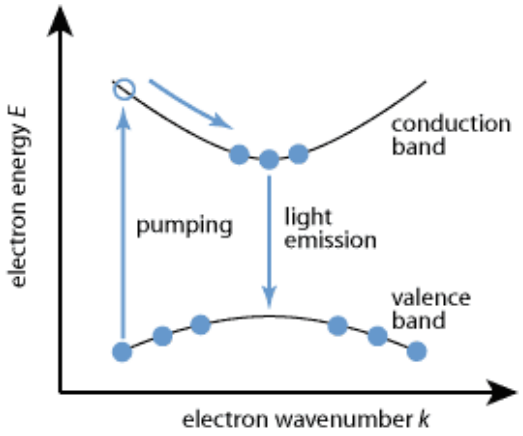

Figure 1.1 *Energy versus k relation for a bulk semiconductor. Physical origin of gain: a pump beam with energies greater than E_g can excite electrons in the valence band to the conduction band. The recombination between holes in the VB and electron in the CB yields to spontaneous and stimulated emission.*

1.1 Energy states[2]

Within the conduction and valence band of a three-dimensional periodic crystalline bulk semiconductor medium, each energy state has a wave function of the form,

$$\boldsymbol{\psi_c(\bar{r}) = u_{c\bar{k}}(\bar{r})e^{j\bar{k}\cdot\bar{r}}} \qquad \text{Eq. 1.1}$$

where $u_{c\bar{k}}(\bar{r})$ has the periodicity of the crystalline lattice. The energy of electrons in the conduction band for a state with a given $\bar{k}$ (known as the parabolic approximation of the energy band structure) is

$$\boldsymbol{E(|\bar{k}|) - E_C = \frac{\hbar^2|\bar{k}|^2}{2m_e}} \qquad \text{Eq. 1.2}$$

A similar expression is obtained for energy states in the valence band,

$$\boldsymbol{E_V - E(|\bar{k}|) = \frac{\hbar^2|\bar{k}|^2}{2m_h}} \qquad \text{Eq. 1.3}$$

E_C is the bottom of the conduction band and E_V is the top of the valence band. The effective masses of the electrons and holes are m_e and m_h.

1.2 Density of energy states

There are a large number of such states per unit energy range (or per unit |k| range), called the density of states. The resultant density of states per unit volume expressions (for bulk materials) in the conduction and valence bands are well known,

$$\boldsymbol{\rho_C(E - E_C)dE = \frac{1}{2\pi^2}\left(\frac{2m_e}{\hbar^2}\right)^{3/2}(E - E_C)^{1/2}dE, \qquad E > E_C} \qquad \text{Eq. 1.4}$$

$$\boldsymbol{\rho_C}\left(\left|\overline{\boldsymbol{k}}\right|\right)\boldsymbol{d}\left|\overline{\boldsymbol{k}}\right| = \frac{\left|\overline{\boldsymbol{k}}\right|^2}{\boldsymbol{\pi^2}}\boldsymbol{d}\left|\overline{\boldsymbol{k}}\right| \qquad \text{Eq. 1.5}$$

and

$$\boldsymbol{\rho_V}(\boldsymbol{E_V}-\boldsymbol{E})\boldsymbol{dE} = \frac{\mathbf{1}}{\mathbf{2}\boldsymbol{\pi^2}}\left(\frac{\mathbf{2}\boldsymbol{m_h}}{\hbar^2}\right)^{3/2}(\boldsymbol{E_V}-\boldsymbol{E})^{1/2}\boldsymbol{dE}, \qquad \boldsymbol{E} > \boldsymbol{E_V} \qquad \text{Eq. 1.6}$$

$$\boldsymbol{\rho_V}\left(\left|\overline{\boldsymbol{k}}\right|\right)\boldsymbol{d}\left|\overline{\boldsymbol{k}}\right| = \frac{\left|\overline{\boldsymbol{k}}\right|^2}{\boldsymbol{\pi^2}}\boldsymbol{d}\left|\overline{\boldsymbol{k}}\right| \qquad \text{Eq. 1.7}$$

Here, the band gap energy E_g is $E_C - E_V$. Note that the density of states as a function of $\left|\bar{k}\right|$ is the same for holes and electrons. This means that, for direct transitions with no change in *k*, the density of induced transitions (as a function of $\left|\bar{k}\right|$) is the same as the density of either the upper or the lower energy states in (1.4-1.7).

1.3 Fermi distribution and carrier densities

The probability of the occupation of the energy states by electrons at equilibrium obeys the Fermi statistical distribution,

$$\boldsymbol{f}(\boldsymbol{E}) = \frac{\mathbf{1}}{\boldsymbol{e}^{(\boldsymbol{E}-\boldsymbol{E_F})/\boldsymbol{kT}}+\mathbf{1}} \qquad \text{Eq. 1.8}$$

where E_F is the Fermi level, k is Boltzmann's constant and T is the absolute temperature on the Kelvin scale. At equilibrium, there is only one Fermi level E_F, situated approximately at the middle of the energy gap. However, in a quasi-equilibrium situation, the probability distributions of electrons in the conduction band and in the valence band have different E_F. When electrons and holes are injected into an active region, there is a quasi-Fermi level, E_{FC}, used for describing the steady state electron distribution in the conduction band, and a quasi-Fermi level, E_{FV}, for the valence band. The $f_C(E)$ and $f_V(E)$ describe separately the probability of occupying the state by electrons at E in the conduction and in the valence band. The hole (i.e. the absence of electrons) distribution is $[1 - f_C(E)]$ in the conduction band and $[1 - f_V(E)]$ in the valence band. Figure 1.2 illustrates the Fermi levels, the band diagram of a direct semiconductor as a function of $\left|\bar{k}\right|$ of the electronic (and hole) state, the Fermi levels, the f_C and the f_V. The Fermi levels are shown with $E_{FC} > E_C$ and $E_{FV} < E_V$, describing the occupation probability of the energy states in degenerate semiconductors.

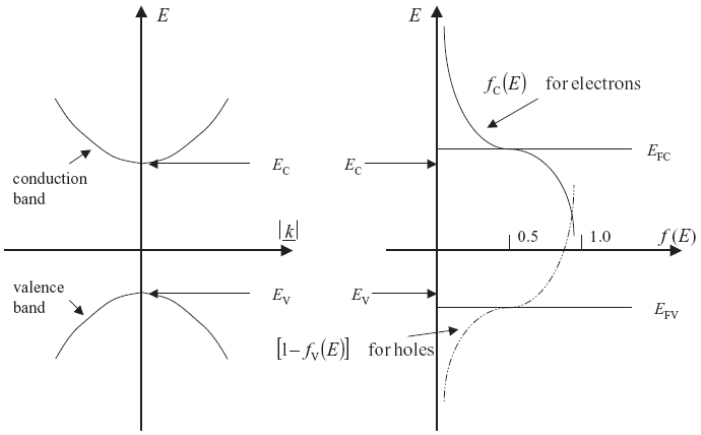

Figure 1.2 *Energy E versus k relation and level occupation probability* $\boldsymbol{f_{C,V}(E)}$ *for conduction and valence bands under thermal equilibrium within each band.*

How are the quasi-Fermi levels controlled by electron and hole densities? The total number of electrons per unit volume in the conduction band, n_C, is given by integration of the product of $\rho_C(E)$ and $f_C(E)$. At 0 K and for electrons, according to Eq. 1.8, all the states above E_{FC} in the conduction band are empty and all the states below E_{FV} in the valence band are occupied. Thus,

$$\boldsymbol{n_C = \int_{E_C}^{\infty} \rho_C(E) f_C(E) dE} \qquad \text{Eq. 1.9}$$

at temperatures close to 0 K becomes:

$$\boldsymbol{n_C \approx \int_{E_C}^{E_{FC}} \rho_C(E) dE = \frac{1}{2\pi^2}\left(\frac{2m_C}{\hbar^2}\right)\frac{2E_{FC}^{3/2}}{3}} \qquad \text{Eq. 1.10}$$

A similar expression for n_V is obtained for the holes. The significance of Eq. 1.10 is that the total number of injected electrons n_C in the conduction band (and the holes in the valence band, n_V) controls the value of quasi-Fermi levels, E_{FC} (and E_{FV}).

The carrier density, thus the Fermi level, is controlled by current injection. The Fermi level in turn controls the gain of the laser material.

1.4 Absorption and stimulated emission

Stimulated emission (or absorption) can take place only when the upper energy state in the conduction band is occupied by an electron (or empty) and when the lower electron energy state in the valence band is empty (or non-occupied by electrons, i.e. occupied by holes). Alternatively, we say that emission takes place when an electron and a hole recombine, and absorption takes place when the radiation generates an

electron–hole pair. Thus, for a specific pair of energy states, the probability for net emission to take place, between an energy state E_2 in the conduction band and state E_1 in the valence band, is proportional to:

$$\boldsymbol{f_C(E_2)[1-f_V(E_1)]-f_V(E_1)[1-f_C(E_2)]=f_C(E_2)-f_V(E_1)} \quad \text{Eq. 1.11}$$

For direct transitions, the $|\bar{k}|$ of the electrons and holes (generated or recombined) does not change, or $k_{electron} \approx k_{hole}$ with $\Delta k \approx 0$. Most semiconductor lasers use direct semiconductor transitions because direct transition probabilities between individual states are much larger than the indirect transitions that involve a change of k. Let the photon energy of the radiation be $h\nu$; then $E_2 - E_1$ should equal the photon energy. The upper and lower levels, E_2 and E_1, for the energy states with eigenvalue $\bar{k}$ are given in Eqs. 1.2 and 1.3:

$$\boldsymbol{E_2 = E_C + \frac{\hbar^2|\bar{k}|^2}{2m_e}}, \quad \text{Eq. 1.12}$$

$$\boldsymbol{E_1 = E_V + \frac{\hbar^2|\bar{k}|^2}{2m_h}}, \quad \text{Eq. 1.13}$$

so

$$\boldsymbol{E_2 - E_1 = h\nu = E_g + \frac{\hbar^2|\bar{k}|^2}{2m_r}}, \quad \text{Eq. 1.14}$$

with

$$\boldsymbol{E_g = E_C - E_V}, \quad \text{Eq. 1.15} \qquad \boldsymbol{\frac{1}{m_r} = \frac{1}{m_e} + \frac{1}{m_h}}, \quad \text{Eq. 1.16}$$

where m_r is the reduced effective mass of the electron–hole pair and E_g is the energy of the band gap. This is a result of the parabolic approximation of the energy band diagram. There are many pairs of energy states that have the same $h\nu$ within a range $d\nu$.

1.5 Transparency condition and population inversion

In the 0 K approximation, f_C and f_V are either zero or unity:

$$\boldsymbol{f_C = u(E_2 - E_{FC}) = u\left(-E_{FC} + E_C + \frac{\hbar^2|\bar{k}|^2}{2m_e}\right)}, \quad \text{Eq. 1.17}$$

$$\boldsymbol{f_V = u(E_1 - E_{FV}) = u\left(-E_{FV} + E_V + \frac{\hbar^2|\bar{k}|^2}{2m_h}\right) = u\left(E_2 - E_g - \frac{\hbar^2|\bar{k}|^2}{2m_r} - E_{FV}\right)} \quad \text{Eq. 1.18}$$

Here, u is the unit step function that equals unity for positive arguments and zero for negative arguments. For a given $h\nu$ (i.e. $E_2 - E_1$) of the radiation, the $|\bar{k}|$ value is given by (1.14). In

order to obtain gain, we need $f_C = 0$, $E_2 < E_{FC}$ and $f_V = 1$, $E_1 > E_{FV}$, or $E_2 - E_1 < E_{FC} - E_{FV}$. Similarly, for absorption we need $E_2 > E_{FC}$, and $E_1 < E_{FV}$.

At other temperatures, we also have gain when

$$\boldsymbol{E_g \leq E_2 - E_1 \leq E_{FC} - E_{FV}}. \qquad \text{Eq. 1.19}$$

Therefore, $E_{FC} - E_{FV} = E_2 - E_1$ is known as the transparency condition of semiconductor lasers. This condition is equivalent to that required for population inversion in solid state and gaseous lasers. E_{FC} (and E_{FV}) is determined by the density of electrons n_C (and holes n_V) in the conduction (and the valence) band. Eq. 1.10 showed this relationship. In other words, there is an n_C (and n_V) value required for achieving transparency, N_{tr}. If the injected carrier density becomes larger than N_{tr}, the semiconductors exibits net gain; if this active medium is then placed in a suitable cavity, laser action occurs when this net gain suffices to overcome cavity losses. Thus, to obtain laser action, injected carriers must reach some threshold value N_{th} larger than N_{tr} by a sufficient margin to allow net gain to overcome cavity losses. Semiconductors laser pumping can be achieved in a number of ways; by far the most convenient way of excitation involves using a laser diode.

1.6 Quantum well semiconductor materials

A double-heterostructure consists of a thin layer of active medium sandwiched between two layers with wider band gap E_g. If the thickness of the active layer is greatly reduced to a point where the dimension becomes comparable to the de Broglie wavelength, a quantum well (QW) double –heterostructure laser is produced. The well thickness L_z is typically in the range of 50 to 150 Å. The more favorable optical property of QWs is that its density of states is lower than the density of states in a bulk material. In fact, as the k_z component is fixed, the density of states per unit volume becomes:

$$\boldsymbol{\rho_{2D}(|\bar{k}|)d|\bar{k}| = \frac{1}{L_z}\frac{|\bar{k}|}{\pi}d|\bar{k}|} \qquad \text{Eq. 1.20}$$

The number of injected carriers required to achieve the transparency condition or the threshold condition for laser oscillation is thus much less in quantum well materials than in the bulk. This effect is significant when L_z is less than 200 Å.

Quantum well structures are typically grown epitaxially on InP or GaAs substrates. Well layers usually have a smaller band gap E_Γ, and barrier layers have a larger band gap E_g, as illustrated

in figure 1.3 for a single well among barriers. The growth direction is designated here as the z axis.

If a large amount of optical gain or absorption is required, multiple quantum wells (MQWs) can be used, with a spacing typically chosen large enough to avoid overlap of the corresponding wave functions: the barrier thickness is typically less than 100 Å, just larger than the evanescent tail of the wave functions of the energy states for quantum wells. For lattice matched well and barrier layers, the materials in the quantum wells have the same periodic crystalline variation in the *xy* directions as the host lattice. The total discontinuity of the band gap energy ΔE_g at the well–barrier interface, $E_g - E_\Gamma$, comprises ΔE_C of the conduction band and ΔE_V of the valence band. In the lateral x and y directions, the material thickness and composition are uniform; to limit the beam size in these directions one must then use a separate confinement structure.

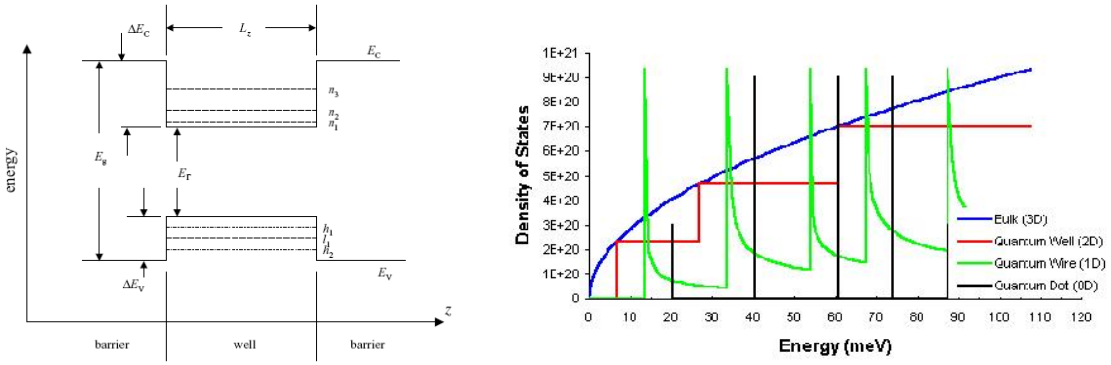

Figure 1.3 *Energy levels Energy band diagram and energy levels of electrons and holes in a quantum well. The thickness of the well is* L_z. *The well with an energy band gap* E_Γ *is sandwiched between barriers with a larger energy band gap* E_g. *The energy levels of the electrons are shown as* n_1, n_2 *and* n_3. *The energy levels of the heavy holes are shown as* h_1 *and* h_2, *while the first energy level of the light holes is shown as* l_1. *(right) Density of states for bulk semiconductors, quantum well, quantum wire and quantum dot.*

1.7 Resonant modes of semiconductor lasers

Resonant cavities of semiconductor lasers are formed on material structures grown epitaxially on semiconductor substrates. They differ from cavities of solid state and gas lasers in several ways. Their dimensions are different. Whereas cavities of solid state and gas lasers have reflectors with lateral dimensions of millimeters and cavity lengths of centimeters or meters, the cavities of semiconductor lasers have typical lateral dimensions of micrometers. The length of a typical long semiconductor laser is less than few hundred micrometers. Whereas the fields of oscillating modes are mostly contained within the gain region in solid state and gas lasers, the size of semiconductor laser resonant modes is often larger than the gain region.

Attenuation of the mode outside the gain region may be high. Thus, optical confinement of the resonant mode is an important design consideration. In some semiconductor lasers, resonance in the longitudinal direction can be obtained by distributed feedback as well as by end reflection. Cavity design must be consistent with the material structure design aimed at current confinement and carrier leakage reduction.

Interest in photonic crystal microcavities, compared to other semiconductor-based structures such as micropillars, microdisks and microtores, relies on the fact that they can exhibit the smallest mode volumes $V \sim 0.3(\lambda/n)^3$. This characteristic can be now simultaneously achieved with very high quality factors ($Q = \omega/\Delta\omega$), up to 10^6, thanks to recent progress in photonic crystal technology and microcavity engineering.

A high Q-factor combined with a very small mode volume can lead to a dramatic enhancement of the spontaneous emission rate of an emitter in resonance with the cavity mode and even to the strong coupling regime between this emitter and the cavity. The factor of merit for spontaneous emission enhancement, known as the Purcell factor[3], is:

$$\boldsymbol{F_P = \frac{3}{4\pi^2}\left(\frac{\lambda_c}{n}\right)^3\left(\frac{Q}{V}\right)} \qquad \text{Eq. 1.21}$$

where (λ_c/n) is the wavelength within the materials and V is the mode volume, in cubic wavelength, of the cavity. All these effects open the route towards single-photon sources[4], single-quantum-dot lasers[5], quantum logical optical gates[6], photonic switches based on photon blockade[7] and, more generally, to quantum electrodynamics in a solid-state cavity. In the next chapter the physics governing the propagation of the electromagnetic radiation within photonic crystals, and the way exploited to confine light at the wavelength scale, is briefly presented.

REFERENCES:

[1] http://www.rp-photonics.com.

[2] William S.C. Chang: Principles of Lasers and Optics, Cambridge University Press, 2005; O. Svelto, Principles of Lasers, Fourth Ed., Plenum Press, 1998.

[3] E.M. Purcell, Phys. Rev., 1946, 69, 681.

[4] S. Laurent, S. Varoutsis, L. Le Gratiet, A. Lemaître, I. Sagnes, F. Raineri, A. Levenson, I. Robert-Philip, I. Abram, Appl. Phys. Lett., 2005, 87, 163107.

[5] S. Strauf, K. Hennessy, M.T. Rahker, Y.S. Choi, A. Badolato, L.C. Andreani, E.L. Hu, P.M. Petroff, D. Bouwmeester, Phys. Rev. Lett., 2006, 96, 127404.

[6] L.M. Duan, H.J. Kimble, Phys. Rev. Lett., 2004, 92, 127902.

[7] K.M. Birnbaum, A. Boca, R. Miller, A.D. Boozer, T.E. Northrup, H.J. Kimble, Nature, 2005, 436, 87.

CHAPTER 2

Photonic Crystal: a magic tool for light manipulation

Since the pioneering demonstration by E. Yablonovitch et al. of a three-dimensional (3D) photonic band gap in the microwave domain,[1] photonic crystals have received a continually growing interest. In the optical domain, most of the works on semiconductor-based photonic crystals have concentrated on two-dimensional structures with the perspective of applications to photonic integrated circuits (PICs) and, more generally, to optical telecommunications. Although technological difficulties made the progress slower than expected, outstanding results recently obtained on photonic crystal microcavities,[2] microguides[3] and microlasers[4] as well as on the integration of these devices,[5] have indeed marked a turning point in the development of 'all-photonic' integrated circuits. In most cases, the device performance still relies on the strong confinement of light that is achieved thanks to photonic band gap effects. However, photonic crystals can also be used in their transmission bands where they exhibit remarkable dispersion properties, opening, in turn, the perspective of new optical functionalities and novel devices. Slow light,[6] super-collimation,[7] superprism,[8] and negative refraction,[9] are some of the fascinating phenomena which strongly motivate the community at this time.

Photonic crystals (PC) are periodic dielectric media, whose modulation, that can extend on one or more directions, allows the control of electromagnetic waves having wavelengths comparable with the PC periodicity. This periodicity can generate by diffraction:

- Some ranges of frequencies at which the density of photonic modes approaches zero, and, as a result, interdicted for photons propagation, called Band Gap (BG).
- Some range of frequency showing a high density of modes, theoretically infinite, which means a group velocity going to zero.[10]

The information about the kinetics of photons inside a given medium are all included inside its band diagram that can be derived from the Maxwell equations in a periodic dielectric medium, as will be discussed in the next section.

By perturbing the crystal periodicity, it is possible to create a single localized mode or a set of closely spaced modes, having frequencies within the BG of the unperturbed PC (i.e. a peak in the crystal's density of state localized inside the BG). If this happen, the defect-induced state must be evanescent inside the unperturbed PC, or in other words, the defect mode cannot penetrate inside the PC: it is forced to stay inside the defect and it decays exponentially inside the PC.

If a linear sequence of unit cells is modified, the linear defects can guide light: the light propagating in the waveguide, with a frequency within the BG of the PC, is confined to the defect and propagates along it.[11] These properties of PC have enabled exciting new ways to control light and construct integrated optical devices.[12]

2.1 Maxwell Equation and periodic media: Band Diagrams

From a general point of view, we are interested in the modification induced by a periodic dielectric medium on the propagating electromagnetic wave. The propagation of light inside a PC as well as inside any linear and lossless media, is governed by the macroscopic Maxwell equations that, in SI units are:

$$\bar{\nabla} \cdot \bar{H}(\bar{r}, t) = 0 \qquad \text{Eq. 2.1}$$

$$\bar{\nabla} \times \bar{E}(\bar{r}, t) + \mu_0 \frac{\partial \bar{H}(\bar{r}, t)}{\partial t} = 0 \qquad \text{Eq. 2.2}$$

$$\bar{\nabla} \cdot [\varepsilon(\bar{r}) \bar{E}(\bar{r}, t)] = 0 \qquad \text{Eq. 2.3}$$

$$\bar{\nabla} \times \bar{H}(\bar{r}, t) - \varepsilon_0 \varepsilon(\bar{r}) \frac{\partial \bar{E}(\bar{r}, t)}{\partial t} = 0 \qquad \text{Eq. 2.4}$$

Where $\bar{E}$ and $\bar{H}$ are functions of time and space that can be expanded into a set of harmonic modes, separating the time dependence from the spatial one:

$$\bar{H}(\bar{r}, t) = \bar{H}(\bar{r}) e^{-i\omega t} \qquad \text{Eq. 2.5}$$

$$\bar{\boldsymbol{E}}(\bar{\boldsymbol{r}},\boldsymbol{t}) = \bar{\boldsymbol{E}}(\bar{\boldsymbol{r}})\boldsymbol{e}^{-\boldsymbol{i}\boldsymbol{\omega}\boldsymbol{t}} \qquad \text{Eq. 2.6}$$

Then the decoupled equations for the magnetic and electric field become:

$$\bar{\nabla} \times \left(\frac{1}{\varepsilon(\bar{r})}\bar{\nabla} \times \bar{\boldsymbol{H}}(\bar{\boldsymbol{r}})\right) = \left(\frac{\omega}{c}\right)^2 \bar{\boldsymbol{H}}(\bar{\boldsymbol{r}}) \quad \bar{\nabla} \times \left(\frac{1}{\varepsilon(\bar{r})}\bar{\nabla} \times \bar{\boldsymbol{E}}(\bar{\boldsymbol{r}})\right) = \left(\frac{\omega}{c}\right)^2 \bar{\boldsymbol{E}}(\bar{\boldsymbol{r}}) \qquad \text{Eq. 2.7}$$

To make this equation looks more like a traditional eigenvalue problem we identify the left side of the above equation as an operator $\hat{\Theta}$ acting on $\bar{H}(\bar{r})$:

$$\hat{\boldsymbol{\Theta}}\bar{\boldsymbol{H}}(\bar{\boldsymbol{r}}) = \left(\frac{\omega}{c}\right)^2 \bar{\boldsymbol{H}}(\bar{\boldsymbol{r}}) \qquad \boldsymbol{with} \quad \hat{\boldsymbol{\Theta}} = \bar{\nabla} \times \frac{1}{\varepsilon(\bar{r})}\bar{\nabla} \times \qquad \text{Eq. 2.8}$$

The eigenvectors $\bar{H}(\bar{r})$ are the spatial patterns of the harmonic modes, and the eigenvalues $(\omega/c)^2$ are proportional to the squared frequencies of those modes.

In a PC the information about the periodicity is contained in the dielectric function, so that, for a given wavevector $\bar{R}$ of the direct lattice it is possible to write:

$$\boldsymbol{\varepsilon}(\bar{\boldsymbol{r}} + \bar{\boldsymbol{R}}) = \boldsymbol{\varepsilon}(\bar{\boldsymbol{r}}) \qquad \text{Eq. 2.9}$$

The operator $\hat{\Theta}$ is Hermitian and possesses the same translation symmetry. According with the Bloch's theorem we can chose the eigenstates $\bar{H}(\bar{r})$ to have the form of a plane wave, times a function with the periodicity of the PC lattice:

$$\bar{\boldsymbol{H}}_{\bar{\boldsymbol{k}}}(\bar{\boldsymbol{r}}) = \boldsymbol{e}^{i\bar{\boldsymbol{k}}\cdot\bar{\boldsymbol{r}}}\bar{\boldsymbol{h}}_{\bar{\boldsymbol{k}}}(\bar{\boldsymbol{r}}) \qquad \text{Eq. 2.10}$$

where

$$\bar{\boldsymbol{h}}_{\bar{\boldsymbol{k}}}(\bar{\boldsymbol{r}} + \bar{\boldsymbol{R}}) = \bar{\boldsymbol{h}}_{\bar{\boldsymbol{k}}}(\bar{\boldsymbol{r}}) \qquad \text{Eq. 2.11}$$

and $\bar{k}$, Bloch's wavevector, belongs to the first Brillouin zone of the reciprocal lattice.[13]

The allowed modes (for photons) result from the calculation of $\bar{h}_{\bar{k}}$ and of $\omega(\bar{k})$ for every wavevector $\bar{k}$ of the first Brillouin zone. The ensemble of the discrete solutions of ω constitutes the band diagram of the considered optical system.

2.2 Bi-dimensional triangular lattice

In this paragraph, we present a bi-dimensional triangular lattice, reported in figure 2.1(a). The triangular symmetry is generally preferred for the crystal since it allows obtaining an in-plane band gap at least for one of the two polarizations of the light: the TE polarization with the electric field in the PC plane for holes array, or the TM polarization with the electric field perpendicular to the PC plane for the pillars array (see figure 2.1(c) for the case of holes array). Since the functions $\omega_n(\bar{k})$ posses the symmetry of the point group, we need not to consider them at every $\bar{k}$ point in the Brillouin zone.

The smallest region within the Brillouin zone for which the $\omega_n(\bar{k})$ are not related by symmetry is called the irreducible Brillouin zone. This latter correspond to the green region in figure 2.1(b) marked out by the high symmetry point Γ, K, M and it is sufficient to obtain the description of the dispersion properties of this PC. The ΓK direction of the reciprocal lattice corresponds to the nearest neighbors of the real lattice, while the ΓM direction corresponds to the direction of the second neighbors. Now that the study's domain for the curve dispersion has been defined, we can analyze the band diagram, calculated with the plane waves method described in the following chapter.

It clearly appears that the photon behavior is deeply affected when they travel inside a periodic structure instead of a homogeneous medium. Photons, that do not interact when travelling

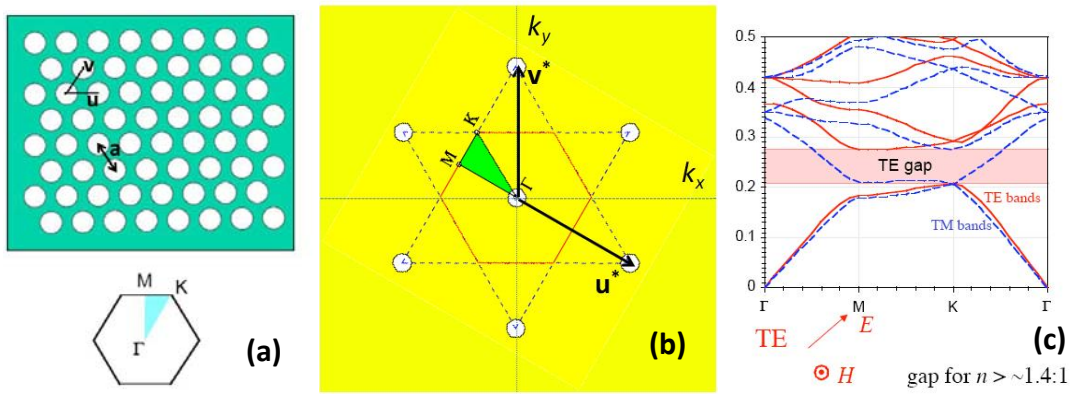

Figure 2.1 *(a) Triangular crystal lattice, with period a and primitive vectors of the unit cell u,v. (b) Reciprocal lattice and 1st Brillouin zone (red line hexagon). The primitive vectors of the reciprocal lattice u^*,v^* are also reported, together with the representation of the irreducible Brillouin zone (green triangle).The vertices of this zone are the high symmetry points Γ,K,X, and the lines connecting these point, ΓK, ΓM and MK, are the high symmetry directions. (c) Band diagram associated with a triangular lattice. The modes with TE polarization present a forbidden band, that is not present for the TM modes.*

through a homogeneous medium, are now forced to "see" other photons by the mediation of the periodic medium.

The travelling light is diffused by the lattice and undergoes multiple reflections that are strongly destructive near the high symmetry point of the Brillouin zone. This, given a strong index contrast, can involve the appearance of a range of energy forbidden for photon propagation at the border along the high symmetry directions.

On the other hand the density of electromagnetic (EM) states, associated with the symmetry point of the band diagram, results greatly enhanced. Near this point the slope of the band is very small and the crystal supports slow light modes (SLMs). In fact, starting from the relation $\omega - \omega_0 = \frac{1}{2}\alpha(\bar{k} - \bar{k}_0)^2$ for the dispersion bands, the group velocity for photons is defined as:

$$\boldsymbol{v_g = \frac{\partial \omega}{\partial \bar{k}} = \alpha\left(\bar{k} - \bar{k}_0\right) = \frac{\alpha}{\sqrt{A}}} \qquad \text{with} \quad \boldsymbol{A = \alpha \tau_0} \qquad \text{Eq. 2.12}$$

where α is the band curvature, A is the mode size and τ_0 is the photon lifetime. If the curvature α is very small, the mode size becomes smaller than the irradiated area, and wave guided photons injected by the incident wave do not escape out from the illuminated area before being coupled back to the radiated modes. In other words, owing to their small group velocity, SLMs experience a stronger effective electromagnetic interaction with their environment than conventional modes with larger group velocity. This property makes SLMs an asset in achieving enhanced non-linear effects,[14] or low threshold laser emission.[15] However the main drawback of the modes of a defect free crystal is that they are spatially delocalized. This leads to practical problems in the design of compact photonic microstructures, and also implies a more fundamental problem: if the mode size is only limited by its losses, or alternatively, if a large quality factor requires a large PC structure, haw can be possible to design a structure exploiting band-edge SLMs with an high ratio of the quality factor Q to the mode volume V, necessary to foster enhanced radiation dynamics? For this reason new approaches based on graded lattice have been proposed, in such a way to confine these modes.[16]

2.3 Photonic Crystal slabs

Photonic Cristal slabs derive from 2D-PCs, that are periodic along two of their axis and homogeneous along the third axis, introducing a finite dimension along the homogeneity axis. The typical arrangement of a PC slab in semiconductor technology is that of a periodic array of holes etched through one or several semiconductor layers forming a planar waveguide. They have been proposed as a more-easily fabricated alternative to true three-dimensionally periodic photonic crystals. PC slabs present two relevant advantage: they are compatible with microstructuring techniques currently employed that do not allow to obtain large etching depth, and, as they are compatible with classical wave guided optics, they satisfy the basic condition for the integration of PC inside integrated photonic circuit. Although their structure and properties strongly resemble those of two dimensional crystals, slab systems require a fundamentally different, three-dimensional approach. The finite height extension of these structures causes the loss of invariance along the z direction. Furthermore the vertical structuration can introduce losses that are not foreseen for the 2D case, lead in to the introduction of the notions of light cone and photon lifetime (see figure 2.2(b)).

In PC slabs, light waves are confined by a combination of in-plane BG confinement and vertical total-internal-reflection (TIR) confinement.[17] A typical specimen, consisting of a triangular lattice of air holes on a dielectric slab, is shown in Figure 2.2(a). For certain values of holes spacing, the crystal can have a BG in the *xy* plane: it can exist only for specific direction or also for any direction within the plane. Inside this gap, no extended states are permitted, and incident light is reflected. The triangular lattice offers, in two dimensions, the maximum of forbidden bands, associated with all crystallographic directions. The information about the kinetics of photons inside a given medium are all included inside its band diagram: in our case, these are the ensemble of relations governing the wavelength and frequency of modes propagating within a bi-dimensional triangular lattice.

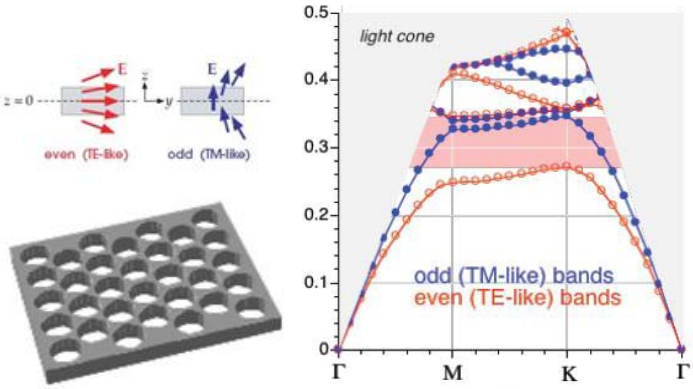

Figure 2.2 *PC slab derives from 2D-PC introducing a finite dimension along the axis of homogeneity. It is possible to distinguish between even and odd modes, depending on their symmetry with respect to the mirror plane of the slab. The light cone appears: the modes in the light cone are modes propagating in the air; the modes above are confined in the slab.*

2.4 Vertical structuration and mode parity

The EM field translation invariance along z typical of infinite 2D-PCs is broken by the vertical structuration, and the EM field must obey the field continuity condition at the dielectric interfaces. The guiding slab can support, depending on its thickness, modes showing a gradually higher numbers of vertical oscillations: the fundamental mode shows a half-oscillation inside the guiding slab, the higher order modes present nodes inside it. Due to the lack of translational symmetry in the vertical direction, it is no more possible to think in terms of TE and TM polarized modes, since they are no more decoupled, but it is possible to distinguish between symmetric (even) and antisymmetric (odd) modes, looking to their symmetry with respect to the horizontal symmetry plane bisecting the slab.

These even and odd states have strong similarities with TE and TM states, respectively, in two dimensions; in fact, in the mirror plane itself, the even and odd states are purely TE, and TM,

respectively. It is not surprising, then, that the slab of rods has a gap in its odd modes, and the slab of holes has a gap in its even modes. One important thing to be outlined is that the odd modes vanish at the slab center, and thus cannot interact with an active material placed at the center of the slab; for this reason we will work only with even modes. What explained above is rigorously true only for slab surrounded by air, where the symmetry plane exists, but can be extended for slab on a low index substrate, provided that the index contrast is high enough for the guided modes to be sufficiently localized within the slab, so that the surrounding is only a small perturbation. In fact, in order to maintain the distinction between even and odd guided modes, it is only necessary to preserve mirror symmetry where the guided modes have non-negligible amplitude.

2.5 The light cone

The element distinguishing slabs from ordinary photonic crystals is the light cone, a continuum of states indicated by a shaded region in figure 2.2(b). The light cone consists of states, or radiation modes, that are extended infinitely in the region outside the slab. For a homogeneous medium, with index n, the light cone is defined as the region above the light line, defined as:

$$\boldsymbol{\omega}(\boldsymbol{k}_{//}) = \frac{\boldsymbol{c}}{\boldsymbol{n}}\boldsymbol{k}_{//} \qquad \text{Eq. 2.13}$$

where $k_{//}$ is the component of the propagation vector projected in the guide plane.

Guided modes, which are states localized to the plane of the slab, can only exist in the regions of the band diagram outside the light cone. Any state that lies below the light cone in the band diagram cannot couple with radiation modes. Thus, the discrete bands below the light cone are guided, i.e. the states are infinitely extended within the plane of the slab, but decay exponentially into the surrounding region. This confinement is analogous to total internal reflection, and is due to the guided modes seeing a higher effective index in the slab than in the surrounding regions. When a guided band reaches the edge of the light cone, it becomes a resonant state: it extends, albeit with low amplitude, infinitely far into the background, and cannot be used to permanently confine light within the slab.

In conclusion, considering a 2D-PC of finite height, three types of modes can be considered:

- ✓ The modes belonging to the continuum of the light cone region, which are the sinusoidal solutions of the propagation equation of a plane waveguide in all the point of the space, and thus are completely delocalized.

- ✓ The guided modes, completely confined inside the waveguide, that cannot couple with radiation modes, and thus posses a theoretical infinite lifetime within the waveguide. These modes are located below the light line.
- ✓ The quasi-guided modes, strongly localized inside the slab, but that have a non-zero radiation component induced by the lattice, responsible of losses in the vertical direction. These kinds of modes, located inside the light cone, constitute the resonances of the radiative continuum.

2.6 Linear defects: PC waveguide and microcavities

As anticipated in the introduction, by introducing a defect inside the PC it is possible to generate one or more modes with frequencies localized inside the BG, and thus modes that exponentially decay inside the PC.[18] This engineered defect has been exploited for a great

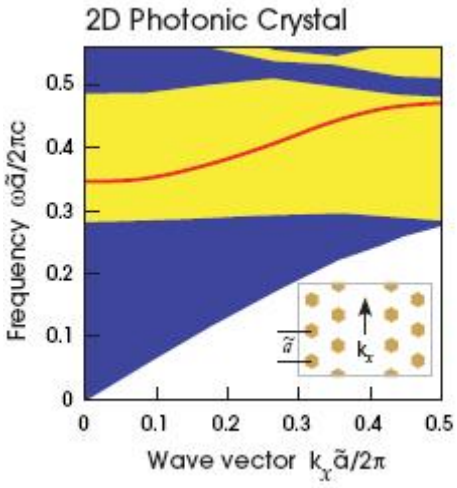

Figure 2.3 *Band diagram for a W1 waveguide: a propagation state appears within the band gap of the PC. The frequencies associated with that level are localized inside the defect by diffraction and can propagate for long distance without losses.*

number of applications, like microcavities, waveguides, channel-drop filters, lossless bends, wide angle splitters, non linear switches, bistable switches, and so on.[19] Without making a detailed description of the different possible defects realized, we simply report the two most common configurations, concerning bi-dimensional lattice of holes:

- The omission of localized holes, to obtain resonant microcavities.
- The removal of row of holes resulting on corridors for light based on diffraction processes, rather than on total internal reflection, like in traditional waveguides.

This latter is represented in the band diagram above. The PC showed in the inset of figure 2.3 still has one direction within the plane for which discrete translational symmetry is preserved;

in this case, the x directions. Thus the corresponding wavevector k_x is still a conserved quantity. For this reason the structure acts as a waveguide: it is a truly channel along which light propagates with a group velocity $v_g = \frac{d\omega}{dk_x}$ that can be either positive (forward-propagating modes) or negative (backward-propagating modes). Like in the case of the unperturbed PC, described in section 2.1, the ensemble of the discrete solutions $\omega(k_x)$ generates the dispersion band for the propagation of light inside the linear defect, where a mode to be guided needs a combination (k_x, ω) that is forbidden in the crystal. Moreover, thanks to the periodic structure of waveguide edges, the band becomes flat like in the unperturbed PC, and thus the group velocity can go to zero (slow light modes). Recent experiments carried out by the Vlassov's group showed that the speed of light was reduced by a factor of more than 100 in a W1 waveguide.[20] In analogy with the bi-dimensional case several approaches have been proposed for the confinement of these SLMs along the k_x direction, in such a way to obtain very small mode volume.[21] Last decisive progress was accomplished by the Noda's group, first on small elongated cavities of the L3 type,[22] then on the so-called 'photonic heterostructures.[23] The photonic heterostructure is made of a small photonic crystal waveguide section sandwiched between two similar waveguides but with a slightly different lattice period. Because there is no hole to scatter the light at the cavity edges (i.e. at the edges of the middle waveguide section), the level of out-of-plane scattering losses is much lower than in other systems. Impressive results obtained on photonic heterostructures in the silicon membrane technology are now approached in III–V semiconductors.[24] Another approach, that leads to a predicted Q-factor of $\sim 7\times10^7$ is based on the modulation of the line defect. The confinement in the direction of a line defect results from the existence of a mode gap in the waveguide. The location of the mode gap can be changed by changing the geometrical parameters (such as the width) of line-defect waveguides. This makes it possible to create a local confinement potential within theoretically lossless waveguides.[25]

The confinement properties, which can lead to extremely high Q-factors, provided that the boundaries of the resonator are carefully adjusted, have been explained by Song et al. by looking at the complex dispersion relation of the W1 waveguide using an analytic continuation of the wave vector.[26]

However all the approaches reported above require processes that are at the utmost of the present technological capability. Here an original and technologically less extreme approach, based on a locally induced change of the effective index of the semiconductor waveguide, is

presented. This has been obtained by a successive deposition of a PMMA rectangle above the W1 waveguide. Similar approaches have been at the same time proposed independently by Noda et al[27] and Smith et al.[28]

The confinement properties of these heterostructures have been demonstrated qualitatively using an envelope formalism inspired to the work of Charbonneau-Lefort et al.[29], which adapts the formalism originally applied to electrons in a perturbed periodic lattice to the case of optical modes inside a PC heterostructure.

REFERENCES

[1] E. Yablonovitch, T.J. Gmitter, K.M. Leung, Phys. Rev. Lett., 1991, 67, 2295.

[2] T. Asano, B.S. Song, S. Noda, Opt. Express, 2006, 14, 1996.

[3] E. Dulkeith, S.J. McNab, Y.A. Vlasov, Phys. Rev. B, 72, 115102, (2005); S. Assefa, S.J. McNab, Y.A. Vlasov, Opt. Lett., 2006, 31 745.

[4] H.-G. Park, S.H. Kim, S.H. Kwon, Y.G. Ju, J.K. Yang, J.H. Baek, S.B. Kim, Y.H. Lee, Science, 2004, 305, 1444.

[5] K. Asakawa, M. Sugimoto, K. Watanabe, N. Ozaki, A. Mizutani, Y. Takata, Y. Kitagawa, H. Ishikawa, N. Ikeda, K. Awazu, A. Watanabe, S. Nakamura, S. Ohkouchi, K. Inoue, M. Kristensen, O. Sigmund, P.I. Borel, R. Baets, New J. Phys., 2006, 8, 208.

[6] M. Notomi, K. Yamada, A. Shinya, J. Takahashi, C. Takahashi, I. Yokohama, Phys. Rev. Lett., 2001, 87, 253902.

[7] H. Kosaka, T. Kawashima, A. Tomita, M. Notomi, T. Tamamura, T. Sato, S. Kawakami, Appl. Phys. Lett., 1999, 74, 1212.

[8] H. Kosaka, T. Kawashima, A. Tomita, M. Notomi, T. Tamamura, T. Sato, S. Kawakami, Phys. Rev. B, 1998, 58, R10096.

[9] M. Notomi, Phys. Rev. B, 2000, 62, 10696; C. Luo, S.G. Johnson, J.D. Jouannopoulos, J.B. Pendry, Phys. Rev. B, 2002, 65, R201104; P.V. Parimi, W.T. Lu, P. Vodo, J. Sokoloff, J.S. Derov, S. Sridhar, Phys. Rev. Lett., 2004, 92, 127401.

[10] C. Grillet Microcomposant Optique a base de Cristaux Photoniques bidimensionels pour l'optique integree, Ph.D. Thesis, Ecole Centrale de Lyon, 2003

[11] J.A. Joannopoulos, S.G. Johnson, J.N. Winn, R.D. Meade; Photonic Crystals : Molding the Flow of Light, 2nd edition, Princeton University Press, 2007

[12] A. Mekis, J. C. Chen, I. Kurland, S. Fan, P. R. Villeneuve, J. D. Joannopoulos, Phys. Rev. Lett., 1996, 77, 3787; X. Letartre, C. Seassal, C. Grillet, P. Rojo-Romeo, P. Viktorovitch, M. Le Vassor d'Yerville, D. Cassagne, C. Jouanin, Appl. Phys. Lett., 2001, 79, 2312; M. Loncar, D. Nedeljkovic, T. P. Pearsall, J. Vuckovic, A. Scherer Appl. Phys. Lett., 2002, 80, 1689; Y. Akahane, M. Mochizuki, T. Asano, Y. Tanaka, S. Noda, Appl. Phys. Lett., 2003, 82, 1341; S. –H. Kim, H. –Y. Ryu, H. –G. Park, G. –H. Kim, Y. –S. Choi, Y. –H. Lee, Appl. Phys. Lett., 2002, 81, 2499; S. Fan, S. G. Johnson, J. D. Joannopoulos, C. Manolatou, H. A. Haus J. Opt. Soc. Am. B, 2001, 18, 162; M. Loncar, T. Yoshie, A. Scherer, P. Gogna, Y. Qiu, Appl. Phys. Lett., 2002, 81, 2680.

[13] N. W. Ashcroft and N. D. Mermin, Solid State Phisics, Ed: Thomson Brooks/Cole.

[14] A.M. Yacomotti, P. Monnier, F. Ranieri, B. Ben Bakir, C. Seassal, R. Raj, J. A. Levenson, Phys. Rev. Lett., 2006, 97, 143904.

[15] C. Monat, C. Seassal, X. Letartre, P. Regreny, P. Rojo-Romeo, P. Viktorovitch, M. Le Vassor d'Yerville, D. Cassagne, J. P. Albert, E. Jalaguier, S. Pocas, and B. Aspar, Appl. Phys. Lett., 2002, 81, 5102; B. Ben Bakir, C. Seassal, X. Letartre, P. Viktorovitch, M. Zussy, L. Di Cioccio, and J. M. Fedeli, Appl. Phys. Lett., 2006, 88, 081113.

[16] K. Srinivasan, O. Painter, Opt. Expr., 2003, 11, 579; K. Srinivasan, P. E. Barclay, O. Painter, Opt. Expr., 2004, 12, 1458; F. Bordas, M. J. Steel, C. Seassal, A. Rahmani, Opt. Expr., 2007, 15, 10890; F. Bordas, C. Seassal, E. Dupuy, P. Regreny, M. Gendry, M. J. Steel, A. Rahmami, CLEO/QELS May 7-11 2007, Baltimore.

[17] S. G. Johnson, S. Fan, P. R. Villeneuve, J. D. Joannopoulos, L. A. Kolodziejski, Phys. Rev. B, 1999, 60, 5751.

[18] E. Yablonovitch, T. J. Gmitter, R. D. Meade, A. M. Rappe, K. D. Brommer, J. D. Joannopoulos, Phys. Rev. Lett., 1991, 67, 3380.

[19] R. D. Meade, K. D. Brommer, A. M. Rappe, J. D. Joannopoulos, Phys. Rew. B, 1991, 44, 13772; A. Mekis, J. C. Chen, I. Kurland, S. Fan, P. R. Villeneuve, J. D. Joannopoulos, Phys. Rev. Lett., 1996, 77, 3787; S. Fan, P. R. Villeneuve, J. D. Joannopoulos, H. A. Haus, Phys. Rev. Lett., 1998, 80, 960; X. Letartre, C. Seassal, C. Grillet, P. Rojo-Romeo, P. Viktorovitch, M. Le Vassor d'Yerville, D. Cassagne, C. Jouanin, Appl. Phys. Lett., 2001, 79, 2312; S. Fan, S. G. Johnson, J. D. Joannopoulos, C. Manolatou, H. A. Haus, J. Opt. Soc. Am. B, 2001, 18, 162; K. Srinivasan, O. Painter, Opt. Exp., 2002, 10, 670; M. Notomi, A. Shinya, S. Mitsugi, G. Kira, E. Kuramochi, T. Tanabe, Opt. Expr., 2005, 13, 2678.

[20] Y.A. Vlasov, M. O'Boyle, H.F. Hamann, S.J. McNab, Nature, 2005, 438, 65.

[21] Y. Akahane, T. Asano, B. S. Song, S. Noda, Nature, 2003, 425, 944; B.S. Song, S. Noda, T. Asano, Y. Akahane, Nature Mater., 2005, 4, 207; E. Kuramochi, M. Notomi, S. Mitsugi, A. Shinya, T. Tanabe, T. Watanabe, Appl. Phys. Lett., 2006, 88, 041112; T. Asano, B.-S. Song, Y. Akahane, S. Noda, IEEE J. Sel. Topics Quantum Electron., 2006, 12, 1123; Y. Tanaka, T. Asano, S. Noda, IEEE J. Sel. Topics Quantum Electron., 2008, 26, 11, 1532.

[22] Y. Akahane, T. Asano, B.S. Song, S. Noda, Nature, 2003, 425, 944.

[23] B.-S. Song, S. Noda, T. Asano, Y. Akahane, Nature Mater., 2005, 4, 207; Y. Tanaka, T. Asano, S. Noda, J. Lightwave Techn., 2008, 26, 1532.

[24] E. Weidner, S. Combrié, A. de Rossi, N.V.Q. Tran, S. Cassette, Appl. Phys. Lett., 2007, 90, 101118.

[25] E. Kuramochi, M. Notomi, S. Mitsugi, A. Shinya, T. Tanabe, Appl. Phys. Lett., 2006, 88, 041112.

[26] B.-S. Song, T. Asano, S. Noda, New J. Phys., 2006, 8, 209.

[27] S. Tomljenovic-Hanic, C. M. de Sterke, M. J. Steel, B. J. Eggleton, Y. Tanaka, S. Noda, Opt. Expr., 2006, 15, 17250.

[28] C. L. C. Smith, D. K. C. Wu, M. W. Lee, C. Monat, S. Tomljenovic-Hanic, C. Grillet, B. J. Eggleton, D. Freeman, Y. Ruan, S. Madden, B. Luther-Davies, H. Giessen, Y.-H. Lee, Appl. Phys Lett, 2007, 91, 121103.

[29] M. Charbonneau-Lefort, E. Istrate, M. Allard, J. Poon, E. H. Sargent, Phys. Rev. B, 2002, 65, 125318.

CHAPTER 3

Computational methods and modeling tools

Mathematical and computational tools are of basic importance for the study of optical systems. These tools solve the Maxwell equation for periodic (or translationally-symmetric) systems, such as photonic crystals or waveguides, giving quantitative theoretical predictions. This makes it possible and preferable to optimize the design of PCs on a computer, and then manufacture them. There are two common computational approaches to studying dielectric structures such as photonic crystals: the frequency- and the time-domain. Frequency-domain methods are in many ways better-suited to calculating band structures and eigenstates. We have employed the open-source software MPB (MIT Photonic Bands a software package developed at MIT from Steven G. Jonhson), that compute fully-vectorial eigenmodes of Maxwell's equations with periodic boundary conditions by preconditioned conjugate-gradient minimization of the block Rayleigh quotient in a plane wave basis.[1]

The other approach is the direct simulation of Maxwell's equations over time on a discrete grid by finite-difference time-domain (FDTD) algorithms. The FDTD method is a very general method for calculating electromagnetic field distributions in structures of arbitrary geometry.[2] It can be very accurate since it is based on a direct discretization of Maxwell's equations, both for time and space, where the differentials are replaced by finite differences, making no assumptions on

the kind of solution or the propagation direction of waves. Starting from a given field distribution, driven by sources at given locations, the time-evolution of the electromagnetic field is calculated over a given spatial domain. Another advantage of the FDTD is that it provides results for a large range of frequencies in a single run. For these reasons, it is well suited for modeling photonic crystal structures and to compute the evolution of the fields, as the transmission and the resonance decay-time. We have employed Tessa, a three-dimensional simulation software for optical systems, based on the FDTD method, and developed in the INL laboratory, Ecole Centrale de Lyon.[3]

3.1 Plane waves method

The plane waves method is a frequency-domain method, taking advantage of the spatial periodicity of $\varepsilon(\bar{r})$ to expand both $\varepsilon(\bar{r})$ and the electromagnetic field in truncated Fourier series. The terms in the series are *N* plane-waves:[4]

$$\boldsymbol{\eta}(\bar{\boldsymbol{r}}) = \sum_{\boldsymbol{m=1}}^{\boldsymbol{N}} \boldsymbol{\eta}(\bar{\boldsymbol{G}}_{\boldsymbol{m}}) \boldsymbol{e}^{\boldsymbol{i}\bar{\boldsymbol{G}}_{\boldsymbol{m}}\cdot\bar{\boldsymbol{r}}} \qquad with\ \boldsymbol{\eta}(\bar{\boldsymbol{r}}) = \boldsymbol{\varepsilon}(\bar{\boldsymbol{r}})^{-\mathbf{1}} \qquad \text{Eq. 3.1}$$

$$\bar{\boldsymbol{H}}(\bar{\boldsymbol{r}}) = \sum_{\boldsymbol{m=1}}^{\boldsymbol{N}} \bar{\boldsymbol{h}}(\bar{\boldsymbol{G}}_{\boldsymbol{m}}) \boldsymbol{e}^{\boldsymbol{i}(\bar{\boldsymbol{k}}+\bar{\boldsymbol{G}}_{\boldsymbol{m}})\cdot\bar{\boldsymbol{r}}} \qquad \text{Eq. 3.2}$$

where $\bar{G}_m$ are the reciprocal lattice vectors related with the lattice vector $\bar{R}_m$ through:

$$\bar{\boldsymbol{G}}_{\boldsymbol{m}} \cdot \bar{\boldsymbol{R}}_{\boldsymbol{n}} = \mathbf{2}\boldsymbol{\pi}\boldsymbol{\delta}_{\boldsymbol{m,n}} \qquad \text{Eq. 3.3}$$

and $\bar{k}$ are wave vectors of the 1st Brillouin zone.

Eqs. (3.1) and (3.2) become exact as the numbers *N* of basis functions go to infinity, assuming a complete basis.

Using (3.1) and (3.2), (2.8) becomes:

$$\sum_{\boldsymbol{m=1}}^{\boldsymbol{N}} \left(\bar{\boldsymbol{k}} + \bar{\boldsymbol{G}}_{\boldsymbol{m}}\right) \cdot \left(\bar{\boldsymbol{k}} + \bar{\boldsymbol{G}}_{\boldsymbol{n}}\right) \cdot \boldsymbol{\eta}(\bar{\boldsymbol{G}}_{\boldsymbol{m}} - \bar{\boldsymbol{G}}_{\boldsymbol{n}}) \cdot \bar{\boldsymbol{h}}_{\boldsymbol{m}} = \left(\frac{\boldsymbol{\omega}}{\boldsymbol{c}}\right)^{\mathbf{2}} \bar{\boldsymbol{h}}_{\boldsymbol{n}} \qquad \text{Eq. 3.4}$$

This method allows the calculation of the band diagram of homogeneous photonic crystals. In order to calculate the dispersion curves of more complex structures, like a linear waveguide, this method must be adapted. The introduction of the linear defect, a row of omitted holes along the first neighbors' direction for the W1 guide, breaks the periodicity and introduces a favored direction for the modes propagation. However, the plane wave method requires the periodicity along the three space directions. To retrieve this periodicity, the elementary cell is replaced with a supercell (figure 3.1), containing several unit cells, and obeying the system symmetry. The repetition of the supercell along the three directions leads to a lattice of parallel waveguides. The supercell dimension along the *y* direction must be sufficient to prevent

artificial interactions, without correspondence in reality, between modes propagating in neighboring waveguides.

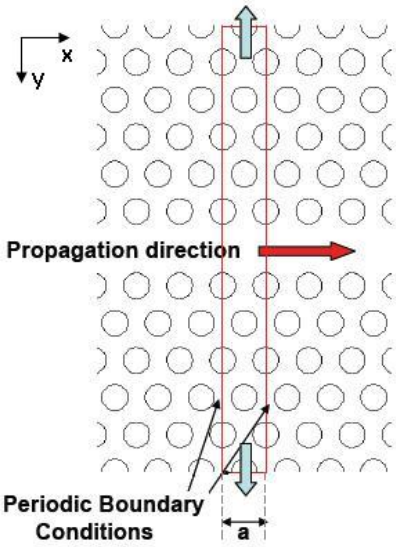

Figure 3.1 *Supercell employed for the calculation of the W1-PC guide.*

3.2 FDTD Modeling

The FDTD method works directly solving the Maxwell equations in the time domain, utilizing the finite difference approximation.

For a homogeneous, non-dispersive, non-conductor and non-magnetic materials, the Maxwell equations in Cartesian coordinate can be written as:

$$\begin{cases} \frac{\partial H_x}{\partial t} = \frac{1}{\mu}\left(\frac{\partial E_y}{\partial z} - \frac{\partial E_z}{\partial y}\right) \\ \frac{\partial H_y}{\partial t} = \frac{1}{\mu}\left(\frac{\partial E_z}{\partial x} - \frac{\partial E_x}{\partial z}\right) \\ \frac{\partial H_z}{\partial t} = \frac{1}{\mu}\left(\frac{\partial E_x}{\partial y} - \frac{\partial E_y}{\partial x}\right) \\ \frac{\partial E_x}{\partial t} = \frac{1}{\varepsilon}\left(\frac{\partial H_z}{\partial y} - \frac{\partial H_y}{\partial z}\right) \\ \frac{\partial E_y}{\partial t} = \frac{1}{\varepsilon}\left(\frac{\partial H_x}{\partial z} - \frac{\partial H_z}{\partial x}\right) \\ \frac{\partial E_z}{\partial t} = \frac{1}{\varepsilon}\left(\frac{\partial H_y}{\partial x} - \frac{\partial H_x}{\partial y}\right) \end{cases} \quad \text{Eq. 3.5}$$

The numerical solution of these equations derives from the spatial and temporal finite difference discretization. The work space is divided into a uniform 3D grid ($\Delta x = \Delta y = \Delta z = \Delta$) of elementary cells. This discretization obviously introduces an uncertainty on the simulated object, which will reflect on a numerical dispersion, to be minimized. In practice, the value of Δ depends on the wavelength and refractive index of the structure according to:

$$\Delta \leq \frac{\lambda}{10n} \quad \text{Eq. 3.6}$$

resulting in a value of 0.05 μm for a wavelength of about 1.5 μm and a refractive index of $\sim$3. The Δt step then results from the relation:

$$\boldsymbol{\Delta t \sim \frac{\Delta}{2c}} \qquad \text{Eq. 3.7}$$

Now, the derivatives ($\nabla \times$ and $\partial/\partial t$) of the Maxwell equations can be approximated by finite difference:

$$\boldsymbol{\frac{\partial f}{\partial x}(x,t) = \frac{f\big|_{x+\Delta x/2}^{t} - f\big|_{x-\Delta x/2}^{t}}{\Delta x} + O[(\Delta x)^2]} \qquad \text{Eq. 3.8}$$

$$\boldsymbol{\frac{\partial f}{\partial t}(x,t) = \frac{f\big|_{x}^{t+\Delta t/2} - f\big|_{x}^{t-\Delta t/2}}{\Delta t} + O[(\Delta t)^2]} \qquad \text{Eq. 3.9}$$

where f stand for all the components of the $\bar{E}$ and $\bar{H}$ field.

The propagation in time, in particular, uses a "leap-frog" scheme where the $\bar{E}$ fields at time t are computed from the $\bar{E}$ field at time $t - \Delta t$ along with the $\bar{H}$ fields at time $t - \Delta t/2$, and vice versa for $\bar{H}$ fields at $t + \Delta t/2$. In this way, the $\bar{E}$ and $\bar{H}$ field patterns are marched through time, offset by half of a time step Δt.

This implementation is based on Yee's mesh, where the electric and magnetic field components are evaluated at different grids having the same pitch, shifted over half grid spacing, both in space and in time.[5] The half step sizes have been introduced for obtaining accurate approximations of the derivates; the algorithm proceeds with full step size.

When Maxwell's differential equations are examined, it can be seen that the change in the E-field in time (the time derivative) is dependent on the change in the H-field across space (the curl). This result in the basic FDTD time-stepping relation: at any point in space, the updated value of the E-field in time is dependent on the stored value of the E-field and the numerical curl of the local distribution of the H-field in space (Yee 1966). The H-field is time-stepped in a similar manner. At any point in space, the updated value of the H-field in time is dependent on the stored value of the H-field and the numerical curl of the local distribution of the E-field in space. The iteration of the E-field and H-field updates results in a marching-in-time process wherein sampled-data, analogs of the continuous electromagnetic waves under consideration, propagate in a numerical grid stored in the computer memory.

For obvious reasons of calculus volume and hence of memory and time, the space volume of our simulations has to be limited. In order to simulate open boundaries, perfectly matched layers PML are added around the edges of the computational region. A PML is an artificial absorbing layer designed in such a way to have no reflections from the boundaries. TESSA uses

the MUR absorbing conditions that have performance of the order of per-cent of amplitude reflection for waves normally incident on their surface.[6]

To compute the system response at some frequencies it remains only to define and to put in opportune places the sources for the electromagnetic field injection and the detectors. In our simulation we have utilized punctual sources which simulates an emitting dipole, with Gaussian profile emission centered at desired frequencies. The temporal profile *f(t)* is related to the Gaussian amplitude in the frequency domain through the Fourier transform.

The number of iteration N_{it} of the simulations depends from the quality factor of the investigated structure, defined as $Q = \omega\tau$; generally speaking the time duration of the simulations t_{Simul} must be longer than the photon lifetime: $t_{Simul} = N_{it}\Delta t > \tau$. To study the behavior of our structures, the dipole is put inside the W1 guiding region (above the PMMA rectangle), with arbitrary emission directions in the PC slabs plain. The adopted procedure for the study of our heterostructure is the following:

1. A large band-width pulse (short pulse in time domain) is firstly placed inside the waveguide/heterostructure to excite the mode(s). The simulation is let going on after the source is turned off. The fields bouncing around inside the system are then analyzed to extract the frequencies and decay rates of resonant mode(s) using sophisticated signal-processing methods such as Harminv.[7]
2. Once the frequencies of the modes are determined, it is needed to run the simulation again with a narrow-bandwidth (long-time) pulse to excite only the mode in question to obtain the field pattern. (Unless only the longest-lifetime mode is wanted, in which case it is sufficient to let the simulation run long enough for the other modes to decay away.) Given the field patterns, it is also possible to find the modal volumes, and thus the Purcell factor.

3.3 The envelope approximation formalism

As already saw in section 2.1, in a periodic dielectric media, with dielectric constant $\varepsilon(\bar{r})$, the electric field modes $\bar{E}_{n\bar{k}}$, with frequencies ω_n, obey Eq. 2.7, and can be expressed as Eq. 2.6. The electric field modes are all orthogonal with respect to the dielectric constant:

$$\int \overline{\boldsymbol{E}}^{*}_{\boldsymbol{n'\bar{k}'}}(\bar{\boldsymbol{r}}) \cdot \boldsymbol{\varepsilon}(\bar{\boldsymbol{r}})\overline{\boldsymbol{E}}_{\boldsymbol{n\bar{k}}}(\bar{\boldsymbol{r}})\boldsymbol{d\bar{r}} = \boldsymbol{\delta}_{\boldsymbol{n,n'}}\boldsymbol{\delta}\left(\overline{\boldsymbol{k}} - \overline{\boldsymbol{k}}'\right) \qquad \text{Eq. 3.10}$$

and analogously, for the Bloch functions:

$$\frac{1}{V_0}\int \bar{\boldsymbol{u}}^*_{n'\bar{k}}(\bar{r})\cdot\boldsymbol{\varepsilon}(\bar{r})\boldsymbol{u}_{n\bar{k}}(\bar{r})d\bar{r} = (2\pi)^3\boldsymbol{\delta}_{n,n'} \qquad \text{Eq. 3.11}$$

where V_0 represent the unit cell of volume.

Introducing a spatially varying perturbation $\Delta(\bar{r})$ of the dielectric constant, which varies slowly over the unit cell (i.e. the length scale of the perturbation is large compared to the lattice constant of the PC), the wave equations becomes:

$$\bar{\nabla}\times\left(\frac{1}{\boldsymbol{\varepsilon}(\bar{r})}\bar{\nabla}\times\bar{\boldsymbol{E}}_{\boldsymbol{\lambda}}(\bar{r})\right) = \left(\frac{\omega_\lambda}{c}\right)^2[\mathbf{1}+\boldsymbol{\Delta}(\bar{r})]\bar{\boldsymbol{E}}_{\boldsymbol{\lambda}}(\bar{r}) \qquad \text{Eq. 3.12}$$

where the subscript λ refers to perturbed quantities. Expanding the perturbed mode on the basis of the unperturbed modes:

$$\bar{\boldsymbol{E}}_{\boldsymbol{\lambda}}(\bar{r}) = \sum_{\boldsymbol{n}}\int \boldsymbol{W}_{\boldsymbol{n}}(\bar{\boldsymbol{k}})\bar{\boldsymbol{E}}_{\boldsymbol{n}\bar{\boldsymbol{k}}}(\bar{r})d\bar{\boldsymbol{k}} \qquad \text{Eq. 3.13}$$

where $W_n(\bar{k})$ are functions that define the mode's expansion in k space. Putting (3.13) into the wave equation results in:

$$\sum_{\boldsymbol{n}}\int \boldsymbol{W}_{\boldsymbol{n}}(\bar{\boldsymbol{k}})\boldsymbol{\omega}^2_{\boldsymbol{n}}(\bar{\boldsymbol{k}})\bar{\boldsymbol{E}}_{\boldsymbol{n}\bar{\boldsymbol{k}}}(\bar{r})d\bar{\boldsymbol{k}} = \sum_{\boldsymbol{n}}\int \boldsymbol{W}_{\boldsymbol{n}}(\bar{\boldsymbol{k}})\boldsymbol{\omega}^2_{\boldsymbol{n}}\boldsymbol{\varepsilon}(\bar{r})[\mathbf{1}+\boldsymbol{\Delta}(\bar{r})]\bar{\boldsymbol{E}}_{\boldsymbol{n}\bar{\boldsymbol{k}}}(\bar{r})d\bar{\boldsymbol{k}} \qquad \text{Eq. 3.14}$$

Exploiting the orthogonality of the electric field mode and of the Bloch functions, the two approximations, of perturbation varying over a length scale much larger than the crystal periodicity, and of orthogonality of all Bloch mode, even if they are not taken at the same wave vector (it entails that the perturbation causes negligible coupling between bands), (3.14) can be written as:

$$\boldsymbol{\omega}^2_{\boldsymbol{n}}(-\boldsymbol{i}\bar{\boldsymbol{\nabla}})\boldsymbol{F}_{\boldsymbol{n}}(\bar{r}) = \boldsymbol{\omega}^2_{\boldsymbol{\lambda}}[\mathbf{1}+\boldsymbol{\Delta}(\bar{r})]\boldsymbol{F}_{\boldsymbol{n}}(\bar{r}) \qquad \text{Eq. 3.15}$$

with

$$\boldsymbol{F}_{\boldsymbol{n}}(\bar{r}) = \int \boldsymbol{W}_{\boldsymbol{n}}(\bar{\boldsymbol{k}})\boldsymbol{e}^{\boldsymbol{i}\bar{\boldsymbol{k}}\cdot\bar{r}}d\bar{\boldsymbol{k}} \qquad \text{Eq. 3.16}$$

where $\omega_n^2(-i\bar{\nabla})$ is the operator deriving from $\omega_n^2(\bar{k})$ by replacing k_x, k_y, and k_z by the derivatives $-i\,\partial/\partial x$, $-i\,\partial/\partial y$, and $-i\,\partial/\partial z$. $F_n(\bar{r})$ are the Fourier transform of $W_n(\bar{k})$. The operators $\omega_n^2(-i\bar{\nabla})$ are the envelope functions of the heterostructures modes. (3.15) is the envelope equation that applies to any type of PC, and, once the band diagram is determined by other methods, allows obtaining analytic expression for the frequency and the envelope of the heterostructure. The next step is to apply the envelope formalism to a PC W1 guide, in which the effective index has been locally perturbed (see figure 3.2). Consider a W1 waveguide in the *x-y* plane, and a mode propagating along the unperturbed guide with wave vector k_0 and frequency ω_n.

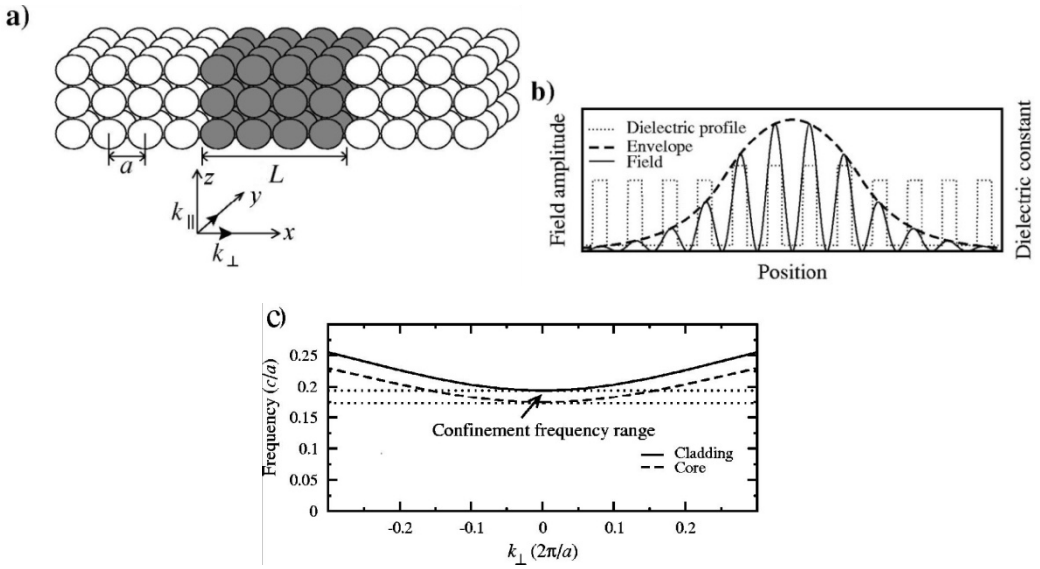

Figure 3.2 *(a) PC slab waveguide: the PC has slightly higher average refractive index in the central core region than in the surrounding regions. (b) Picture of the envelope approximation formalism: the fast varying features of the electromagnetic field are due to the crystal while its envelope is determined by the shape of the heterostructure. (c) Photonic crystal waveguiding: photons with frequency in the region delimited by the two dotted lines can exist only in the core.*

The perturbation Δ_0 is a function of *x* only and can be defined as:

$$\Delta(\boldsymbol{x}) = \begin{cases} \Delta_0 & \boldsymbol{if}\ |\boldsymbol{z}| < \frac{\boldsymbol{L}}{\boldsymbol{2}} \\ \boldsymbol{0} & \boldsymbol{if}\ |\boldsymbol{z}| > \frac{\boldsymbol{L}}{\boldsymbol{2}} \end{cases} \qquad \text{Eq. 3.17}$$

By expanding the operator $\omega_n^2(-i\overline{\nabla})$ in the vicinity of k_0, and keeping up to the second order in the Taylor expansion, the envelope equation becomes:

$$\frac{\boldsymbol{1}}{\boldsymbol{2m^*}}\frac{\boldsymbol{d^2 f_{nk_0(x)}}}{\boldsymbol{dx^2}} = \{\boldsymbol{\omega_n^2(k_0) - \omega_\lambda^2[1 + \Delta(x)]}\}\boldsymbol{f_{nk_0}(x)} \qquad \text{Eq. 3.18}$$

with

$$\boldsymbol{F_{nk_0}(x) = e^{ik_0 x} f_{nk_0}(x)} \qquad \text{Eq. 3.19}$$

where m* is an effective-mass-like term, describing the curvature of the band. This term is called effective mass by analogy with the effective mass of electrons in the initial application domain of this formalism. ω_λ is the frequency of the confined mode. The solution of such equation for a constant value of Δ_0, which is the case for our heterostructure, by applying the correct continuity conditions, can be written as:

$$\boldsymbol{f_{nk_0}} = \begin{cases} \boldsymbol{\cos(Kx)}, & \boldsymbol{for}\ |\boldsymbol{x}| < \frac{\boldsymbol{L}}{\boldsymbol{2}} \\ \boldsymbol{e^{\gamma\left(\frac{L}{2} - |x|\right)} \cos\left(K\frac{L}{2}\right)}, & \boldsymbol{for}\ |\boldsymbol{x}| > \frac{\boldsymbol{L}}{\boldsymbol{2}} \end{cases} \qquad \text{Eq. 3.20}$$

with

$$\boldsymbol{K = \sqrt{2m^*\{\omega_\lambda^2[1 + \Delta(x)] - \omega_n^2(k_0)\}}} \qquad \text{Eq. 3.21}$$

and

$$\boldsymbol{\gamma = \sqrt{2m^*[\omega_n^2(k_0) - \omega_\lambda^2]}} \qquad \text{Eq. 3.22}$$

The effective mass m^* is the second derivative of the square frequency to the parallel wave vector; it is linked to the curvature of the band α through the relation:

$$\boldsymbol{\frac{1}{m^*} = \frac{\partial^2\omega_n^2}{\partial k_x^2}\Big|_{k_0} = 2\omega_0\alpha} \qquad \text{Eq. 3.23}$$

This equation shows that the effective mass is inversely proportional to the band curvature. From the equations above, we can conclude that the efficiency of the confinement is higher for slow Bloch modes than for conventional (fast) modes: the lower the band curvature, the better the spatial confinement (see figure 3.2(c)). As can be seen in the equations, the size of the strip (L) and the effective index difference (Δ) also play a role in the confinement efficiency. If the effective index difference is small, L has to be large enough to obtain an efficient confinement within the PC region covered by the strip. On the other hand, if Δ is high, the cosine function oscillates faster and efficient lateral confinement can be achieved with a narrower strip. Furthermore there is a compromise between the size of the strip and the effective index difference between the covered and uncovered regions of the W1 waveguide.

REFERENCES

[1] S. G. Johnson, J. D. Joannopoulos, Opt. Expr., 2001, 8, 173.

[2] A. Taflove, Computational Electrodynamics: The Finite Difference Time Domain Method, Artech House Inc., Boston, 1995; R. M. de Ridder, R. Stoffer, Tutorial, presented at the summerschool on "Nanoscale linear and non-linear optics" at the International School of Quantum Electronics, Erice, Sicily (Italy), 2-14 July 2000.

[3] http://alioth.debian.org/projects/tessa/

[4] R.D. Meade, A.M. Rappe, K.D. Brommer, J.D. Joannopoulos, O.L. Alerhand, Phys. Rev. B, 1993, 48, 8434.

[5] K. S. Yee, IEEE Trans. Antennas Propagat., 1966, AP-14, 302.

[6] G. Mur, IEEE Trans. Electrom. compatib., 1981, 23, 37; B. Enquist, A. Majda, Mathematics of Computation, 1977, 114, 185.

[7] M. R. Wall, D. Neuhauser, J. Chem. Phys., 102, (20), 8011, (1995); V. A. Mandelshtam, H. S. Taylor, J. Chem. Phys., 1997, 107, 6756.

CHAPTER 4

Experimental tools

Photonic crystals are periodic object with period of nanometers scale. The fabrication of such structures requires lithographic technology with accuracy at the 10 nm level.

Several lithography techniques for photonic crystal devices have been proposed, like deep UV laser lithography,[1] laser interference lithography (LIL)[2] and focused ion beam lithography.

E-beam lithography, EBL, is the most popular method for fabricating PCs. It is very precise (typical resolution 5 nm) and versatile. Its weakness is the slowness that anyway is not a problem for the realization of a demonstrator.

After the lithography step the pattern defined on a resist layer must be transferred into the device layer. This can be done through a process of anisotropic etching. Photonic crystal applications impose stringent requirements: the etching profile should have minimal surface roughness and vertical sidewalls. Moreover, the etching depth should be controlled accurately.

Although it is quite an old technique, standard reactive ion etching (RIE) can be successfully applied for obtaining PCs structures with high anisotropy and low sidewall roughness.

4.1 Electron Beam Lithography

In the EBL process a focalized electron beam scans the sample surface, that has been covered with the electron sensitive resist, in such a way to produce the desired patterns. It is realized using a scanning electron microscope (SEM) adapted for the lithography. The main components of a SEM are the electron gun, the optical column, and the vacuum system. The electron gun constitutes the source of primary electrons and consists in a tungsten filament functioning as a cathode. A voltage is applied to the filament, causing a warming. The anode, which is positive with respect to the filament, forms powerful attractive forces for electrons. This causes electrons to accelerate toward the anode. Some accelerate right by the anode and on down the column, to the sample. The optical column, contain several optical elements, like electromagnetic lenses, apertures, deflection systems, alignment coils, blanking plates, and stigmators providing for the beam focalization, for the deflections necessary during the sample scanning, and, if necessary for the beam shutdown. The beam-blanker allows to shutdown the beam before the sample surface, without switching off it, and it is useful to move on the sample without exposing.

When a SEM is used, the column must always be under vacuum, for many reasons. If the sample is in a gas filled environment, an electron beam cannot be generated or maintained because of a high instability in the beam. Gases could react with the electron source, causing it to burn out, or cause electrons in the beam to ionize, which produces random discharges and leads to instability in the beam. The transmission of the beam through the electron optic column would also be hindered by the presence of other molecules. Those other molecules, which could come from the sample or the microscope itself, could form compounds and condense on the sample. This would lower the contrast and obscure detail in the image. For these reasons the electron gun and the sample stage are maintained at 10^{-7} Pa and 10^{-4} Pa respectively. Other important components of the system are the Faraday cage, the isolation valve, and the electron counter.

A Faraday cage mounted on the sample stage, is used to measure the beam current in order to ensure the correct dose for resist exposure. The sample stage is grounded with a wire that, passing through a pico-amperometer, gives the beam current to be used for the dose determination. The column will also typically have an isolation valve that allows the chamber to be vented for maintenance while the gun is still under vacuum and operational.

Finally, the system needs a method of detecting the electrons for focusing, deflection calibration, and alignment mark detection. Usually this is a silicon solid state detector similar to a solar cell, mounted on the end of the objective lens just above the sample. The EBL is controlled by an ELPHY Quantum hardware pattern generator (PG) that is a specifically designed 16 bit, 2.5 MHz DAC vector scan beam deflection PC board installed into a state of the art Windows computer. All required functions are fully integrated into one software, from pattern design, exposure parameter management, pattern overlay alignment to step and repeat exposures.[3] The pattern design is graphically generated in the GDSII format, a binary format that supports a hierarchical library of structures (called "cells"). Cells may contain a number of objects, including:

- Boundary, which may be used to represent polygons or rectangles,
- Box, which may be used to represent rotated rectangles,
- Path, which may be used to represent wires,
- Text, for annotation either on the CAD screen or the device,
- Sref, to include an instance of one structure (cell) inside another, and
- Aref, similar to Sref but providing an array instance of a cell.

There are 64 available Layers, numbered 0 to 63. Each primitive object (Boundary, etc.) lies on one of these layers. Each layer number typically represents one mask or electron-beam exposure step in a process.

Then the pattern generator converts the intermediate format to machine-specific form. Each designed structure is decomposed from the PG in a matrix of point of coordinate (*x,y*), spaced out of Δx and Δy: the electron beam is sequentially positioned on each matrix point for a fixed dwell time t_{dwell} depending on the resist. The Δx, Δy value depends on the microscope magnification (M), and decrease for higher magnification. In this work the lithography has been performed with a magnification of 2000X, and the corresponding minimum step size is 0.001 μm. Once that the beam current, the magnification and the dwell time have been set up, the exposure dose can be valued as the ratio between the incident current and the exposed surface:

$$\boldsymbol{D_{expos}} = \frac{\boldsymbol{I_{beam} \cdot t_{dwell}}}{\boldsymbol{\Delta x \cdot \Delta y}} \qquad \text{Eq. 4.1}$$

The Δx, Δy spacing allows also determining the maximum write field size; the elphy quantum utilizes 16 bit converters, thus the maximum step numbers is 2^{16}=65536, and for the object

realization we dispose of a grid of 65356 · 65356 point. It follows that, for a step size of 0.001 µm, the maximum write field is:

$$(65536 \cdot 0.001\ \mu m) \cdot (65536 \cdot 0.001 \mu m) \cong 65 \cdot 65\ \mu m$$

By choosing a lower magnification the write field increases, but the resolution, i.e. the minimum dimension of the patterned objects, reduces. So the choice of the magnification is a compromise between the desired structure extension, and the required resolution. The resolution is limited also by the scattering phenomena of the primary electrons within the resist and with the below substrate.

The possible events resulting from the interaction between the beam and the sample, and limiting the quality of the lithography are:

- Forward scattering: electrons penetrating in the resist undergo multiple collisions that can diffuse them, causing a larger impressed area with respect to the irradiated one.
- Generation of secondary electrons: as a consequence of collision with resist molecules the primary electrons give a part of their energy, generating secondary electrons, that cause a resist over-exposition.
- Back scattered electrons: when primary electrons arrive to the substrate, they can be back-scattered, inducing a further resist impression.
- Proximity effect: because of forward and back scattering events, the dose in each single point strongly depends from the contribute from the surrounding points.

Moreover, the final extension of the pattern depends also from the interactions between the resist and the develop solution.

4.2 Resist

Resist for EBL are polymeric materials which change their solubility, when exposed to the e-beam radiation.

These resists can be divided in two main groups, positive and negative resists. In positive resist electron irradiation breaks polymer backbone bonds, leaving fragments of lower molecular weight, that are selectively washed away from a solvent developer, thus forming a positive tone pattern in the resist film. Negative resists work by cross-linking the polymer chains together, rendering them less soluble in the developer. The quality of a resist depends on:

1. *Resolution:* is the resist capability to define small structures
2. *Sensitivity:* defined as the required minimum dose for a correct exposition

The polymethyl methacrylate (PMMA) resist, employed in this project, is a versatile polymeric material. It is the most commonly used as a high resolution positive resist for direct writing e-beam as well as x-ray and deep UV microlithography processes. Standard PMMA products cover a wide range of film thicknesses and are formulated with 495,000 & 950,000 molecular weight (MW) resins in either chlorobenzene or the safer solvent anisole.

4.3 Reactive Ion Etching

Reactive ion etching (RIE) is a dry etching technology using chemically reactive plasma to transfer the pattern from the resist to the materials to be microfabricated. The plasma is generated under low pressure (vacuum) by an electromagnetic field. High-energy ions from the plasma attack the wafer surface and react with it.[4]

A typical RIE system consists of a cylindrical vacuum chamber, with a wafer platter situated in the bottom portion of the chamber. The wafer platter is electrically isolated from the rest of the chamber, which is usually grounded. Gas enters through small inlets in the top of the chamber, and exits to the vacuum pump system through the bottom. The types and amount of gas used vary depending upon the etch process. Gas pressure is typically maintained in a range between few millitorr and few hundred millitorr by adjusting gas flow rates. Plasma is initiated in the system by applying a strong (few hundred watts) radio frequency (RF) electromagnetic field, with a frequency of 13.6 MHz, to the wafer platter. The oscillating electric field ionizes the gas molecules by stripping them of electrons, creating plasma.

In each cycle of the field, the electrons are electrically accelerated up and down in the chamber, sometimes striking both the upper wall of the chamber and the wafer platter. At the same time, the much more massive ions move relatively little in response to the RF electric field. When electrons are absorbed into the chamber walls they are simply fed out to ground and do not alter the electronic state of the system. However, electrons absorbed into the wafer platter cause the platter to build up charge due to its DC isolation. This charge build up develops a large negative voltage on the platter. The plasma itself develops a slightly positive charge due to the higher concentration of positive ions compared to free electrons.

Because of the large voltage difference, positive ions tend to drift toward the wafer platter, where they collide with the samples to be etched. The ions react chemically with the materials on the sample surface, but can also knock off (sputter) some material by transferring him a part of their kinetic energy. Due to the mostly vertical delivery of reactive ions, reactive ion etching

can produce very anisotropic etch profiles, which contrast with the typically isotropic profiles of wet chemical etching.

Etching conditions (in RIE system) depend strongly on the many process parameters, such as pressure, gas flows, and RF power.

4.4 Optical characterization set-up

The optical set-up for the optical characterizations of the laser sources is reported in figure 4.1. The pump source is a pulsed laser diode, with emission centered at 780 nm (VPSL-0808-150-S-9-B, power max=150mW, pulse width ~6.5 ns, period 110 ns), and with intensity variable from 0 to 26 μA. It is focalized on the sample by a long distance focal objective lens (20x).

The intensity value on the sample depends also from the objective used, in particular for a 20x objective the conversion factor F_C between the output diode power (expressed in mW) and the incident intensity on the sample (expressed in µA) has been calculated to be:

$$\boldsymbol{F_C = \frac{2.286}{DC(\%)}} \qquad \boldsymbol{with\ DC(\%) = \frac{pulse\ duration}{pulse\ period} \times 100} \qquad \text{Eq. 4.2}$$

where DC is the duty-cycle, describing the fraction of time that a pulse train is in an "active" state.

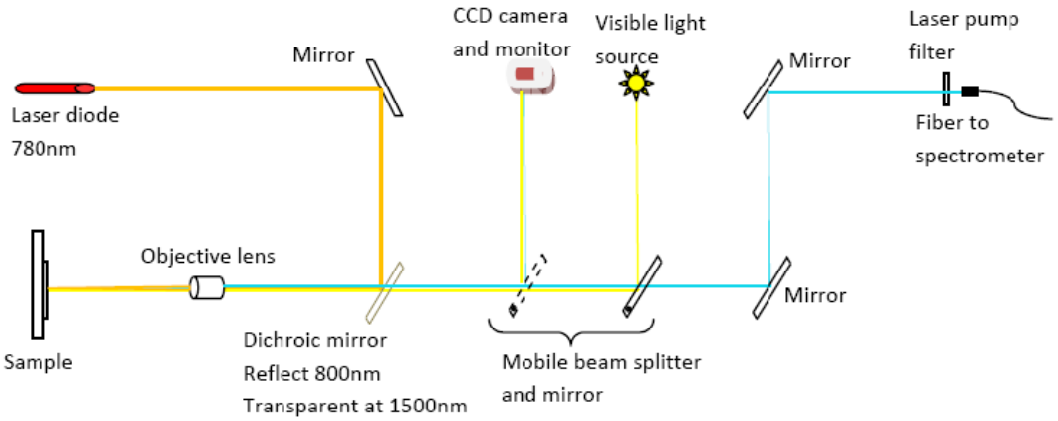

Figure 4.1 Setup for the optical characterization of the samples.

The mobile mirror and beam slitter allow monitoring the position of the laser beam on the sample, through a CCD camera. The white light has a path collinear with the excitation beam and, after being focalized on the sample and collected with a long working distance microscope objective (Mitutoyo), is deflected to the CCD camera (an array of 512 InGaAs photodiodes, CCD-like, from Jobin-Yvon) by the beam splitter, together with a small part of the 780 nm beam that is transmitted from the dichroic mirror (the dichroic mirror doesn't reflect the 100% of the 780 nm radiation and the part that is transmitted is sufficient to be seen by the CCD camera).

This system is very useful to focalize the laser pump at a precise point on the photonic crystal. After this alignment the mobile mirror and beam splitter are removed from the optical path, and the sample emission, collected and collimated by the objective lens, reaches the fiber and the spectrometer (Jobin-Yvon-Spex 550) to record the emission spectrum. The spectrometer is equipped with a CCD detector head, cooled with liquid N_2, and allows reaching resolution of 0.1 nm.

REFERENCES

[1] W. Bogaerts, V. Wiaux, D. Taillaert, S. Beckx, B. Luyssaert, P. Bienstman, R. Baets, IEEE J. Sel. Topics in Quantum Electr., 2002, 8, 928.

[2] L. Vogelaar, W. Nijdam, H. van Wolferen, R. M. de Ridder, F. B. Segerink, E. Fluck, L. Kuipers, N. F. van Hulst, Advanced Materials, 2001, 13, 1551.

[3] http://www.raith.com.

[4] http://en.wikipedia.org/wiki/Reactive_ion_etching.

CHAPTER 5

Effective index microcavity laser

In this chapter we will describe the experimental work necessary for the realization of a PC-2D microcavity on a III-V (InP) slab on a silica substrate. The choice of InP slab is motivated by its transparency at the telecommunication wavelength, and by the possibility of easily inserting active light sources, engineered to emit at the telecom wavelength, inside this slab.

The experimental section is organized following the temporal sequence of steps necessary to obtain and properly characterize the final devices:

- Sample preparation
- Computational step
- Lithographic step
- Characterization step

All these steps, except the first one and part of the second, have been performed by myself as a part of my activity. The samples preparation, described above for clearness, has been done by P. Regreny concerning the epitaxial growth of the InP-based heterostructure, and by J.M. Fedeli and L. Di Cioccio for the wafer bonding technology. The 3D dispersion curves of the modes of a W1 waveguide have been calculated by Frederic Bordas with a 3D plane wave method,

together with the estimation of the confinement factor, calculated with the Charbonneau-Lefort formalism.

5.1 Sample preparation

The guiding PC layer consists in a 250 nm thick InP membrane. On its center, is present a multi-quantum well region including four $InAs_{0.65}P_{0.35}$ quantum wells 50 Å thick, separated by InP barriers of 200 Å.

The samples are grown by solid source molecular beam epitaxy (MBE) on 2" semi-insulating InP wafers. A 500-nm-thick InGaAs sacrificial layer was first grown on the InP (001) substrate. The multi-QWs emission band has a spectral width of about 200-nm around a wavelength of 1500 nm and presents a high quantum yield, enabling efficient laser operation. Except for the sacrificial layer, the optical thickness of the whole heterostructure is (250 nm). The membrane thickness has been chosen to be equal to half of the telecommunication wavelength in the slab (250 nm $\sim \lambda/2n$ at 1.55 µm). This configuration allows maximizing the coupling between the light emitted from the active zone and the fundamental TE guided mode, whose field profile shows a maximum at the slab center, and ensures also the mono-mode nature of light propagating with TE polarization, thus avoiding coupling effects between different modes induced from the PC.[1]

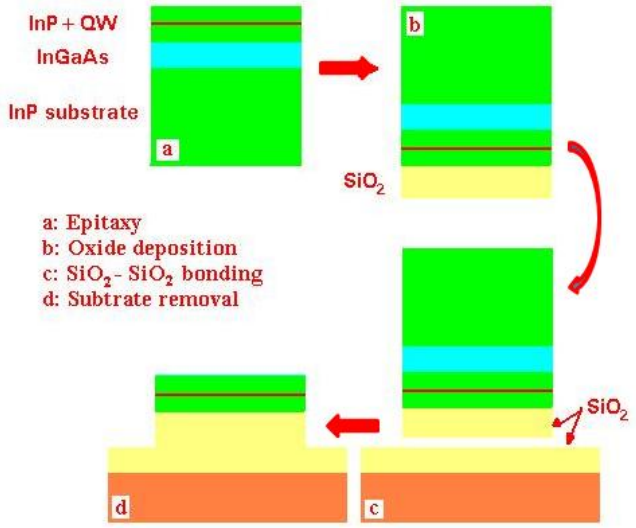

Figure 5.1 *Four step process for the production of an InP slab bonded on a SiO_2 substrate.*

The InP wafer and the heterostructure were bonded onto a silicon wafer at room temperature by means of SiO_2–SiO_2 bonding.[2] The total SiO_2 layer, below the III-V heterostructure, is 800 nm thick, which is sufficient to prevent significant optical coupling with the silicon wafer. The InP substrate was subsequently removed by wet chemical etching, selective with regard to the

$InGa_{0.53}As_{0.47}$ sacrificial layer, using an HCl-based solution.[3] The sacrificial layer was selectively etched relative to InP using a $FeCl_3$-based solution. A 90 nm thick layer of SiO_2 has been growth as a hard mask for future etching processes.

5.2 Computational step

As already outlined, the computational step is of fundamental importance to optimize the device performance. It allows identifying the desired PC parameters for the lithographic step, and thus to save time.

The first step is the W1 band diagram calculations with the 3D plane wave method, using the supercell method described in chapter 3. Since this system is symmetric with respect to the translation along the *x* direction, the structure is given by a periodic repetition, with period *a*, along the first neighbors direction; the supercell periodicity is necessary only along the *y* direction. Thereby the reciprocal lattice will be also one-dimensional of period π/a along the ΓK direction. The propagating wave along the guide will be diffracted on a series of orders of the propagation constant on the component along the guide axis obeying:

$$\boldsymbol{k_x = k_{0x} \pm 2m\pi/a} \qquad \text{Eq. 5.1}$$

So the representation of the band diagram can be reduced to the interval $0 < k_x < \pi/a$ where k_x is the Bloch wave vector projected along the guide axis. The dispersion diagram of a W1 guide realized in a triangular lattice, presenting a filling factor of 40%, is reported in figure 5.2(a). It shows the modes below the light line, which are guided theoretically without losses and the maps relative to the spatial distribution of the z-component of the magnetic field H_z. The two modes can be discriminated according to the H_z parity with respect to the σ_y mirror plane. The mode showing a field distribution symmetric with respect to the mirror plane is called even and is represented in red in the figure, while the mode that is anti-symmetric with respect to the same plane is called odd mode and is represented in blue.

The PC structure is designed to exploit the low group velocity mode located around point A of figure 5.2(a), at the edge of the first Brillouin zone. If one increases locally the effective index of the membrane, the bands are shifted to lower values of the reduced frequency, see figure 5.2(b).

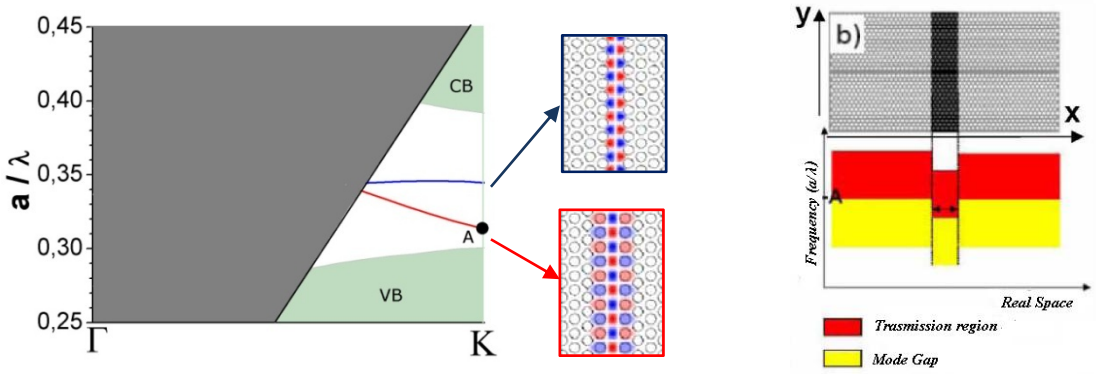

Figure 5.2 *(a) Calculated band diagram for the 2D photonic crystal slab with a triangular lattice and containing a line defect formed by a missing row of air holes. The dark grey area corresponds to the light cone, while the green zones correspond to the conduction and valence bands. The blue curve is the odd guided mode, while the red one corresponds to the even mode. (b) The PMMA strip over the PC waveguide locally lowers the energy of the waveguided mode creating a band gap: photons with this lower energy are trapped inside the region under the PMMA strip.*

This results in a photonic heterostructure whose confinement properties, deriving from the effective index shift and the local curvature of the band associated with the waveguide mode, can be estimated applying the formalism developed by Charbonneau-Lefort et al. and described in section 3.3. The results for the mode e_{g1} are reported in figure 5.3. From the band diagram of the W1 waveguide, we estimate the unmodified waveguide frequency to be $\omega_n = 0.31235$ and the effective mass to be $m^* = 7.34 \times 10^{-19} m^{-2} s^2$. We also estimate the value of Δ, from the effective index change induced by the PMMA deposition, to be $\Delta = 0.06$. The mode frequency obtained from these parameters is quite uniform across different heterostructure sizes L: $\omega_\lambda = 0.31230\ c/a$ for $L = 4a$ and $\omega_\lambda = 0.3121\ c/a$ for $L = 10a$. The first envelope on figure 5.3 (black solid line) is calculated for $L = 4a$, whereas the second one (red dashed line) is calculated for $L = 10a$.

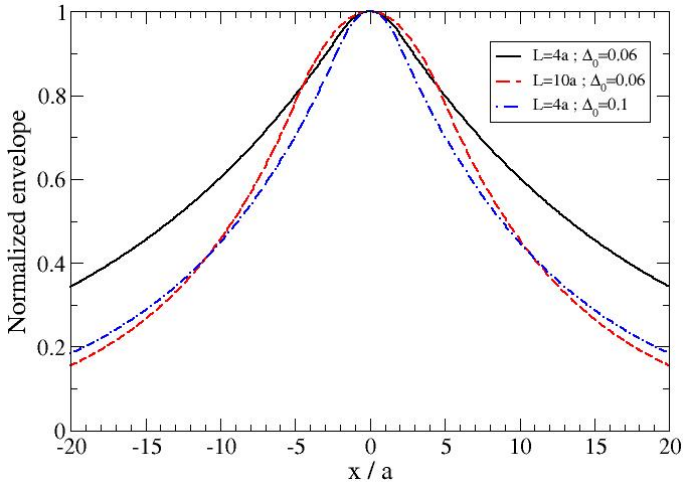

Figure 5.3 *Calculation of envelopes in the (x,z) plane at the middle of the waveguide for three different configurations extending from –20a to +20a.*

The third one (blue dash and dotted line) is calculated for $L = 4a$, and a Δ value hypothetically obtained from a higher index material instead of the PMMA: $\Delta = 0.1$. The calculated frequency with this parameter is $\omega_\lambda = 0.3099\ c/a$. This figure illustrates the interplay between Δ and L: the increase of them reduces the width of the envelope. To obtain rigorous and quantitative analysis, it is necessary to use the 3D finite difference time domain (3D-FDTD) model.

Using the TESSA 3D-FDTD open-source software, a W1 waveguide patterned in a 250 nm thick InP membrane, with and without the PMMA strip above has been modeled. The lattice parameter and the air filling factor (respectively 473 nm and 40%) have been chosen to have

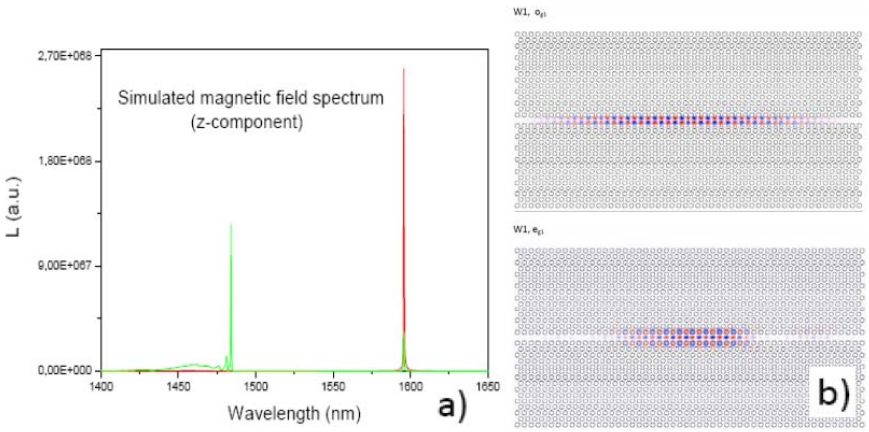

Figure 5.4 *Simulated Hz field spectrum (a) and map of the eg1 mode at 1596 nm and of the o_{g1} mode at 1484 nm for the W1 configuration (b).*

the band-edge mode corresponding to point A, at around 1550 nm, in figure 5.2(a). The first simulation has been performed to find the resonant mode of the W1.

The first step is the design of the optical structure to be simulated, using the python module, provided with Tessa. Processing this file, HDF5 files are generated; they contain the information of the structure to be simulated. With the HDF5 file, it is possible to make the FDTD simulation file running, to study the behavior of the injected field inside the structure. The first simulation should be performed using a large Gaussian peak as excitation source to excite all the resonance modes of the structure.

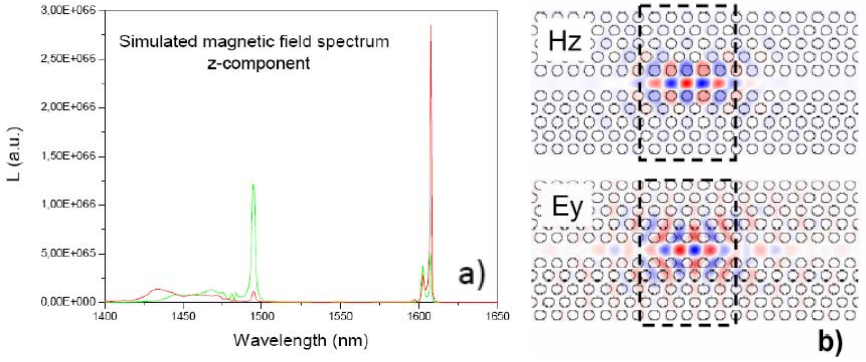

Figure 5.5 *Simulated Hz field spectrum (a) and (b) map of the e_{g1} mode at 1607 nm for the W1+PMMA configuration, the dashed rectangles correspond to the location of the PMMA strip.*

Using the results of this simulation it is possible to extract the resonant mode(s) frequency. With successive simulations, where the excitation source is spectrally thin enough to excite only one resonant mode, it is then possible to extract also the two dimensional maps of the field distribution. The results obtained for a W1 with the parameters given above are reported in figure 5.4, showing the calculated spectrum for the W1 waveguide. The waveguide was excited with a Gaussian dipole source centered at 1550 nm. The calculated spectrum shows two main peaks at 1484 and 1596 nm, corresponding to the odd o_{g1} and even e_{g1} modes at *K* point respectively. The same simulations have also been performed placing the emitted dipole inside the W1 waveguide and under the PMMA slab for the W1+PMMA configuration (figure 5.5a). The calculated spectrum shows two main peaks at 1494 and 1607 nm, with quality factors of 771 and 4273 respectively. The Q factors of these modes would be much higher in the case of a suspended membrane, which offers a higher refractive index contrast between the InP slab and the surrounding media. However, since our goal is to develop stable devices, like microlasers, we have chosen to pattern a PC structure on an InP-based heterostructure bonded onto fused silica, mechanically stable, and exhibiting a better thermal behavior. In the case of our asymmetric structure, radiated losses of such resonant modes are therefore relatively high. However, as we will see, despite these losses, room-temperature lasing can be achieved.

Figure 5.5(b) shows the simulated magnetic (*z*-component) and electric (*x,y*-component) field map for the mode at 1607nm. This figure clearly shows that this mode is well localized inside the waveguiding region under the PMMA strip. It is possible to calculate the modal volume and the Purcell factor of the structure starting from the HDF5 output files. In fact they contain the information about the dielectric constant value in the space and the E field distribution within the simulated domain. The effective modal volume is obtained according with:

$$V_{mod}^{eff} = \frac{\int_V \varepsilon(\bar{r})|\bar{E}(\bar{r})|^2 d^3r}{max[\varepsilon(\bar{r})|\bar{E}(\bar{r})|^2]}. \qquad \text{Eq. 5.2}$$

This leads to a modal volume of only 1.31 $(\lambda/n)^3$, which means that the resonant mode is effectively concentrated at the center of the cavity. Under optimal conditions of spatial and spectral overlap between the source and the cavity mode, this cavity would exhibit a Purcell Factor of about 250 for the e_{g1} mode.

5.3 Electron Beam Lithography and Reactive Ion Etching

The structure generated with Tessa, has been translated into real samples through lithographic processes. The W1 waveguide has been firstly defined on a PMMA resist film by electron beam lithography with a modified JEOL JSM5500 scanning electron microscope, governed by a RAITH e-beam lithography ELPHY QUANTUM system. (filament W, 25 kV max, electrostatic beam blanking, correction of the proximity effect, 100x100 μm^2 field, sub-100 nm resolution). In the second step the pattern is transferred from the PMMA resist to the InP slab with RIE.

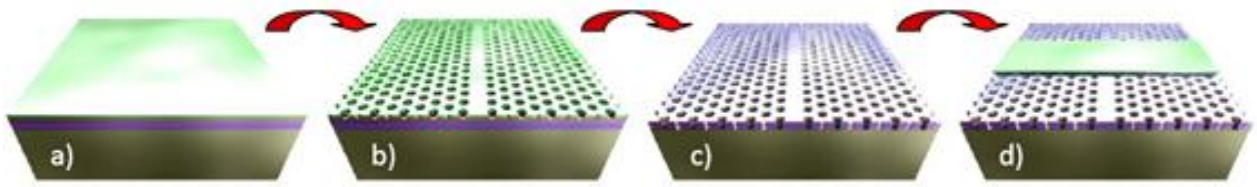

Figure 5.6 *Schematic representation of the experimental procedure necessary to obtain the W1+PMMA structure: (a) A 110 nm thick resist film is spin-coated on the sample surface; (b) the PC W1 structure is realized on the resist by Electron Beam Lithography (EBL) and then c) is transferred on the InP layer by means of Reactive Ion Etching (RIE); finally d) a PMMA strip is patterned above the PC with EBL.*

Once more, the W1+PMMA structure must be firstly drawn. The Elphy Quantum system allows to draw the structure, and to put different elements, to be realized in sequence, on different layers: for example, in this work we have put the alignment marks and the W1 in the first layer, and the superimposed PMMA strip on the second one. Firstly we have realized layer 1.

In order to match the desired lattice parameters for the triangular lattice (Λ=470-500 nm, air filling factor of about 40%) we have tested several holes radius and beam doses. To take into account the proximity effect, we have chosen a nominal value of radius lower than the desired one and we have tested different dose ranges (Table 5.1). In particular each 65 μm X 65 μm write field contains four W1 structures, each one consisting in a $51 \times \Lambda$ long and $31 \times \sqrt{3}/2\,\Lambda$ array of holes with triangular symmetry (see figure 5.8(b)).

		PC3				PC4				PC5	
		imposted radius and periode				imposted radius and periode				imposted radius and periode	
		r=130 nm	a=473 nm			r=110 nm	a=473 nm			r=120nm	a=473 nm
		measured ϕ and periode				measured ϕ and periode				measured ϕ and periode	
name	dose	d	a	name	dose	d	a	name	dose	d	a
a	1	342	484	a	1,2	298	480	a	1,1	301	480
d	1,2	347	498	d	1,4	304	486	d	1,3	311	480
b	1,4	367	491	b	1,6	307	481	b	1,5	319	583
c	1,6	399	497	c	1,8	320	490	c	1,7	343	485
e	1	316	477	e	1,2	298	479	e	1,1	312	477
h	1,2	335	478	h	1,4	301	481	h	1,3	325	488
f	1,4	356	488	f	1,6	312	482	f	1,5	337	472
g	1,6	380	496	g	1,8	315	488	g	1,7	374	490

Table 5.1 *Experimental parameters (hole diameter and period) obtained from the SEM micrographs of the W1 samples.*

The e-beam lithography has been performed with a magnification of 2000X, corresponding to a write field size of 65 *μm* X 65 *μm* (in fact the write field area depends on the magnification). After the lithography, the sample has been extracted from the JEOL machine and developed in a MIBK:IPA=1:1 solution in order to remove the PMMA in the exposed areas and has been finally subjected to a post-backing process at 100°C for 60 seconds. The quality of the patterning of the PMMA has been observed with an optical microscope, before transferring it to the InP slabs by means of RIE with a seven step etching process that is schematically described in figure 5.7 and summarize above:

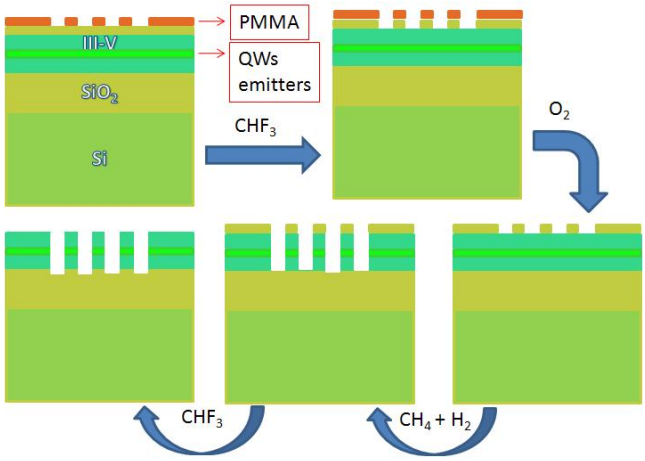

Figure 5.7 *Schematic representation of all the steps of the RIE process. The first step is the transfer of the pattern to the hard mask using a CHF_3 based etching. Then, after the PMMA removal, the pattern is transferred to the III-V heterostructure, using a gas mixture of CH_4 and H_2. Finally the hard mask is removed with CHF_3.*

The pattern generated on the PMMA resist film, is firstly transferred to the SiO_2 layer, by using a CHF_3 gas, then to the III-V heterostructure, using a gas mixture of CH_4 and H_2. Finally, the SiO_2 mask is removed and the sample is cleaned from the carbon impurities deposited during the etching process.

Step	Gas (sccm)	Pressure (mtorr)	Time (min)	RF Power (Watt)	Description
1	CH_4 (20)	100	5	300	Camera passivation (no sample inside)
2	CHF_3 (16)	15	10	100	Etching of the SiO_2 hard mask
3	O_2 (20)	100	3	100	Removing of PMMA
4	CH_4 (15) H_2 (30)	30	6	200	Etching of the InP layer
5	O_2 (20)	100	3	100	Cleaning sample from carbon deposited during step 4
6	CHF_3 (16)	15	10	100	Removing of the SiO_2 hard mask
7	O_2 (20)	100	3	100	Cleaning sample from carbon deposited during step 6

Table 5.2 *Etching parameters used for the PC realization with EBL.*

After having verified the quality of the first lithography, the sample undergoes another EBL step where the PMMA strip, above the W1, is defined. Strip of PMMA with thickness of 110 nm and 6 periods large, is patterned perpendicularly to the W1 waveguide, across the entire PC width, with accuracy on the order of few nanometers. The alignment marks, generated during the first lithographic step, have been used to align the PMMA strip above the PC without exposing the resist.

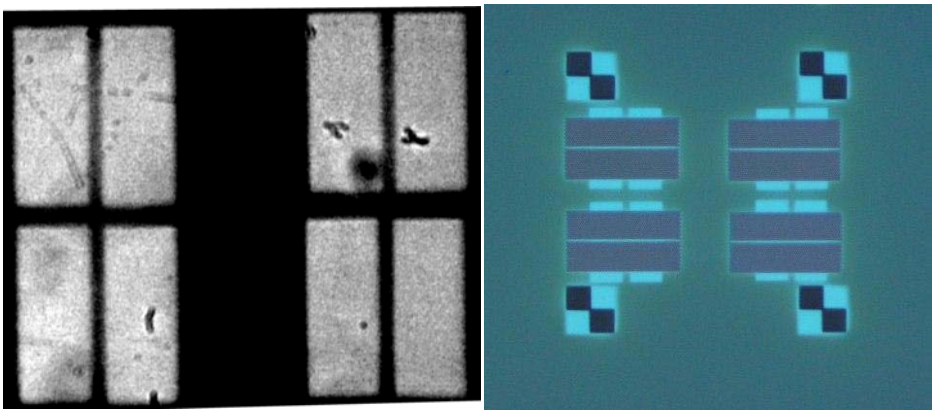

Figure 5.8 *(a) Dose test for the determination of the correct exposure current. The dose decreases moving from the first structure (left top) to the last one (right bottom). Only the last dose is the right one, while the previous doses were too high, resulting on a resist over-exposition. (b) Imagine of the 65 µm x 65 µm write field with the alignment marks on his apexes and four W1+PMMA structures inside.*

5.4 Sample characterization

The W1 heterostructure has been observed with optical microscope and SEM. The optical microscope image shows the quality of the structures lithographically defined on the resist after the development.

It is also helpful to verify the correct alignment of the PMMA strip with the W1. To check the

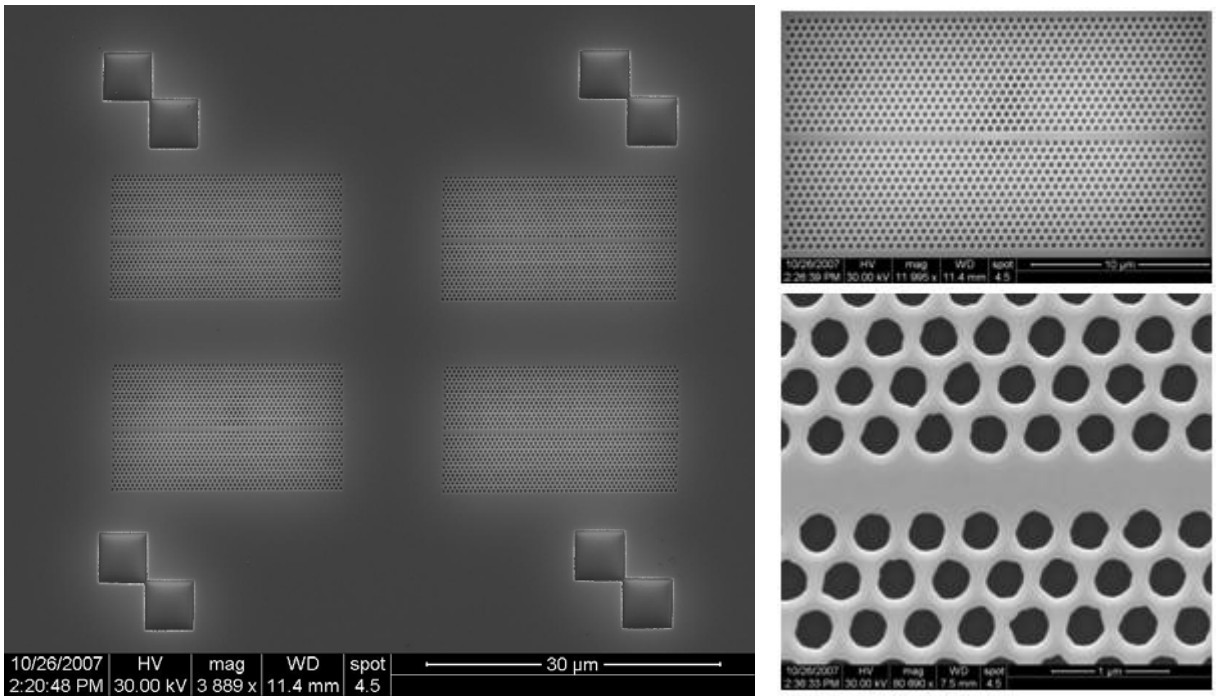

Figure 5.9 *SEM image of a write field and of one W1 waveguide. The lattice period and hole radius are 478 nm and 154 nm respectively.*

quality of the PC in details, the samples have also been observed with SEM, and the results are reported in figures 5.9 and 5.10. The most promising samples have been characterized with the optical set-up described in section 4.4 to verify their potentiality as laser sources.

The first characterizations have been performed on the photonic crystal without the PMMA strip, to see the emission characteristics of the W1 waveguide.

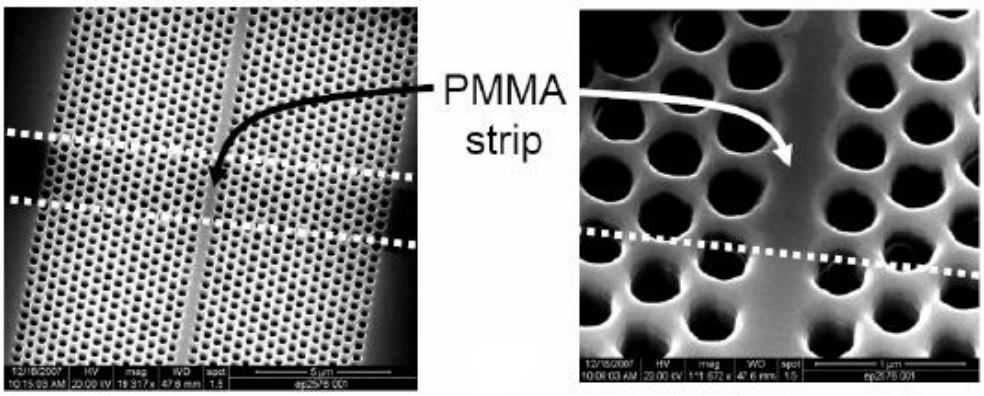

Figure 5.10 *SEM image of the W1+PMMA cavity (b). The lattice period and hole radius are 478 nm and 154 nm respectively.*

Figure 5.11(a) reports the emission spectrum of the unpatterned heterostructure (brown line), and of four W1+PMMA structures, with small differences in the hole diameter. The photoluminescence spectrum of the quantum wells from the unpatterned heterostructure is wide, covering about 200 nm in the 1400-1600 nm range. The spectra of the W1 and W1+PMMA show an intense peak. The variation of the peak intensity as a function of the pump power is reported in figure 5.11(b), for both configurations. For the W1+PMMA configuration the laser threshold is around 1.6 mW.

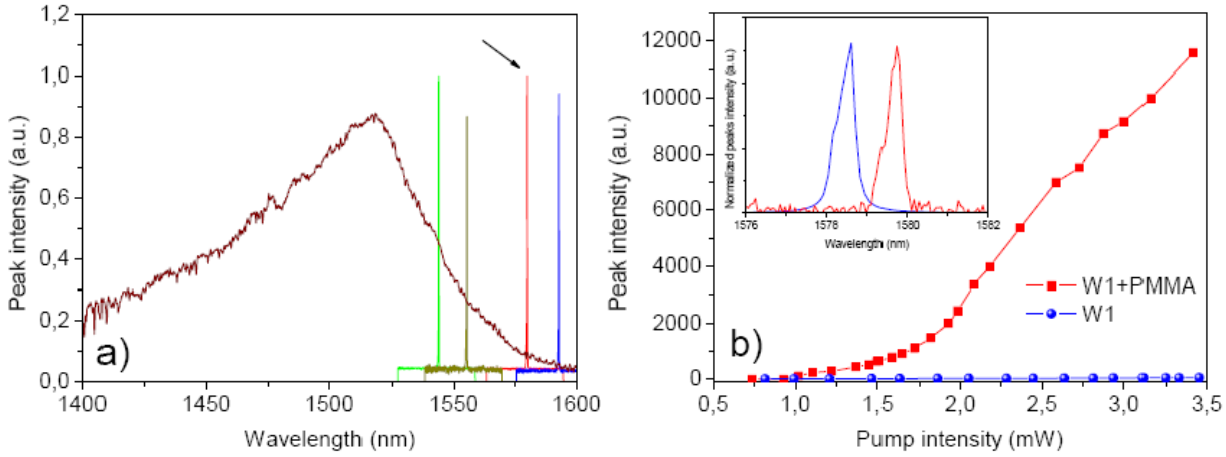

Figure 5.11 *(a) Spectrum of the spontaneous emission (brown line) and of the resonant peaks of four different structures (small changes in the holes radius). (b) laser intensity plotted against the incident pump power (7 ns pulse, 6% duty cycle) for one of the structures (indicated with the black arrow). The inset shows the peaks shape for the W1 (blue) and W1+PMMA (red) structures below lasing threshold.*

However the measured laser threshold is higher than the real value because it is obtained considering that all the optical pump power is absorbed by the InP barrier, while previous simulations demonstrated that only 35% of the pump power is effectively absorbed. For the W1 configuration the lasing threshold has not been reached within the pumping energy range explored, possibly because the pumped area (~3 µm) is less than the effective volume of the SBM. For this reason even if the inversion condition has been achieved inside this area it would vanish at the edge by absorption. The inset of figure 5.11(b) shows the emitted peak relative to the W1 and W1+PMMA configuration: a shift to longer wavelength of the emission peak in the W1+PMMA configuration can be observed, as anticipated in the discussion and in agreement with the simulation results.

To evaluate the effect of the cavity width, a second set of measurements has been performed, using a PMMA strip with about 1 µm width. The effective modal volume for this cavity, obtained from the simulation, is around $1.29(\lambda/n)^3$, nearly the same as for the 3 µm large PMMA strip with a corresponding Purcell Factor of 137. Figure 5.12 shows the emitted light

versus the input one obtained for this configuration. From these curves the lasing threshold remains approximately unchanged, as expected, giving the nearly unchanged mode volume. The main change is the increase of the slope efficiency, probably due to a higher directivity of the emission and therefore a better output coupling.

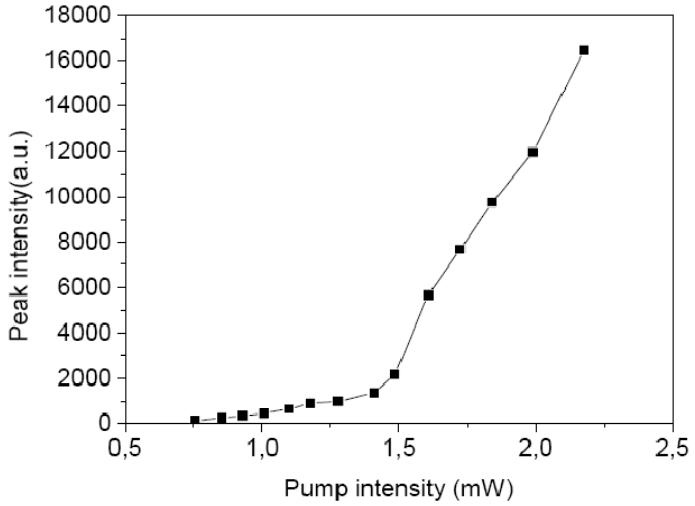

Figure 5.12 *Power in versus power out curve showing the power at the laser wavelength versus the incident pump power. The width of the PMMA strip is around 1 µm, and the pump pulse is around 7 ns long (6% duty cycle).*

5.5 Conclusions

In this chapter the theoretical study and the experimental realization of a microcavity for small mode volume photon confinement have been presented. The efficient spatial optical confinement is achieved using a local effective index modulation in a W1 PC waveguide supporting a low group velocity mode at the edge of the first Brillouin zone. The physics of the confinement is explained through a simple model based on the envelope formalism. First test devices, comprising a W1-PC waveguide and a dielectric strip, on an InP-based multi-quantum well heterostructure bonded onto fused silica has been fabricated and optically characterized. The index modulation is achieved by electron beam patterning of a PMMA strip above the PC, which created a local increase of the effective index of the waveguide. Optical measurements have been performed on our structures and reproducible results have been obtained in agreement with the theoretical predictions. Laser emission is obtained with W1+PMMA structures at room temperature, with an estimated effective threshold of about 0.5 mW with PMMA strips 1 and 3 µm wide. The simple and reproducible production process, together with the robustness and mechanical stability of the device, make this type of low threshold lasers good candidates for both surface-emitting and coupled-to-waveguide laser devices. Moreover

the high Purcell Factor of 250 for the 3 μm wide PMMA strip could lead to applications in the field of integrated quantum photonics. Finally, it should be emphasized that, by changing the shape of the dielectric layer, other prototype designs for cavity-confined or guided slow light modes can be fabricated in a similar fashion.

REFERENCES

[1] P. Pottier, C. Seassal, X. Letartre, J. L. Leclercq, P. Viktorovitch, D. Cassagne, C. Jouanin, J. Lightwave Technol., 1999, 17, 2058.

[2] C. Seassal, P. Rojo-Romeo, X. Letartre, P. Viktorovitch, G. Hollinger, E. Jalaguier, S. Pocas, B. Aspar,Electron. Lett., 2001, 37, 222.

[3] C. Seassal, C. Monat, J. Mouette, E . Touraille, B. Ben Bakir, H. Hattori, J. L. Leclercq, X. Letartre, P. Rojo-Romeo, and P. Viktorovitch, IEEE J. Sel. Top. in Quantum Electron., 2005, 11, 395.

CHAPTER 6

Non Linear Optics

6.1 Introduction to non-linear optics

Before the discovery of laser sources by Maiman in the 1960's the equations governing the propagation of light within a medium always manifested a linear feature.

In the linear regime the electric polarization $\bar{P}$ can be assumed to be linearly proportional to the electric field strength of a crossing optical field:

$$\overline{\boldsymbol{P}}^{(1)} = \boldsymbol{\varepsilon_0 \chi \overline{E}} \qquad \text{Eq. 6.1}$$

with ε_0 vacuum permittivity, and χ medium susceptibility.

Based on this linear assumption the Maxwell's equations can be written as:

$$\boldsymbol{\nabla^2 \overline{E} = -\frac{\varepsilon}{c^2}\frac{\partial^2 \overline{E}}{\partial t^2}} \qquad \text{Eq. 6.2}$$

where ε is the dielectric constant, related to the susceptibility by the relation:

$$\boldsymbol{\varepsilon = 1 + 4\pi\chi} \qquad \text{Eq. 6.3}$$

(6.2) has only terms proportional to the first power of the electric field. As a result, coupling between different light beams, or between different frequencies of a light beam, crossing the medium simultaneously, is not possible. In other word this means that the medium cannot act as a source for the generation of new frequencies. The attenuation of the beam propagating in an absorptive medium can be written as:

$$\boldsymbol{\frac{dI}{dz} = -\alpha I} \qquad \text{Eq. 6.4}$$

where I is the beam intensity, z the variable along the propagation direction, and α the absorption coefficient.

Integrating (6.4) leads to the Lambert-Beer law:

$$\boldsymbol{I(z) = I(0)e^{-\alpha z}} \qquad \text{Eq. 6.5}$$

The meaning of the Lambert-Beer law is that the attenuation of a beam travelling across the medium is linearly proportional to its initial intensity.

α is related to extinction coefficient k, indicating the amount of absorption of the incident wave, from the relation:

$$\boldsymbol{\alpha = \frac{2\omega k}{c}} \qquad \text{Eq. 6.6}$$

This latter in turn is related to the refractive index of the medium according to:

$$\boldsymbol{n_C = n_0 + ik = \sqrt{\varepsilon} = \left[1 + 4\pi\chi^{(1)}\right]^{1/2}} \qquad \text{Eq. 6.7}$$

where $n_C(\omega)$ is the complex refractive index constituted of a real and an imaginary component. The two parts are linked together through the Kramers-Krönig relations: $n_0 = Re\sqrt{\varepsilon} = c/v_m$ is the refractive index describing the dispersive processes, and $k(\omega) = Im\sqrt{\varepsilon}$ is the extinction coefficient.

This is the linear response of the medium, valid at low field intensity.

When an intense field interacts with an optical medium the linear assumption is no longer adequate. The polarization in now described by replacing (6.1) with a power series:

$$\boldsymbol{\overline{P} = \varepsilon_0\left(\chi^{(1)} \cdot \overline{E} + \chi^{(2)} \cdot \overline{E}\overline{E} + \chi^{(3)} \cdot \overline{E}\overline{E}\overline{E} + \cdots\right) = \overline{P}^{(1)} + \overline{P}^{(2)} + \overline{P}^{(3)} + \cdots} \qquad \text{Eq. 6.8}$$

where $\chi^{(n)}$ is the n^{th}-order susceptibility, that is a material coefficient represented by a (*n+1*)-rank tensor.

The Maxwell's equation becomes:

$$\boldsymbol{\nabla^2\overline{E} = -\frac{\varepsilon}{c^2}\frac{\partial^2\overline{E}}{\partial t^2} - \frac{4\pi}{c^2}\frac{\partial^2\overline{P}^{NL}}{\partial t^2}} \qquad \text{Eq. 6.9}$$

$\overline{P}^{NL} = \overline{P} - \overline{P}^{(1)}$ is the non linear polarization term: it is negligible in the linear regime, and becomes important in the non-linear one. P^{NL} is a source term: it can generate new frequencies or modify the incident one.

To clarify this sentence it can be useful to consider the simple case of a monochromatic incident field

$$\boldsymbol{\overline{E} = E_0\cos(\omega t - kz)} \qquad \text{Eq. 6.10}$$

Inserting (6.10) in (6.8), and considering only the first three terms of the power series expansion it results in:

$$\boldsymbol{P = \chi^{(1)} E_0 \cos(\omega t - kz) + \chi^{(2)} E_0^2 \cos^2(\omega t - kz) + \chi^{(3)} E_0^3 \cos^3(\omega t - kz) + \cdots}$$ Eq. 6.11

This equation can be written as:

$$\boldsymbol{P = \chi^{(1)} E_0 \cos(\omega t - kz) + \frac{1}{2}\chi^{(2)} E_0^2 [1 + \cos(2\omega t - 2kz)] +}$$

$$\boldsymbol{+ \frac{1}{4}\chi^{(3)} E_0^3 [3\cos(\omega t - kz) + \cos(3\omega t - kz)]}$$ Eq. 6.12

This equation clearly shows the presence of new frequencies related to the non linear polarization. The $\chi^{(2)}$ term presents two contributions: the first one is frequency independent, the second one exhibits a frequency dependence at 2*ω*. The frequency independent contribution describes the *optical rectification*: the appearance of a static electric field within the non-linear medium. The other one is known as the *second harmonic generation*: the incident radiation at frequency *ω* is converted to radiation at doubled frequency. The $\chi^{(3)}$ term also consists of two contributions, depending respectively on *ω* and on *3ω*. The second one, depending on *3ω,* leads to *third harmonic generation*. The term describing a response at frequency *ω*, leads to the non-linear contribution to the complex refractive index experienced by a wave at frequency *ω*. The real part of the refractive index, in presence of this type of non-linearity can be represented as:

$$\boldsymbol{n = n_0 + n_2 I}$$ Eq. 6.13

where n_0 is the linear refractive index, $I = (n_0 c/8\pi)E^2$ is the intensity of the incident wave, and n_2 is a constant characterizing the strength of the optical non-linearity, defined as:

$$\boldsymbol{n_2 = \frac{12\pi^2}{n_0^2 c} Re\left(\chi^{(3)}\right)}$$ Eq. 6.14

where $Re\left(\chi^{(3)}\right)$ is the real component of the third order optical susceptibility.

The refractive index dependence on the field intensity is known as *Kerr effect*.

Analogously it is possible to define the absorption coefficient as:

$$\boldsymbol{\alpha = \alpha_0 + \beta I}$$ Eq. 6.15

with α_0 the linear absorption coefficient, and β the *two-photon absorption* coefficient related to the imaginary part of the susceptibility as:

$$\boldsymbol{\beta = \frac{3\pi}{\varepsilon_0 c n_0^2 \lambda} Im\left(\chi^{(3)}\right)}$$ Eq. 6.16

Generally speaking, the linear absorption will be described by the imaginary part of $\chi^{(1)}$ and, for nonlinear absorption, the *m*-photon absorption will be expressed by the imaginary component of $\chi^{(2m-1)}$.

6.2 Non linear optical properties

In this chapter, the general formulas for the nonlinear susceptibilities and their properties will be firstly introduced.

The radiation electric field can be written as sum of components at different frequencies ω_n:

$$\bar{\boldsymbol{E}}(\bar{\boldsymbol{r}},\boldsymbol{t}) = \sum_{\boldsymbol{n}>0} \bar{\boldsymbol{E}}_{\boldsymbol{n}}(\bar{\boldsymbol{r}},\boldsymbol{t}) = \sum_{\boldsymbol{n}>0} \boldsymbol{E}_{\boldsymbol{n}} \boldsymbol{e}^{-i\omega_n t} + \boldsymbol{c}.\boldsymbol{c}. = \sum_{\boldsymbol{n}>0} \boldsymbol{A}_{\boldsymbol{n}} \boldsymbol{e}^{i(\bar{k}_n \cdot \bar{r} - \omega_n t)} + \boldsymbol{c}.\boldsymbol{c}. \quad \text{Eq. 6.17}$$

The running index (*n > 0*) means that the summation must be taken over positive frequencies only.

Because the electric field $\bar{E}$ is a real quantity, the frequency components in (6.17) must satisfy the condition:

$$\boldsymbol{E}_{\boldsymbol{n}}^{*} \equiv \boldsymbol{E}(\boldsymbol{\omega}_{\boldsymbol{n}})^{*} = \boldsymbol{E}(-\boldsymbol{\omega}_{\boldsymbol{n}}) \qquad \boldsymbol{A}_{\boldsymbol{n}}^{*} \equiv \boldsymbol{A}(\boldsymbol{\omega}_{\boldsymbol{n}})^{*} = \boldsymbol{A}(-\boldsymbol{\omega}_{\boldsymbol{n}}) \quad \text{Eq. 6.18}$$

The expression for the electric field can be rewritten as sum over all frequencies, both positive and negative:

$$\bar{\boldsymbol{E}}(\bar{\boldsymbol{r}},\boldsymbol{t}) = \sum_{\boldsymbol{n}} \boldsymbol{E}(\boldsymbol{\omega}_{\boldsymbol{n}}) \boldsymbol{e}^{-i\omega_n t} = \sum_{\boldsymbol{n}} \boldsymbol{A}(\boldsymbol{\omega}_{\boldsymbol{n}}) \boldsymbol{e}^{i(\bar{k}_n \cdot \bar{r} - \omega_n t)} \quad \text{Eq. 6.19}$$

A similar notation can be used also for the polarization:

$$\bar{\boldsymbol{P}}(\bar{\boldsymbol{r}},\boldsymbol{t}) = \sum_{\boldsymbol{n}} \boldsymbol{P}(\boldsymbol{\omega}_{\boldsymbol{n}}) \boldsymbol{e}^{-i\omega_n t} \quad \text{Eq. 6.20}$$

The component *i* of the polarization can be decomposed in different order terms:

$$\boldsymbol{P}_{\boldsymbol{i}}(\boldsymbol{\omega}_{\boldsymbol{n}}) = \boldsymbol{P}_{\boldsymbol{i}}^{(1)}(\boldsymbol{\omega}_{\boldsymbol{n}}) + \boldsymbol{P}_{\boldsymbol{i}}^{(2)}(\boldsymbol{\omega}_{\boldsymbol{n}}) + \boldsymbol{P}_{\boldsymbol{i}}^{(3)}(\boldsymbol{\omega}_{\boldsymbol{n}}) + \cdots \quad \text{Eq. 6.21}$$

where

$$\boldsymbol{P}_{\boldsymbol{i}}^{(1)}(\boldsymbol{\omega}_{\boldsymbol{n}}) = \boldsymbol{\varepsilon}_{\boldsymbol{0}} \sum_{\boldsymbol{j}} \boldsymbol{\chi}_{\boldsymbol{ij}}^{(1)}(\boldsymbol{\omega}_{\boldsymbol{n}}) \boldsymbol{E}_{\boldsymbol{j}}(\boldsymbol{\omega}_{\boldsymbol{n}}) \quad \text{Eq. 6.22}$$

$$\boldsymbol{P}_{\boldsymbol{i}}^{(2)}(\boldsymbol{\omega}_{\boldsymbol{n}} = \boldsymbol{\omega}_{\boldsymbol{p}} + \boldsymbol{\omega}_{\boldsymbol{q}}) = \boldsymbol{\varepsilon}_{\boldsymbol{0}} \sum_{\boldsymbol{jk}} \sum_{\boldsymbol{pq}} \boldsymbol{\chi}_{\boldsymbol{ijk}}^{(2)}(\boldsymbol{\omega}_{\boldsymbol{n}} = \boldsymbol{\omega}_{\boldsymbol{p}} + \boldsymbol{\omega}_{\boldsymbol{q}}) \boldsymbol{E}_{\boldsymbol{j}}(\boldsymbol{\omega}_{\boldsymbol{p}}) \boldsymbol{E}_{\boldsymbol{k}}(\boldsymbol{\omega}_{\boldsymbol{q}}) \quad \text{Eq. 6.23}$$

$$\boldsymbol{P}_{\boldsymbol{i}}^{(3)}(\boldsymbol{\omega}_{\boldsymbol{n}} = \boldsymbol{\omega}_{\boldsymbol{p}} + \boldsymbol{\omega}_{\boldsymbol{q}} + \boldsymbol{\omega}_{\boldsymbol{r}}) = \boldsymbol{\varepsilon}_{\boldsymbol{0}} \sum_{\boldsymbol{jkl}} \sum_{\boldsymbol{pqr}} \boldsymbol{\chi}_{\boldsymbol{ijkl}}^{(3)}(\boldsymbol{\omega}_{\boldsymbol{n}} = \boldsymbol{\omega}_{\boldsymbol{p}} + \boldsymbol{\omega}_{\boldsymbol{q}} + \boldsymbol{\omega}_{\boldsymbol{r}}) \boldsymbol{E}_{\boldsymbol{j}}(\boldsymbol{\omega}_{\boldsymbol{p}}) \boldsymbol{E}_{\boldsymbol{k}}(\boldsymbol{\omega}_{\boldsymbol{q}}) \boldsymbol{E}_{\boldsymbol{l}}(\boldsymbol{\omega}_{\boldsymbol{r}}) \quad \text{Eq. 6.24}$$

Here the indices *j,k,l* refer to the Cartesian coordinates of the fields involved in the interaction and the summation over *p,q,r* is related to the degeneracy properties of $\omega_p, \omega_q, \omega_r$. In fact, for a process, the sum $(\omega_p + \omega_q + \omega_r)$ is to be fixed, although the individual terms of the sum can be varied.

The various order susceptibilities of a medium are the key parameters to describe the nonlinear coupling between different incident waves, as well as the generation of new-frequency radiation through the induced nonlinear electric polarization of the medium.

The optical susceptibilities are characteristic of the material, so some symmetry properties of the medium allow a simplification of the expression of χ, which is normally constituted by numerous terms, when the interaction needs high nonlinear order description.

For the third-order susceptibility, for example, the symmetry properties are as follows.[1]

1- *Reality of the fields*: since the fields are physically measurable quantities, hence are real, it is correct to consider:

$$\left[\boldsymbol{\chi}^{(3)}_{ijkl}(\boldsymbol{\omega_1}, \boldsymbol{\omega_2}, \boldsymbol{\omega_3})\right]^* = \boldsymbol{\chi}^{(3)}_{ijkl}(-\boldsymbol{\omega_1}, -\boldsymbol{\omega_2}, -\boldsymbol{\omega_3}) \qquad \text{Eq. 6.25}$$

2- *Intrinsic permutation symmetry*: susceptibilities obtained by exchanging the order of both the incoming fields and their Cartesian indexes are equivalent:

$$\boldsymbol{\chi}^{(3)}_{ijkl}(\boldsymbol{\omega_1}, \boldsymbol{\omega_2}, \boldsymbol{\omega_3}) = \boldsymbol{\chi}^{(3)}_{ijkl}(\boldsymbol{\omega_2}, \boldsymbol{\omega_1}, \boldsymbol{\omega_3}) = \boldsymbol{\chi}^{(3)}_{ijkl}(\boldsymbol{\omega_3}, \boldsymbol{\omega_1}, \boldsymbol{\omega_2}) = \cdots \qquad \text{Eq. 6.26}$$

3- *Symmetries for lossless media*: the transparent media have a real susceptibility. When the medium is lossless and its interaction with the fields does not involve frequencies near the resonance frequencies of the systems, all the frequencies of the nonlinear susceptibility, including those of the incoming fields and of the nonlinear polarization, can be interchanged if also the Cartesian indexes are interchanged simultaneously.

$$\boldsymbol{\chi}^{(3)}_{ijkl}(\boldsymbol{\omega_1}, \boldsymbol{\omega_2}, \boldsymbol{\omega_3}) = \boldsymbol{\chi}^{(3)}_{ijkl}(-\boldsymbol{\omega_1}, -\boldsymbol{\omega_2}, -\boldsymbol{\omega_3}) \qquad \text{Eq. 6.27}$$

5- *Kleinman's symmetry*: under the condition that the field frequencies are lower than the resonance frequencies of the material system, the nonlinear susceptibility is independent of frequency. This is equivalent to change the indices of χ without changing the frequencies:

$$\boldsymbol{\chi}^{(3)}_{ijkl}(\boldsymbol{\omega_1}, \boldsymbol{\omega_2}, \boldsymbol{\omega_3}) = \boldsymbol{\chi}^{(3)}_{jkli}(\boldsymbol{\omega_1}, \boldsymbol{\omega_2}, \boldsymbol{\omega_3}) = \cdots \qquad \text{Eq. 6.28}$$

6- *Spatial symmetry*: some spatial symmetries of the material are useful to reduce the number of independent non-zero tensor components of the susceptibility. One of these is the inversion symmetry causing the vanishing of all the components of even-order susceptibilities. So, to have a measurable even-order process, it is necessary to avoid the inversion symmetry of the system.

6.3 Parametric and non-parametric processes

The different non-linear optical processes can be grouped into two families: the parametric and the non-parametric processes. In parametric processes the light matter interactions does not entail an energy exchange: the material behaves as a catalyst for the interactions between the different frequencies of the applied fields. The initial and final quantum mechanical states of the system are identical, and the population is excited from the ground state to a virtual level only for a time interval of the order of $\hbar/\Delta E$, according with the uncertainty principle, where ΔE is the energy difference between the virtual level and the nearest real level. A parametric process is always described by a real susceptibility, and the total field energy is always conserved.

The non-parametric processes involve an energy exchange between the matter and the incident field, whose frequency must be resonant with the transition energies of the absorbing materials. Thus in these processes there is a population transfer between two real levels. Non-parametric processes are described by the complex susceptibility, and the total field energy needs not to be conserved, because it can be transferred to or from the material medium.

It is demonstrated that all the non-parametric processes are described by a susceptibility $\chi^{(n)}$, with odd *n* and that all the processes described by a susceptibility $\chi^{(n)}$, with even *n* are parametric.

In this work we are mainly interested in the study of a non parametric process, the two photon absorption (TPA), described by the third order susceptibility.

6.4 Calculation of the non-linear susceptibility

Based on the scheme of quantum electrodynamics it is possible to give a rigorous description of the non-linear susceptibilities. These expressions are important because they show how the nonlinear coefficients are dependent on the material parameters, such as the transition dipole moments and the energy levels of the systems. The model generally employed is semi-classical: the media composed of atoms and molecules are described using the quantum mechanical theory, while the light radiation is described by the classical Maxwell's theory.[2] In the next section, the non-liner susceptibilities are obtained from the solution of the Schrödinger's equation, applied to the atomic wavefunctions. This formalism leads to an accurate description of non-resonant response of atomic systems, but cannot describe adequately the near-resonance processes. In order to take into account resonant processes, it is necessary to

introduce the density matrix formalism, which is a special approach based on both quantum mechanics and statistical physics. Using this formalism, described in section 6.6, it is possible to predict many possible nonlinear optical responses of the medium for a given condition of the input intense optical field.

6.5 Susceptibility from the Schrödinger equation calculation

The properties of the atomic (molecular) system are described through the time dependent Schrödinger's equation:

$$\boldsymbol{i\hbar\frac{\partial\psi}{\partial t}=\hat{H}\psi} \qquad \text{Eq. 6.29}$$

whose solutions are the eigenfunctions $\psi_n(\bar{r},t)$.

Here $\hat{H}$ is the Hamiltonian operator:

$$\boldsymbol{\hat{H}=\hat{H}_0+\hat{V}(t)} \qquad \text{Eq. 6.30}$$

where $\hat{V}(t)$ is the Hamiltonian operator of the interaction between the optical field and an atom.

It has the form:

$$\boldsymbol{\hat{V}(t)=-\hat{\mu}\cdot\tilde{E}(t)} \qquad \text{Eq. 6.31}$$

where $\hat{\mu}=-e\hat{r}(t)$ is the electric dipole moment operator, -e is the electron charge, and $\tilde{E}(t)$ is the electric field, expressed as :

$$\boldsymbol{\tilde{E}(t)=\sum_p \bar{E}(\omega_p)e^{i\omega_p t}} \qquad \text{Eq. 6.32}$$

If there is not an external electric field, $\hat{H}=\hat{H}_0$, the Schrödinger equation possesses solutions in the form of stationary states:

$$\boldsymbol{\psi_n(\bar{r},t)=u_n(\bar{r})e^{i\omega_n t}} \qquad \text{Eq. 6.33}$$

with $u_n(\bar{r})$ spatially varying part of the wave function that satisfies the time dependent Schrödinger equation:

$$\boldsymbol{\hat{H}_0 u_n(\bar{r})=E_n u_n(\bar{r})} \qquad \text{Eq. 6.34}$$

For convenience, they are chosen to be a complete set of orthonormal functions:

$$\boldsymbol{\int u_m^*(\bar{r})u_n(\bar{r})d^3r=\delta_{mn}} \qquad \text{Eq. 6.35}$$

When there is an external field crossing the medium, $\hat{V}(t)$ must be considered and it is necessary to use perturbation theory in order to solve the Schrödinger equation.

The Hamiltonian is written as:

$$\boldsymbol{\hat{H}=\hat{H}_0+\lambda\hat{V}(t)} \qquad \text{Eq. 6.36}$$

with λ varying continuously between 0 and 1 and representing the strength of the interaction.

The eigenfunctions $\psi(\bar{r},t)$ can be expanded in a power series in λ:

$$\boldsymbol{\psi(\bar{r},t) = \psi^{(0)}(\bar{r},t) + \lambda\psi^{(1)}(\bar{r},t) + \lambda^2\psi^{(2)}(\bar{r},t) + \cdots} \quad \text{Eq. 6.37}$$

By introducing (6.37) in (6.29) and decoupling in a set of equations proportional to λ^N that must satisfy the equality separately, it results in:

$$\begin{cases} \boldsymbol{\lambda^0 \rightarrow i\hbar\frac{\partial\psi^{(0)}}{\partial t} = \hat{H}_0\psi^{(0)}} & \boldsymbol{(a)} \\ \boldsymbol{\lambda^1 \rightarrow i\hbar\frac{\partial\psi^{(1)}}{\partial t} = \hat{H}_0\psi^{(1)} + \hat{V}(t)\psi^{(0)}} & \boldsymbol{(b)} \\ \vdots & \\ \boldsymbol{\lambda^N \rightarrow i\hbar\frac{\partial\psi^{(N)}}{\partial t} = \hat{H}_0\psi^{(N)} + \hat{V}(t)\psi^{(N-1)}} & \boldsymbol{(c)} \end{cases} \quad \text{Eq. 6.38}$$

Equation (6.38a) is just the Schrödinger equation without the external field. Assuming that the atom is initially in the ground state g it results in:

$$\boldsymbol{\psi^{(0)}(\bar{r},t) = u_g(\bar{r})e^{-i\omega_g t}} \quad \text{Eq. 6.39}$$

The other equations can be solved by expanding the $\psi^{(N)}(\bar{r},t)$ in terms of the set of wave functions $u_n(\bar{r})$:

$$\boldsymbol{\psi^{(N)}(\bar{r},t) = \sum_l a_l^{(N)}(t)u_l(\bar{r})e^{-i\omega_l t}} \quad \text{Eq. 6.40}$$

Here, the expansion coefficient $a_l^{(N)}(t)$ represents the amplitude of probability that, to the N$^{\text{th}}$-order in the perturbation, the atom is in the energy eigenstate l at time *t.*

Substituting (6.40) inside (6.38c) results in a system of equations of the form:

$$\boldsymbol{i\hbar\sum_l \dot{a}_l^{(N)}u_l(\bar{r})\,e^{-i\omega_l t} = \sum_l a_l^{(N-1)}\hat{V}u_l\,(\bar{r})e^{-i\omega_l t}} \quad \text{Eq. 6.41}$$

where the dot denotes the time derivative.

By multiplying both side from the left by u_m^* and integrating over the space, (6.41) results in:

$$\boldsymbol{\dot{a}_m^{(N)} = -\frac{i}{\hbar}\sum_l V_{ml}\,a_l^{(N-1)}e^{i\omega_{ml}t}} \quad \text{Eq. 6.42}$$

where

$$\boldsymbol{V_{ml} = \langle \mathbf{u}_m|\hat{V}|\mathbf{u}_l\rangle = \int u_m^*\,\hat{V}\mathbf{u}_l d^3r} \quad \text{Eq. 6.43}$$

Finally, time integrating, (6.42) results in:

$$\boldsymbol{a_m^{(N)}(t) = -\frac{i}{\hbar}\sum_l \int_{-\infty}^{t} dt' V_{ml}(t')a_l^{(N-1)}(t')e^{i\omega_{ml}t'}} \quad \text{Eq. 6.44}$$

In (6.44) the N$^{\text{th}}$-order expansion coefficient depends on the (N-1)$^{\text{th}}$-order one. Starting from $a_l^{(o)} = \delta_{lg}$, it is thus possible, to obtain all the higher order terms.

Using (6.31) and (6.32) the obtained expression for $a_m^{(1)}$ is:

$$\boldsymbol{a_m^{(1)}(t) = \frac{1}{\hbar}\sum_p \frac{\bar{\mu}_{mg}\cdot\bar{E}(\omega_p)}{\omega_{mg}-\omega_p}e^{i(\omega_{mg}-\omega_p)t}} \quad \text{Eq. 6.45}$$

with

$$\bar{\mu}_{mg} = \int u_m^* \hat{\mu} u_g d^3 r \quad \text{Eq. 6.46}$$

Analogously it is possible to obtain the expression of $a_m^{(2)}$ and $a_m^{(3)}$:

$$a_n^{(2)}(t) = \frac{1}{\hbar^2} \sum_{pq} \sum_m \frac{[\bar{\mu}_{nm} \cdot \bar{E}(\omega_q)][\bar{\mu}_{mg} \cdot \bar{E}(\omega_p)]}{(\omega_{ng} - \omega_p - \omega_q)(\omega_{mg} - \omega_p)} e^{i(\omega_{mg} - \omega_p - \omega_q)t} \quad \text{Eq. 6.47}$$

$$a_v^{(3)}(t) = \frac{1}{\hbar^3} \sum_{pqr} \sum_{mn} \frac{[\bar{\mu}_{vn} \cdot \bar{E}(\omega_r)][\bar{\mu}_{nm} \cdot \bar{E}(\omega_q)][\bar{\mu}_{mg} \cdot \bar{E}(\omega_p)]}{(\omega_{vg} - \omega_p - \omega_q - \omega_r)(\omega_{ng} - \omega_p - \omega_q)(\omega_{mg} - \omega_p)} e^{i(\omega_{vg} - \omega_p - \omega_q - \omega_r)t} \quad \text{Eq. 6.48}$$

Linear susceptibility:

The expectation value of the electric dipole is:

$$\langle \tilde{p} \rangle = \langle \psi | \hat{\mu} | \psi \rangle \quad \text{Eq. 6.49}$$

where ψ comes from (6.37) with λ equal to 1.

The polarization per atom, which is the induced dipole moment, at the first-order is given by:

$$\langle \tilde{p}^{(1)} \rangle = \langle \psi^{(0)} | \hat{\mu} | \psi^{(1)} \rangle + \langle \psi^{(1)} | \hat{\mu} | \psi^{(0)} \rangle \quad \text{Eq. 6.50}$$

The linear polarization for *N* atoms is:

$$\langle \bar{P}^{(1)} \rangle = N \langle \bar{p}^{(1)} \rangle = \sum_p \bar{P}^{(1)}(\omega_p) e^{-i\omega_p t} \quad \text{Eq. 6.51} \qquad P_i^{(1)}(\omega_p) = \sum_p \chi_{ij}^{(1)} E_j(\omega_p) \quad \text{Eq. 6.52}$$

Using this relation, it is possible to determine the form of the linear optical susceptibility:

$$\chi_{ij}^{(1)}(\omega_p) = \frac{N}{\hbar} \sum_m \left(\frac{\mu_{gm}^i \mu_{mg}^j}{\omega_{mg} - \omega_p} + \frac{\mu_{gm}^j \mu_{mg}^i}{\omega_{mg}^* + \omega_p} \right) \quad \text{Eq. 6.53}$$

with μ_{mg} representing the matrix element of the dipole moment operator, evaluated between the *m* and *g* states, and known as dipole transition moment.

The transition frequency ω_{mg} is expressed as a complex quantity:

$$\omega_{mg} = \omega_{mg}^{(0)} - i\gamma_m/2 \quad \text{Eq. 6.54}$$

Here, $\omega_{mg}^{(0)}$ is the (real) transition frequency identifying the energy difference between the two states and γ_m is the population decay rate from the upper level *m*. In this way, the damping effects are introduced, even if this choice cannot explain correctly all the dephasing processes: these effects will be described by the density matrix theory.

The first and the second terms of (6.53) are respectively the resonant and the non resonant contributions to the linear susceptibility. State *g* is generally identified as the ground state of the system and *m* is a virtual state representing one of the energy eigenstates of the system.

When the incident field has a frequency $\omega_p = \omega_m - \omega_g = \omega_{mg}$, this frequency can be absorbed by the system (see figure 6.1(a)). In this case, the first term, and consequentially the first-order optical response, increases.

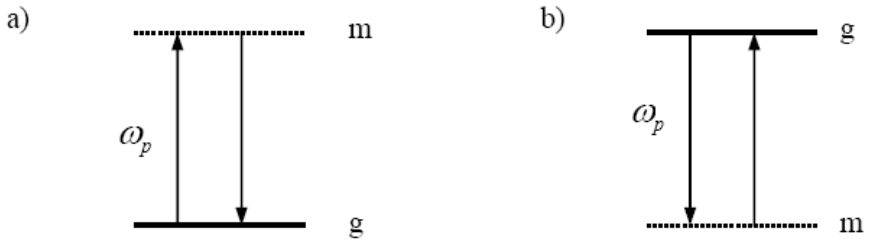

Figure 6.1 *Energy diagrams for resonant (a) and non resonant (b) contributions to linear susceptibility.*

In the second term the frequency ω_p is emitted by the system and has a positive sign in (6.53). Using the same procedure, it is possible to calculate the second and the third-order susceptibility.

2nd order susceptibility

The 2nd order contribution to the induced dipole moment per molecule can be expressed, analogously to (6.50), as:

$$\langle \tilde{\boldsymbol{p}}^{(2)} \rangle = \langle \boldsymbol{\psi}^{(0)} | \hat{\boldsymbol{\mu}} | \boldsymbol{\psi}^{(2)} \rangle + \langle \boldsymbol{\psi}^{(1)} | \hat{\boldsymbol{\mu}} | \boldsymbol{\psi}^{(1)} \rangle + \langle \boldsymbol{\psi}^{(2)} | \hat{\boldsymbol{\mu}} | \boldsymbol{\psi}^{(0)} \rangle \qquad \text{Eq. 6.55}$$

The second order susceptibility is:

$$\boldsymbol{\chi}^{(2)}_{ijk}(\boldsymbol{\omega_p} + \boldsymbol{\omega_q}, \boldsymbol{\omega_q}, \boldsymbol{\omega_p}) = \frac{N}{\hbar^2} \wp_1 \sum_{mn} \left(\frac{\mu^i_{gn} \mu^j_{nm} \mu^k_{mg}}{(\omega_{ng} - \omega_p - \omega_q)(\omega_{mg} - \omega_p)} + \frac{\mu^j_{gn} \mu^i_{nm} \mu^k_{mg}}{(\omega^*_{ng} + \omega_q)(\omega_{mg} - \omega_p)} + \right.$$

$$\left. \frac{\mu^j_{gn} \mu^k_{nm} \mu^i_{mg}}{(\omega^*_{ng} + \omega_q)(\omega^*_{mg} + \omega_p + \omega_q)} \right) \qquad \text{Eq. 6.56}$$

with $\wp_1$ denoting the intrinsic permutation operator.

Third order susceptibility

The 3rd order contribute is:

$$\langle \tilde{\boldsymbol{p}}^{(3)} \rangle = \langle \boldsymbol{\psi}^{(0)} | \hat{\boldsymbol{\mu}} | \boldsymbol{\psi}^{(3)} \rangle + \langle \boldsymbol{\psi}^{(1)} | \hat{\boldsymbol{\mu}} | \boldsymbol{\psi}^{(2)} \rangle + \langle \boldsymbol{\psi}^{(2)} | \hat{\boldsymbol{\mu}} | \boldsymbol{\psi}^{(1)} \rangle + \langle \boldsymbol{\psi}^{(3)} | \hat{\boldsymbol{\mu}} | \boldsymbol{\psi}^{(0)} \rangle \qquad \text{Eq. 6.57}$$

And the third order susceptibility can be expressed as:

$$\boldsymbol{\chi}^{(3)}_{ijkh}(\boldsymbol{\omega_\sigma}, \boldsymbol{\omega_p}, \boldsymbol{\omega_q}, \boldsymbol{\omega_p}) =$$

$$\frac{N}{\hbar^3} \wp_1 \sum_{mnv} \left(\frac{\mu^k_{gv} \mu^j_{vn} \mu^i_{nm} \mu^h_{mg}}{(\omega_{vg} - \omega_r - \omega_q - \omega_p)(\omega_{ng} - \omega_q - \omega_p)(\omega_{mg} - \omega_p)} + \frac{\mu^j_{gv} \mu^k_{vn} \mu^i_{nm} \mu^h_{mg}}{(\omega^*_{vg} + \omega_r)(\omega_{ng} - \omega_q - \omega_p)(\omega_{mg} - \omega_p)} + \right.$$

$$\left. \frac{\mu^j_{gv} \mu^i_{vn} \mu^k_{nm} \mu^h_{mg}}{(\omega^*_{vg} + \omega_q)(\omega^*_{ng} + \omega_r + \omega_q)(\omega_{mg} - \omega_p)} + \frac{\mu^j_{gv} \mu^i_{vn} \mu^h_{nm} \mu^k_{mg}}{(\omega^*_{vg} + \omega_r)(\omega^*_{ng} + \omega_r + \omega_q)(\omega^*_{mg} + \omega_r + \omega_q + \omega_p)} \right) \qquad \text{Eq. 6.58}$$

Figure 6.2 identifies the resonances for the four terms in (6.58).

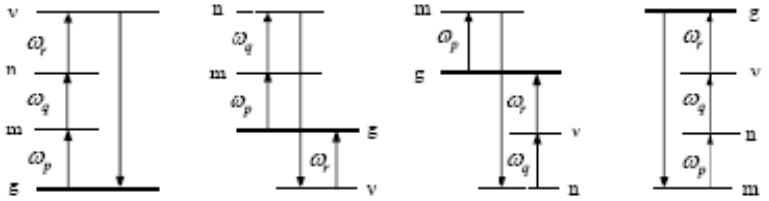

Figure 6.2 *Location of the resonances of the terms in the expression 6.58.*

6.6 Density matrix formalism of quantum mechanics

The density matrix formalism (DM) is capable to effectively describe the resonant processes. This formalism is a combination of quantum mechanics, perturbation theory and macroscopic statistical mechanics.

The DM formalism till starts from the basic laws of quantum mechanics (6.29) and (6.30), with the wave functions represented as:

$$\boldsymbol{\psi_s(\bar{r},t) = \sum_n C_n^s(t) u_n(\bar{r})} \qquad \text{Eq. 6.59}$$

where the terms $u_n(\bar{r})$ obey to (6.34) and (6.35), and $C_n^s(t)$ express the probability amplitude that the atom, which is known to be in state *s*, is in the energy eigenstate *n* at time *t*.

Substituting (6.59) into (6.29) results in:

$$\boldsymbol{i\hbar \frac{d}{dt} C_m^s(t) = \sum_n H_{mn} C_n^s(t)} \qquad \text{Eq. 6.60}$$

That is an equation analogous to the Schrödinger equation, but is written in terms of probability amplitudes.

The expectation value of any observable quantity A can be calculated in terms of wave functions of the system:

$$\boldsymbol{\langle A \rangle = \langle \psi_s | \hat{A} | \psi_s \rangle = \sum_{mn} C_m^{s*} C_n^s A_{mn}} \qquad \text{Eq. 6.61}$$

This formalism allows describing a system which initial and final states are known. When this is not verified, for example because the atoms interact one with another by means of collisions, it is necessary to describe the system statistically through the DM formalism:

$$\boldsymbol{\rho_{nm} = \sum_s p(s) C_m^{s*} C_n^s} \qquad \text{Eq. 6.62}$$

with $p(s)$ denoting the probability for the system to be at state *s,* and n, m running over all the energy eigenstates of the system.

The diagonal DM elements ρ_{nn} give the probability that the system is in a energy eigenstate *n*, the off-diagonal elements represent the "coherence" effects between *n* and *m* and are non-zero only in case of coherent overlapping of the two energy eigenstates.

Time differentiating (6.62) results in:

$$\boldsymbol{\dot{\rho}_{nm} = \sum_s \frac{dp(s)}{dt} C_m^{s*} C_n^s + \sum_s p(s) \left(C_m^{s*} \frac{dC_n^s}{dt} + \frac{dC_m^{s*}}{dt} C_n^s \right)} \qquad \text{Eq. 6.63}$$

For the present $p(s)$ is assumed as independent from t, so the first term vanishes.

From (6.61) it is possible to obtain the expression for the terms to be substituted in (6.63):

$$\boldsymbol{C_m^{s*} \frac{dC_n^s}{dt} = \frac{-i}{\hbar} C_m^{s*} \sum_\nu H_{n\nu} C_\nu^s} \qquad \text{Eq. 6.64}$$

$$\boldsymbol{C_n^s \frac{dC_m^{s*}}{dt} = \frac{i}{\hbar} C_n^s \sum_\nu H_{\nu m} C_\nu^{s*}} \quad \text{Eq. 6.65}$$

Thus (6.63) becomes:

$$\boldsymbol{\dot{\rho}_{nm} = \sum_s p(s) \frac{i}{\hbar} \sum_\nu (C_n^s C_\nu^{s*} H_{\nu m} - C_m^{s*} C_\nu^s H_{n\nu}) = \frac{i}{\hbar} \sum_\nu (\rho_{n\nu} H_{\nu m} - H_{n\nu} \rho_{\nu m}) =}$$

$$\boldsymbol{= \frac{i}{\hbar} \left(\hat{\rho}\hat{H} - \hat{H}\hat{\rho}\right)_{nm} = \frac{-i}{\hbar} \left[\hat{H}, \hat{\rho}\right]_{nm}} \quad \text{Eq. 6.66}$$

This equation describes the temporal evolution of the MD as a result of the interaction included in $\hat{H}$. However it does not consider all the interactions, such as relaxation or collision processes, that are not included in $\hat{H}$ and can lead to a non-zero value of $\frac{dp(s)}{dt}$. A phenomenological damping term is added to (6.66) to include such effects in the formalism:

$$\boldsymbol{\dot{\rho}_{nm} = \frac{-i}{\hbar} \left[\hat{H}, \hat{\rho}\right]_{nm} - \gamma_{nm} \left(\rho_{nm} - \rho_{nm}^{eq}\right)} \quad \text{Eq. 6.67}$$

In this relation, $\boldsymbol{\gamma_{nm}}$ is the damping term, it is the relaxation rate coefficient for the decay of $\boldsymbol{\rho_{nm}}$ to the equilibrium condition $\boldsymbol{\rho_{nm}^{eq}}$. The relaxation coefficients for the off diagonal elements can be written as:

$$\boldsymbol{\gamma_{nm} = \frac{1}{2} (\Gamma_n + \Gamma_m) + \gamma_{nm}^{col}} \quad \text{Eq. 6.68}$$

Γ_n and Γ_m represent the total decay rates of population from levels *n* and *m* respectively. The term γ_{nm}^{col} is the pure dephasing rate for the processes that do not involve transfer of population.

Inserting (6.30) into (6.67) the commutator $\left[\hat{H}, \hat{\rho}\right]$ splits into two terms. The commutator of $\hat{H}_0$ and $\hat{\rho}$ can be written as:

$$\boldsymbol{\left[\hat{H}, \hat{\rho}\right]_{nm} = (E_n - E_m) \rho_{nm} = \hbar \omega_{nm} \rho_{nm}} \quad \text{Eq. 6.69}$$

Thus (6.67) becomes:

$$\boldsymbol{\dot{\rho}_{nm} = -i\omega_{nm} \rho_{nm} - \frac{i}{\hbar} \sum_\nu (V_{n\nu} \rho_{\nu m} - \rho_{n\nu} V_{\nu m}) - \gamma_{nm} \left(\rho_{nm} - \rho_{nm}^{eq}\right)} \quad \text{Eq. 6.70}$$

This equation cannot be solved analytically, but can be solved using a perturbation expansion, where V_{ij} is replaced by λV_{ij}, with λ ranging between 0 and 1, and representing the strength of the perturbation.

The solutions of (6.70) take the form of power series in λ:

$$\boldsymbol{\rho_{nm} = \rho_{nm}^{(0)} + \lambda \rho_{nm}^{(1)} + \lambda^2 \rho_{nm}^{(2)} + \cdots} \quad \text{Eq. 6.71}$$

Putting (6.71) into (6.70) results in a set of decoupled equations, each one satisfying (6.70) separately:

$$\begin{cases} \dot{\boldsymbol{\rho}}_{\boldsymbol{nm}}^{(\boldsymbol{0})} = -\boldsymbol{i\omega_{nm}\rho_{nm}^{(0)}} - \boldsymbol{\gamma_{nm}}\left(\boldsymbol{\rho_{nm}^{(0)}} - \boldsymbol{\rho_{nm}^{eq}}\right) & (\boldsymbol{a}) \\ \dot{\boldsymbol{\rho}}_{\boldsymbol{nm}}^{(\boldsymbol{1})} = -(\boldsymbol{i\omega_{nm}} + \boldsymbol{\gamma_{nm}})\boldsymbol{\rho_{nm}^{(1)}} - \frac{\boldsymbol{i}}{\hbar}\left[\widehat{\boldsymbol{V}}, \widehat{\boldsymbol{\rho}}^{(\boldsymbol{0})}\right]_{\boldsymbol{nm}} & (\boldsymbol{b}) \\ \vdots & \\ \dot{\boldsymbol{\rho}}_{\boldsymbol{nm}}^{(\boldsymbol{N})} = -(\boldsymbol{i\omega_{nm}} + \boldsymbol{\gamma_{nm}})\boldsymbol{\rho_{nm}^{(N)}} - \frac{\boldsymbol{i}}{\hbar}\left[\widehat{\boldsymbol{V}}, \widehat{\boldsymbol{\rho}}^{(\boldsymbol{N-1})}\right]_{\boldsymbol{nm}} & (\boldsymbol{c}) \end{cases} \quad \text{Eq. 6.72}$$

These equations can be integrated in order to obtain the density matrix elements expression used to calculate the expectation value of any observable quantity, such as the induced dipole moment and the correlated optical susceptibility. We remark that every order equation is dependent on the result of the previous one. Equation (6.72a) describes the recovery of statistical equilibrium in the absence of any external field. The steady-state solution is: $\rho_{nm}^{(0)} = \rho_{nm}^{eq}$. Using this expression, the first order solution can be calculated using (6.72b), and so on for all the higher order solutions.

Linear Susceptibility

The first order solution of (6.72) can be written as:

$$\boldsymbol{\rho_{nm}^{(1)}(t)} = \boldsymbol{e^{-(i\omega_{nm}+\gamma_{nm})t}} \int_{-\infty}^{\boldsymbol{t}} \boldsymbol{dt'} \frac{\boldsymbol{-i}}{\hbar}\left[\widehat{\boldsymbol{V}}(\boldsymbol{t'}), \widehat{\boldsymbol{\rho}}^{(\boldsymbol{0})}\right]_{\boldsymbol{nm}} \boldsymbol{e^{(i\omega_{nm}+\gamma_{nm})t'}} \quad \text{Eq. 6.73}$$

Here $\hat{V}(t')$ is given by (6.31) and (6.32).

Using this expression, (6.73) can be written as:

$$\boldsymbol{\rho_{nm}^{(1)}(t)} = \hbar^{-1}\left(\boldsymbol{\rho_{mm}^{(0)}} - \boldsymbol{\rho_{nn}^{(1)}}\right)\sum_{\boldsymbol{p}} \frac{\bar{\mu}_{nm}\cdot\bar{E}(\omega_p)e^{-i\omega_p t}}{(\omega_{nm}-\omega_p)-i\gamma_{nm}} \quad \text{Eq. 6.74}$$

The expectation value of the induced dipole moment is:

$$\langle\tilde{\boldsymbol{\mu}}(\boldsymbol{t})\rangle = \boldsymbol{tr}\left(\widehat{\boldsymbol{\rho}}^{(\boldsymbol{1})}\widehat{\boldsymbol{\mu}}\right) = \sum_{\boldsymbol{nm}} \boldsymbol{\rho_{nm}^{(1)}}\bar{\boldsymbol{\mu}}_{\boldsymbol{mn}} = \sum_{\boldsymbol{nm}} \hbar^{-1}\left(\boldsymbol{\rho_{mm}^{(0)}} - \boldsymbol{\rho_{nn}^{(0)}}\right)\sum_{\boldsymbol{p}} \frac{\bar{\mu}_{mn}[\bar{\mu}_{nm}\cdot\bar{E}(\omega_p)]e^{-i\omega_p t}}{(\omega_{nm}-\omega_p)-i\gamma_{nm}} \quad \text{Eq. 6.75}$$

Decomposing $\langle\tilde{\mu}(t)\rangle$ into its frequency components:

$$\langle\tilde{\boldsymbol{\mu}}(\boldsymbol{t})\rangle = \sum_{\boldsymbol{p}}\langle\bar{\boldsymbol{\mu}}(\boldsymbol{\omega_p})\rangle\boldsymbol{e^{-i\omega_p t}} \quad \text{Eq. 5.76}$$

and defining the linear susceptibility by the equation:

$$\bar{\boldsymbol{P}}(\boldsymbol{\omega_p}) = \boldsymbol{N}\langle\bar{\boldsymbol{\mu}}(\boldsymbol{\omega_p})\rangle = \boldsymbol{\chi^{(1)}}(\boldsymbol{\omega_p})\cdot\bar{\boldsymbol{E}}(\boldsymbol{\omega_p}) \quad \text{Eq. 6.77}$$

it is possible to calculate the expression for the susceptibility, which, in Cartesian coordinates, is:

$$\boldsymbol{\chi_{ij}^{(1)}}(\boldsymbol{\omega_p}) = \frac{\boldsymbol{N}}{\hbar}\sum_{\boldsymbol{nm}}\left(\boldsymbol{\rho_{mm}^{(0)}} - \boldsymbol{\rho_{nn}^{(0)}}\right)\frac{\mu_{mn}^{i}\mu_{nm}^{j}}{(\omega_{nm}-\omega_p)-i\gamma_{nm}} \quad \text{Eq. 6.78}$$

In this relation, μ_{mn}^{i} and μ_{nm}^{j} are the dipole moment components for the transition between *m* and *n*; *i* and *j* are the Cartesian components of the electric fields. ω_{nm} are the characteristic transition frequencies from *n* to *m* states and γ_{nm} is the element of the relaxation matrix.

It is important to observe that the transition between two states with the same population $\left(\rho_{mm}^{(0)} \approx \rho_{nn}^{(0)}\right)$ does not contribute to the summation in $\chi^{(1)}$.

In order to understand the meaning of 6.78, it can be useful to consider a system with all the population at the ground level, denoted as a. Mathematically this means:

$$\boldsymbol{\rho_{aa}^{(0)} = 1}, \qquad \boldsymbol{\rho_{mm}^{(0)} = 0} \text{ for } \boldsymbol{m \neq a} \qquad \text{Eq. 6.79}$$

The linear susceptibility can now be written as:

$$\boldsymbol{\chi_{ij}^{(1)}(\omega_p) = \frac{N}{\hbar}\frac{\mu_{an}^{i}\mu_{na}^{j}}{(\omega_{na}-\omega_p)-i\gamma_{na}} = \frac{N}{\hbar}\mu_{an}^{i}\mu_{na}^{j}\frac{(\omega_{na}-\omega_p)+i\gamma_{na}}{(\omega_{na}-\omega_p)^2+\gamma_{na}^2}} \qquad \text{Eq. 6.80}$$

The real and imaginary parts of (6.80) are shown in figure 6.3.

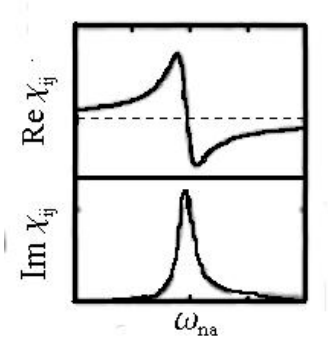

Figure 6.3 *Resonance nature of the linear susceptibility.*

Non-linear susceptibility

The second-order susceptibility is given from:

$$\boldsymbol{\rho_{nm}^{(2)}(t) = e^{-(i\omega_{nm}+\gamma_{nm})t}\int_{-\infty}^{t} dt' \frac{-i}{\hbar}\left[\hat{V}(t'), \hat{\rho}^{(1)}\right]_{nm} e^{(i\omega_{nm}+\gamma_{nm})t'}} \qquad \text{Eq. 6.81}$$

with

$$\boldsymbol{\left[\hat{V}, \hat{\rho}^{(1)}\right]_{nm} = -\sum_{\nu}\left(\bar{\mu}_{n\nu}\rho_{\nu m}^{(1)} - \rho_{n\nu}^{(1)}\bar{\mu}_{\nu m}\right)\cdot \tilde{E}(t)} \qquad \text{Eq. 6.82}$$

Using a procedure analogous to that used in the derivation of the linear susceptibility, it is possible to derive the formula for $\chi^{(2)}$. In this case it is necessary to evaluate every frequency component of $\chi^{(2)}$. For example, the term containing the sum frequency $(\omega_p + \omega_q)$can be expressed by:

$$\boldsymbol{\chi_{ijk}^{(2)}(\omega_p+\omega_q, \omega_q, \omega_p) = \frac{N}{2\hbar^2}\sum_{mn\nu}\left(\rho_{mm}^{(0)} - \rho_{\nu\nu}^{(0)}\right)\left\{\frac{\mu_{mn}^{i}\mu_{n\nu}^{j}\mu_{\nu m}^{k}}{[(\omega_{nm}-\omega_p-\omega_q)-i\gamma_{nm}][(\omega_{\nu m}-\omega_p)-i\gamma_{\nu m}]} + \right.}$$

$$\boldsymbol{\frac{\mu_{mn}^{i}\mu_{n\nu}^{k}\mu_{\nu m}^{j}}{[(\omega_{nm}-\omega_p-\omega_q)-i\gamma_{nm}][(\omega_{\nu m}-\omega_q)-i\gamma_{\nu m}]} + \frac{\mu_{n\nu}^{i}\mu_{mn}^{j}\mu_{\nu m}^{k}}{[(\omega_{\nu n}-\omega_p-\omega_q)-i\gamma_{\nu n}][(\omega_{\nu m}-\omega_p)-i\gamma_{\nu m}]} +}$$

$$\boldsymbol{\left.\frac{\mu_{n\nu}^{i}\mu_{mn}^{k}\mu_{\nu m}^{j}}{[(\omega_{\nu n}-\omega_p-\omega_q)-i\gamma_{\nu n}][(\omega_{\nu m}-\omega_q)-i\gamma_{\nu m}]}\right\}} \qquad \text{Eq. 6.83}$$

In Eq. 6.83, μ_{mn}^{i} is the dipole moment related to the transition from the state *n* to the state *m* and the labels *i,j,k* indicate the Cartesian coordinates of the electric fields at frequency $\omega_p + \omega_q$, ω_q, or ω_p.

Analogously, the third-order susceptibility can also be obtained. The total expression consists of 48 terms that are obtained from the permutation of the input frequencies ω_p, ω_q, and ω_r in (6.84):

$$\boldsymbol{\chi_{kijh}^{(3)}(\omega_p+\omega_q+\omega_r,+\omega_r,\omega_q,\omega_p)} =$$

$$\frac{N}{\hbar^3}\wp_1\sum_{vnml}\boldsymbol{\rho_{ll}^{(0)}}\left\{\frac{\mu_{lv}^{k}\mu_{vn}^{j}\mu_{nm}^{i}\mu_{ml}^{h}}{[(\omega_{vl}-\omega_p-\omega_q-\omega_r)-i\gamma_{vl}][(\omega_{nl}-\omega_p-\omega_q)-i\gamma_{nl}][(\omega_{ml}-\omega_p)-i\gamma_{ml}]}+\right.$$

$$\frac{\mu_{lv}^{h}\mu_{vn}^{k}\mu_{nm}^{j}\mu_{ml}^{i}}{[(\omega_{nv}-\omega_p-\omega_q-\omega_r)-i\gamma_{nv}][(\omega_{mv}-\omega_p-\omega_q)-i\gamma_{mv}][(\omega_{vl}+\omega_p)+i\gamma_{vl}]}+$$

$$\frac{\mu_{lv}^{i}\mu_{vn}^{k}\mu_{nm}^{j}\mu_{ml}^{h}}{[(\omega_{nv}-\omega_p-\omega_q-\omega_r)-i\gamma_{nv}][(\omega_{vm}+\omega_p+\omega_q)+i\gamma_{vm}][(\omega_{ml}-\omega_p)-i\gamma_{ml}]}+$$

$$\frac{\mu_{lv}^{h}\mu_{vn}^{i}\mu_{nm}^{k}\mu_{ml}^{j}}{[(\omega_{mv}-\omega_p-\omega_q-\omega_r)-i\gamma_{mv}][(\omega_{nl}+\omega_p+\omega_q)+i\gamma_{nl}][(\omega_{vl}+\omega_p)+i\gamma_{vl}]}+$$

$$\frac{\mu_{lv}^{j}\mu_{vn}^{k}\mu_{nm}^{i}\mu_{ml}^{h}}{[(\omega_{vn}+\omega_p+\omega_q+\omega_r)-i\gamma_{vn}][(\omega_{nl}-\omega_p-\omega_q)-i\gamma_{nl}][(\omega_{ml}-\omega_p)-i\gamma_{ml}]}+$$

$$\frac{\mu_{lv}^{h}\mu_{vn}^{j}\mu_{nm}^{k}\mu_{ml}^{i}}{[(\omega_{nm}+\omega_p+\omega_q+\omega_r)-i\gamma_{nm}][(\omega_{mv}-\omega_p-\omega_q)-i\gamma_{mv}][(\omega_{vl}+\omega_p)+i\gamma_{vl}]}+$$

$$\frac{\mu_{lv}^{i}\mu_{vn}^{j}\mu_{nm}^{k}\mu_{ml}^{h}}{[(\omega_{nm}+\omega_p+\omega_q+\omega_r)-i\gamma_{nm}][(\omega_{vm}+\omega_p+\omega_q)+i\gamma_{vm}][(\omega_{ml}-\omega_p)-i\gamma_{ml}]}+$$

$$\left.\frac{\mu_{lv}^{h}\mu_{vn}^{i}\mu_{nm}^{j}\mu_{ml}^{k}}{[(\omega_{ml}+\omega_p+\omega_q+\omega_r)-i\gamma_{ml}][(\omega_{nl}+\omega_p+\omega_q)+i\gamma_{nl}][(\omega_{vl}+\omega_p)+i\gamma_{vl}]}\right\} \qquad \text{Eq. 6.84}$$

In the case of non resonance excitation, (6.84) reduces to (6.58) by neglecting the terms ($i\gamma_{\alpha\beta}$) in the denominators.

6.7 Two Photon Absorption

The two-photon absorption process is characterized by the simultaneous absorption of two photons from a light source. In this section, only a phenomenological approach will be presented to better explain the properties of this process, while in the next chapter, two real systems, studied in this work, will be presented.

As it is represented in figure 6.4, after the interaction with the first photon the system enters a state of polarization described as a coherent overlap of the initial state with the virtual state of the molecule. Before the coherent state decays, a second photon is employed to excite the system to a real excited state. When the input intensity increases, multi-photon absorption

processes, characterized by the simultaneous absorption of three or more photons, can occur in the system.

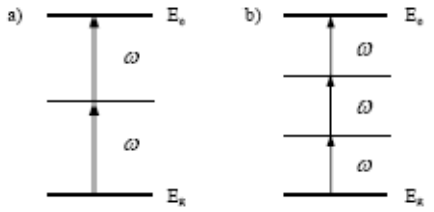

Figure 6.4 *Two-photon absorption (a) and three-photon absorption (b).*

In all cases, the system is transparent to the frequency ω at low input energies. The probability to have absorption of two or more photons increases at high incident energies. In particular, the variation of the incident intensity with the optical path is given by:

$$\frac{\partial I}{\partial z} = \alpha I - \beta I^2 - \gamma I^3 - \cdots \qquad \text{Eq. 6.85}$$

where α, β, and γ are the one, two and three photons absorption coefficient, with $\alpha \gg \beta \gg \gamma$. At low incident intensity only the first term becomes important, while the other terms become non-negligible only at high intensity, due to their non-linear dependence on I.

β depends on the third order susceptibility according to:

$$\beta = \frac{3\pi}{\varepsilon_0 c n^2 \lambda} Im\left[\chi^{(3)}(-\omega; \omega, -\omega, \omega)\right] \qquad [\beta] = cm/W \qquad \text{Eq. 6.86}$$

Analogously, the three-photon coefficient depends on the imaginary part of $\chi^{(5)}$:

$$\gamma = \frac{3\pi}{\varepsilon_0 c^2 n^2 \lambda} Im\left[\chi^{(5)}(-\omega; \omega, -\omega, \omega, -\omega, \omega)\right] \qquad \text{Eq. 6.87}$$

For TPA process, at a molecular scale, it is possible to define the TPA cross-section $\sigma^{(2)}$ as a microscopic quantity, describing the 3rd order non linear response of a single absorber:

$$\sigma^{(2)} = \frac{\hbar\omega\beta}{N} \qquad \left[\sigma^{(2)}\right] = cm^4 s/(molecules \cdot photons) \qquad \text{Eq. 6.88}$$

where *N* is the number of absorbing species.

Being a 3rd order process, the TPA is present in all the materials, but its absorption cross section often is many orders of magnitude smaller than that of a one photon process. For that reason TPA active species need to be engineered to reach higher values.

The common unit for the $\sigma^{(2)}$ is the Göppert Mayer, from the first researcher that predicted the possibility to have a TPA event. It is defined as:

$$1GM = 10^{-50}\, cm^4 s/(molecules \cdot photons)$$

The first measured values of $\sigma^{(2)}$ for organic chromophores were only few units, but this value can be improved through a suitable design of the molecular structure.

REFERENCES

[1] G. S. He, S. H. Liu, Physiscs of Nonlinear Optics,Word Scientific Ed., 1999.

[2] R. W. Boyd, Nonlinear Optics, Academic Press, 1992.

CHAPTER 7

Experimental Techniques

Optical spectroscopic techniques allow to investigate the optical characteristics of organic and inorganic system.

In this chapter the optical spectroscopy techniques and the equipment used in this work will be outlined. First the classical steady state absorption measurement techniques are introduced. Then the experimental measurements performed using a Femtosecond Ti-sapphire regenerative-amplifier system will be presented.

The set-up for the characterization of the frequency up-converted lasing emission in solution and in bulk configuration will be described. Finally the equipment employed for the ASE characterization of sol-gel films, containing organic dye or QDs as active medium for the amplified emission, will be analyzed.

7.1 Absorption Measurements

The absorption measurements in this work are performed using a Varian Cary 300 absorption spectrometer. The spectrometer is configured using a double beam geometry in order to eliminate the effects of the solvent and cuvette. The absorption spectra of solutions and sol-gel films, spin-coated on quartz substrates, have been collected in the range 250-1000 nm.

7.2 Femtosecond Laser Amplifier Facility

The femtosecond laser-amplifier facility allows studying ultrafast processes in physical samples such as organic or inorganic semiconductors.

All the experiments described in this chapter are performed with a femtosecond amplified laser system by Spectra Physics. It comprises a Titanium-Sapphire oscillator (Tsunami) pumped by the second harmonic of a Nd:YVO_4 laser (Millennia) and amplified by a regenerative optical amplifier (Spitfire) pumped by the second harmonic of a Q-switched Nd:YLF laser (Merlin).

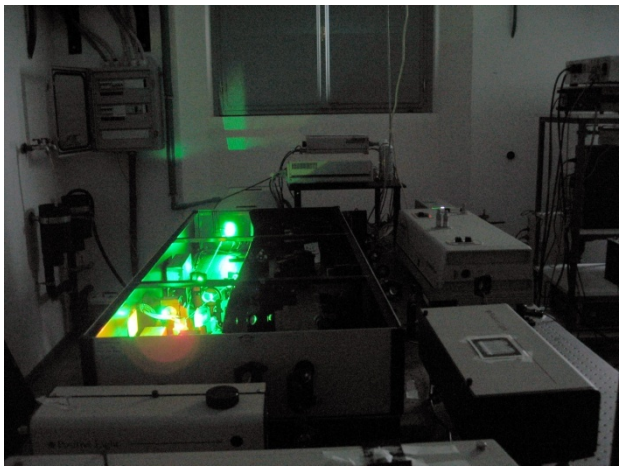

Figure 1 *Femtosecond amplified laser system.*

The laser beam from the oscillator is a train of femtosecond pulses at 82 MHz repetition rate, each of approximately 80 fs duration and energy of few nJ. The oscillator is tunable within the range 750-840 nm but in all experiments the wavelength is set at 806 nm. The pulses are subsequently amplified inside the Spitfire, whose performance is based upon the Chirped Pulse Amplification.[1]

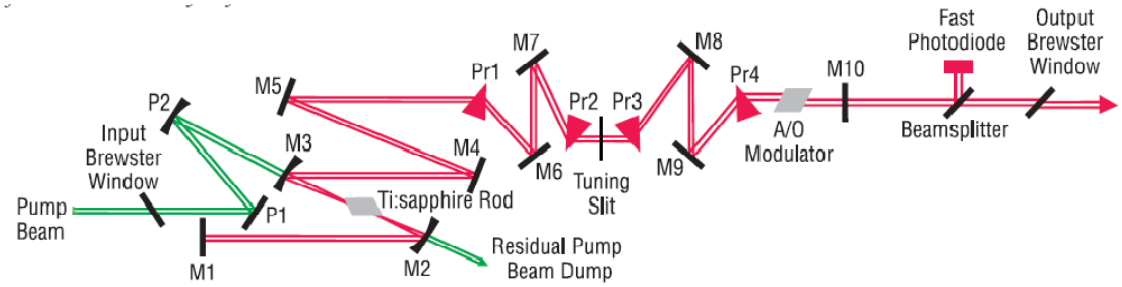

Figure 7.2 *Tsunami femtosecond cavity layout.*

The pulses entering the amplifier are at first stretched in time, then undergo amplification up to almost 100.000 times and finally are sent to the compressor which restores the initial temporal duration. The output pulses of the laser system have the following features: wavelength of 806

nm with 10 nm bandwidth, repetition rate ranging from 1 Hz to 1 KHz, average time duration of 150 fs and energy for single pulse in the order of 1 mJ.

During the experimental measurements, the beam properties – time duration, energy and beam waist – were periodically verified. In particular, the time duration is determined by means of an external autocorrelation experiment in a BBO crystal,[2] the energy content is sampled with a pyroelectric detector (Molectron J3-0,5m) and the spatial shape of the beam is measured with a CCD camera (Pulnix TM-7CN).

7.3 Setup for lasing emission of push-pull molecule in solution

In order to study the two-photon pumped gain of organic dye in solution the following experimental layout was used. The experimental set-up for the optical amplifier is shown in figure 7.2.

The excitation source is the amplified Ti-sapphire laser centered at 800 nm, with maximum pulse energy of 800 µJ. The output energy is attenuated by means of neutral density filters. The pulse repetition frequency has been reduced to 10 Hz, by controlling the Pockels cells in the regenerative amplifier, in order to avoid thermal blooming effects. The pump beam is focalized with a lens (F=200 mm) on a 1 cm path quartz cuvette containing the solution. At high concentration of dye molecule, the feedback between the facets of the cuvette could lead to lasing, without using any external cavity.

The laser signal, emitted from the opposite cuvette facet with respect to that of the incoming pump beam, and collimated using a second lens having 20 cm focal length, is focalized into an optical fiber connected with a spectrometer (Ocean Optics) by using a lens with a focal length of 10 cm. A cut-off filter is placed before the fiber in order to eliminate the pump beam.

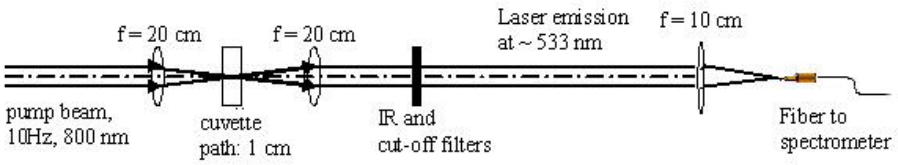

Figure 7.3 *Experimental set-up for the characterization of the two-photon lasing emission in solution.*

7.4 Setup for lasing emission of push-pull molecule in GTZ bulk sample

The lasing properties of bulk sample have also been characterized. The optical set-up required for this measure, showed in figure 7.3, is similar to that described in the previous section, with the addition of an optical resonator.[3] This latter is required for providing the feedback required

for lasing. The sample has been placed between two plane dielectric mirrors. The M1 mirror has a reflectivity of 10% for 800 nm and of 50% for 530 nm radiation.

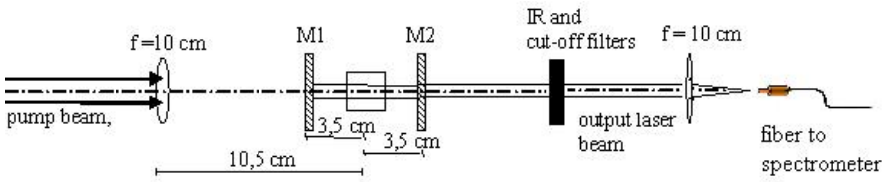

Figure 7.4 *Experimental set-up for the characterization of the two-photon lasing emission of bulk samples.*

7.5 Set-up for the ASE characterization of sample in thin film configuration

Light amplification has been measured by using the variable strip length method (VLS): measurements have been performed as a function of the pumping strip length.[4] This set-up allows obtaining the ASE threshold energy and the gain of the different samples, in waveguiding configuration, upon irradiation with a fs laser, at 400 nm (one-photon pumping) and 800 nm (two-photon pumping).

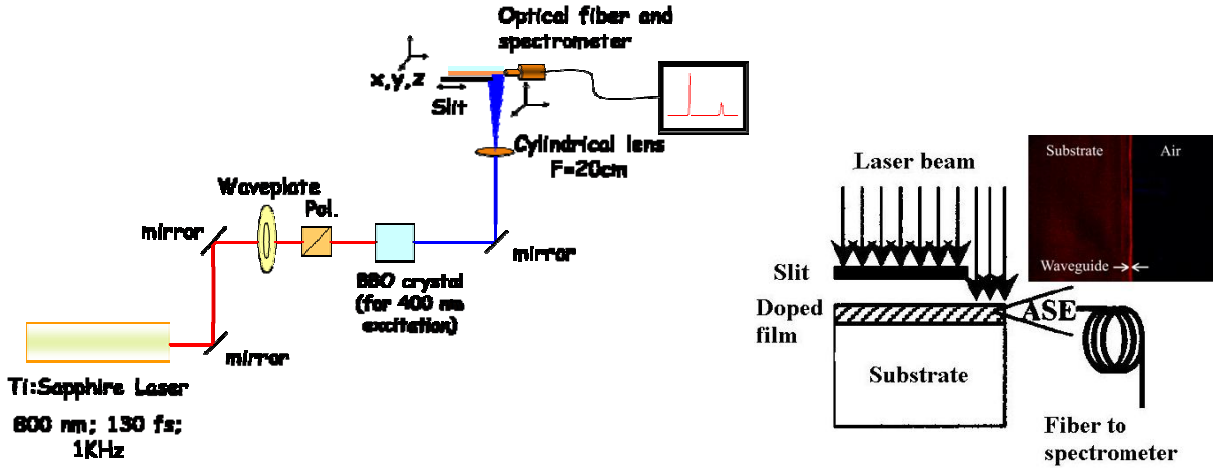

Figure 7.5 *Schematic representation of the optical set-up utilized for the VLS measurements, both at one- and two- photon excitation. The pump intensity can be continuously changed by acting on the wave plate, and the length of the stripe focalized on the sample can be adjusted with the movable slit. The laterally emitted signal is collected through a fiber and analyzed with a spectrometer. On the right inset, a picture of the waveguide section is depicted. It can be seen that the emitted radiation is guided inside the active film.*

The sample is optically excited with the Ti:Sapphire amplified laser system with pulses of 150 fs and 1KHz repetition rate at 800 nm, in a stripe-like geometry with variable length. With a BBO doubling crystal and a cut-off filter, a 400 nm wavelength beam is obtained. The intensity of the input beam is varied with neutral filters and, for a fine tuning, with a half wave plate followed by a polarizer.

The beam is focused with a 20 cm focal length cylindrical lens onto the sample. The sample edge emitted beam, in a lateral configuration, was detected by an optical fiber connected to a micro-spectrometer (Ocean Optics), with a typical collection setup shown in figure 7.4.

7.6 Set-up for the DFB microcavity characterization

The experimental setup used to characterize the DFB devices is sketched in figure 7.5. The sample resides in a mobile stage allowing micrometer movements in plane and in vertical directions.

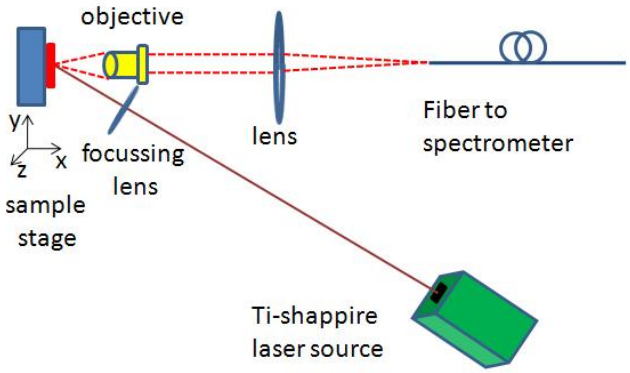

Figure 7.6 *Overview of the used experimental set-up.*

It is optically pumped using 800 nm light from the amplified Ti-Sapphire laser system and 1 kHz repetition rate. Using a BBO doubling crystal and a cut-off filter a 400 nm wavelength beam can also been obtained.

The pump laser light is focused by means of a lens onto the structures on the sample. The emitted light from the sample is collected and collimated from the objective lens, and focused into an optical fiber by a lens (f=10 cm) . The fiber then guides the light to a spectrometer for analysis.

REFERENCES

[1] D. Strickland, G. Mourou, Opt. Commun., 1985, 56, 219.

[2] K.L. Sala, G.A. Kenny-Wallace and G.E. Hall, IEEE J. of Quantum Electronics, 1980, QE-16, 90.

[3] G. S. He, J. D. Bhawalkar, C. Zhao, P. N. Prasad, IEEE J. Quant. Electr. 1996, 32, 5; G. S He, C. F. Zhao, J. D. Bhawalkar, P. N. Prasad, _Appl. Phys. Lett., 1995, 67, 25.

[4] L. Pavesi, L. Dal Negro, C. Mazzoleni, G. Franza, F. Priolo, Nature, 2000, 408, 440; L. Dal Negro, M. Cazzanelli, N. Daldosso, Z. Gaburro, L. Pavesi, F. Priolo, D. Pacifici, G. Franzò, F. Iacona, Physica E, 2003, 16, 297; M. Casalboni, F. De Matteis, V. Merlo, P. Prosposito, R. Russo, S. Schutzmann, Appl. Phys. Lett., 2003, 83, 416; L. Dal Negro, P. Bettotti, M. Cazzanelli, D. Pacifici, L. Pavesi, Opt. Comm., 2004, 229, 337.

CHAPTER 8

Materials for up-converted lasing

Materials possessing high value of TPA cross section play an important role for their practical use in technological applications. The application fields for such materials are multi-photon microscopy,[1] light-induced 3D micro-fabrication,[2] ultra-high-density optical data storage,[3] and frequency up-conversion.[4] This latter is particularly demanding because, besides the requirement of high TPA cross section and two-photon induced emission, it needs also the materials stability at the high pulse fluencies required for optical state inversion.

In this chapter, two materials used as active species for the two photon pumped (TPP) lasing, will be presented. These species are an organic cromophore, named OHPEP, and an II-VI semiconductor quantum dot (QD).

Some theoretical models, describing simple structures, will be exposed in order to explain the nonlinear optical response of materials in terms of their structure.

8.1 Dipolar D-π-A organic chromophores

In this section we will analyze some basic concepts used to study the TPA properties of push-pull molecules. These compounds are characterized by an electron donor group (D) and an electron acceptor one (A), connected by a π conjugation path:

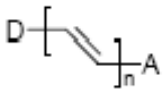

Figure 8.1 *Schematic representation of molecular structure of polyenic D-A system.*

Push-pull molecules are characterized by a low-lying high-intensity absorption band, related to the intramolecular charge transfer (ICT) between the D and A groups. This transition is associated to a large dipole change allowing a large static quadratic hyperpolarizability β. The two-state expression for β is:[5]

$$\boldsymbol{\beta} \propto \boldsymbol{\mu_{eg}^2}\, \boldsymbol{\Delta\mu / E_{eg}^2} \qquad \text{Eq. 8.1}$$

Here $\Delta\mu$ is the difference between the permanent dipole moment of the ICT state and that of the ground state, μ_{eg} is the transition dipole moment and E_{eg} is the transition energy.

Because of the asymmetric structure of molecule, reported in figure 8.1, the low-lying absorption band related to ICT phenomenon is allowed both by one-photon absorption (OPA) and two-photon absorption (TPA).[6]

In order to obtain (8.1), and analogously the other nonlinear optical quantities, in the Sum Over States (SOS) calculation only two states (the ground and the ICT state) contribute to the nonlinear optical response. The ground state structure is a combination of the neutral and the zwitterionic (with charge-separation) forms. For a polyenic D-π-A structure, the limiting-resonance forms are reported in figure 8.2.

Figure 8.2 *Two limiting-resonance forms of polyenic D-A structure.*

When the D and A groups are weak, the ground state is dominated by the neutral form and the structure is characterized by a high degree of Bond Length Alternation (BLA; i.e. alternation of single and double bonds). On the contrary, when the D and A substituent are strong, the contribution of the limiting-resonance forms in the ground state is large and consequently the BLA decreases. In this case, the polarity of the solvent has an important role in the determination of the importance of the charge-separated forms in the description of the states. In particular, by increasing the polarity of the solvent, the charge separation is favored and the nonlinear polarizability increases. This effect of the solvent on NLO properties is in accord with the experimental evidences in linear solvatochromic optical responses for organic chromophores.[7] Considering a two-state model, the molecular Hamiltonian has the form:

$$\boldsymbol{H} = \begin{vmatrix} \boldsymbol{E_N} & \boldsymbol{-t} \\ \boldsymbol{-t} & \boldsymbol{E_z} \end{vmatrix} \quad \text{Eq. 8.2}$$

Here, E_N and E_z are the energies of the neutral and the zwitterionic forms respectively, t is the interaction non-diagonal matrix element between the two resonance forms.

The normalized wavefunctions of the ground and the excited state are combinations of the neutral and the zwitterionic forms:

$$|\boldsymbol{\psi_g}\rangle = \mathbf{cos}\frac{\boldsymbol{\theta}}{\mathbf{2}}|\boldsymbol{\psi_N}\rangle + \mathbf{sin}\frac{\boldsymbol{\theta}}{\mathbf{2}}|\boldsymbol{\psi_Z}\rangle \quad \text{Eq. 8.3}$$

$$|\boldsymbol{\psi_e}\rangle = -\mathbf{sin}\frac{\boldsymbol{\theta}}{\mathbf{2}}|\boldsymbol{\psi_N}\rangle + \mathbf{cos}\frac{\boldsymbol{\theta}}{\mathbf{2}}|\boldsymbol{\psi_Z}\rangle \quad \text{Eq. 8.4}$$

In the range $0 \leq \theta \leq \pi/2$, the ground state is dominated by the neutral form and, viceversa, in the range $\pi/2 \leq \theta \leq 0$, the zwitterionic form is the most important.

In this model, two parameters are introduced in order to have a simple description of the nonlinear optical response. The first is the parameter t defined by:

$$-\boldsymbol{t} = \langle \boldsymbol{\psi_Z}|\boldsymbol{H}|\boldsymbol{\psi_N}\rangle \quad \text{Eq. 8.5}$$

The parameter t is always positive: it diminishes with the length of the conjugation path or with deviations from planarity of the π bridge.

The second factor is the energy difference between the zwitterionic and the neutral forms:

$$\boldsymbol{V} = \langle \boldsymbol{\psi_Z}|\boldsymbol{H}|\boldsymbol{\psi_Z}\rangle - \langle \boldsymbol{\psi_N}|\boldsymbol{H}|\boldsymbol{\psi_N}\rangle \quad \text{Eq. 8.6}$$

Using the last equations, the value of θ is given by:

$$\mathbf{tan}\,\boldsymbol{\theta} = \frac{\mathbf{2}\boldsymbol{t}}{\boldsymbol{V}} \quad \text{Eq. 8.7}$$

It is possible to derive the expressions for the ground (μ_g) and the excited (μ_e) states dipoles, the transition dipole (μ_{eg}) and the energy gap (E_{eg}) assuming that the mutual transition dipole is negligible:

$$\langle \boldsymbol{\psi_N}|\boldsymbol{\mu}|\boldsymbol{\psi_Z}\rangle = \mathbf{0} \quad \text{Eq. 8.8}$$

$$\boldsymbol{\mu_g} = \langle \boldsymbol{\psi_g}|\boldsymbol{\mu}|\boldsymbol{\psi_g}\rangle = \frac{\boldsymbol{\mu_N}+\boldsymbol{\mu_Z}-\boldsymbol{\mu_{CS}}\,\mathbf{cos}\,\boldsymbol{\theta}}{\mathbf{2}} \quad \text{Eq. 8.9}$$

$$\boldsymbol{\mu_e} = \langle \boldsymbol{\psi_e}|\boldsymbol{\mu}|\boldsymbol{\psi_e}\rangle = \frac{\boldsymbol{\mu_N}+\boldsymbol{\mu_Z}+\boldsymbol{\mu_{CS}}\,\mathbf{cos}\,\boldsymbol{\theta}}{\mathbf{2}} \quad \text{Eq. 8.10}$$

$$\boldsymbol{\mu_{eg}} = \langle \boldsymbol{\psi_e}|\boldsymbol{\mu}|\boldsymbol{\psi_g}\rangle = \frac{\boldsymbol{\mu_{CS}}\,\mathbf{sin}\,\boldsymbol{\theta}}{\mathbf{2}} \quad \text{Eq. 8.11}$$

$$\boldsymbol{E_{eg}} = \frac{\mathbf{2}\boldsymbol{t}}{\boldsymbol{sen\theta}} \quad \text{Eq. 8.12}$$

In these expressions, μ_{CS} is the difference between μ_Z and μ_N, where μ_Z and μ_N are the dipoles of the zwitterionic and the neutral forms respectively. All these expressions depend on the angle θ. It is useful to define the quantity (MIX), expressed by:[8]

$$\boldsymbol{MIX = -\cos\theta = -\frac{V}{\sqrt{V^2-4t^2}}} \qquad \text{Eq. 8.13}$$

If the neutral form is more energetically stable than the zwitterionic one ($V > 0$), the ground and the first excited states are dominated by the neutral and the zwitterionic forms respectively and $-1 < MIX < 0$.

From the two-state model, the dipolar term of the third-order susceptibility is useful to determine the expression for the TPA cross-section. Near to the two-photon resonance condition (E_{eg}~$2\hbar\omega$) and if $\hbar\omega \gg i\gamma_{eg}$, $\chi^{(3)}$ is given by:

$$\boldsymbol{\chi^{(3)}(-\omega;\omega,-\omega,\omega) = \left[\frac{\mu_{eg}^2\Delta\mu_{eg}^2}{E_{eg}^2(-i\hbar\gamma_{eg})}\right] = i\frac{\mu_{eg}^2\Delta\mu_{eg}^2}{E_{eg}^2\hbar\gamma_{eg}}} \qquad \text{Eq. 8.14}$$

The expression of $\sigma^{(2)}$, introduced in paragraph 6.7, for dipolar molecules can be written as:

$$\boldsymbol{\sigma_D^{(2)} = \frac{3\pi\hbar\omega}{\varepsilon_0 cn^2\lambda N} Im\left[\chi^{(3)}(-\omega;\omega,-\omega,\omega)\right] = \frac{3\pi\hbar\omega}{\varepsilon_0 cn^2\lambda N}\frac{\mu_{eg}^2\Delta\mu_{eg}^2}{E_{eg}^2\hbar\gamma_{eg}}} \qquad \text{Eq. 8.15}$$

where γ_{eg} is the excited-state linewidth. The quantities in (8.10) are the same as those reported in (8.7) and can be further written as function of the MIX parameter.

Substituting the new relations, (8.10) can be rewritten in:

$$\boldsymbol{\sigma_D^{(2)}(\omega^*) \propto \frac{\mu_{CS}^4(1-MIX^2)MIX^2}{\gamma_{eg}t^2}} \qquad \text{Eq. 8.16}$$

The variation of $\sigma_D^{(2)}$ as a function of the parameter MIX is reported in figure 8.3.

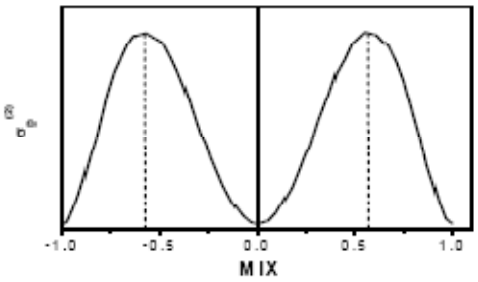

Figure 8.3 *Variation of* $\boldsymbol{\sigma_D^{(2)}}$ *versus MIX.*

The TPA cross-section for dipolar D-π-A molecules has a minimum at MIX=0. The maximum value is at $\pm 1/\sqrt{3}\,(V = \mp\sqrt{2}t)$, corresponding to an intermediate structure between the neutral and the zwitterionic forms. The maximum values of $\sigma_D^{(2)}$ can be obtained by choosing the nature of the end-groups which permit the tunability of the energy gap V, in order to reach

the optimal $MIX = \pm 1/\sqrt{3}$ values. $\sigma_D^{(2)}$ can also be enhanced by lengthening the distance between the donor and the acceptor [end] groups in order to increase μ_{CS}^4/t^2.

8.2 OHPEP

The organic chromophore investigated as a materials for the up-conversion lasing is called OHPEP. It is showed in figure 8.4, and had been synthesized from the Prof. Pagani group at the Materials Science Departments of the Milano-Bicocca University.

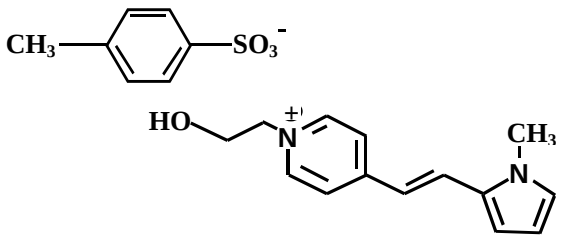

Figure 8.4 OHPEP molecular structure.

This molecule is a push pull system where a π-deficient heterocycle, the hydroxyl-pyridinium group, acts as electron-withdrawing group, and a π-excessive heterocycle, the pyrrole ring, as electron-donor group. The terminal hydroxyl group has been introduced on the pyridinium group to favor the inclusion in sol-gel matrices.[9] In fact it can lead to covalent bonding with the gel frame, allowing to good dispersion even at molar concentration up to 10^{-2}.

When the TPA mechanism is involved, the NLO system is excited through the simultaneously absorption of two photons in the near-IR range. Once promoted to the excited state by a TPA process, the organic molecule can undergo one-photon fluorescence emission to return to the ground state. As the emission frequency is similar to that corresponding to linear absorption, it follows that the two-photon induced fluorescence frequency is consistently higher than that absorbed during the TPA process (figure 8.5 left).

This means that, in contrast with common organic dyes, where visible emission is generated after the absorption of UV radiation, exploiting TPA organic molecule it is possible to have visible emission by pumping in the near-IR.

Another interesting property of this system is the possibility of tuning the emission wavelength by changing the lateral substituent of the aromatic rings. By this way it is possible to explore a broad wavelength range of laser emission (figure 8.5 right).

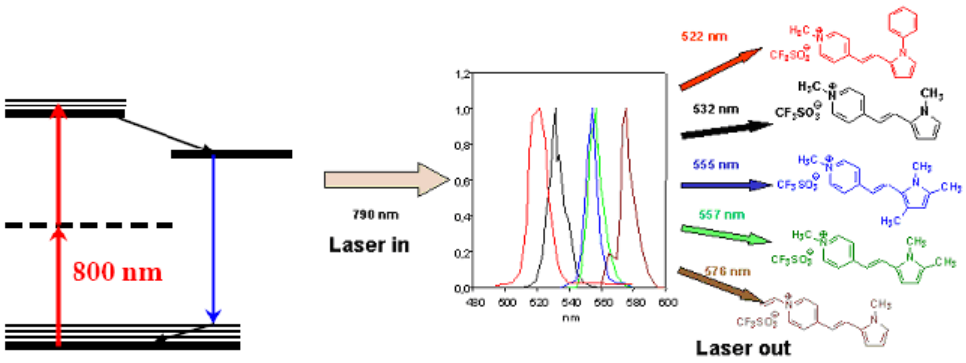

Figure 8.5 *(left) Frequency up-converted fluorescence via two photon absorption. The excitation process is constituted by the simultaneous absorption of two photons. (right) Normalized cavity lasing emissions of push-pull molecules of the same family of OHPEP. The pumping laser is at 790 nm, while the emissions are in the 500-600 nm wavelength range.*

8.3 Efficient insertion in Sol-Gel matrices

As introduced in section 8.2, the OHPEP molecule has been functionalized with a terminal hydroxyl group to favor its dispersion inside sol-gel films for the realization of solid-state devices. This group is capable to generate covalent bonds with the inorganic silica network.

To prepare homogenous bulk or film samples, the chromophore has been added to the sol and let reacting under stirring for one night. Bulk samples are prepared by storing the precursor sol in an oven at 60°C for 24 hour, while thin films can be deposited on several substrates (quartz, soda-lime, silicon) by spin coating.

By this way homogeneous sample are obtained for concentration up to $\sim 10^{-2}$ M.

8.4 Semiconductor quantum dots

Consisting of only few hundred thousand atoms, QDs constitute a bridge between the solid state and the single atom. Hence they exhibit properties that are a mix between the solid state and the atomic properties. QDs are semiconductor nanocrystals whose sizes are smaller than the Bohr radius of excitons (~5 nm or CdSe). This size corresponds to the regime of strong quantum confinement, for which the spatial extent of the electronic wave function is comparable to that of the dot. As a result of this geometrical constraint, electrons feel the presence of the boundaries and respond to changes in particle size by adjusting their energy.[10] This phenomenon is known as quantum size effect. As a result the emission wavelength also depends on their size, that can be controlled through the synthesis. This allows dealing with color selectable lasing medium.

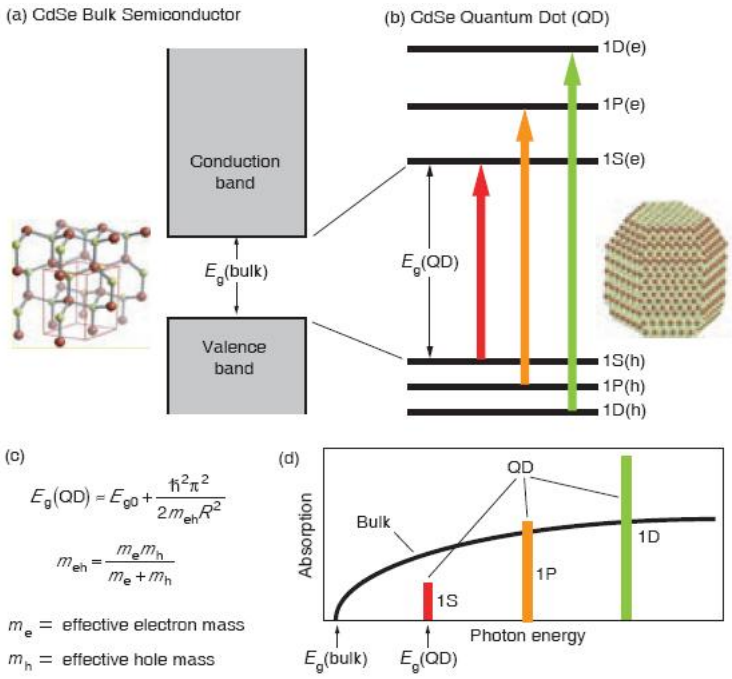

Figure 7.6 *(a) A bulk semiconductor such as CdSe has continuous conduction and valence Energy bands separated by a fixed energy gap E_g(bulk). Electrons normally occupy all states up to the edge of the valence band, whereas states in the conduction band are empty. (b) A QDs is characterized by discrete atomic-like states with energies determined by the QDs radius. (c) The expression for the size dependent separation between the lowest electron and hole QD states, E_g(QD), obtained with the spherical quantum box model. (d) Schematic representation of the absorption spectrum of a bulk semiconductor (black line) and of the discrete absorption spectrum of a QD (colored bars).*

The quantum size effect can be described by a quantum box model, in which the electron motion is restricted in all the three dimension by impenetrable walls.[11] For a spherical QD, with radius R, this model predicts that the size-dependent contribution to the energy gap is proportional to $1/R^2$: this implies that the gap increases as the QD size decrease. Another consequence of the quantum size effect is that the continuous energy bands of bulk semiconductors change to discrete atom-like energy level.

In QDs the density of state near the edge of the valence and conduction bands is lower compared with bulk semiconductors, and the spacing between electronic level (hundreds of meV) is greater that the available thermal energy. These properties imply respectively a lower and a temperature independent lasing threshold.

The electron energy spectrum and optical transition probabilities can be calculated, for a spherical nanocrystal, with an infinite potential barrier, by using the effective mass approximation applied to a two band semiconductor with parabolic and isotropic valence and conduction band. This simplified model has been modify during the last years to include finite well, Coulomb interactions, non parabolicity of the conduction band, and confinement induced mixing of valence sub-bands. Without entering into the details of these theoretical mode, a

two-level system with twofold spin-degenerate states, implies that optical gain (i.e., population inversion) begins at a carrier density of $N_{eh} = 1$ (N_{eh} is the number of e-h pairs per dot on average), with gain saturation (i.e., complete population inversion) at $N_{eh} = 2$. This implies that the QD band-edge gain is primarily due to two e-h pair states.

The main problems limiting the performance of these materials as lasing materials are mainly two. The defects or dangling bonds on the surface of the dot, leading to electronic states that lie within the material's energy gap. Electrons can relax into those states, whereupon they typically undergo either non-radiative or radiative decay to the ground state. This effect is particularly important in small QDs, where the surface to volume ration is very high, but can be limited by properly passivating the QDs surface.

The other mechanism in competition with the optical gain is the Auger recombination, where the e-h recombination energy is not released as a photon, but is transferred to a third particle (electron or hole) that is excited to a higher energy state.[12] Auger recombination is greatly enhanced in QDs with respect to the bulk semiconductors, because of the relaxation of the translation momentum conservation and of the enhancement of the Coulomb interactions, and hinders the development of lasing. When QDs are pumped into high-energy excited states, population inversion and the buildup of optical gain are only possible if the relaxation down to the emitting (ground) state is faster than the Auger process time, which is strongly time dependent.

Recently semiconductors QDs have been investigated also as promising materials for non-linear optics, as they possess a large TPA cross section and they give rise to efficient fluorescence emission and to amplified spontaneous emission. Both theoretical and experimental approaches predicted that a two photon absorption cross section could be as high as 10^4 Göpper Mayer (1 GM = 10^{-50} cm^4s), two to three orders of magnitude larger than those of typical organic, and comparable quantum yields with respects to that of organic.

The third-order nonlinearity of various semiconductor QDs has been investigated and it has been found that the surface quality plays an important role in determining their optical properties. In particular, it has been demonstrated that an efficient surface capping, especially through the growth of wider band-gap inorganic shell in a core/shell structure, can largely improve the nonlinear optical absorption.[13] Going from bulk materials to quantum confinement dimensions in QDs, the nonlinear absorption becomes more intense. The enhancement of the third-order nonlinearity characterizing the QDs can be attributed to the concentration of

exciton oscillator strength. In fact, as the particle size decreases, the series of transitions at slightly different energies in the bulk are compressed by quantum confinement effect into a single and intense transition in a quantum dot. Therefore, the oscillator strength of the QD is concentrated into few transitions. The two photon absorption coefficient is by this way enhanced when the size is less than the bulk Bohr diameter.[14] For ZnS the TPA cross-section of nm-scale QDs is five times higher than the bulk sample.[15] It is experimentally and theoretically demonstrated that, for CdSe and CdTe QDs with dimensions near to the exciton size, the TPA cross-section values decrease with a reduction in the QD size even when they are normalized by the volume.[16] This new class of materials is very promising for their high TPA efficiency with respect to organic media.[17]

8.5 CdSe-CdS-ZnS Quantum dot doped ZrO_2 waveguide

In this section we will describe the properties of semiconductors quantum dots provided from the collaboration with Prof. P. Mulvaney (University of Melbourne - Australia) and A. Martucci (University of Padova). They are based on a core of CdSe and a multiple shell composed of CdS and ZnS, synthesized through chemical protocols.[18]

Nanocrystalline CdSe σ_2 values have been theoretically predicted and experimentally shown to reach magnitudes of 10^4 GM.[19] Such values are a staggering two to three orders of magnitude larger than those of typical organic dyes (i.e. ~100 GM for Rhodamine B). Owing to the higher σ_2 values and comparable quantum yields, quantum dots need lower excitation fluencies to generate similar light emission intensities.

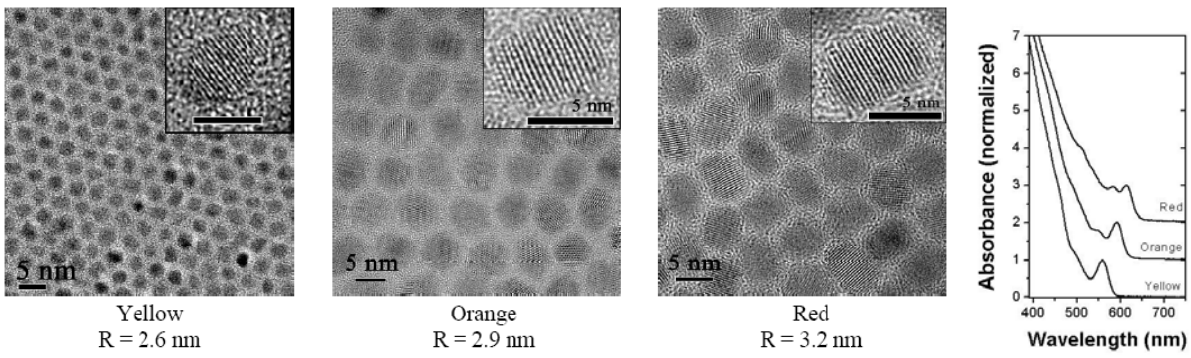

Figure 8.7 *Characterization of CdSe-CdS-ZnS quantum dots. (left) High resolution transmission electron microscopy images of the yellow, orange, and red nanocrystals. For each image (including the insets) the scale bar is 5 nm. (right) Absorption spectra of the three different sized CdSe-CdS-ZnS QDs utilized in this study.*

QDs of different radius, and thus different emission wavelengths have been studied: the analyzed radii and corresponding absorption wavelengths are 2.6 nm (yellow), λ_{PL}= 573 nm, 2.9 nm (orange), λ_{PL}= 604 nm, and 3.2 nm (red), λ_{PL}= 626 nm.

The wide-gap inorganic semiconductor, such as ZnS, seems to greatly improve "electronic" passivation of NC surfaces, resulting, in particular, in a significant increase in the photoluminescence quantum yield.[20] Moreover, the FQY values decrease when the dimensions of the nanoparticles increase, as a consequence of an increasing surface trapping and, consequently, nonradiative carrier losses that partially deactivate the fluorescence.[21] The wide-gap semiconductor used for overcoating the core allows one to significantly improve emission quantum yields by reducing surface-related non radiative carrier losses.[22] The traps can be either on the surface of the QD,[23] at the core-shell interface,[24] or in the surrounding matrix itself.[25] The latter factor therefore implies that a careful selection of a suitable host matrix is necessary to achieve stable QD composites.

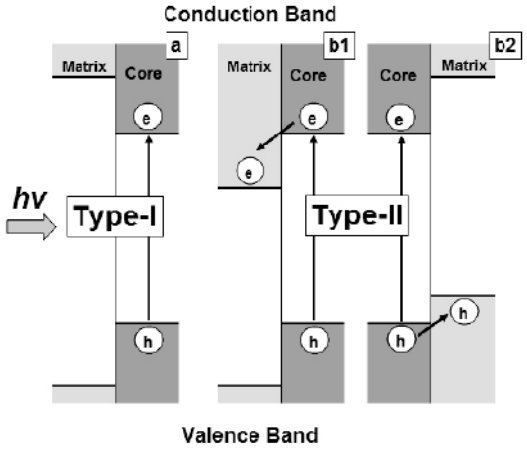

Figure 8.8 *The localization of the electron and hole carriers across a heterostructure interface in a type-I (a) and in a type-II (b1,2) configuration.*

The matrix used as host for the nanocrystal is a zirconia sol gel matrix. It has been prepared by mixing $Zr(OPr)_4$ and acetyl acetone on 1:1 molar ratio, and diluting in isopropanol. This matrix acts as a type-I host for all CdSe QD sizes, as illustrated in figure 8.8. In a Type I structure, the conduction and valence electrons in the dopant cannot in principle access the matrix because it is energetically unfeasible.[26]

8.6 One and two photon excitation scheme in CdSe-CdS-ZnS quantum dots

To better understand the physical origin of this shift it is convenient to consider the QDs energy level scheme reported in figure 8.9. Regardless of the pumping mechanism (one- or two-photon), we pump the carriers in the semi-continuum region, from where they decay to the lowest excited state, which is one dictated by a Poisson state-filling model, within ~1 ps.

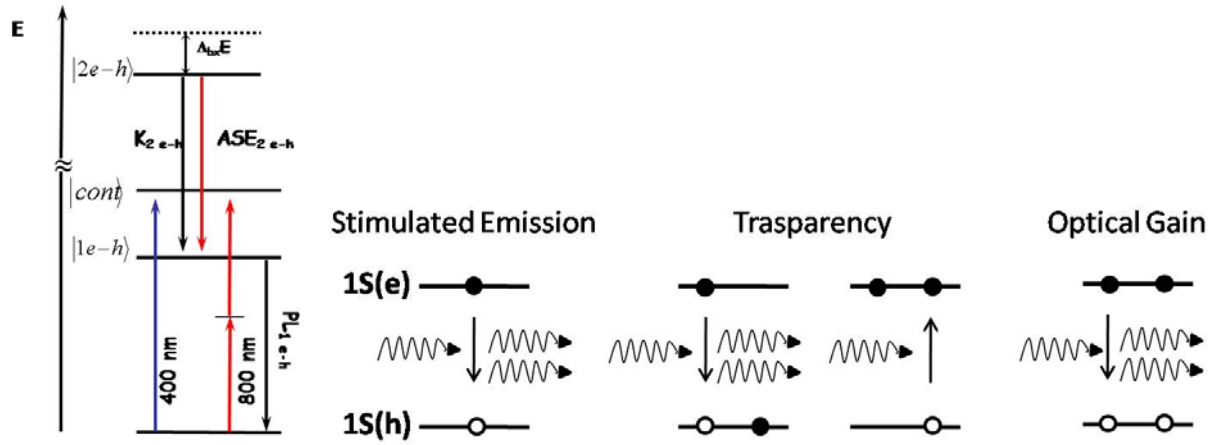

Figure 8.9 (left) *Schematic representation of the absorption processes in a quantum dot species. Under both one- and two-photon excitation of excitons into the semi-continuum region, relaxation of the excited carriers is known to occur to the lowest excited state within ~1 ps. For cases where two electron-hole pairs have been created, the lowest excited state is shown to experience an interaction energy* Δ_{bx} *which can be either positive (carrier repulsion) or negative (exciton attraction). Optical gain and consequently amplified stimulated emission originates from this state. The lifetime of the optical gain is intrinsically limited by the rate of the nonradiative Auger recombination,* k_{2e-h}*, to the one electron-hole pair state. The single exciton decays naturally through spontaneous emission (*PL_{1e-h}*). It should be noted that the depiction of the states in this diagram are on a relative energy scale as to highlight the differences between single- and multi-exciton state transitions and not to give absolute energy values of the states themselves. (right) Schematic representation of the QDs emission properties. From left to right: Stimulated emission occurs when a photon induces the excited electron to decay. The emitted photon has the exact phase, frequency and polarization of the incoming one. For a ground state containing two electrons, exciting only one electron (population equality) can lead to two equally probable events: the incoming photons stimulated the excited photons to decay, producing an extra photon, or the photon excites the ground state electron and is absorbed. There is not net gain or loss of photons. Optical gain occurs if there are more electrons in the excited state than in the ground state (population inversion) because photon absorption is inhibited. If the population inversion is established in a bulk system, and if the gain from stimulated emission is larger than losses, the system will exhibit ASE. In a laser, an ASE-capable medium is placed in a reflecting cavity, and thus the photon field builds itself.*

Then the exciton can decay to the ground state trough spontaneous emission. As anticipated in section 8.4, optical gain in QDs originates from nanoparticles that contain two e-h pairs. When a second exciton is generated inside the nanocrystal, it undergoes a Coulomb interaction with the previous one. This interaction, that is significantly increased with respect to the bulk semiconductors because of the quantum confinement, leads to an energy shift of the bi-

excitonic level, that can be either positive or negative. Consequently the amplified stimulated emission, originating from this state, is shifted with respect to the photoluminescence.

For moderately well passivated dots, nonradiative Auger relaxation of doubly excited particles, dominates over surface trapping and imposes an intrinsic limit on the lifetimes of the optical gain. When QDs are pumped into high-energy excited states, population inversion and the buildup of optical gain are only possible if the relaxation down to the ground state is faster than the Auger process time.

REFERENCES

[1] W. Denk, J. H. Strickler,W. W. Webb, Science 1990, 248, 73; C. Xu, W. Zipfel, J. B. Shear, R. M. Williams, W. W. Webb, Proc. Natl. Acad. Sci. USA 1996, 93, 10763.

[2] S. Maruo, O. Nakamura, S. Kawata, Opt. Lett., 1997, 22, 132; S. Kawata, H.-B. Sun, T. Tanaka, K. Takada, Nature, 2001, 412, 697.

[3] D. Parthenopoulos, P. M. Rentzepis, Science 1989, 24, 843; B. H. Cumpston, S. P. Ananthavel, S. Barlow, D. L. Dyer, J. E. Ehrlich, L. L. Erskine, A. A. Heikal, S. M. Kuebler, I.-Y. S. Lee, D. McCord, J. Qin, H. RÃckel, M. Rumi, X.-Li Wu, S. R. Marder, J. W. Perry, Nature 1999, 394, 51.

[4] X. Wang, D. Wang, W. Jiang, M. Jiang, Opt. Mater., 2002, 20, 217; Y.-fang Zhou, S.-yu Feng, X.-mei Wang, J. of Molec. Struct. 2002, 613, 91; A. Abbotto, L. Beverina, R. Bozio, S. Bradamante, G. A. Pagani, R. Signorini, Synth. Metals, 2001, 121, 1755; G. S. He, C. F. Zhao, C.-K. Park, P. N. Prasad, R. Burzynski, Opt. Comm., 1994, 111, 82; K.Shirota, H.-B. Sun, S. Kawata, Appl. Phys. Lett. 2004, 84, 1632; X. H. Yang, J. M. Hays, W. Shan, J. J. Song, E. Cantwell, Appl. Phys. Lett. 1993, 62, 1071; I. A. Akimov, J. T. Andrews, F. Henneberger, Phys. Rev. Lett. 2006, 96, 067401; C. Zhang, F. Zhang, T. Zhu, A. Cheng, J. Xu, Q. Zhang, S. E. Mohney, R. H. Henderson, Y. A. Wang, Opt. Lett., 2008, 33 (21) 2437.

[5] M. Barzoukas, C. Runser, A. Fort, M. Blanchard-Desce, Chem. Phys. Lett., 1996, 257 ,531.

[6] K. D. Bonin, T. J. McIlarth, J. Opt. Soc. Am. B, 1984, 1, 52.

[7] N. Sharma, S. K. Jain, R. C. Rastogi, Spectrochim. Acta A, 2007, 66, 171.

[8] W. H. Thompson, M. Blanchard-Desce, J. T. Hynes, J. Phys. Chem. A, 1998, 102, 7712.

[9] A. Abbotto, R. Bozio, G. Brusatin, A. Facchetti, M. Guglielmi, P. Innocenzi, M. Meneghetti, G. Pagani, R. Signorini, SPIE Proc., 1999, 18, 3803.

[10] V. I. Klimov, Los Alamos Science, 2003, 28, 214.

[11] Al. L. Efros and A. L. Efros, Sov. Phys. Chem., 1982, 16, 772.

[12] V. I. Klimov, J. Phys. Chem. B 2002, 104, 6112.

[13] Semiconductor and Metal nanocrystals, 2004, Ed. V. I. Klimov, Marcel Dekker Inc.; A.D. Lad, P. P. Kiran, G. R. Kumar, S. Mahamuni, Appl. Phys. Lett., 2007, 90, 133113.

[14] J. López Gondar, R. Cipolatti, G. E. Marques, J. Braz. of Physics, 2006, 36, 3b, 960; J. He, W. Ji, G. H. Ma, S. H. Tang, H. I. Elim, W. X. Sun, J. of Appl. Phys., 2004, 95, 6381

[15] V.V. Nikesh, A. Dharmadhikari, H. Ono, S. Nozaki, Appl. Phys. Lett., 2004, 84, 4602.

[16] Padhila. L.A. et al. Opt. Exp., 2005, 13, 6460; L. A. Padilha, J. Fu, D. J. Hagan, E. W. Van Stryland, C. L. Cesar, L. C. Barbosa, C. H. B. Cruz, D. Buso, A. Martucci, Phys. Rev. B., 2007, 75, 075325

[17] D. R. Larson, W. R. Zipfel, R. M. Williams, S. W. Clark, M. P. Bruchez, F. W. Wise, W. W. Webb, Science, 2003, 300, 1434.

[18] Li J. J. et al., J. Am. Chem. Soc. 2003, 125, 12567; van Embden, P. Mulavaney, Langmuir, 2005, 21, 10226.

[19] S.-C. Pu, M.-Ju Yang, C.-C. Hsu, C.-W. Lai, C.-C. Hsieh, S. H. Lin, Y.-M. Cheng, P.-T. Chou, Small 2006, 2, 1308 ; M. E. Schmidt, S. A. Blanton, M. A. Hines, and P. Guyot-Sionnest, Phys. Rev. B, 1996, 53, 12629.

[20] V. I. Klimov, A. A. Mikhailovsky, D. W. McBranch, C. A. Leatherdale, M. G. Bawendi, Science, 2000, 287, 1011.

[21] V. I. Klimov, A. A. Mikhailovsky, Su Xu, A. Malko, J. A. Hollingsworth, C. A. Leatherdale, H.-J. Eisler, M. G. Bawendi, Science, 2000, 290, 314.

[22] Piryatinski, A. et al. Nanoletters, 2007, 7, 108-115; R. Xie, U. Kolb, J. Li, T. Basché, A. Mews, J. Am. Chem. Soc., 2005, 127, 7480

[23] D. E. Gómez, J. van Embden, J. Jasieniak, T. A. Smith, P. Mulvaney, Small, 2006, 2, 204.

[24] L. Manna, E. C. Scher, L.-S. Li, A. P. Alivisatos, J. Am. Chem. Soc., 2002, 124, 7136.

[25] J. L. Blackburn, D. C. Selmarten, A. J. Nozik, J. Phys. Chem. B, 2003, 107, 14154.

[26] J. Jasieniak, J. Pacifico, R. Signorini, A. Chiasera, M. Ferrari, A. Martucci, P. Mulvaney, Adv. Funct. Mater., 2007, 17, 1654.

CHAPTER 9

The Sol-Gel process: a useful tool for the preparation of solid-state devices

The generation of integrated solid state devices, based on nonlinear, as well as linear, optical active materials, is one of the major wish in modern technology. Therefore, the maintenance of the optical properties of the dyes, in going from solution to solid materials, is indispensable.

The synthesis and the characterization of the optimal guest-host system play an important role in the design of a material possessing the functional properties required by the device they are made for. In this context, the sol-gel chemistry is an important technique for the synthesis of solid-state materials usable in optics and photonics applications. This synthesis combines the great flexibility of choice in the experimental parameters (precursors, synthetic routes, catalysts, ...) to the possibility of obtaining samples with different shapes (films or bulks, with various thicknesses, or powders). Besides, the relative low temperatures, employed in sol-gel synthesis, prevent the damaging of the chromophores, often organic species, embedded in the material.

The sol-gel process was born as a method for the synthesis of pure inorganic powders of Ti-, Si-, Al-, Zr-oxides. One of the first studies was done by Stober et al.[1] which showed that, using ammonia as a catalyst for the Tetraethoxysilane hydrolysis reaction, it was possible to control both the morphology and the size of the final silica powders. Successively, this technique has been

largely exploited for the realization of films for a great variety of applications and functionalities: in microelectronics,[2] electrochromic films for smart windows and displays,[3] semiconductor or superconductor films, materials for catalysis[4], and so on.

Nowadays, the exploitation of new precursors, containing organic group covalently bonded to the silicon atom, makes the sol-gel process an important technique in several kinds of applications where the soft-chemistry is required.

The importance of these materials consists on the great opportunity to have a synergic effect due to the close coexistence of an organic and an inorganic network, mixed at a nanometric scale. The advantages of the organically modified materials, with respect to those obtained with the classic inorganic sol-gel recipes, are the higher mechanical and optical performances, low porosity, no sensitivity to the humidity and suitability for obtaining thick films without cracking.

In the first part of this chapter some details about the steps characterizing the sol-gel method will be presented, in order to emphasize the key features that influence the sol-gel process.

Successively, more attention will be dedicated to the use of hybrid organic-inorganic precursors for the preparation of optical materials. Some details about their reactivity will be described and, in the last part, some applications will be analyzed.

9.1 The sol-gel process

The main chemical reactions involved in the sol gel synthesis are the hydrolysis and condensation reactions leading to the inorganic network formation:

$$M(OR)_n + mH_2O \underset{esterification}{\overset{hydrolysis}{\rightleftharpoons}} M(OH)_m(OR)_{n-m} + mROH \qquad \text{Eq. 9.1}$$

$$2M(OH)_m(OR)_{n-m} \underset{alcoholysis}{\overset{alcoholic\ cond.}{\rightleftharpoons}} (RO)_{n-m}(HO)_{m-1}M-O-M(OH)_m(OR)_{n-m-1} + ROH \qquad \text{Eq. 9.2}$$

$$2M(OH)_m(OR)_{n-m} \underset{hydrolysis}{\overset{acqueous\ cond.}{\rightleftharpoons}} (RO)_{n-m}(HO)_{m-1}M-O-M(OH)_{m-1}(OR)_{n-m} + H_2O \qquad \text{Eq. 9.3}$$

In these equations R is generally an alkyl group (C_xH_{2x+1}). The main difference is between the alkoxysilane precursors (where *M* is the silicon metal) and the transition (Zr-, Ti-, V-,...) and semimetal (B-, Al-,...) ones.

Most used between silicon alkoxides is the tetraethoxysilane (TEOS), where the substituent is an ethoxy group:

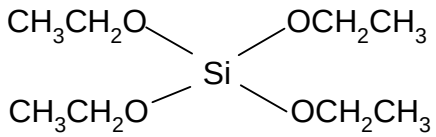

Figure 9.1 *Molecular structure of TEOS.*

The change of the chain length of the substituents induces some differences in the reactivity of the silane, as it will be described later.

The second class of precursors can be generally distinguished from the silicates by the greater chemical reactivity resulting from the lower electronegativity of the transition metal.[5] These metals exhibit several coordination states, allowing a spontaneous coordination expansion upon reaction with water or other nucleophilic reagents.

In the hydrolysis and condensation reactions reported above, the $HO^{\delta-}$ acts as nucleophilic group, which attacks the positive charged metal. Hence, the reactivity towards the hydrolysis increases when the electronegativity decreases or, alternatively, when the partial charge increases. This effect is enlightened by the data reported in table 9.1.

Alkoxide	Electronegativity χ	Part. positive charge δ_M	Ionic Radius R (Å)	Coordination number (N)
$Si(OPr^i)_4$	1.74	+0.37	0.40	4
$Ti(OPr^i)_4$	1.32	+0.60	0.64	6
$Zr(OPr^i)_4$	1.29	+0.64	0.87	7
$Ce(OPr^i)_4$	1.17	+0.75	1.02	8

Table 9.1 *Electronegativity, partial positive charge on the metal, ionic radius and coordination number data of the metals in some alkoxydes precursors.*

These data explain the low reactivity of Si-alkoxydes with respect to the transition metal precursors. In the first case it is often necessary to use some catalysts to increase the reaction rate and, on the contrary, some chelating agents are indispensable to stabilize the transition metal precursors. Common complexing agents are the acetic acid[6] or diketones, which exhibit keto-enol tautomerization, such as acetylacetone and acetoacetate.[7] These bidentate molecules reduce some of the active functionalities of the tetrafunctional precursors.

9.2 Hydrolysis

In these sections, we will examine only the features of the reactions for silicate precursors. During the first step of the process, the nucleophilic oxygen, contained in water, attacks the silicon atom and the alkoxides groups (-OR) are replaced by hydroxyl groups (-OH) through an S_{N2} mechanism.

Hydrolysis is facilitated in the presence of homogenizing agent, generally an alcohol, which permits the miscibility of alkoxide and water. It should be emphasized that the addition of solvents may promote esterification and depolymerization reactions, avoiding the incoming sol-gel reactions.

The hydrolysis is most rapid in the presence of catalysts, especially if the alkoxide groups are long. Many factors influence the hydrolysis kinetics, such as the nature and the concentration of the catalyst (acid, base), the nature of the solvent, the type of alkoxide and the temperature. The most used catalysts are inorganic acids (HCl, HNO_3, H_2SO_4), basic species (NH_4OH, NaOH) or Lewis basis (n-Bu_4NF, NaF). In acidic conditions, H^+ attacks the alkoxy group and, besides, the metal is more positive and can be attacked by water:

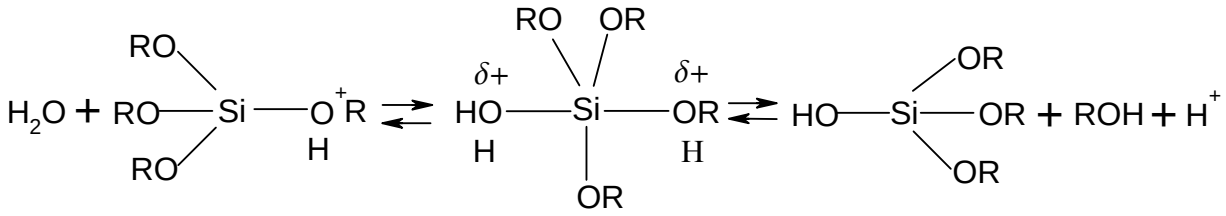

Figure 9.2 *Hydrolysis mechanism in acidic condition.*

The hydrolysis rate constant in this case increases when the lateral substituents reduce the steric (spatial) hindrance and when they stabilize the partial positive charge on the central metal. The basicity scale for the substituents is: (SiO-) < (HO-) < (RO-) < (R-). Hence, the presence of an alkoxide RO- group increases the electronic density on the Si more that a SiO- group, which is formed by condensation reactions. The hydrolysis rate diminishes after the first stages in acid-catalyzed sol, but the contrary occurs in basic conditions.

In basic conditions, the OH^- groups attack the Si atom and they can replace the alkoxy groups in a second step. The more negative substituent stabilizes the partially charged intermediate specie, favoring the hydrolysis. The presence of the SiO^-, a good electron acceptor, speeds up the hydrolysis after the first steps. The mechanism of the hydrolysis in basic conditions is depicted as:

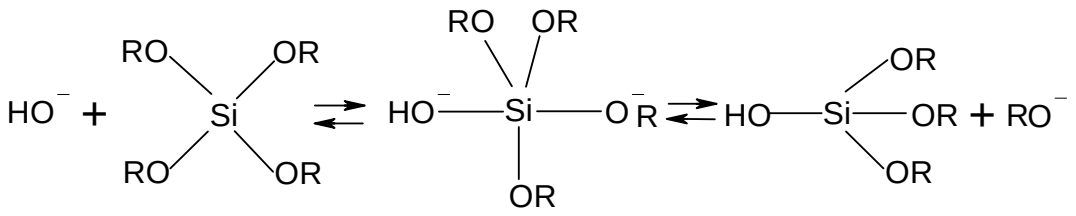

Figure 9.3 *Hydrolysis mechanism in basic condition.*

9.3 Condensation

The second step of the process is based on the condensation reaction. Polymerization to form siloxane bonds occurs by either an alcohol- or a water-producing condensation reaction. It has been shown by Engelhardt et al. that a typical sequence of condensation products is monomer, dimer, linear trimer, cyclic trimer, cyclic tetramer, and higher order rings.[8] This sequence of condensation requires both depolymerization (ring opening) and the availability of monomers which are in solution equilibrium with the oligomeric species and/or are generated by depolymerization.[9]

The rate of these ring opening polymerizations and monomer addition reactions is dependent upon the environmental pH. In polymerizations below pH 2, the condensation rates are proportional to the $[H^+]$ concentration. Because the solubility of silica is quite low below pH 2, formation and aggregation of primary silica particles occur together and ripening (i.e., growth of a network) contributes little to growth after particles exceed 2 nm in diameter. Thus, developing gel networks are composed of exceedingly small primary particles.

It is generally agreed that between pH 2 and pH 6 condensation rates are proportional to $[OH^-]$ concentrations. Condensation preferentially occurs between more highly condensed species and those less highly condensed and somewhat neutral. This suggests that the rate of dimerization is low, however, once dimers form, they react preferentially with monomers to form trimers, which in turn react with monomers to form tetrameters. Cyclization occurs because of the proximity of the chain ends and the substantial depletion of the monomer population. Further growth occurs by addition of lower molecular weight species to more highly condensed species and aggregation of the condensed species to form chains and networks. The solubility of silica in this pH range is again low and particle growth stops when they reach 2-4 nm in diameter.[10]

Above pH 7, occurs the same polymerization as in the pH 2 to pH 6 range. However, in this pH range, condensed species are ionized and therefore, mutually repulsive. Growth occurs primarily through the addition of monomers to the more highly condensed particles rather than by particle aggregation. Due to the greater solubility of silica and the greater size dependence of solubility above pH 7, particles grow in size and decrease in number as highly soluble small particles dissolve and reprecipitate on larger, less soluble particles. Growth stops when the difference in solubility between the smallest and largest particles becomes indistinguishable. This process is referred to as Ostwald ripening. Particle size is therefore, mainly temperature dependent: higher

temperatures produce larger particles. Additionally, in this pH range, the growth rate depends upon the particle size distribution.

As with hydrolysis, condensation can proceed without catalyst, however, their use in organosiloxanes is highly helpful. Furthermore, the same type catalysts are employed: generally those compounds which exhibit acidic or basic characteristics.

It is generally believed that the acid-catalyzed condensation mechanism involves a protonated silanol species. Protonation of the silanol makes the silicon more electrophilic and thus susceptible to nucleophilic attack. The most basic silanol species (silanols contained in monomers or weakly branched oligomers) are the most likely to be protonated. Therefore, condensation reactions may occur preferentially between neutral species and protonated silanols situated on monomers, end groups of chains, etc.

The most widely accepted mechanism for the base-catalyzed condensation reaction involves the attack of a nucleophilic deprotonated silanol on a neutral silicic acid:

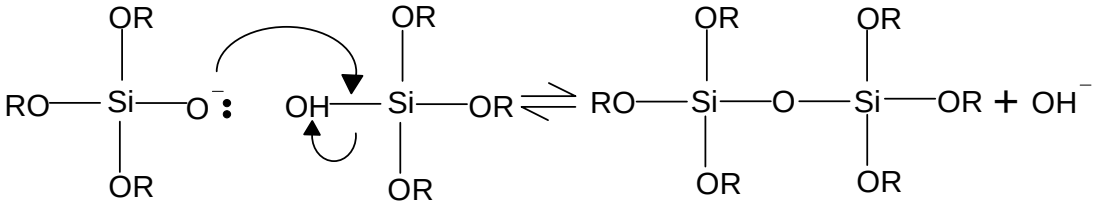

Figure 9.4 Nucleofilic attack to form silos sane bond.

Furthermore, it is generally believed that the base-catalyzed condensation mechanism involves penta- or hexa-coordinated silicon intermediates or transition states, similar to that of a S_{N2} type mechanism.

Many factors affect the resulting silica network, such as, pH, temperature and time of reaction, reagent concentrations, catalyst nature and concentration, H_2O/Si molar ratio, and aging temperature. However, it can generally be said that sol-gel derived silicon oxide networks, under acid-catalyzed conditions, yield primarily linear or randomly branched polymers which entangle and form additional branches resulting in gelation. On the other hand, silicon oxide networks derived under base-catalyzed conditions yield more highly branched clusters which do not interpenetrate prior to gelation and thus behave as discrete clusters.

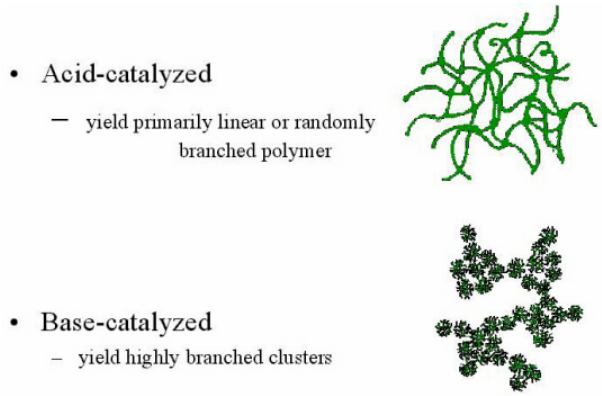

Figure 9.5 *Summary of Acid/Base sol-gel conditions.*

9.4 Gelification

As the sol particles grow and collide, condensation occurs and macroparticles form. The sol becomes a gel when it forms a tridimensional network which can support a stress elastically. This is typically defined as the gelation point or gelation time, t_{gel}. There is no activation energy that can be measured and the point where the sol changes from a viscous fluid to an elastic gel cannot be precisely defined. The change is gradual as more and more particles become interconnected.

One of the most precise methods to measure t_{gel} consists of the measurement of the viscoelastic response of the gel as a function of shear rate. The shear modulus is a complex quantity expressed by the relation:

$$\boldsymbol{G = G'(\omega) + iG''(\omega)} \qquad \text{Eq. 9.4}$$

Where *G'* is the storage modulus arising from the elastic component of the sol-gel and *G"* is the loss modulus coming from the viscous component. The rapid increase in the storage modulus near t_{gel} is consistent with the concept that the interconnection of the particles becomes sufficient to support a load elastically.

There is at least one indication that the gelation time is not only an intrinsic property of the sol, but depends on many factors, such as the effects of the alkoxy groups and the solvent, the type and the concentration of the catalyst, the temperature, the quantity of water, the size of the container. It is often difficult to model the global effect of these factors on the determination of the gelation time. The considerations generally derive from experimental evidences. For example, it has been seen that long molecules of solvent and large substituent groups increase the gelation time.

Besides, the amount of water for hydrolysis has a dramatic influence on gelation time, for low water contents, generally an increase of the amount of hydrolysis water decreases the gelation time, although there is a dilution effect. For higher water contents, the gelation time increases

with the quantity of water. The location of the minimum in the curve t_{gel} *vs* R (with $R=H_2O/Si(OR)_4$) depends on the experimental conditions, such as the nature of the chemicals, the catalyst, and the temperature.

9.5 Drying

The gel is a tridimensional network of oxide where the liquid fills the pores. This liquid can be extracted above the critical temperature (T_c) and critical pressure (P_c) of the liquid.

Under these conditions, there is no longer any distinction between the liquid and vapor phases and, by this way, there is no liquid-vapor interface and no capillary pressure. This process, called "supercritical drying", prevents the material from cracking during the shrinkage.[11] The final sample is called aerogel.

More commonly, the liquid evaporates upon thermal treatment, towards a formation of a xerogel when the pores become empty. The specific surface area of the gel is large (> 400 m^2/g) and the dimensions of the pores are small (< 10nm).

In the first phase of drying, the decrease in volume of the gel is equal to the volume of the liquid lost by evaporation. The network modifies towards the formation of pores with a superficial meniscus characterized by a radius r.

The first stage of drying is called "the constant rate period" because the rate of evaporation per unit area of the drying surface is independent of time.

This process continues until the critical point when the matrix becomes rigid and resists toward a successive shrinkage. The meniscus radius becomes equal to the pore radius and is able to penetrate the bulk. In the "falling rate period" the liquid evaporates, firstly, through partially empty pores, and after, by diffusion of its vapor to the surface.

This is a critical step for the process because the material can undergo fracture. A distribution of pore sizes exists in these materials, and some pores can empty before others, generating a pressure gradient between adjacent pores with different diameters.

The modulus of the gel is very high and the compressive stress is in the order of 100 MPa.

The pores that empty first (at the larger end of the distribution) stop shrinking and can only passively shrink under the influence of nearby saturated pores. The possibility of cracking at this point is great, due to the high stresses and low strain tolerance of the material.

There are three main possibilities of avoiding the cracking of the sol-gel material. One consists on the use of supercritical drying process, as mentioned before. The second is the use of surfactants

or DCCA (drying control chemical additives)[12] which, added to the solution, reduce the interfacial energy and thereby decrease the capillary stress. The last one involves the use of hybrid organic-inorganic precursors which will be described in the next section.

9.6 Dehydration and densification

An important step in the sol-gel synthesis is the densification of the material, involving the removal of surface silanol (Si-OH) bonds from the pore network. Porous materials, made by sol-gel method, are optically transparent with interconnected porosity and possessing sufficient strength to be used as unique optical components. This is possible only if the material is thermally and chemically stabilized: the pores become unable to rehydrate. The free water within the ultra porous gel structure (i.e., physisorbed water) can be removed with a thermal treatment at about 170°C. The dehydration is completely reversible, up to about 400 °C. Only at higher temperatures, the dehydration process is irreversible as a result of the shrinkage and sintering across pores. The densification is complete between 850 and 1000°C when also the single hydroxyl groups condensate.

9.7 Hybrid organic-inorganic nanocomposites

The mild synthetic conditions offered by the sol-gel process (metal-organic precursors, organic solvent, low processing temperature, processing versatility of the colloidal state) allow the mixing of inorganic and organic components at the nanometric scale.[13]

These materials being at the interface of organic and inorganic realms are highly versatile offering a wide range of possibilities to elaborate tailor made materials in terms of processing and chemical and physical properties.[14]

Depending on the nature of the interface between the organic component and the inorganic counterpart it is possible to divide these materials into two distinct classes.

In class I, the organic counterpart (organic molecule, oligomers, biocomponent, polyfunctional polimers), are incorporated into the metal-oxide-based networks, or hybrid siloxane-oxide matrices by mixing them metal alkoxides or/and organosilanes in a common solvent.

The organics, that can be cross linkable, can interact or be trapped within the inorganic component through a large set of fuzzy interactions, such as H-bonds, π-π interactions, van der Waals force.

The host matrix can be made of an inorganic structure (silica, titania, etc.) or a hybrid skeleton (organosilicas, etc.).

These materials, exhibiting infinite microstructures, can be transparent and easily shaped as films or bulks. They are generally polydisperse in size and locally heterogeneous in chemical composition.

In class II hybrid materials, the organic and inorganic components are linked together through strong bonds (covalent or iono-covalent). Organically modified metal alkoxides are the molecular precursors used for this purpose.[15] The chemistry of hybrid organic-inorganic networks is mainly developed around silicon containing materials. Currently, the most common way to introduce an organic group into an inorganic silica network is to use organo-alkoxysilane molecular precursors of general formula $R'_nSi(OR)_{4-n}$ with *n*=1,2,3. In most sol-gel conditions the $Si-C$ bond remains stable towards hydrolysis, and R' group introduces focused new properties to the inorganic network (flexibility, hidrophobicity, refractive index modification, optical response, etc.). R' also decreases the inorganic crosslinking due to the partial reduction of reactivity around the silicon atom. This allows obtaining sample with high densification degree at low temperatures, much lower than the densification temperatures of the inorganic counterpart. In this case, the organic chains fill the pores between the inorganic oxide chains, avoiding formation of cracks during the drying stage.[16]

The R' group can be any organofunctional group: if it is a simple non-hydrolysable organic group ($Si-CH_3, Si-phenyl, etc.$) it will have a network modifying effect, if it can react with itself or with other polymerisable units (R' contains a vinyl, methacryl, or an epoxy group for example), it acts as a network former.[17]

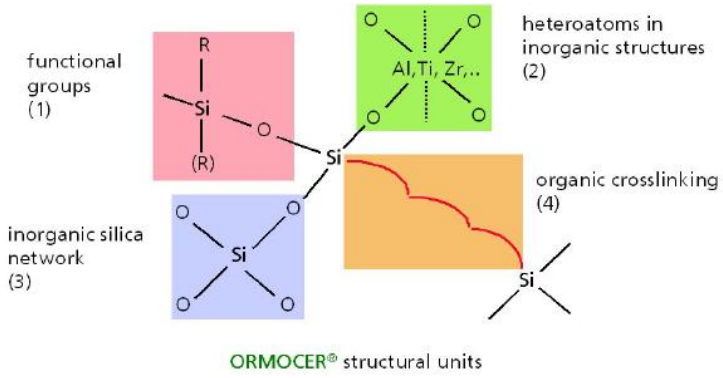

Figure 9.6 *Schematic representation of all the possible reactions that lead to the organic and inorganic network formation.*

The sol-gel synthesis of siloxane based hybrid organic-inorganic compounds usually involves di- or tri-functional organosilanes co-condensed with metal alkoxides, mainly $Si(OR)_4$, $Ti(OR)_4$,

$Zr(OR)_4$, $Al(OR)_3$. Each of these components has specific roles that have been reviewed and discussed extensively.[18]

Tri-functional alkoxysilanes and metal alkoxides are efficient crosslinkers leading, after co-condensation, to hybrid materials having high Young's modulus ($E > 10\ GPa$) and high glass transition temperature. Di-functional alkoxysilanes co-condensed metal alkoxides generate linear polymers and cyclic oligomers behaving as hybrid elastomers and exhibiting low Young's modulus ($E = 5 - 100\ MPa$) and low glass transition temperature. Therefore, the mixing of these different molecular precursors (tri- and di-functional alkoxysilane, metal alkoxides, functional macromonomers, etc.) allows tuning the mechanical and functional properties of hybrid materials.

9.8 A network former: 3-Glicidoxypropyl-trimethoxysilane

The 3-Glycidoxypropyl-trimethoxysilane (GPTMS) is a hybrid tri-functional precursor, which have been largely exploited in many applications.[19]

The organic group of GPTMS contains an epoxide ring, that is characterized from the presence of polar $C - O$ bonds and from an elevate tensile strain, making it more reactive with respect to bigger ethers.[20] Thus the ring opening lead to low energy and therefore more stable compounds.

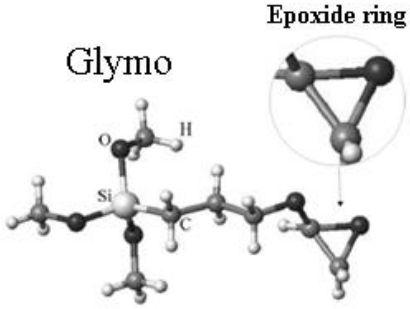

Figure 9.7 *Structure of GPTMS molecule.*

The epoxy group can undergo hydrolysis or alcoholysis forming the corresponding diol or β-hydroxy ethers or polyaddition reactions giving polyether linkages. The reaction follows a S_{N2} mechanism, entailing a nucleofilic attack on one of the carbon atoms of the ring.

The contemporary polymerization of the alkoxide and epoxide groups leads to the growth of compenetrated inorganic and organic network. Often, the inorganic condensation and the organic polymerization are antagonists because the first constitutes a steric hindrance for the second one and viceversa.

As for the inorganic counterpart also the epoxide ring opening should be hasten by using a proper catalyst in the synthesis. The most commonly catalysts are Lewis acids, such as Zirconium,

Titanium and Aluminum alkoxides, that, being part of the inorganic network, also concur to determine the optical and mechanical properties, such as the refractive index and the scratch resistance of the final product.

Some references[21] compare the catalytic effect of the metal alkoxides on the ring cleavage efficiency, even if it is often difficult to operate with the same synthetic conditions in order to isolate only the effect of the catalysts. From the results of the ^{13}C-NMR experiments it is possible to evaluate the residual unopened epoxy ring, using different metal alkoxides and varying their concentrations. Authors show that the maximum in ring-opening and condensation degree is found in hybrid sols and gels with 10% mole metal alkoxides. At this concentration, the activity of the metal alkoxides increases in the order:

$Si(OEt)_4, Ti(OEt)_4, Zr(OBu^n)_4, Ta(OEt)_5, Sn(OBu^t)_4, Al(OBu^s)_3, Al(OEtOBu)_3$

Alternatively the organic polymerization can be promoted using a thermal initiator,[22] or can be induced by UV irradiation[23] either during the sol formation or after the film deposition. In the latter case the polyether chain formation induces further volume shrinkage of the silicate network and a refraction index increase, that can be exploited for the production of modulated surface structures or waveguides.

9.9 Applications of hybrid materials

The properties of hybrid materials can be widely employed for academic and industrial applications.

The main topics in which these materials are used are:[24]

- *Protective and decorative coatings*[25]

Hybrid coatings have been developed to strengthen parts of paper, to enhance specific properties of polymers used in industry (polyethylene, cellulose, etc.) or to reduce the abrasion of leather. Concerning scratch and abrasion resistance applications they are in general based on epoxy functionalized alkoxysilanes polycondensed with Al, Ti, Zr compounds. Hybrid materials are also used in automotive coatings, where protection from environmental factors, such as UV and chemical attack is also required.

Decorative hybrid coatings can find application as packaging glass, glass sheets for furniture and sanitary appliances, glass in architecture, in the building industry, and glazing in automotive sector.

- *Barrier systems*[26]

The interest in hybrid materials as barrier systems has been increased in the last decades as a result of the requirements to develop much more sophisticated materials in fields such as solar cells, optics, electronics, food packaging, etc. The flexible nature of these materials results in an optimized encapsulation process and especially in good protection of the edge area, and allows them to adapt to non-planar surfaces.

- *Dental applications*[27]

Inorganic-organic hybrid materials can be used as filling composites in dental applications. These composites feature tooth-like properties; they easily penetrate into the cavity and harden quickly under the effect of blue light. Moreover, these materials feature minimum shrinkage, are non-toxic, and sufficiently non-transparent to X-rays.

- *Microelectronics*[28]

Organically modified resins retain important roles in electrical component coatings such as resistors and molding compounds, as well as spin-on dielectrics in microelectronics interlayer and multilayer dielectric and planarization applications.

The advantage of tuning the hybrid's flexibility and adhesion properties allows their use on flexible substrate, even as optical waveguides. Their easy chemistry offers a perfect fit for implementation as an optical waveguide material in systems like transmitters and receivers in medium and long distance telecommunication, thermo optical switches and couplers, etc., as the laser sources as well the glass-fibers work in these low-loss windows.

- *Micro-optics*[29]

Hybrid materials have been employed to produce free-standing micro-optical elements through a combined lithographic and embossing process as well as to produce interference optical coatings such as dielectric mirrors and reflectors.

- *Photovoltaic cell applications*[30]

All solid state organic-inorganic hybrid dye-sensitized solar-cells are studied to eliminate the practical problems of liquid electrolyte use like degradation with time, cell sealing, handling, etc.

These are only few of the applications for hybrid organic-inorganic composites. The most exciting feature of this new class of materials is the possibility to engineer the synthesis of structures from the molecular to the nanometric or micrometric scales, to satisfy the requirements for a variety of

applications from biological and chemical sensing, catalysis, selective separation to optical communications and optical devices.

9.10 Sol-gel matrices for up-conversion lasing

Sol-gel materials to be used as host for the NLO active dyes must have low optical losses, be dense at temperature low enough to avoid thermal degradation of the chromophores,[31] allow incorporation of the doping molecules in large amounts without segregation effects, and protect them from the photodegradation due to the combined effect of oxygen and light.

In this context organic-inorganic hybrid materials, composed of inorganic oxide structures and interpenetrated cross-linked organic polymers are useful. The hybrid network can combine the most important glass-like with the polymer-like properties.[32]

In particular hybrid materials present improved mechanical and optical properties with respect to their purely inorganic counterparts, together with a lower porosity and with the possibility to obtain films with thickness in the micrometer range with single step deposition.

Organic molecules, can be easily incorporated into hybrid siloxane-oxide matrices through physical or chemical links, thanks to the chemical similarity with the organic component of the host, thus avoiding aggregation effects. Moreover the low synthesis temperature allows preserving these active species from the thermal degradation.

In next section, the synthesis of the hybrid sol-gel matrices will be presented. Successively their optical and micro-structural properties will be analyzed and finally few results concerning the incorporation of the organic chromophore, provided from Prof. Pagani group, inside these matrices will be reported.

9.11 Synthesis of hybrid matrices as host for chromophores incorporation

Different matrices have been prepared in collaboration with the group of Prof. Guglielmi (University of Padova).

All the investigated systems start from the hybrid silicate precursor, GPTMS, together with transition metal alkoxides, such as germanium, titanium, zirconium alkoxides that allow increasing the film refractive index.

All the synthesis have been prepared with the final purpose of obtaining films with excellent mechanical and optical properties and low losses. Moreover they will behave like host for the active species, avoiding aggregation even at high concentration ($\sim 10^{-2}$ M), and preserving their

emission properties. All these parameters must be satisfied in view of application as active waveguide in a DFB configuration to fabricate solid-state lasing devices.

Here the protocols for the sol-gel synthesis of the different matrices are briefly reported, together with the ultimate aim for which they have been synthesized:

G7Ge3: the GPTMS is pre-hydrolyzed with water for one night under magnetic stirring. This step is necessary in order to compensate the higher reactivity of the germanium alkoxide with respect to that of GPTMS. Then NaOH (NaOH(1M)/GPTMS=0.0003) and 2-Methoxyethanol (2-MetOH) are added and, after 10 minutes, the germanium tetraethoxide is added together with the relative amount of water. This solution is kept under reflux at 80°C for 1 hours and 30 minutes. The molar ratio between the GPTMS and the second precursors is equal to 7:3.

This solution has been prepared in order to obtain UV-patternable films, for the production of the DFB gratings, on the film to air interface, by exposing the film to a UV-lamp through a suitable mask. In fact, by performing the synthesis in basic condition it is possible to obtain highly homogeneous sample, with low porosity and low optical losses, preserving the epoxide ring un-opened. The ring opening can thus be induced later thermally or with UV light, together with film shrinkage and a refractive index increases.[33]

G7Ti3: the GPTMS is pre-hydrolyzed with water for one night under magnetic stirring. This step is necessary in order to compensate the higher reactivity of the germanium alkoxide respect to that of GPTMS. Then NaOH (NaOH(1M)/GPTMS=0.0003) and 2-MetOH are added and, after 10 minutes, the second precursor Ti-isopropoxide, previously diluted in 2-MetOH, is mixed to the GPTMS solution. This solution is kept under stirring for 3 hours at room temperature. The molar ratio between the GPTMS and the second precursors is equal to 7:3.

This synthesis was originally conceived with the purpose of increasing the refractive index of the film and the index contrast of the DFB gratings. Afterwards the evidence of a strong photocatalytic activity of these films towards the organics has discouraged their application as host for the chromophores. However the film shrinkage, up to 60%, obtained as a results of the organic component decomposition of the GPTMS, when the films are exposed to UV-light, has been exploited as a promising way to obtain diffractive optical elements.

GTZ: GPTMS and tetraethoxysilane (TEOS) are co-hydrolyzed for 3 hours under reflux at 80°C with acidified water and methanol as solvent. The solution with $Zr(OBu^t)_4$, acetylacetone and the residual solvent is rapidly added to the GPTMS and TEOS solution and refluxed at the same

temperature for 1.5 hours. The molar ratios used are: GPTMS:TEOS:$Zr(OBu^t)_4$ = 9:3:1; GPTMS+TEOS:H_2O = 1:3.3; GPTMS:HCl = 1:0.004; $Zr(OBu^t)_4$:AcAc = 1:1.

This matrix was already demonstrated to be a suitable host for the push-pull chromophore, called OHPEP.[34] Both film and bulk samples have been prepared starting from that sol, showing a really high temporal stability of the guest chromophore and unaltered emission properties.

GTA: GPTMS and tetraethoxysilane (TEOS) are co-hydrolyzed for 1 hour under reflux at 80°C. A solution of N-[(3-trimetoxysilyl)propyl]ethylenediamine (TMESPE) and methanol is added immediately afterward, and the mixture is left under stirring at room temperature for 10 minutes prior to film deposition. The molar ratio employed are: GPTMS:TEOS = 7:3, TMESPE:(GPTMS+TEOS) = 0.47, H_2O:SiO_2 = 2.

The TMESPE acts as a strong base that promote the inorganic polymerization and simultaneously catalyze the epoxide ring opening. Moreover it has an effect of network modifier, because the organic group that terminates the amine functionalities will directly bond to the silica backbone and will react by a coupling reaction with the epoxide ring of GPTMS.[35] It causes a very rapid increase of the gelation time, and thus transparent and homogeneous film can be prepared only depositing the film few minutes after the TMESPE addition.

These matrices have been optimized to increase the chromophores photostability, since the presence of amine groups is demonstrated to significantly reduce the photobleaching effect due to the combined action of light and oxygen.[36]

9.12 Structural analysis

FT-IR spectra of the deposited films have been performed in order to investigate the chemical microstructure, both regarding the inorganic skeleton and the organic component. The results are reported in figure 9.8. The basic environment inhibits the activity of the Ge alkoxide, which is well known to produce the epoxy polymerization at a reaction temperature of 80°C, behaving as Lewis acid.[37] This fact is confirmed by the presence of the two band of the epoxide ring at 3050 and 2995 cm^{-1} (C-H stretching), 1260 cm^{-1} (ring breathing), and 900 cm^{-1} (antisymmetric ring stretching).

These bands are absent or weak in films obtained from the other solutions. The FTIR absorption spectra, in the 1250-875 cm^{-1} range, show several contributions. In this interval the main band at around 1110 cm^{-1} is related to the asymmetric stretching mode of the C-O-C bond of the propylic chain. The band at 1060 cm^{-1} corresponds to the Si-O-Si symmetric stretching mode.

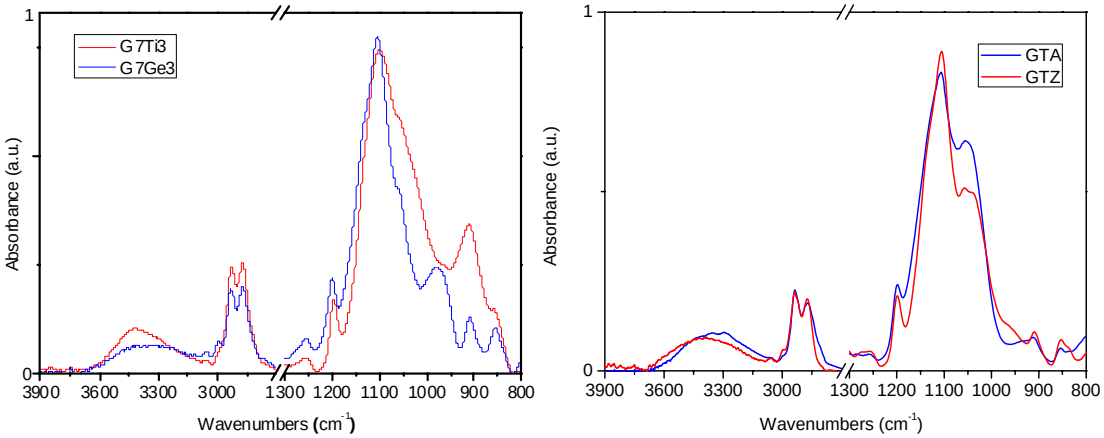

Figure 9.8 *FT-IR spectra of the four different synthesized sol-gel films.*

The two peaks at 2930 and 2870 cm^{-1} are related to the stretching vibration of the CH_3 and CH_2 groups of the propilyc chain. The band at 960 cm^{-1} in the G7Ge3 sample is indicative of the Si-O-Ge bond. This band move to 940 cm^{-1} for the Si-O-Ti bond in the G7Ti3 film, and is partially covered from the Si-OH and $Si-O^-$ contribution at 910 cm^{-1}.

9.13 UV-Visible absorption spectra

The UV-Vis absorption spectra are necessary to verify the matrices transparency in the visible range, where the chromophores absorb and emit. Moreover they allow to observe that the insertion inside the matrices do not alter the optical properties of the chromophore and also to check their temporal stability and resistance to the thermal or light exposition treatments.

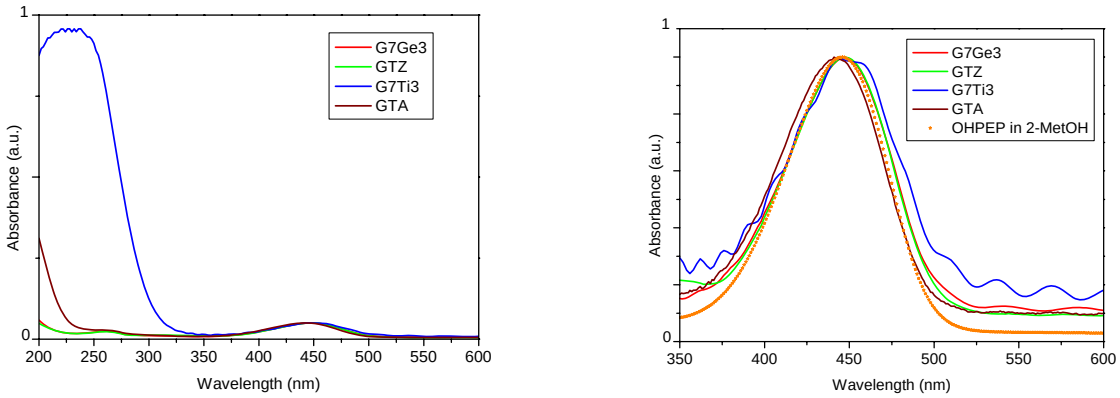

Figure 9.9 *UV-Visible spectra of the four matrices doped with the OHPEP. All the films are transparent from 350 to 800 nm. The sharp absorption band below 350 nm for the G7Ti3 sample is due to the presence of titanium oxo-clusters. On the right is reported a magnified details of the OHPEP absorption band inside the different host systems and in 2-Methoxyethanol solution.*

Figure 7.9(left) shows the normalized absorption spectra of the investigated matrices doped with OHPEP. All matrices possess high transparency in the whole visible region, until 800 nm, and hence

are good host materials for dyes. On the right are reported the absorption bands of the push-pull chromophore OHPEP inside the different matrices and of its 2-MetOH solution. It should be evidenced as the inclusion inside all the different matrices does not alter the absorption properties of the OHPEP with respect to the 2-Methoxyethanol solution.

REFERENCES

[1] W. Stober, A. Fink, E. J. Bohn, Colloid Interface Sci., 1968, 26, 62.

[2] R. Singh, S. Chandra, IEEE Transactions on dielectrics and electrical insulation, 2004, 2, 264; J. Perez, P. M. Vilarinho, A. L. Kholkin, Thin solid films, 2004, 449, 20; S.H Hu, X.J. Meng, G.S. Wang, J.L. Sun, D.X. Li, J. of Crystal growth , 2004, 264, 307.

[3] A. Patra, K. Auddy, D. Ganguli, J. Livage, P. K. Biswas, Materials letters, 2004, 58, 1059; P. Nishio, T. Tsuckiya, Solar energy materials and solar cells, 2001, 68, 279; E. Özkan, F. Z. Tepehan, Solar energy materials and solar cells, 2001, 68, 265; M. Deepa, N. Sharma, P. Varshney, S. P. Varma, S. A. Agnihotry, J. Mater. Sci., 2000, 35, 5313.

[4] Z. Q. Yu, C. X. Wang, C. L., X. T. Gu, N. Zhang, J. of crystal growth, 2003, 256, 210.

[5] J. Livage, F. Babonneau, C. Sanchez, Sol-gel optics: processing and applications Ed. L.C. Klein, Kluwer Pub. 1994; H. Schmidt, H. Scholze, A. Kaiser, J. Non-Cryst. Solids, 1984, 63, 1.

[6] M. Kevin, R. Reisfeld, Opt. Mater., 1997, 8, 37; Y. Sorek, M. Zevin, R. Reisfeld, T. Hurvits, S. Ruschin, Chem. Mater., 1997, 9, 670.

[7] Zhan, Z. and Zeng, H.C. J. of Non-Cryst. Solids, 1999, 243, 26; L.L. Hench, J.L. Noqués, Sol-gel optics: processing and applications, Springer, 1994.

[8] G. Engelhardt, W. Altenburg, D. Hoebbel, W. Wieker, Anorg. Allg. Chem., 1977, 428, 43.

[9] C.J. Brinker and G.W. Scherer, Sol-Gel Science: The Physics and Chemistry of Sol-Gel Processing (Academic Press, Inc.: New York, 1990).

[10] K.D. Keefer, in: Silicon Based Polymer Science: A Comprehensive Resource; eds. J.M. Zeigler and F.W.G. Fearon, ACS Adv. in Chem. Ser. No. 224, (Amer. Chem. Soc.: Washington, DC, 1990) pp. 227.

[11] V. A. Rao, S.D. Baghat, Solid State Sciences, 2004, 6, 945.

[12] V. K. Parashar, V. Raman, O. P. Bahl, J. of Non-Cryst. Solids, 1996, 201, 150; R. F. S. Lenza, W. L. Vasconcelos, J. of Non-Cryst. Solids, 2003, 330, 216; Lenza R. et al. J. of Mater. Science, 2004, 39, 1363; Niznansky, D. and Rehspringer J.L. J. of Non-Cryst. Solids, 1995, 180, 191; Rao A. P. and Rao A. V. Materials Letters, 2003, 57, 3741.

[13] C. Sanchez, B. Julian, P. Belleville, M. Popall, J. Mater. Chem., 2005, 15, 3559.

[14] C. Sanchez, P. Gomez-Romero, Functional Hybrid Materials, Wiley VCH, Weinheim, 2004.

[15] H. Schmidt, B. Seiferling, Mater. Res. Soc. Symp. Proc., 1986, 73, 739.

[16] H. Schmidt, J. of Non-Cyst. solids, 1989, 112, 419; H. Schmidt, J. of Non-Cryst. solids., 1985, 73, 681.

[17] C. Sanchez, B. Julián, P. Belleville, M. Popall, J. Mater. Chem., 2005, 15, 3559; G. Schottner, Chem. Mater. 2001, 13, 3422.

[18] H. Schmidt, M. Popall, Sol-Gel Optics I; J. D. Mackenzie, D. R. Ulrich, Proc. SPIE 1328, Washington, 1990, p249.

[19] P. Innocenzi, A. Sassi, G. Brusatin, M. Guglielmi, D. Faretto, R. Bersani, A. Venzo, F. Babonneau, Chemistry of Materials 13, 3635, 2001.

[20] T.W. Graham Solomons, Chimica Organica, 1998.

[21] Hoebbel, D., Nacken, M. and Schmidt, H. J. of Sol-Gel Science and Techn. 2001, 21, 177; Lee, T.H. et al. J. of Sol-Gel Science and Techn. 2002, 27, 23.

[22] Kasemann R, Bruck S, Schmidt H. Proc. of SPIE 1994, 2288, 321.

[23] G. Brusatin, G. Della Giustina, M. Guglielmi, P. Innocenzi, Progr. in Solid State Chem., 2006, 34, 223.

[24] J.D. Mackenzie, E.P. Bescher, J. of Sol-gel Sci.Techn., 1998, 13, 371; G. Schottner, J. Kron, A. Deichmann, J. of Sol-gel Sci.Techn., 1998, 13, 183; C.Sanchez, G.J.De A.A.Soler-Illia, F.Ribot, D.Grosso, Comptes Rendus Chimie 2003, 6, 1131.

[25] K. H. Haas, S. Amberg-Schwab, K. Rose, G. Schottner, Surf. Coat. Techn., 1999, 111, 72, K. H. Haas, K. Rose, Rev. Adv. Mater. Sci., 2003, 5, 47; G. Schottner, Chem. Mater.,2001, 13, 3422.

[26] S. Amberg-Schwab, H. Katschorek, U. Weber, A. Burger, J. Sol-Gel Sci. Technol., 2003, 26, 699.

[27] H. Wolter, W. Storch, C. Gellermann, Mater. Res. Soc. Symp. Proc. 1996, 435, 67.

[28] R. Houbertz, G. Domann, J. Schulz, B. Olsowski, L. Fröhlich, W. S. Kim, Appl. Phys. Lett., 3004, 84, 1105; J. Serbin, A. Egbert, O. Ostendorf, B. N. Chichkov, R. Houbertz, G. Domann, J. Schulz, C. Cronauer, L. Fröhlich, Opt. Lett., 2003, 28, 301.

[29] A. Bräuer, P. Dannberg, G. Mann, M. Popall, MRS Bull., 2001, 26, 519

[30] J. Kruger, R. Plass, M. Grätzel, Appl. Phys. Lett., 2002, 81, 367; W. U. Huynh, J. J. Dittmer, A. P. Alivisatos, Science, 2002, 295, 242.

[31] C. Sanchez, B. Lebeau, MRS Bull., 2001, 377.

[32] P. Innocenzi, G. Brusatin, J. of. Sol-gel Sci. Technol., 2003, 26, 967; D.L. Ou, A.B. Seddon, J. of. Sol-gel Sci. Technol. 1997, 8, 139; A. Jitianu, M. Gartner, M. Zaharescu, D. Cristea, E. Manea, Mater. Science and Engin. C 2003, 23, 301.

[33] B. Alonso, D. Massiot, F. Babonneau, G. Brusatin, G. Della Giustina, T. Kidchob, P. Innocenzi, Chem. Mater., 2005, 17, 3172; G. Brusatin, G. Della Giustina, M. Guglielmi, M. Casalboni, P. Prosposito, S. Schultzmann, G. Roma, Mater. Sci. Engin. C, 2007, 27, 1022; G. Della Giustina, M. Guglielmi, G. Brusatin, F. Romanato, 2007, 27, 1382.

[34] A. Abbotto, R. Bozio, G. Brusatin, A. Facchetti, M. Guglielmi, P. Innocenzi, M. Meneghetti, G. A. Pagani, R. Signorini, SPIE 1999, 3803, 18.

[35] G. Brusatin, M. Guglielmi, P. Innocenzi, F. Babonneau, J. Sol-Gel Sci. Technol., 2003, 26, 303.

[36] G. Brusatin, P. Innocenzi, A. Abbotto, L. Beverina, G. A. Pagani, M. Casalboni, F. Sarcinelli, R. Pizzoferrato, J. Europ. Ceram. Soc., 2005, 24, 1853.

[37] P. Innocenzi, G. Brusatin, G. Della Giustina, F. Babonneau, B. Alonso, D. Massiot, Chem. Mater., 2005, 17 3172.

CHAPTER 10

Up-converted emission

In recent years, a considerable amount of effort has been devoted to frequency up conversion laser materials and devices which produce a shorter wavelength (in the visible or UV range) lasing output when pumped at longer wavelength (IR). Two major approaches can be used to reach this goal. One is based on sequential stepwise multi-photon in rare-earth doped materials;[1] the other is based on direct two-photon absorption induced population inversion in dye solutions[2] and dye doped-solid matrices.[3] The development of dye-doped thin films or channel waveguide lasers looks more promising because of the benefits of low cost, high compactness and compatibility with other micro-optic elements or integrated optical circuits.

In this chapter we show the up-converted lasing properties in dimethyl sulfoxide solution of the push-pull chromophores, OHPEP, already described in chapter 8. Some attempts at embedding this organic dye in sol-gel materials have been made and the lasing properties have been tested.

Further, we will show the results of amplified spontaneous emission of the semiconductor quantum dots embedded in a zirconia matrix. Our experiments reveal the lasing properties after one-photon (at 400 nm) and two-photon pumping (at 800 nm).[4] The two-photon optical pumping of semiconductor nanoparticles is the first case reported in literature.

10.1 Optical characterization of the chromophore in solution

We have characterized the OHPEP absorption and emission properties in DMSO solution at a concentration of 10^{-2} M. The results are reported in figure 10.1. The amplified spontaneous emission peak (green line) has been obtained using the optical set up described in section 7.4.

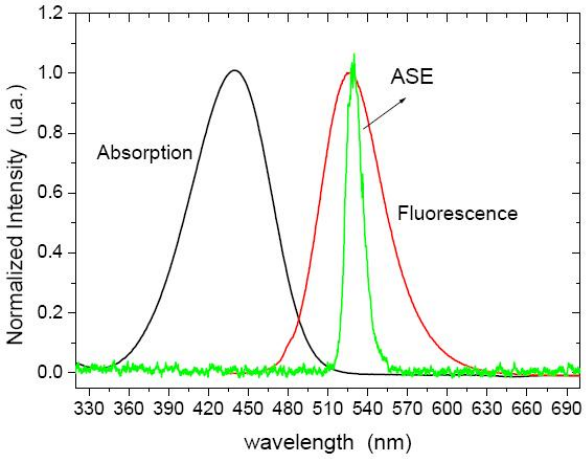

Figure 10.1 *Normalized absorption (black line), one photon induced fluorescence (red line), and two photon pumping ASE (green line) spectra of the OHPEP solution 10^{-2} M in DMSO.*

Comparing the ASE signal with the emission spectrum (red line) measured with a spectrofluorimeter two main features can be observed: a red-shift and a narrowing of the ASE signal with respect to the one-photon induced fluorescence.

The first aspect can be explained by the reabsorption effect in a high concentration and thick solution sample: only the wavelengths beyond the red-edge of the absorption band can be amplified. The second feature is due to combination of the reabsorption and the gain effects: the blue part of the emission spectrum cannot reach lasing due to reabsorption losses and the gain of the red-tail part of the fluorescence band does not reach the threshold for amplification.

10.2 Optical characterization of the OHPEP-GTZ bulk sample

The emission properties of the chromophore homogeneously dispersed within a GTZ sol gel matrix have been characterized using the set-up described in section 7.5. By placing the bulk sample into an optical cavity it is possible to observe two-photon pumped lasing emission. Unfortunately the extremely poor photostability of the chromophore at the high energies, required to reach the population inversion, does not allow to characterize the emitted signal.

10.3 Optical characterization in thin film configuration

The ASE properties of the molecules embedded in sol-gel matrices, in the thin film configuration, has been tested to value their potential as materials for solid state integrated devices

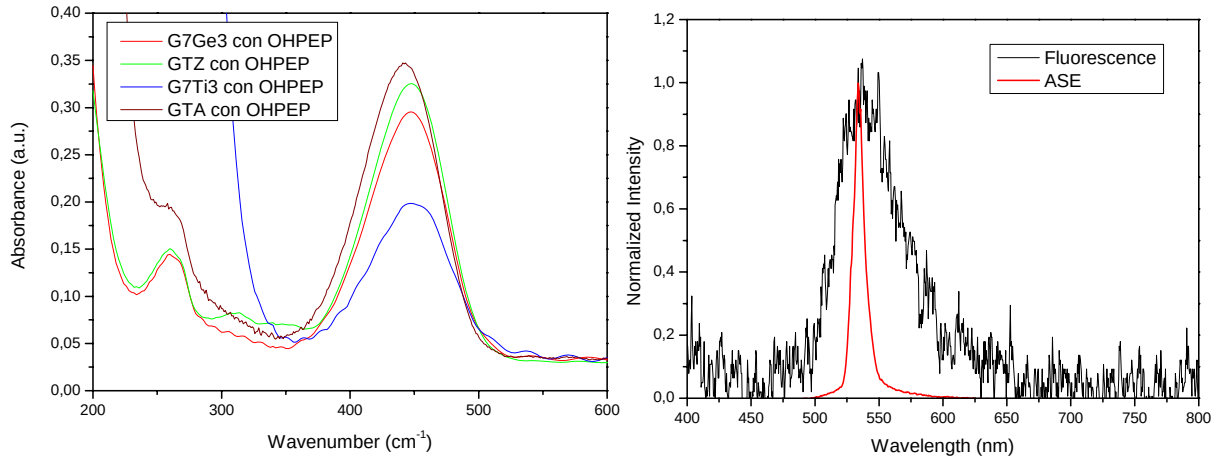

Figure 10.2 *(left) UV-Visible absorption spectra of sol-gel matrices doped with the OHPER chromophore. (right) two photon induced fluorescence (black) and ASE (red) for optical pumping at 800 nm.*

The investigated matrices are described in chapter 9, and the chromophore concentration is always about 10^{-2} M. Figure 10.2(left) reports the linear absorption spectra of the OHPEP in four different matrices. The spontaneous and ASE emission has also been measured using the optical set-up reported in section 7.6. The result for a GTA film is reported in figure 10.2(right). Unfortunately the organic fluorophores are extremely unstable upon laser irradiation. Because of the relatively small thickness of the film, the ASE threshold energy is high and the photobleaching of the dye occurs after few second of exposition. This fact make impossible to measure the ASE threshold and the gain, and doubt the possibility to employ such chromophore for frequency up-conversion solid state devices. For that reason, we have exploited the possibility to employ inorganic emitters instead of organic chromaphores for such applications. Inorganic emitters are supposed to be superior to conventional dyes as they naturally possess larger σ_2 values resulting in significantly higher PL stability factors.

10.4 ASE emission in ZrO_2-QDs composite sol gel films

Using the same set-up, the emission properties of our ZrO_2-QDs composite sol gel films have been characterized. Figure 10.4 shows the ASE signals generated under two-photon optical excitation at 800 nm at room-temperature. An overlay of the spontaneous PL signals at low power in the composites is also included. A similar figure can be reported for one-photon excitation. Notably, the ASE peak always appears on the red-side of the PL maximum with a

calculated energy difference of ~ - 25–35 meV. This is indicative of a biexciton state, where a negative interaction energy (Δ_{bx}) causes a red-shift of the biexciton resonance to a lower-energy from that of single electron-hole pair.[5]

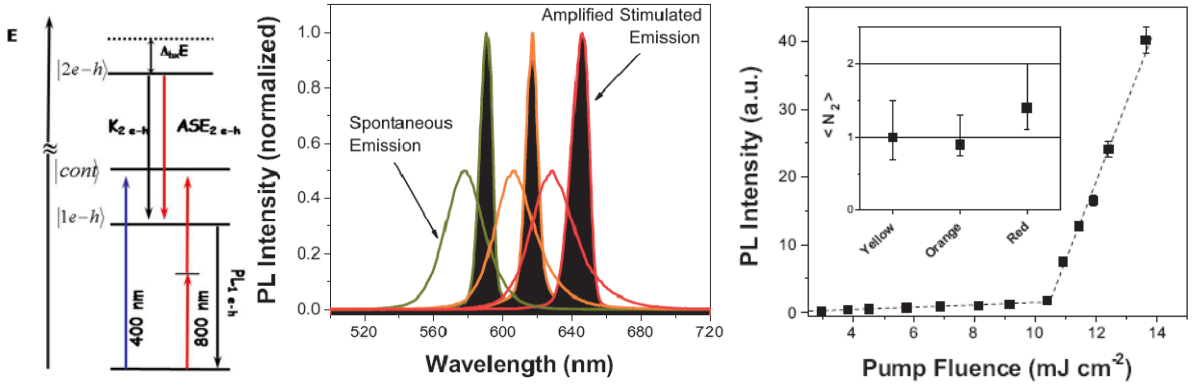

Figure 10.3 *(left) Amplified stimulated emission spectra obtained from a 1-D amplifier setup for different sized CdSe-CdS-ZnS nanocrystal inclusions at an 800 nm pump wavelength. The steady state photoluminescence obtained from the films are also shown for each corresponding sample. (right) Variable fluency measurement showing the threshold of a typical orange emitting composite of ~ 10.4 mJ/cm^2. Inset shows a comparative view of the average number of electron-hole pairs needed to achieve amplification for the different colored samples. The error bars represent the spread in values obtained experimentally as well as slight errors in the measured spot-size area.*

The exciton-exciton interaction, which physical origin is described in chapter 8, causes the energy difference between the photoluminescence, originating from the single exciton decaying, and the amplified spontaneous emission, originating from the biexcitonic state.

For moderately well passivated dots, nonradiative Auger relaxation of doubly excited particles, dominates over surface trapping and imposes an intrinsic limit on the lifetimes of the optical gain. When QDs are pumped into high-energy excited states, population inversion and the buildup of optical gain are only possible if the relaxation down to the ground state is faster than the Auger process time.

The ASE threshold energies are determined both for one- and two-photon pumping mechanism, by recording the emission spectra at varying incident energies. The threshold data, upon 400 and 800 nm irradiation, are reported in Tables 10.1 and 10.2.

Sample	Radius (nm)	Solution PL_{MAX} (nm)	Threshold f_1 (mJ/cm^2)	σ_1 (cm^2)	$<N_1>$	g(cm^{-1})
Yellow	**2.6**	**573**	**0.55**	**9.4E-16**	**1.0**	**100**
Orange	**2.9**	**604**	**0.38**	**2.0E-15**	**1.5**	**151**
Red	**3.2**	**625**	**0.15**	**5.4E-15**	**1.6**	**88**

Table 1 *Parameters describing the CdSe-CdS-ZnS QDs and obtained data for one-photon excitation at 400 nm.*

The single photon optical pumping mechanism makes use of the high one photon absorption cross-sections (σ_{CdSe}) of semiconductor nanocrystals, with $\sigma_{CdSe,1\ photon}\sim10^{-15}$ cm^2.

Sample	Threshold f_2 (mJ/cm^2)	σ_2 (GM)	<N_2>	g(cm^{-1})
Yellow	**19.8**	**2450**	**1.0**	**106**
Orange	**10.8**	**7400**	**0.9**	**116**
Red	**7.0**	**26000**	**1.4**	**144**

Table 2 *Obtained data for two-photon excitation at 800 nm.*

Neglecting saturation at the pump energy and assuming a temporal pulse pump width less than the recombination time, the average number of electron-hole pairs, $\langle N_1\rangle$, generated by a single laser pulse is calculated for a given pump fluence, f(photons/cm^2), simply as $\langle N_1\rangle = f\sigma_1$. A high absorption cross-section is therefore advantageous for low threshold lasing. The value of σ_{CdSe} is proportional to the volume of the nanocrystal.

For two-photon excitation the average number of e-h pairs created for every photon pair is given as $\langle N_2\rangle = f_2^2\,\sigma_2/\tau_p$, where σ_2 is the two-photon absorption cross-section and τ_p is the pulse duration. It differs from $\langle N_1\rangle$ as it is dependent on the square of the incoming fluence and the temporal pulse width. A high local fluence and short pulses are therefore particularly advantageous for exciton generation with this pumping mechanism.

Under degenerate two-photon optical excitation above the exciton resonance at 800 nm (1.55 eV), two photons are simultaneously absorbed whereas normally the excitation would be from a single photon of double the energy (400 nm = 3.1 eV).

Regarding the threshold data reported in Tables 10.1 and 10.2, we can observe that the threshold fluence values in the 2-photon regime at 800 nm are in general ~20–30 times larger than that measured for 1-photon regime. Using the threshold fluence data it is possible to calculate the average number of electron-hole pairs for both pumping mechanisms ($\langle N_1\rangle$ and $\langle N_2\rangle$). The gain threshold for CdSe QDs is estimated to be close to one e-h pair per dot on average ($\langle N\rangle\sim1.4$), consistent with a population-inversion mechanism in a simple two-level system. This value is well approached in both regimes. Such results highlight that the generation of optical gain states in these systems is very important.

In Figure 10.4 is reported the temporal stability of the ASE emission of the red-QDs under one- and two-photon excitation. Extremely high stability is observed with excitation at 400 nm with no appreciable loss in ASE observed after 1 h of illumination (that corresponds to 3.6*10^6 pulses at 1 KHz repetition rate). For excitation at 800 nm we observe a comparably high

stability factor with up to 70% of the original ASE intensity retained following a similar time period.

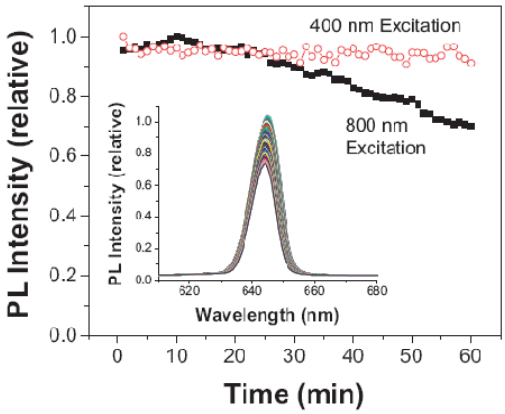

Figure 10.4 *A comparison of the temporal stability of the red composite with optical excitation in the 1-photon (400 nm, 'o') and 2-photon (800 nm, '■') regimes. The repetition rate of the laser was 1 kHz corresponding to ~3.6 x 10^6 pulses over the course of the experiment. Included in the inset is an overlay of the ASE spectra obtained during the stability measurement at 800 nm excitation.*

To our knowledge this is the largest stability ever measured: it is high especially compared with that of organic dyes. Such stability factors demonstrate the true viability of quantum dots as two-photon absorbers, particularly under high fluencies. We have noted that laser induced sample damage was observed during illumination at fluencies above ~60 mJ/cm^2 (400 GW/cm^2).

In order to determine if graded-seal nanocrystals are suitable for optical gain media, variable stripe measurements (VSL) have been performed at room temperature. The effective modal gain was extracted by numerically fitting experimental data to an Auger limited 1-D amplifier model similar to the analytic model proposed by Chan et al[6]:

$$\frac{dI_{bx}(z)}{dz} = g(z)exp\left(-\frac{z-z_0}{l_a}\right)I_{bz}(z), \text{ where } \begin{cases} z < z_0, g(z) = 0 \text{ and } I_{bx}(z) = 0 \\ z \geq z_0, g(z) = g \end{cases} \quad \text{Eq. 1}$$

$$\frac{dI_{sx}(z)}{dz} = J_{sp} \quad \text{Eq. 2}$$

$$I(z) = I_{bx}(z) + I_{sx}(z) \quad \text{Eq. 3}$$

Here I_{bx} and I_{sx} are the bi- and single- exciton emission intensities, respectively, J_{sp} is the spontaneous emission factor accounting for the magnitude of incoherent spontaneous emission, z_0 is an offset fitting parameter allowing for pump beam in homogeneity at the sample edge and consequently the ASE onset, and l_a is defined as the biexciton lifetime multiplied by the speed of light. This simple model only applies if z_0 is small because waveguide losses and re-absorption in that case are minimized. In Figure 10.5 we show a typical VSL measurement which in this case features a red composite optically pumped at 800 nm. This

data is fitted to the Auger limited model to give an overall modal g ~144 cm^{-1}. For comparison, the commonly applied classical one dimensional amplifier model is also included with the lower g ~82 cm^{-1}. In both cases because the spontaneous emission is known to arise from a different state to the ASE, both of them are therefore accounted independently. Clearly for systems where the gain decay occurs nonradiatively through Auger recombination as opposed to depletion through stimulated emission, the Auger limited model is the more suitable. The extracted gain coefficients, for one and two-photon pumping, have been extracted for all the investigated sample, and their values, ranging between ~100–160 cm^{-1}, are reported in Table 10.1 and 10.2. These depend strongly on the sample studied, the volume fraction of quantum dot inclusion and the observed losses in the waveguides.

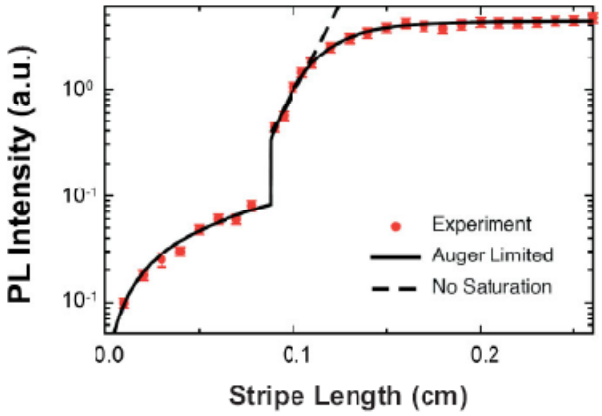

Figure 10.5 *A typical stripe measurement performed on a red quantum dot composite film. The experimental data (■) is fitted both with an Auger limited 1-D amplifier model (—) and with a classical 1-D amplifier model with no saturation (- -).*

10.5 Conclusion

In this chapter we have analyzed the ASE properties of organic compounds and semiconductor core-shell quantum dots, to check their potentiality as active materials for solid state up-converted lasers. In the first case it is possible to detect the ASE emission of the dyes in solution pumped by two-photon excitation. Unfortunately, when inserted in a solid state matrix, these materials manifest a drastically poor photo-stability under intense laser radiation. Despite the intense effort toward the synthesis of different sol-gel matrices, engineered to promote good chromophores dispersion and to prevent the emission quenching, we never succeeded to measure stable amplified emission from these systems. On the contrary, semiconductors core-shell QDs, dispersed in a zirconia matrix, show excellent ASE properties, together with an extraordinary stability in time, under one- and two-photon excitation.

Based on these results, one can envisage that there is a real possibility to develop infra-red optically pumped micron-sized laser, through the use of low two-photon lasing threshold QDs materials.

REFERENCES

[1] X. B. Chen, M. X. Li, K. Li, Y. Feng, S. Z. Bi, G. Y. Zhang, Y. G. Sun, Opt. Comm., 1999, 160, 364; X. Qin, T. Yokomori, Y. Ju, Appl. Phys. Lett., 2007, 90, 073104.

[2] G. S. He, L. Yuan, P. N. Prasad, A. Abbotto, A. Facchetti, G. A. Pagani, Opt. Comm., 1997, 140, 49 ; X. Wang, D. Wang, W. Jiang, M. Jiang, Opt. Mater., 2002, 20, 217 ; Y.-fang Zhou, S.-yu Feng, X.-mei Wang, J. of Molec. Struct., 2002, 613, 91; A. Abbotto, L. Beverina, R. Bozio, S. Bradamante, G. A. Pagani, R. Signorini, Synth. Metals, 2001, 121, 1755.

[3] G. S. He, C. F. Zhao, C.-K. Park, P. N. Prasad, R. Burzynski, Opt. Comm., 1994, 111, 82; K. Shirota, H.-Bo Sun, S. Kawata, Appl. Phys. Lett., 2004, 84, 1632.

[4] Jasieniak, J.J., Fortunati, I., Gardin, S., Signorini, R., Bozio, R., Martucci, A. and Mulvaney, P. Adv. Mater. 2008, 20, 69.

[5] V. Klimov, S. Hunsche, H. Kurz, Phys. Rev. B 1994, 50, 8110; V. I. Klimov, S. A. Ivanov, J. Nanda, M. Achermann, I. Bezel, J. A. McGuire, A. Piryatinski, Nature, 2007, 447, 441.

[6] Y. Chan, J. S. Steckel, P. T. Snee, J.-M. Caruge, J. M. Hodgkiss, D. G. Nocera, M. G. Bawendi, Appl. Phys. Lett., 2005, 86, 073102.

CHAPTER 11

DFB lasers

In the previous chapter we have demonstrated population inversion and amplified spontaneous emission in Zirconia films doped with core-shell CdSe Qds, where the term spontaneous means that the chain reaction in the gain material is caused by a photon created by a spontaneous decay.

ASE is enhanced by feedback as the emitted photons are sent through the medium multiple times, stimulating more photons, before being emitted out from the lasers. The number of the round trip is proportional to the quality factor of the laser. Several laser geometries have been studied, first of all, the microcavity laser, in which the gain medium is placed inside a Fabry-Perot resonator.[1] The resonator cavity determines the wavelength of emission and is set to be within the emission spectra of the gain medium. Resonance is only achieved for modes that satisfy the resonance condition of the cavity, leading to a spectral narrowing of the output[2] and allowing control over the emission.[3]

One example of such microcavity laser is the Distributed Bragg Reflector (DBR), which has the gain materials surrounded by alternating layers of high and low refractive index, acting as broadband mirrors.[4]

A different resonator structure is that of spherical or ring microlasers. Emission is coupled to resonant modes of the structure due to its small size and these “whispering gallery” modes are confined around the circumference of the cavity. Single mode lasing have been achieved by varying the diameter of the ring and laser threshold as low as 100 pJ have been reported.[5]

These kinds of lasers have been realized using either organic or inorganic gain media, their main advantages are the easy fabrication and low threshold. Their main drawback is the bad quality of the output emission.

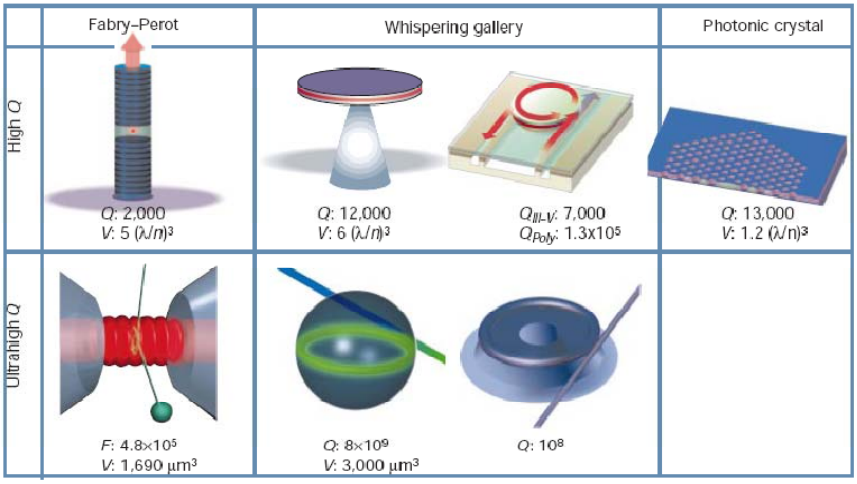

Figure 11.1 *The microcavities are organized according to the confinement method used and by row according to high Q and ultrahigh Q. Representative, measured Qs and Vs are given. n is the material refractive index, and, V, if not indicated, was not available. Microsphere volume V was inferred using the diameter noted in the cited reference and finesse (F) is given for the ultrahigh-Q Fabry–Perot as opposed to Q. Two Q values are cited for the add/drop filter: one for a polymer design, Q_{Poly}, and the second for an III–V semiconductor.*

Another promising resonator architecture is the distributed feedback (DFB) structures.[6] They are gratings, i.e. periodic structures, which are resonant for light waves of a certain wavelength range. An exciting class of periodic optical structures emerged almost twenty years ago.[7] These structures, the photonic crystals, feature a periodicity in two or even three dimensions. If the refractive index contrast of the resulting two or three dimensional periodic structures is high enough, a full band gap makes it possible to fully confine light on a very small scale. Photonic crystals, whose index contrast is lower, can be used as DFB structures, that can be either one or two dimensional.

In a distributed feedback laser, the laser modes receive feedback at one specific wavelength determined by the gratings period of the structure. While the mode is propagating along the structure a small part of its energy is reflected, i.e., coupled into counter-propagating mode. The coupling strength, parameterized by the coupling constant, is influenced by the grating geometry and the refractive index contrast between the substrate and the waveguiding material. The feedback is proportional to the coupling constant multiplied by the coupling length. The coupling strength thus determines the dimension of the corrugated area necessary to achieve the feedback required for lasing: a small value of the coupling constant has to be compensated by larger coupling length.

11.1 1D and 2D DFB devices

The more conventional structure used in most DFB laser is the first order grating providing feedback in the plane, represented in figure 11.2(a). A first order grating has a period that satisfies the first Bragg condition $m\lambda = 2n_{eff}a$, where m is the Bragg order, λ is the wavelength of the light, n_{eff} the effective refractive index and a the period of the structure. In this case the Bragg order is $m = 1$. Its geometry thus corresponds to that of a Bragg reflector grating. This results in laser modes emitting in two directions along the axis of the periodicity.

Figure 11.2(b) shows the second order linear grating. The second Bragg order of the grating provides feedback in the plane, while the first Bragg order is scattered out perpendicularly to the axis of periodicity. This results in vertically emitted laser light.

Figure 11.2(c) represents a first order 2D-grating. This grating can be seen as the superposition of two linear gratings, positioned perpendicular to each other. This results in a rectangular lattice of hole. The laser emits in the four directions of the two orthogonal DFB laser structures.

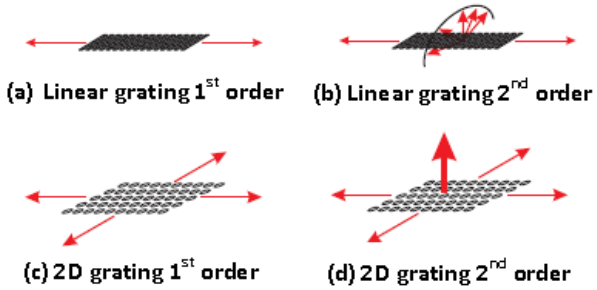

Figure 11.2 *Emission pattern of different DFB structures. The gratings are displayed in black, the laser emission by red arrows.*

The laser pictured in figure 11.2(d) is the second order version of 2(c). The laser features the same emission pattern as the first order laser and, in addition, emission perpendicular to the plane of the photonic crystal. The vertically emitted light from the two superimposed linear gratings interferes constructively perpendicular to the plane defined by the two gratings directions. For large area gratings this results in highly directional radiation out of the grating plane.[8]

Also other gratings geometries are feasible, such as circular[9] or triangular[10] geometries each one having its strengths and weaknesses.

In this thesis second order gratings are considered.

11.2 DFB waveguide laser

To study wave-guided distributed feedback lasers, the combined effect of asymmetric waveguides and Bragg-diffraction gratings has to be considered.[11]

- *Asymmetric waveguide descriptions*

We start considering an asymmetric waveguide structure constituted of the guiding film with refractive index n_f, on a substrate having refractive index $n_s < n_f$, and covered by air ($n_c = 1$). An electromagnetic wave, of vacuum wavelength λ_0 and wavevector $k_0 = 2\pi/\lambda_0 = \omega/c$ propagates inside the film with wavelength:

$$\boldsymbol{\lambda_m = \frac{2\pi}{\beta} = \frac{1}{N}\frac{2\pi}{k_0} = \frac{\lambda_0}{N}} \qquad \text{Eq. 11.1}$$

and wavevector:

$$\boldsymbol{k = n_f k_0} \qquad \text{Eq. 11.2}$$

where $\beta = k\sin\theta$ and $N = n_f \sin\theta$ are respectively the propagation constant and the effective refractive index, and θ is the propagation angle of the wave in the guiding layer.

The allowed propagation angles, θ_k, for TE modes ($\theta_{TE,k}$) and TM modes ($\theta_{TM,k}$) in the waveguide are determined by the resonance condition[12]

$$\boldsymbol{2k_0 n_f d\cos(\theta_\kappa) = 2k_0 dN\cot(\theta_\kappa) = 2\pi\kappa + 2\phi_S + 2\phi_C} \qquad \text{Eq. 11.3}$$

where κ is an integer and ϕ_i with (*i*=*S,C*) are the phase changes of the mode at the interface between *f* and *i*, defied as:

$$\boldsymbol{\phi_{TE,i} = \tan^{-1}\left\{\frac{\left[n_f^2\sin^2\theta - n_i^2\right]^{1/2}}{n_f\cos\theta}\right\}} \qquad \text{Eq. 11.4}$$

and

$$\boldsymbol{\phi_{TM,i} = \frac{n_f^2}{n_i^2}\phi_{TE,i}} \qquad \text{Eq. 11.5}$$

This equation allows to obtain for each propagating mode, i.e. for each κ value, the corresponding propagation angle, and thus the corresponding effective index and propagation constant.

The minimum film thickness d_{min} required so that at least the TE_0 mode propagates along the waveguide under total internal reflection conditions $\theta < \theta_{crit} = \sin^{-1}(n_s/n_f)$ is:

$$\boldsymbol{d_{min,i} = \frac{\lambda_0}{2\pi\left(n_f^2 - n_s^2\right)^{1/2}}\tan^{-1}\left(a_i^{1/2}\right)} \qquad \text{Eq. 11.6}$$

with

$$\boldsymbol{a_{TE}} = \frac{\boldsymbol{n_s^2 - n_c^2}}{\boldsymbol{n_f^2 - n_s^2}} \qquad \text{Eq. 11.7}$$

and

$$\boldsymbol{a_{TM}} = \frac{\boldsymbol{n_f^4}}{\boldsymbol{n_c^4}} \cdot \frac{\boldsymbol{n_s^2 - n_c^2}}{\boldsymbol{n_f^2 - n_s^2}} \qquad \text{Eq. 11.8}$$

- *Waveguided Bragg Grating description*

When the waveguide is periodic, with period Λ, an entering incident plane wave, incident with angle ϕ, will experience the same degree of refractive index change at every periodic interval of Λ, so that it will be reflected in the same direction. For a waveguide consisting of *N* periodic corrugations, there will be *N* reflected wavelets. In order that any two reflected wavelets add up in phase and interfere constructively, the phase difference between the reflected wavelets must be a multiple of 2π. In other words the phase matching or Bragg conditions are:[13]

$$\boldsymbol{\beta} = \frac{\boldsymbol{2\pi}}{\boldsymbol{\lambda_{m,Br}}} = \frac{\boldsymbol{2\pi N}}{\boldsymbol{\lambda_{0,Br}}} = \boldsymbol{p}\frac{\boldsymbol{\pi}}{\boldsymbol{\Lambda}} \qquad \text{Eq. 11.9}$$

where p is an integer and is called the grating order. An integer number, p, of effective wavelengths, $\lambda_{m,Br}$, fits within the distance 2Λ.

The conditions for constructive interference read:

$$\boldsymbol{\Lambda\beta_i - \Lambda\beta_d = 2\pi M} \qquad \text{Eq. 11.10}$$

with $M = 0,1, \ldots, p$, Bragg diffraction order, β_i and β_d propagation constant of the incident and diffracted waves respectively.

For a first-order grating, $p = 1$, $\beta = \pi/\Lambda$, the diffraction order $M = 0$ gives $\beta_d = \beta_i$ (forward emission, $\theta_d = \theta_i$). The diffraction order $M = 1$ gives $\beta_d = -\beta_i$ (backward emission, $\theta_d = -\theta_i$).

For a second-order grating, $p = 2$, $\beta = 2\pi/\Lambda$, the diffraction order $M = 0$ gives $\beta_d = \beta_i$ (forward emission, $\theta_d = \theta_i$). $M = 1$ gives $\beta_d = 0$ (vertical emission, $\theta_d = 0$), and $M = 2$ gives $\beta_d = -\beta_i$ (backward emission, $\theta_d = -\theta_i$).

Both first- and second order gratings have their advantages and weak points. First order gratings provide strong feedback and consequently permit low threshold operation, but are intrinsically edge emitters, with a lot of problems deriving from edge cleaving. Moreover first-order gratings have to be placed near the substrate edges, where the quality of the active films is usually low. In contrast, second-order DFB lasers are easier to fabricate, compared with the first-order one, having the same Bragg wavelength. It can produce high quality and low

divergence beams perpendicular to the waveguide plane, but with the penalty of increased oscillation thresholds due to the increased radiation losses.

C. Karnutschc at al.[14] and Baumann et al.[15], have recently proposed a new approach that allows combining the strength of 1st and 2nd order gratings.

The 2nd order region, providing laser emission perpendicular to the grating plane, is enclosed inside a 1st order region. In this configuration, the surrounding 1st-order region, with grating period $\Lambda_1 = \Lambda_2/2$ provide strong feedback and hence constitute an efficient cavity for the laser process. The width of the 2nd order region results from a compromise between the will to have a good quality edge emitted beams, and the will to have a lasing threshold as low as possible.

Both first- and second order grating can be mono- or bi-dimensional, as schematically depicted in figure 2(a)-(d). The first-order linear grating couples modes satisfying the Bragg condition and propagating along the periodicity axis.

The 2D diffraction induces the coupling of light waves propagating in four directions, resulting in the formation of a 2D standing wave in the grating plane. The corresponding lasing threshold has been demonstrated to be about 20 times lower for 2D-gratings with respect to the linear ones. They show an output slope efficiency of 7.8% instead of 2.2%.[16] The emission pattern from a 1D second-order grating is fan shaped, as expected for a one-dimensional resonator providing confinement only in one direction.[17] The emission perpendicular to the gratings axis is highly confined, the one parallel has high divergence. In contrast, the emission from 2D laser is circular in profile as a result of the 2D confinement provided by the resonator. The mode is symmetric about the two grating axis and the beam is highly directional with very low divergence. Thus, coherent 2D large-area surface-emission with stable longitudinal and lateral modes can be achieved.[18]

11.3 Coupled wave equation in DFB laser

To understand the operational principles of a DFB laser, it is necessary to consider guided wave propagation in a structure with periodic modulation, represented in figure 3. The grating induced dielectric perturbation leads to a coupling between the forward and backward waves associated with a particular laser mode.[19] The coupled-wave approach has been adopted to describe the behavior of DFB structures.[20] This relatively simple approach presents the advantage of being relatively simple and numerically solvable.

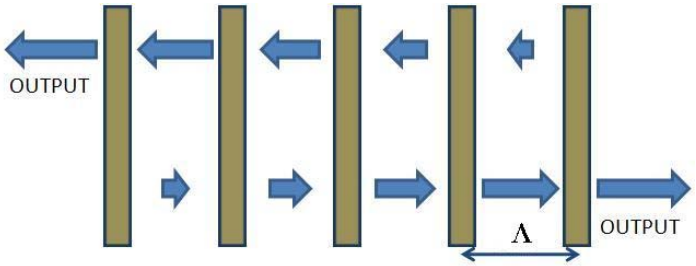

Figure 11.3 *Illustration schematically illustrating laser oscillation in a periodic structure.*

The starting point of the analysis is the time-independent wave equation for a transversally and laterally confined structure:

$$\frac{d^2E}{dz^2} + k^2(z)E = 0 \qquad \text{Eq. 11.11}$$

where, assuming the radiation frequency sufficiently close to the resonance ones,

$$k^2 = k_0^2 n^2(z)\left(1 + i\frac{2\alpha(z)}{k_0 n(z)}\right) \qquad \text{Eq. 11.12}$$

with

$$n(z) = n_0 + \Delta n \cos(2\beta_0 z) \qquad \text{Eq. 11.13}$$

and

$$\alpha(z) = \alpha_0 + \Delta\alpha \cos(2\beta_0 z) \qquad \text{Eq. 11.14}$$

Here n_0 and α_0 are the average value of the medium parameters, $\Delta n \ll n_0$ and $\Delta\alpha \ll \alpha_0$ give the amplitude of the modulation, k and k_0 are the wave propagation constants in the medium and in free space respectively, and $\beta_0 = n_0\omega_B/c = p\,\pi/\Lambda$ is the Bragg propagation constant.

The k constant can be written as:

$$k \approx \beta^2 + 2i\beta\alpha_0 + 4\kappa\beta \cos 2\beta_0 \qquad \text{Eq. 11.15}$$

where

$$\kappa = \frac{\pi\Delta n}{\lambda} + i\frac{\Delta\alpha}{2} \qquad \text{Eq. 11.16}$$

is the coupling coefficient measuring the strength of the backward Bragg scattering and thus the amount of feedback provided by the structure.

A trial solution of (11.11) in the DFB structure could be a linear superposition of two counter propagating waves that grow because of gain and feed energy into each other due to Bragg scattering:

$$E(z) = R(z)e^{-i\beta_0 z} + S(z)e^{i\beta_0 z} \qquad \text{Eq. 11.17}$$

where $R(z)$ and $S(z)$ are complex amplitude terms.

Substituting (11.17) in (11.11), the coupled wave equation can be written as:

$$-\frac{dR}{dz} + (\alpha_0 - i\delta)R = i\kappa S \qquad \text{Eq. 11.18}$$

$$\frac{dS}{dz} + (\alpha_0 - i\delta)S = i\kappa R \qquad \text{Eq. 11.19}$$

Where $\delta = \beta - \beta_0$ is the measure of the departure of the oscillation frequency ω from the Bragg frequency ω_0. At the Bragg condition, $\delta = 0$.

The coupled wave equations (11.18-11.19) describe wave propagation inside the DFB structure, in presence of gain and of the periodic perturbation medium. They can be solved with the appropriate boundary conditions for the wave amplitude:

$$R\left(-\frac{1}{2}L\right) = S\left(\frac{1}{2}L\right) = 0 \qquad \text{Eq. 11.20}$$

with L device length.

The corresponding solutions yield self-consistent steady-state field configurations, i.e., the modes of the periodic structure.

For a device of given length L and given coupling κ, solutions are possible only for a discrete set of gain constants α and associated frequencies δ. The latter are the resonant frequencies of the DFB structure and the former the associated gain value needed to exceed threshold.

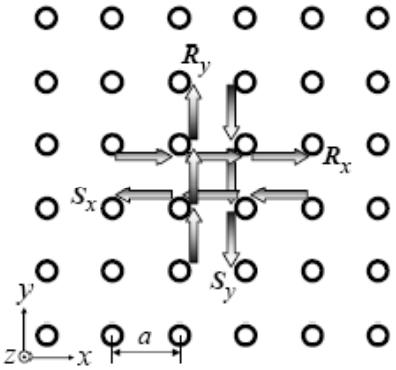

Figure 11.4 *Schematic diagram of the four basic waves in a 2D grating.*

These results can be extended to 2D grating, like that reported in figure 11.4, replacing (11.11) and (11.17) with:[21]

$$\frac{d^2E}{dx^2} + \frac{d^2E}{dy^2} + k^2E = 0 \qquad \text{Eq. 11.21}$$

and

$$E(z) = R_x(x,y)e^{-i\beta_0 x} + S_x(x,y)e^{i\beta_0 x} + R_y(x,y)e^{-i\beta_0 y} + S_y(x,y)e^{i\beta_0 y} \qquad \text{Eq. 11.22}$$

It results in four decoupled equations:

$$-\frac{\partial R_x}{\partial x} + (\alpha_0 - \kappa_0 - i\delta)R_x = (i\kappa_3 - \kappa_0)S_x + i\kappa_2(S_y - R_y) \qquad \text{Eq. 11.23}$$

$$\frac{\partial S_x}{\partial x} + (\alpha_0 - \kappa_0 - i\delta)S_x = (i\kappa_3 - \kappa_0)R_x + i\kappa_2(S_y - R_y) \qquad \text{Eq. 11.24}$$

$$-\frac{\partial R_y}{\partial y} + (\alpha_0 - \kappa_0 - i\delta)R_y = (i\kappa_3 - \kappa_0)S_y + i\kappa_2(S_x - R_x) \qquad \text{Eq. 11.25}$$

$$\frac{\partial S_y}{\partial y} + (\alpha_0 - \kappa_0 - i\delta)S_y = (i\kappa_3 - \kappa_0)R_y + i\kappa_2(S_x - R_x) \qquad \text{Eq. 11.26}$$

Here, the coupling constants κ_2 and κ_3 indicate the coupling in orthogonal and backward direction, respectively, and κ_0 is the surface coupling coefficient, added in order to include surface-emission loss.[22] Unlike the coupled-wave equations in one dimension, the general solutions for (11.23)-(11.26) are not easily found. In order to numerically solve them, it is necessary to use computational tools, as reported below.

11.4 Computational methods

The calculation engine to calculate the band structures is the free program MIT Photonic Bands (MPB), which computes the fully-vectorial eigenmodes of Maxwell's equations with periodic boundary conditions by preconditioned conjugate-gradient minimization of the block Rayleigh quotient in plane wave basis.[23] The details of the software working principles have been briefly illustrated in chapter 3, here the application of the MPB code to 2D and 3D structures calculation is discussed.

11.5 2D Band Structure

The two-dimensional calculations performed using MPB give the eigenmodes of a periodic structure having features in the *xy*-plane. The periodicity can have any vector basis. This means that any periodicity is possible, like for instance the rectangular lattice pictured in figure 11.5. MPB uses periodic boundaries: it considers only the unit cell. The smallest irreducible unit of the photonic crystal, as pictured in figure 11.5, is enough to calculate the behavior of the modes in the crystal. For this unit cell, the frequencies belonging to the modes, whose k-vectors form the boundaries of the irreducible Brillouin zone, are calculated.

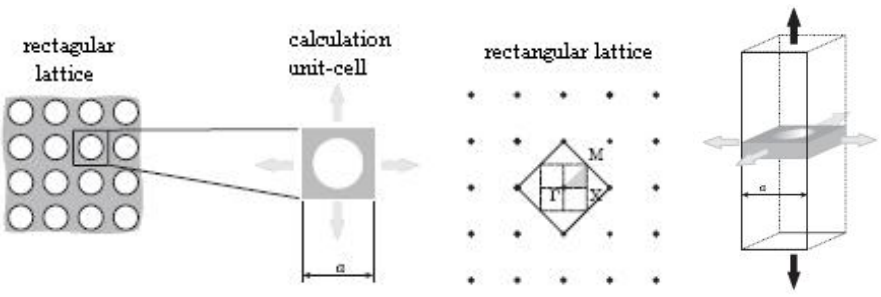

Figure 11.5 *From left to right: 2D view of a rectangular lattice; 2D calculation cell with arrows indicating the direction of periodicity; irreducible Brillouin zone of a rectangular lattice, with the high symmetry points indicated; 3D calculation cell. The grey arrows indicate the direction of periodicity of the grating, the black arrows the vertical periodicity of MPB.*

The main advantage of 2D calculations is the velocity compared to full 3D calculations. Another advantage is given by the fact that the resulting eigenmodes are well resolved as they can only exist fully contained in the structure. However, the limitation to the *xy*-plane means the layer structure in the vertical (*z*-) direction has to be approximated by using an effective dielectric constant for the material of the photonic crystal. This means that 2D calculations are very valuable qualitatively, but not quantitatively.

Calculation parameters for the MPB engine are the number of plane waves to be used, the number of mesh points allowed to smooth abrupt changes in dielectric constant and the tolerance, i.e. the relative change in frequency used as convergence criterion. To judge these parameters the stability of the final solution is considered; if the solution changes significantly when more plane waves, more mesh points or smaller tolerance values are used, then the parameters are still too coarse.

11.6 3D Band Structure

Three dimensional calculations performed using MPB can give accurate eigensolutions of the field in a structure as the full 3D structure is considered. This means that the calculation times are much longer as an additional dimension has to be considered. MPB uses periodic boundaries not only in the lateral directions, as desired, but also in the vertical direction, which is undesired.

The periodicity in the vertical direction results in a superposition of the waveguide layers. The calculation cell, displayed in figure 11.5, therefore has to be large enough in the vertical direction to prevent coupling between the waveguides that are artificially stacked vertically.

Making things worse, the finite dimensions of the calculation cell cause the program to select modes from the vacuum continuum that are eigenmodes of the calculation cell rather than of the structure under investigation. The solution lies in the fact that the vacuum modes have only a small part of their total mode energy in the waveguide.

Thus, monitoring the energy of the mode changing the calculation cell vertical dimension, waveguide gives a criterion that can be used to distinguish between the desired modes and the true vacuum modes and the artifacts.

An additional issue in 3D is the fact that true transverse-electric (TE) and transverse-magnetic (TM) do not exist. The modes can, however, have an even or odd symmetry with respect to the lateral symmetry plane of the 3D structure. If the structure has no lateral symmetry plane, for

instance if the upper cladding is a different material as the substrate, we can only speak of even-like and odd-like modes, meaning that a mode has a predominantly even or odd symmetry.

11.7 Design

The sample we have characterized towards ASE emission is a zirconia sol gel waveguide (n∼1.75, thickness h=250-500 nm) doped with QDs and spin-coated on a quartz substrate (n=1.45). Starting from the active material parameters there are several DFB structures that can be implemented for obtaining the final laser devices. For example, it is possible to realize the pattern below or on the active material. The first approach leads to a lower index contrast (∼0.3 for a quartz/ZrO_2 system) and thus to a lower modes coupling. The latter ones, allows reaching an higher contrast (∼0.75 for ZrO_2/air), but imply a larger distance between the center of the mode, that will be shifted down towards the quartz substrate as it has an higher index than air, and the corrugated layer, resulting in a reduced coupling of the modes. Moreover, in the latter approach, the lithography process must be chosen in order to not alter the active layer guiding and emitting properties.

The DFB laser investigated in this work consists on a bi-dimensional 2^{nd} order gratings realized on the substrate before the light-emitting material deposition. The substrates used for the simulation are both low-index and high-index (with respect to the active layer) materials.

The latter approach has been suggested as a proper way to improve the mode confinement in the waveguide, and to increase the index contrast between the gratings and the active material.[24]

The periodic modulation is realized on a thin, transparent, low losses high refractive index material, deposited on substrate, such as Ta_2O_5 (n∼2.16) or TiO_2 (n∼2.5). The active layer is deposited on top of the high refractive index material. The film thickness must be chosen low enough to ensure the mode to extend in the active materials (i.e. the effective index of the grating slab to be lower than the index of the active layer).

In figure 11.6 are showed the two simulated structures: the left one uses low-index substrate, and the grating consist on a square array of low-index pillars, the right one uses the high-index approach, and the grating is a square pattern of holes.

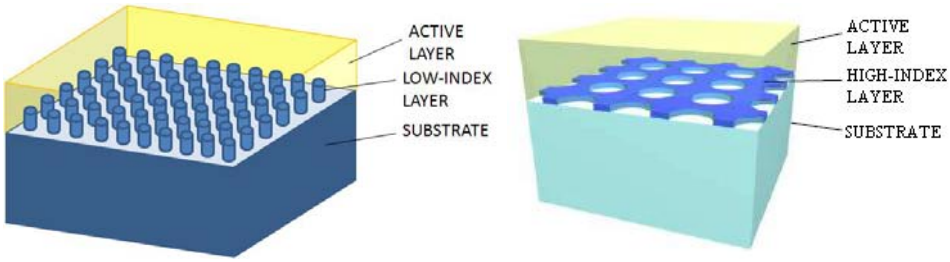

Figure 11.6 *Basic structures of the investigated lasers. (left) The low-index approach: a rectangular array of low index pillars is realized on quartz substrate. (right) High-index grating realized on a thin film (~30 nm).*

Although we will use 3D band diagrams to determine the exact parameters of the laser device, the properties of the grating interesting for lasing applications can be qualitatively illustrated using a 2D photonic band diagram, like that reported in figure 7.

The frequencies are normalized to *c/a*, where *c* is the speed of light and *a* the lattice constant. For a desired emission wavelength λ, the lattice constant can be calculated using the frequency ν of the mode in units of *c*/*a*, by:

$$\boldsymbol{a = \nu\lambda} \qquad \text{Eq. 11.27}$$

The optimum lattice constant *a* is achieved when the wavelength of the laser mode, found using (11.27), coincides with the gain maximum of the organic gain material.

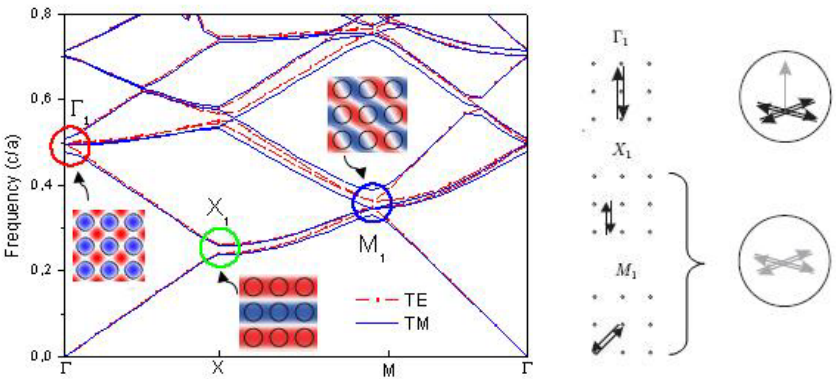

Figure 11.7 *2D-band diagram for the high-index (n=2.16) device represented in figure 6. TE modes are reported in red, TM modes in blue. The mode of interest for vertical emission is indicated with the red circle, while the modes indicated with the green and blue circle show in plane lasing. The Z-components of the magnetic field (for TE modes) are reported inside the band diagrams. The red and blue indicate respectively positive and negative field. On the right is reported the laser feedback in reciprocal space and the emission directions. The Γ_1 mode emit also vertically.*

The band diagram shows the dispersion curves of the modes from which we can identify modes that are candidates for lasing. The lasing modes can be found at the Γ, *X* and *M* points of the irreducible Brillouin zone. Standing waves are formed, exhibiting a flat dispersion curve as their group velocity $v_G = d\omega/dk$ approaches zero.

The feedback mechanisms at different high-symmetry points of the photonic crystal are given in figure 11.7. The laser modes at X_1 and M_1 oscillate in plane whereas the modes at Γ_1 exhibit also vertical emission. The laser modes at the X_1 and M_1 points are first-order DFB modes.

The Γ_1 point (red circle) is particularly interesting, because it corresponds to the point in which the second order grating induces 2D optical coupling and surface emission.

According to (11.27), the grating period has been optimized in such a way to put the normalized frequency corresponding to the Γ_1 point, at 650 nm, where our red-QDs emit.

11.8 Experimental realization

The realization of the DFB structures, by using the parameters obtained from the 3D-MPB simulations, is in progress. First attempt of patterning realization, with e-beam lithography, have been performed in collaboration with Prof. Romanato at the TASC National Laboratory. We decided to utilize a GPTMS/Germanium-tetraethoxide hybrid matrix (n$\sim$1.50) as the patternable substrate. This system has been developed from the group of Prof. Giovanna Brusatin for direct e-beam lithography applications. Thanks to the unreacted epoxide ring in the film, that can polymerize when exposed to e-beam radiation, this system behaves as a negative resist for e-beam lithography.[25]

The hybrid sol (n=1.50) is deposited on quartz substrate (n=1.45) by spin coating. This sample is directly exposed to the e-beam to draw the gratings, and, after the development step, to obtain a regular 2D array of pillars.

The first results obtained are reported in figure 11.8 and 11.9. Figure 11.8 shows a 2nd order DFB grating with 100X100 μm^2 area and $\sim$422 nm of period. The quality of the structure is quite high, demonstrating the potentiality of the sol-gel as resist material. The major problem is related to the pattern distortion, due to charge accumulation typical for lithography performed on a non-conducting substrate.

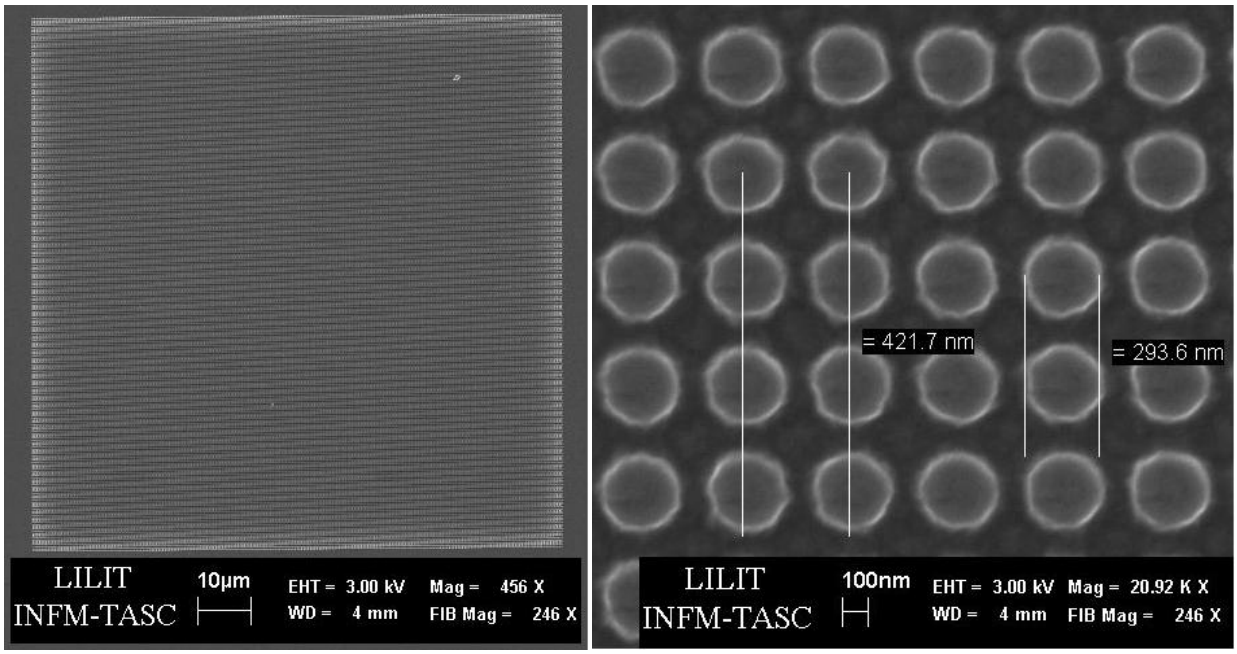

Figure 11.8 *SEM picture of the realized 2nd order grating. On the left it is possible to appreciate the distortion induced from the charge accumulated on the sample during the lithography. The right picture shows a detail of the patterning.*

Other structures have been realized based on the mixed 1st-2nd order architecture, to obtain a higher confinement and to reduce the lasing threshold. The 1st order region, surrounding the 2nd order one, has halved period and pillars radius, and a width of about 15 µm (~70 periods).

The experimental realization of these structures presents the further problem of the correct alignment of the two gratings, as evidenced in figure 11.9.

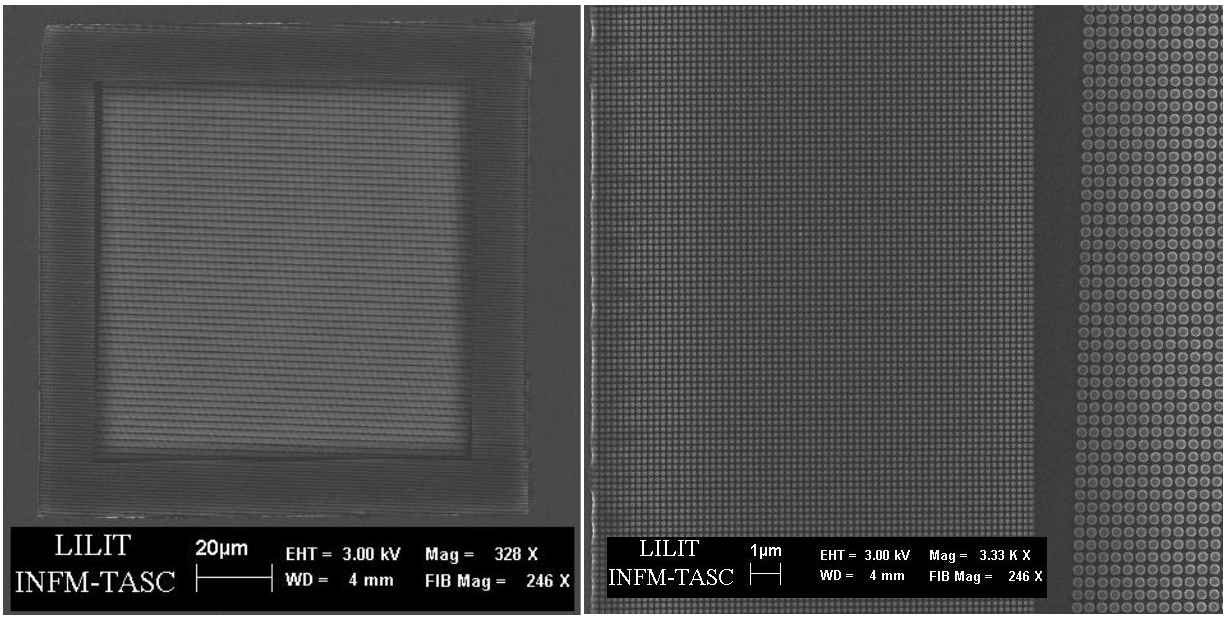

Figure 11.9 *SEM image of a mixed order grating, where the period and radius of the 1st order surrounding mirror is half the values of the core area. The bad alignment between the two gratings is evidenced in the magnified details on the right.*

For that reason, till now we have obtained discrete lithography results only for purely 2nd order grating.

The active material has been deposited on the produced substrates by multiple steps spin-coating. After each deposition step the spin-on glass was annealed at 250 °C for 5 minutes. The resulting film has a thickness of about 330 nm.

TEM section images of the resulting structure have been done to verify that the spin coated solution completely fills the empty area between the pillars.

The results, reported in figure 11.10, seem to show the complete wettability of the gratings surface, and the absence of empty area at interface between the grating and the film.

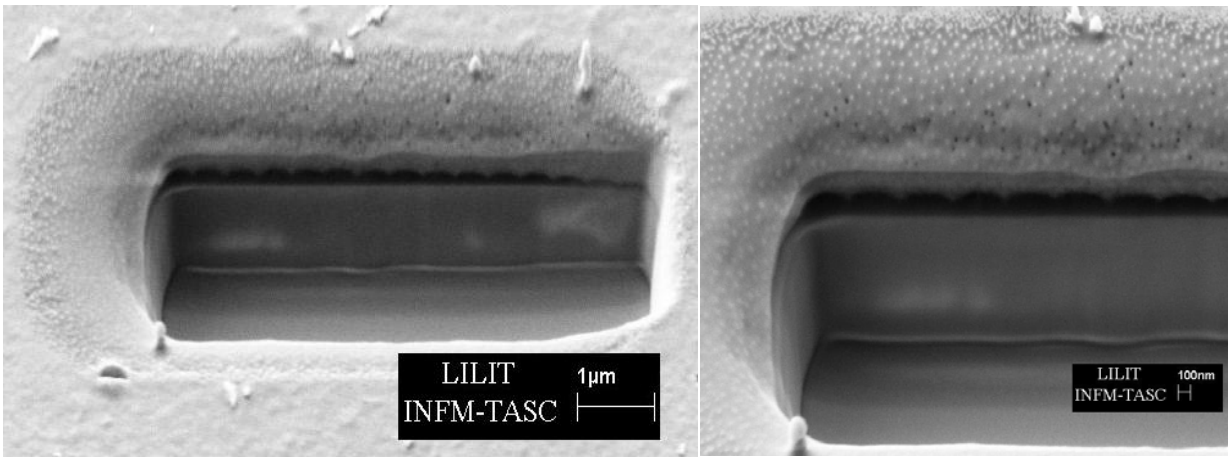

Figure 11.10 *SEM image of the device section, showing the penetration of the active film inside the empty area between the grating pillars.*

11.9 Optical characterization

With the set-up described in section 7.7, it is possible to collect the spontaneous and ASE emission from the sample, and, by pumping on the grating area above threshold, also the laser emission.

Preliminary characterizations have been done, both at 800 nm (two-photon pumping) and 400 nm (one-photon pumping), with this set-up, scanning the whole sample area and collecting the emitted signal.

We succeeded to collect the spontaneous emission and, by pumping at 400 nm also the ASE emission, but we never saw lasing emission.

Unfortunately, the extremely reduced area of the gratings makes the alignment of the pump-beam on the gratings really problematic. Moreover, as the pump beam is now focalized on a spot, instead of a line, like in the ASE measurement, pumping at high intensity causes the burning of the sample. For that reason we cannot understand if the absence of lasing emission

is related to the fact that we are pumping below the threshold, that the κL product is too low to reach lasing, or if we simply never succeed to pump above the grating area.

In order to overcome these problems it is possible to operate in two different directions. On the one hand, by operating on the lithography, in order to obtain larger area gratings or to produce mixed order ones. On the other hand, the set-up should be modified in order to visualized the magnified detail of the investigate sample during the characterization. To this end it is possible to realize a set-up similar to that previously illustrated for the characterization of the photonic crystal microcavity that allow to visualize the sample surface and to direct the pump exactly above the grating area.

11.10 Conclusion

In this chapter we have presented the results of the design and the experimental realization of a DFB laser device, intended to emit up-converted laser light in the visible. Different configurations have been simulated in order to extract the device parameter to be used for the experimental realization. First attempt of grating pattering have been realized, by means of electron beam lithography, using a sol-gel curable film as the resist materials. We have realized both 2^{nd} order and mixed 1^{st}-2^{nd} order gratings. The second configuration seems to be the most promising one, because of the lower laser threshold, but it implies some technological difficulties that, till now, we have been not able to overcome. It has been demonstrated the capability to realize sample with desired thickness, by spin coating ZrO_2 sol gel films doped with QDs as active material.

Few preliminary characterizations have been done using a proper optical set-up; further improvements are necessary, on the lithography and on the optical set-up, in order to succeed in collecting the DFB laser signal.

REFERENCES

[1] M. Tessler, G. J. Denton, R. H. Friend, Nature, 1996, 382, 695; K. J. Vahala, Nature, 2003, 424, 839.

[2] T. Tsutui, N. Takada, S. Saito, E. Ogino, Appl. Phys. Lett., 1994, 65, 1868

[3] D. G. Lidzey, M. A. Pate, D. M. Whittaker, D. C. Bradley, M. S. Weaver, T. A. Fisher, M. S. Skolnick, Chem. Phys. Lett., 1996, 263, 655

[4] I. P. Kaminow, H. P. Weber, E. A. Chandross, Appl. Phys. Lett., 1971, 22, 497; M. Berggren, A. Dodabalapur, R. E. Slusher, Z. Bao, Nature, 1997, 389, 466.

[5] D. M. Mc Gehee, A. J. Heeger, Adv. Mater, 2000, 12, 1655.

[6] H. Kogelnik, C. V. Shank, Appl. Phys. Lett. 1971, 18, 4, 152; H. Kogelnik, C. V. Shank, J. Appl. Phys. 1972, 43,5 2327.

[7] S. John, Phys. Rev. Lett. 1987, 58, 23, 2846; E. Yablonovith, Phys. Rev. Lett., 1987, 58, 20, 2059.

[8] A. Makis, a. Dodabalapur, R. E. Slusher, J. D. Joannopoulos, Opt. Lett., 2000, 25, 13, 942.

[9] C. Bauer, H. Giessen, B. Schnabel, E. –B. Kley, C. Schmitt, U. Scherf, R. F. Mahrt, Adv. Mater. 2001, 13, 15, 1161.

[10] M. Notomi, H. Suzuki, T. Tamamura, Appl. Phys. Lett., 2001, 78, 10, 1325; M. Imada, A. Chutinan, S. Noda, M. Mochizuki, Phys. Rev. B, 2002, 65, 19, 195306.

[11] W. Holzer, A. Penzkofer, T. Pertsch, N. Danz, A. Bräuer, E. B. Kley, H. Tillmann, C. Bader, H. –H. Hörhold, Appl. Phys. B, 2000, 74, 333.

[12] H. Kogelnik, Integrated Optics, ed. by T. Tamir, 1979.

[13] John E. Carroll, James Whiteaway, Dick Plumb, R. G. Plumb, Distributed Feedback Semiconductor Lasers, IET, 1998.

[14] C. Karnuttsch, C. Pflumm, G. Heliotis, J. C. deMello, D. D. C. Bradley, J. Wang, T. Weimann, V. Haug, C. Gärtner, U. Lemmer, Appl. Phys. Lett., 2007, 90, 131104.

[15] K. Baumann, T. Stöferle, N. Moll, R. F. Mahrt, T. Wahlbrink, J. Bolten, T. Mollenhauer, C. Moormann, U. Scherf, Appl. Phys. Lett., 2007, 91, 171108.

[16] G. Heliotis, R. Xia, G. A. Turnbull, P. Andrew, W. L. Barnes, I. D. W. Samuel, D. D. C. Bradley, Adv. Funct. Mater, 2004, 14, 1, 91.

[17] C. Kallinger, M. Hilmer, A. Haugeneder, M. Perner, W. Spirkl, U. Lemmer, J. Feldmann, U. Scherf, K. Mullen, A. Gombert, V. Wittwer, Adv. Mater., 1998, 10, 920.

[18] S. Noda, M. Yokoyama, M. Imada, A. Chutinan, M. Mochizuki, Science, 2001, 293, 1123.

[19] H. Ghafouri-Shiraz, Distributed Feedback Laser Diodes and Optical Tunable Filters, Wiley and Sons, 2003; Bishnu P. Pal, Fundamentals of Fibre Optics in Telecommunication and Sensor Systems, bohem press, 1992.

[20] H. Kogelnik, C. V. Shank, J. Appl. Phys., 1972, 43, 5, 2327.

[21] K. Sakai, E. Miyai, and S. Noda, Appl. Phys. Lett., 2006, 89, 021101 1-3; K. Sakai, E. Miyai, S. Noda, Opt. Expr., 2007, 15, 7, 3981.

[22] I. Vurgaftman, J. Meyer, IEEE J. Quantum. Electron., 2003, 39, 689; R. F. Kazarinov, and C. H. Henry, IEEE J. Quantum Electronics, 1985, 21, 144.

[23] S. G. Johnson, J. D. Joannopoulos, Opt. Expr., 2001, 8, 3, 173.

[24] R. Harbers, Lasing in Organic Photonic-Crystal Structures, Doctoral Dissertation ETH No. 16232; R. Harbers, N. Moll, R. F. Mahrt, D. Erni, W. Bächold, J. Opt. A: Pure Appl. Opt., 2005, 7, S230; R. Harbers, P. Strasser, D. Caimi, R. F. Mahrt, N. Moll, D. Erni, W. Bächold, B. J. Offrein, U. Scherf, J. Opt. A: Pure Appl. Opt., 2006, 8, S273.

[25] G. Della Giustina, M. Guglielmi, G. Brusatin, M. Prasciolu, F. Romanato, J. Sol-Gel Sci. Technol., 2008, 48, 212; G. Brusatin, G. Della Giustina, F. Romanato, M. Guglielmi, Nanotechnol., 2008, 19, 175306.

CHAPTER 12

Photocatalytic Silica-Titania Films

The growing interest towards photocatalytic materials arises from the effort to decrease the environmental pollution. In fact in the previous century the fast population growth brought to an oilfield and nuclear overexploitation with energetic production aim. This has lead to the need of processes and technologies exploiting the solar energy for the purification of gas emission coming from cars and industry. The materials investigated for these kinds of applications are solid state semiconductors capable to photo-oxidize the harmful substances till the complete mineralization.

Among different existing photo-catalysts, titanium dioxide based films have been intensively investigated for their promising mechanical, chemical, electrical and optical properties. In particular great attention have been devoted to the study of the photocatalytic properties of TiO_2 powders and thin films useful for the purification of air and water and the provision of self maintaining clean surfaces. In fact it shows the capability to promote the mineralization of a wide range of organic contaminants, like aromatics, alkanes, alcohols, haloalkanes, dyes, insecticides and surfactants. The photodecomposition of organic compounds is an oxidation reaction, represented by the equation:

$$\boldsymbol{organic + O_2 \xrightarrow{h\nu \geq E_g(TiO_2)} CO_2 + H_2O + mineral\ acids} \qquad \text{Eq. 12.1}$$

where mineral acid is generated when hetero atoms, such as S, N and Cl are present in the organic components.

In semiconductor photo-catalysis ultra-band gap light generates electron-hole pairs that can either recombine or react with surface species. In this second case the photo generated electrons reduce the oxygen, while the photo generated holes mineralize the organic. The latter process probably involves the initial oxidation of surface OH^- groups to hydroxyl radicals which then oxidize the organic and any subsequent intermediates.[1]

It has been demonstrated that the photocatalytic activity strongly depends on the physical properties of the TiO_2, such as the crystal structure (amorphous, anatase, rutile, or brookite), the surface area, the particle size, the surface hydroxyls, and so on. In particular the crystalline structure seems to be the crucial parameter to determine the photocatalytic activity: anatase seems to be the most active phase, while amorphous TiO_2 shows negligible activity by comparison with commercial TiO_2 catalysts.[2] The specific surface area also plays an important role to determine the catalytic activity: small TiO_2 nanoparticles show larger surface area and possess greater activity.

Different methods have been employed to prepare the nanoparticles, such as chemical precipitation, microemulsion, hydrothermal crystallization and sol-gel synthesis.[3] In the sol-gel processes, TiO_2 is usually prepared by hydrolysis and polycondensation reactions of titanium alkoxides, $Ti(OR)_n$, to form oxopolymers, which are then transformed into an oxide network. Because of the high reactivity of titanium alkoxides, some chelating reagents, such as diol, carboxylic acid or diketonate compounds are added during the hydrolysis step. Then, after the condensation step, a calcination treatment at 400°C or more is required to remove the organic molecules from the final products and to complete the crystallization.[4]

We have proposed a new approach for the synthesis of nanocrystalline TiO_2 particles embedded in a mixed silica-titania amorphous and hybrid network, performed at room temperature and without using any chelating agent. The obtained films show a non negligible photocatalytic activity, and can find applications as photocatalytic coatings on thermally degradable substrate. Another possible application has been explored for these films: their potentiality as films for the production of photo-induced relief gratings has been valued. This application derives from the observation that the films photo-activity acts towards their organic components as well as towards other organic pollutants. Thus, the irradiation of the samples induces the decomposition of the organics, leading to fully inorganic films, with thickness decreased of about 60%. The irradiation of the sample through a mask allows obtaining surface relief gratings.

12.1 Heterogeneous photo-catalysis

Photo-catalysis is defined as the acceleration of the velocity of a photo-reaction because of the presence of a catalyst. In fact the hydrocarbons oxidation would proceed slowly without catalytic active substance. The photo-catalyst reduces the activation energy of a given reaction. A heterogeneous photocatalytic system consists on semiconductor particles in close contact with one component of the reactions. Following the exposition of the catalyst to the light, exited states are generated, able to initiate chain reactions such as redox reactions or molecular transformations. Due to their peculiar electronic structure, the semiconductors (metal oxides or sulphurs, like ZnO_2, TiO_2, and ZnS) can act as sensitizers for photo-induced redox processes. They are characterized from the presence of a complete valence band (VB) and an empty conduction band (CB), separated by a forbidden energy range called energy gap (E_g). The band gap is like a wall that electrons must jump in order to become free, and the amount of energy required for the jump is referred as band gap energy and changes from one semiconductor to another. In a semiconductor with a large E_g, electrons in the VB cannot jump to the conduction band without a supplied external energy. Without considering the doping, there are two mechanism of free carriers generation: the thermal excitation (for $E_g < 0.5\ eV$) and the photo-excitation (for $h\nu > E_g$). When a photon with energy $h\nu > E_g$ is absorbed an electron moves up to the conduction band, generating at the same time a positive hole. In ordinary substances, electrons and holes recombine quickly; however in titanium oxide photo-catalyst they recombine more slowly, and thus some of these generated couples can move to the particles surface and can interact with the absorbed molecules: donor (D) or acceptor (A). The percentage of carrier recombination has a major effect on the photocatalytic efficiency. One of the notable features of titanium oxide is the strong oxidative decomposing power of positive holes, which is greater than the reducing power of electrons excited to the conduction band. The surface of a photo-catalyst contains absorbed water. When this water is oxidized by positive holes, hydroxyl radicals (•OH), having strong oxidative decomposing power, are formed. Then, the hydroxyl radicals react with organic matter. If oxygen is present when this process takes place, the intermediate radicals in the organic compounds and oxygen molecules can undergo radical chain reactions and consume oxygen in some cases. In such a case, the organic matter eventually decomposes, ultimately becoming carbon dioxide and water. Under some conditions, organic compounds can react directly with the positive holes, resulting in

oxidative decomposition. Meanwhile, the reduction of oxygen contained in the air occurs as a pairing reaction. As oxygen is an easily reducible substance, the reduction of oxygen takes place instead of hydrogen generation, resulting in the generation of superoxide anions ($\bullet O_2^-$). Superoxide anions attach the intermediate product in the oxidative reaction, forming peroxide or changing to hydrogen peroxide and then to water.

12.2 Titanium dioxide

The titanium dioxide (TiO_2) is a semiconductors oxide that becomes highly reactive when chemically activated from incident light of opportune wavelength ($h\nu > E_g$). Through the direct absorption of incident photon, it can, in fact, participate to surface photo-chemical processes. This strong photo-catalytic activity, that comes from its chemical and physical characteristics, has been investigated starting from 1972 in Japan, with a growing interest in the last years. In particular the TiO_2 results the most effective between the investigate ones for the degradation of a lot of contaminant of interest. The titanium dioxide is employed for electrochemical process, and as pigment for paints and polymer. Its electronic and optic properties have been exploited in numerous applications in gas sensors, anti-reflection coatings for solar cells and processes of energy conversion of photo-chemical energy.

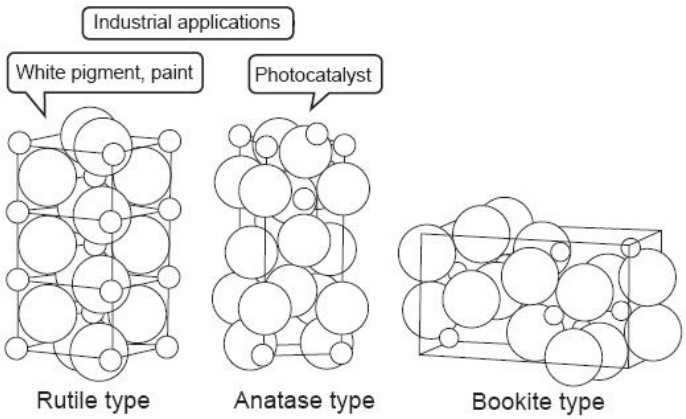

Figure 12.1 *The three different crystalline structures: Rutile, Anatase and Brookite. The fundamental unit of all these forms is an octahedron TiO_6, the difference being in the numbers of shared octahedrons.*

It exists in three different crystalline structures (rutile, anatase and brookite) and in the amorphous phase. The brookite is an orthorhombic phase, while the other two are tetragonal phases, and are the more diffused in nature. In titanium dioxide, Ti atom is surrounded from eight O atoms, forming a distorted octahedron (TiO_6). These octahedrons represent the fundamental structural units of the three polymorph structures and the structural differences derives mainly from the numbers of shared octahedron, two for rutile, three for brookite and

four for anatase. The energy gap (E_g), the refractive index and the density are 3.18 eV, 2.52 and 3.9 g/cc respectively for anatase and 3.03 eV, 2.76 and 4.2 g/cc for rutile. Despite of its higher energy gap, and hence of its absorption edge at lower wavelength, the anatase form is the phase more active as photo-catalyst, and for this reason it is also the more studied and employed for this application.

The main titanium dioxide characteristics are:

- Transparency in the visible region
- High porosity
- High surface affinity
- Low cost and easy production
- Chemically inert, non-toxic, biocompatibility

12.3 Sample preparation

Basic catalyzed hybrid silica-titania sols (G7Ti3) were prepared according with the synthesis procedure reported in chapter 9, and the final sol concentration is 100g/L SiO_2+TiO_2. Finally the sol was sonicated for 30 minutes and then left to react under stirring for five hours at room temperature. All the sols were filtered with a microporous membrane (0,2 μm Millipore) before using. Cleaned silicon wafer, soda-lime or quartz slides were used as substrates. Hybrid silica-titania coating films were obtained from the prepared sol by spin-coating and drying in an oven at 60^0C for 30 min (RT sample).

Before the photocatalytic activity tests the film have been pre-exposed for 10 min to the UV radiation to decompose the organic components present inside the film and to obtain a completely inorganic SiO_2-TiO_2 network (PE film).

The UV-lamp employed for the sample treatments is a Hamamatsu LC5 UV mercury-xenon lamp with a large emission spectrum, and an intensity of 3500 mW/cm^2, at 1 cm distance. The lamp emission spectrum is reported in the inset of figure 12.8.

12.4 FT-IR analysis

The films microstructure has been analyzed by infrared absorption spectra, in the range 400-4500 cm^{-1}, recorded by a Fourier transform infrared spectroscopy (Jasco FT-IR-620), with accuracy of $\pm 1\ cm^{-1}$.

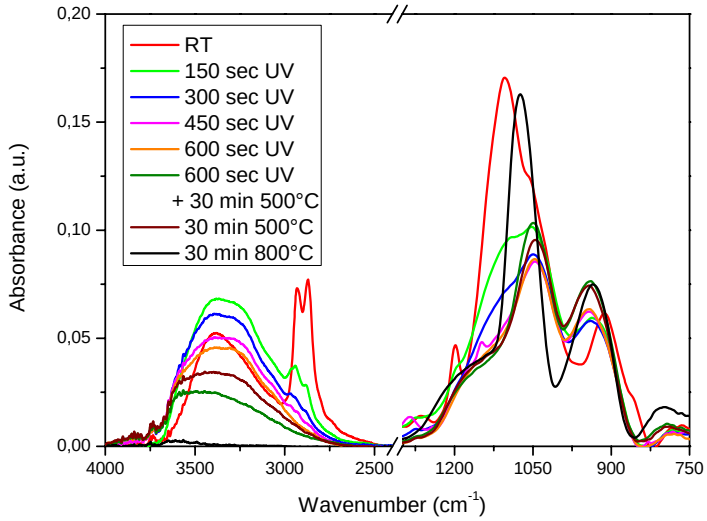

Figure 12.2 *FT-IR spectra of the RT sample before (red line), and after different UV exposition time with the LC5 lamp from 3.5 cm distance, with a corresponding incident intensity (considering the entire emission spectrum) of ~ 450 mW/cm². The spectra of samples treated at 500°C and 800°C are also reported (brown and dark-green spectra respectively).*

The FT-IR spectra of the RT film before and after 1 to 4 sequential 150 seconds step of exposition with the LC5 UV lamp (d ~ 3.5 cm, E ~ 450 mW/cm²) are reported in figure 12.2. A 30 minutes thermal treatment, at 500°C on an unexposed film, and on a 600 sec UV exposed sample, are also reported for comparison. The FT-IR spectra of all the samples show two frequency ranges of great interest. In the first interval, between 3500 and 2500 cm^{-1}, there are the large $\nu_{(O-H)}$ band and the two peaks at 2930 cm^{-1} and 2870 cm^{-1}, relative to the $\nu_{AS}(CH_2)$ and $\nu_S(CH_2)$ respectively.

The $\nu_{(O-H)}$ band can receive four main contributions,[5] as reported in figure 12.3. The type (a) silanol group is characterized by a sharp absorption peak around ~3740 cm^{-1}, and it never appears in any sample, indicating that the silanol groups are mainly hydrogen-bonded. The RT sample shows a narrower (respect to the UV and 500°C treated samples) peaks, indicating of a narrower distribution of silanol groups (only (c) and (d) groups), probably with predominance of type (c) at ~3380 cm^{-1} over type (d) groups at ~3280 cm^{-1}. A contribution of the peaks comes probably also from $\nu_{(O-H)}$ group of 2-MetOH that absorb at 3420 cm^{-1}.[6]

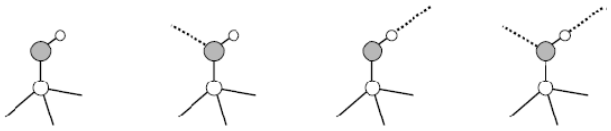

Figure 12.3 *Schematic representation of the four different possible silanol groups, free (a) and linked with different hydrogen bonds (b)-(d):* O *is a Silicon atom,* o *an Oxygen atom,* ● *a hydrogen atom.*

The UV exposition induces an initial (for the first two steps) increase of the band, due to the increase of *Si-OH* groups and to the molecular water released as a result of the decomposition of the organic components. Then, after 450 seconds of UV exposition, when the organic component is almost entirely decomposed, the peak intensity returns to the initial value, but there is an increase of the (d) groups and a lower wavenumber shoulder appears, due to the presence of (b) silanol groups.

The two sharp bands at 2930 and 2870 cm^{-1} can be used to control the organic chain evolution under different UV and thermal treatments: it can be clearly seen that the propylic chain becomes progressively weaker for longer UV-exposition times and it is completely disappeared after 600 seconds exposition. The same effect can be obtained with 30 minutes thermal treatment at 500°C. However in this case the $\nu_{(O-H)}$ band is less intense, probably because the water released from the thermal oxidation of hybrid groups is more efficiently released at this temperature.

The second representative region, in the 1300-700 cm^{-1} range, contains a great number of superimposed peaks. To evaluate the different peaks contribution to the resulting spectra, deconvolutions have been performed with a multi-peaks Gaussian fitting, showed in figure 12.4. The results are reported in Table 12.1.

The first fact that clearly appears in the table is a progressive shift of the inorganic component peaks to larger wavenumbers with increasing UV and thermal treatments, indicative of a progressive stiffening of the film. The RT spectrum is reported in the top portion of figure 12.4. The intense peak [4] at 1107 cm^{-1} is related to $\nu^{AS}_{(C-O-C)}$ bonds of the propylic chain, while the sharp peak [1] at 1200 cm^{-1} is related to the symmetric stretching vibration of CH_2 groups of the propilyc chain, both are related to the presence of the organic component in the RT films. These bands disappear after UV exposition or thermal treatments, indicating a photo- or thermal-decomposition of the organic components.

Peaks		[1]	[2]	[3]	[4]	[5]	[6]	[7]	[8]	[9]
RT	Pos. max [cm^{-1}]	1199	1171	1145	1107	1054	1045	968	912	856
	area	0.90	0.30	1.88	8.21	0.16	9.53	0.55	4.33	0.40
600 sec UV	Pos. max [cm^{-1}]	---	1172	1120	---	---	1045	943	898	---
	area	---	2.18	1.80	---	---	7.93	4.45	1.00	---
UV + 500°C	Pos. max [cm^{-1}]	---	1192	1133	---	---	1048	947	904	---
	area	---	1.20	2.24	---	---	8.31	5.05	1.31	---
800°C	Pos. max [cm^{-1}]	---	1190	1145	---	---	1072	954	916	---
	area	---	2.43	0.85	---	---	10.89	4.14	2.05	---

Table 12.1 *Peaks deconvolution for the RT sample in Figure 12.4. The multiple peaks have been fitted as the accumulation of Gaussian function. The resulting coefficient of determination R^2 and reduced χ^2 are 0.99982 and 4.3*exp(-7) respectively. The peaks positions are reported together with the integrated area, width and height.*

The four shoulders at lower [2], [3] and higher [5], [6] frequencies, with respect to the main band at 1110 cm^{-1}, are assigned respectively to the longitudinal (LO) and transverse (TO) optical components of the asymmetric Si-O-Si stretching vibrations $\nu^{AS}_{(Si-O-Si)}$.[7] The LO shoulder has been fitted with a two peaks deconvolution, and not with only one peak, as same authors reports, because the resulting fit is better. The LO/TO ratio can be correlated with the volume fraction of the residual porosity. In fact longitudinal optical component band of $\nu^{AS}_{(Si-O-Si)}$ in normal incidence transmission spectroscopy, is activated only thanks to the pore light scattering of the IR radiations, such that a fraction of the absorbed light is effectively obliquely incident.[7] According to this hypothesis the LO/TO ratio increases from 0.22 for the RT sample to 0.65 and 0.56 after the 450 and 600 seconds UV treatments respectively, as a consequence of the decomposition of the organic component that leaves pores inside the film. With thermal treatment at 500°C the ratio becomes 0.41 indicating a film densification and decreases to 0.30 for 800°C treatment. The C-H stretching of the epoxy ring and the presence of residual 2-MetOH is evidenced by the presence of the shoulder [9] at 856 cm^{-1}, that disappears after only one 150 seconds step of UV exposition. Finally the broad peak [8] centered at 912 cm^{-1} is probably the results of the superimposition of the *Si-O-Ti*, *Si-OH* and *Si-O*$^-$ groups stretching vibration and of the two 2-MetOH bands at 880 and 960 cm^{-1}.

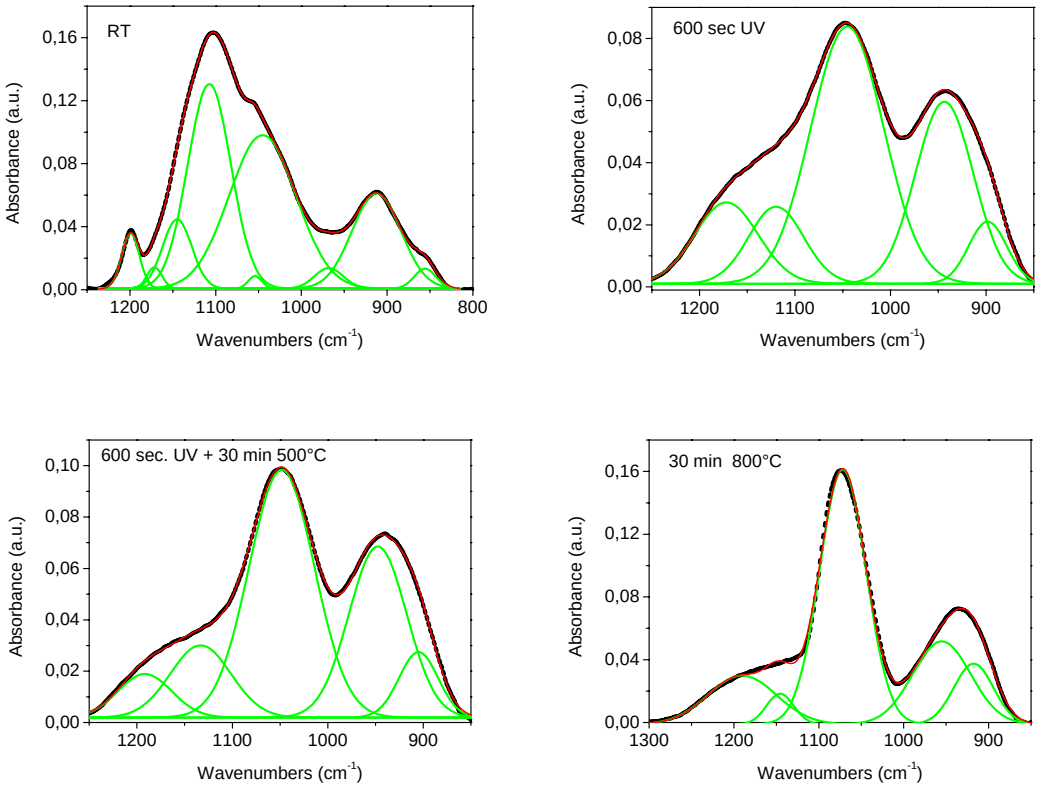

Figure 12.4 *FT-IR absorption spectra in the region 1300-800 cm^{-1} of RT sample, 600 sec UV exposed sample, UV + thermal 500°C annealed sample, and 800°C annealed sample (from top to bottom respectively). The black dotted lines are the recorded spectra, the green lines are the deconvoluted peaks and the red lines are the curves resulting from the fitting.*

After the UV or thermal treatment at 500°C this peak shift to lower frequencies, probably because the solvent contribution disappears. The band is now well fitted with two peaks, the first one centered at 900 cm^{-1} and assigned to the *Si-O*$^{-}$ stretching vibration, while the main one, at 940 cm^{-1}, is assigned to the *Si-O-Ti* and *Si-OH* stretching vibrations.[8] In the sample treated at 800°C this peak can be attributed only to *Si-O-Ti* vibrations, because Si-OH groups are no-more present in the film, as confirmed from the disappearance of the band centered at 3400 cm^{-1}.

After the thermal treatment, at 800°C, the *Si-O-Si* band shifts to 1070 cm^{-1} and increases significantly, while the *Si-O-Ti* band decreases. This means that the number of *Si-O-Si* bonds have been increased, while the *Si-O-Ti* bonds have been decreased, suggesting a segregation of the titanium ions, that left the silicons ions and migrate into a titania rich region, allowing the formation of additional siloxane bridges. The remaining *Si-O-Ti* bond are then mostly located on the surface of the titania cluster. To estimate the *Si-O-Ti* connectivity (Ti dispersion in the Si matrix) it is interesting to use the parameter $D_{(Si\text{-}O\text{-}Ti)}$, defined as:[9]

$$D_{(Si-O-Ti)} = \frac{S_{(Si-O-Ti)}}{S_{(Si-O-Si)}} \cdot \frac{\chi_{Si}}{\chi_{Ti}} \qquad \text{Eq. 12.2}$$

where and are the deconvoluted peak area of the at 940 cm^{-1} and at 1120 and 1170 cm^{-1} respectively; χ_{Si} and χ_{Ti} are the molar proportions of Si and Ti respectively. gives a qualitative estimation of the fraction of *Si-O-Ti* species over the total Ti content, and thus a sort of mixing efficiency. The results obtained are 2.6, 3.4 and 1.8 for the sample irradiated with UV light for 600 sec, and the samples with 500°C and 800°C thermal treatments respectively. The higher D value seems to confirm the Ti ions migration, suggested above, even if this result cannot be considered as quantitative because it is not possible to estimate the *Si-OH* contribution to the *Si-O-Ti* peak.

12.5 UV-Visible Spectroscopy

The sharp absorption band in the UV region is indicative of the tendency of titania, in silica-titania sol gel film to form a separated phase, composed of titania or titanium-oxo clusters of nanometric sizes.[10] This band does not move to longer wavelength after UV or thermal treatments, suggesting that the cluster size and nature do not change. The UV-Visible spectra of the RT and treated samples show no remarkable absorption in the 400-800 nm range (inset in figure).

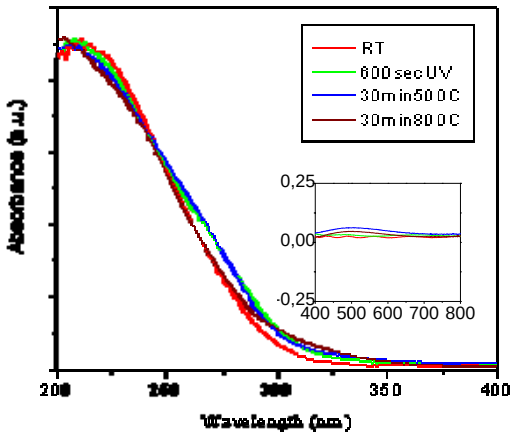

Figure 12.5 *UV-Visible spectra of RT sample and 600secUV and thermal annealed films*.

12.6 Ellispsometric characterization

The ellipsometric measurements of RT sample and after different UV and thermal treatments have been performed. The ellipsometric measurements of the samples were analyzed by fitting a theoretical model of the experimental data. The model utilized was a homogeneous film with Cauchy law dispersion. The extinction coefficient (k) was assumed 0 from 400 to 1200 because no absorbance were detect (figure 12.5). The refractive index calculated becomes more similar

to the densificated matrix (1.68) increasing the time of UV treatment, as reported in figure 12.6.

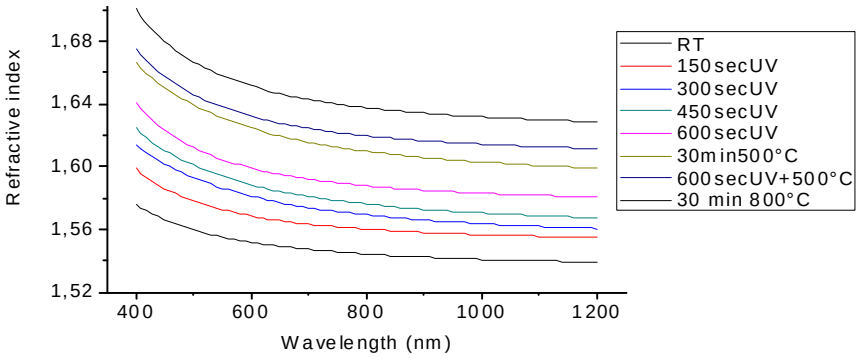

Figure 12.6 *Ellypsometric determination of the refractive index of the RT and treated films in the range 400-1200 nm. A continuous increase in the refractive index for increasing UV exposition time is showed. A further index increases can be achieved after thermal treatment at 500 and 800°C.*

During the UV exposition, as already mentioned, the organic decomposition occurs, leading to a refractive index increases. This phenomenon is attributed to the densification of the film as confirmed by the thickness decrease (table 12.2). The film porosity for the 600 sec UV and for the 30 min at 500°C and 800°C treated samples have been estimated from the Lorentz-Lorentz equation, assuming a pore refractive index of 1:[11]

$$\frac{\left(n_f^2-1\right)}{\left(n_f^2+2\right)} = \frac{(1-V_P)\left(n_m^2-1\right)}{\left(n_m^2+2\right)} \qquad \text{Eq. 12.3}$$

Where V_P is the pore volume fraction, n_f is the measured refractive index, and n_m is the effective index of an inorganic fully densificated matrix, assumed to be 1.68 by extrapolation of Schroeder data.[12] The results are also reported in Tab 12.2.

Sample	Thickness (nm)	Shrinkage (%)	Porosity (%)
RT	800	/	
300 sec UV	393	51	
600 sec UV	281	65	10
500°C x 30 min	261	67	7
600 sec UV + 500°C x 30 min	231	71	6
800°C x 30 min	203	75	3.7

Table 12.2 *Film thickness for the RT sample. The shrinkage calculated respect to the initial thickness, and the porosity after different treatment are also reported. All the data are obtained from the ellypsometric analysis.*

12.7 TEM analysis

In order to investigate the presence and the nature of the TiO_2 clusters, TEM analysis have been performed. Figure 12.7 reports TEM images of an UV-exposed film, where it is possible to see

some crystalline particles of titania, well dispersed in the amorphous background (the same characteristics have been evidenced on non-irradiated samples). The particle diameter is in the range 2-6 nm. The Energy Dispersive Spectroscopy (EDS) analysis has confirmed that the particles showed in the TEM photograph are TiO_2. Most of the particles show a crystalline nature, which, together with the great amount of hydroxyls groups and of the residual film porosity, is responsible of the photocatalytic behavior of the film.

Unfortunately it has been not possible to obtain the unambiguous determination of the crystalline phase of these particles. The electron diffraction pattern is not fully compatible with the anatase and rutile phase, but seems to be the results of the superimposition of the contribute of both these phases.

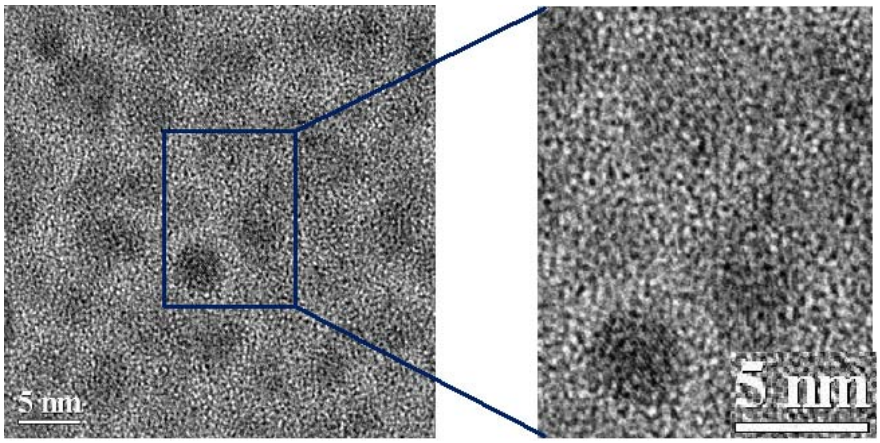

Figure 12.7 *TEM analysis of the 600secUV exposed sample, showing the titanium cluster or radius ranging from 2 to 6 nm.*

12.8 Photocatalytic Activity

The photocatalytic performances of the films towards the degradation of organic compound have been measured using Stearic Acid (SA), as model material. It is a well known reference materials, and provides a reasonable model compound for the type of solid organic films that deposit on exterior glass surface, such as house or office windows. When irradiated with UV light, stearic acid decomposes according to the following reaction:

$$\boldsymbol{CH_3(CH_2)_{16}CO_2H + 26O_2 \xrightarrow{h\nu \geq E_g} 18CO_2 + 18H_2O} \qquad \text{Eq. 12.4}$$

a process involving a transfer of 104 electrons.

A film of SA has been deposited on the photocatalytic substrate, under test, by spin coating at 1500 rpm a solution $8.8*10^{-3}$ M in methanol. This results on initial stearic acid coverage of approximately $1.8x10^{15}$ molecules/cm^{-2}, calculated from the integrated area of the SA peaks in the 2800-3000 cm^{-1} range in the FT-IR spectra. The SA has three peaks in this range: the peaks

at 2958, 2923 and 2853 cm^{-1} due to the asymmetric in-plane *C-H* stretching mode of the CH_3 groups and to the asymmetric and symmetric *C-H* stretching modes of the CH_2 groups respectively.

From the integrated area under these peaks it is also possible to estimate the concentration of SA as a function of the increasing UV exposure time, and so to obtain its photodecomposition rate. A single 6 W UV lamp with maximum emission at 365 nm (~ 1.5 mW/cm^2) and a Hamamatsu LC5 UV mercury-xenon lamp have been used as irradiation sources. The emission profiles of these lamps are shown in figure 12.8, together with the absorption spectrum of the photocatalytic film.

From the absorption spectra it is clear that G7Ti3 films do not absorb at the emission wavelength of the 6W lamp, so it is reasonable to suppose that it do not show any photocatalytic action towards the decomposition of the organic compounds. This fact is confirmed by the FT-IR spectra of the PE film spin coated with stearic acid (figure 12.9). No remarkable differences in the spectra are visible also after 8 hours of exposure. Successive tests have been performed with the LC5 lamp,

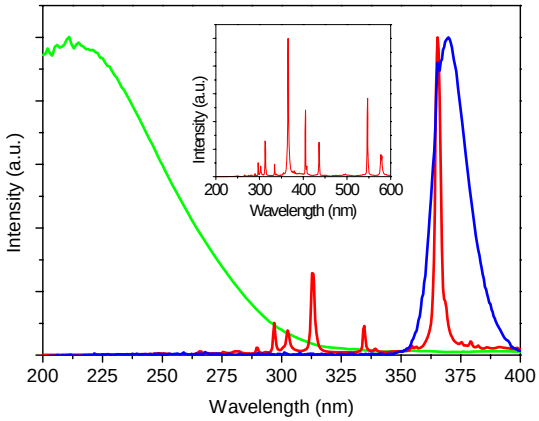

Figure 12.8 *UV absorption spectra (green line) of the G7Ti3 sample, showing absorption edge at around 300 nm. The emission profile of the 6W UV-lamp (blue line) and Hamamatsu LC5 lamp (red line) are also reported. It can be clearly seen that the 6W lamp emits outside of the absorption wavelength of the active sample, while the LC5 lamp presents some emission peaks below 325 nm, where the sample still absorbs.*

possessing several emission bands in a wide spectral range, which cover also the absorption band of the G7Ti3 photocatalytic film (see figure 12.1). In particular this lamp shows four peaks (centered at 290, 297, 303, 313 nm) in the spectral region below 325 nm, the wavelength region where G7Ti3 film start to absorb. This lamp has been used at the distance of 10 cm from the sample, giving an irradiance of ~ 12 mW/cm^2. After only one hour of exposure time, the

stearic acid IR peaks disappear, indicating the complete decomposition of the acid spin coated film (figure 12.9).

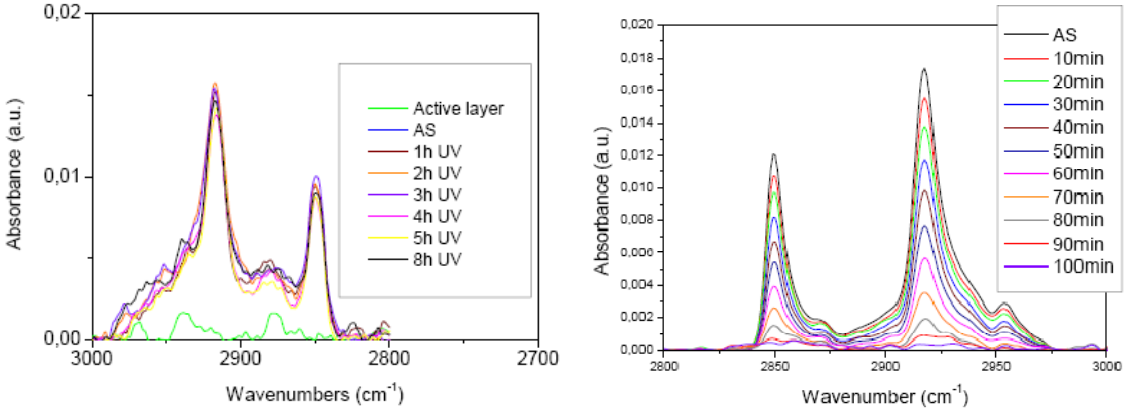

Figure 12.9 *(left) Photocatalytic test performed with a 6W-UV lamp (I ~ 1.5 mW/cm^2). The irradiation up to 8 hours on the PE film spin-coated with stearic acid doesn't produce any remarkable difference in the FT-IR band intensity. (center) Photocatalytic test performed with a LC5 lamp (distance lamp-sample ~10 cm, I ~ 12 mW/cm^2).*

The trend of AS concentration as a function of UV-exposure time is reported in figure 12.10. To confirm the PE film photocatalytic action, a stearic acid film spin coated directly on a Si substrate has also been exposed to the same treatment. In that case also after 2 hours of exposure, the AS peaks only lightly decrease.

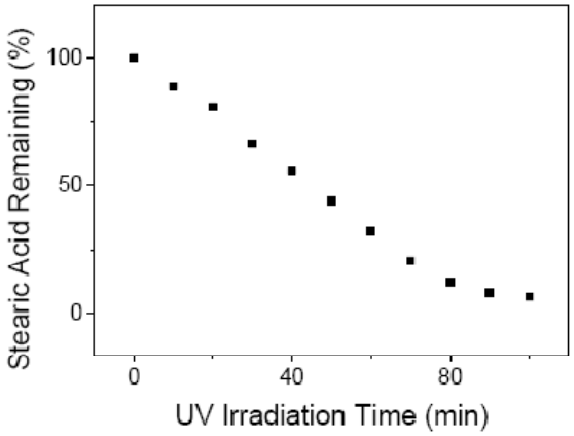

Figure 12.10 Photo-induced decomposition rate of the organic components with the LC5 lamp at an intensity of 12 mW/cm^2.

In order to compare this result with other present in literature, the Formal Quantum Efficiency (FQE) and the Quantum Yield (QY) have also been calculated and reported in Table 12.3.

The quantum yield of the G7Ti3 film is comparable with that of Activ^{TM} film (0.01-0.02), but is lower with respect to the pure titania sol-gel film (0.15-0.18). This extraordinary high photoactivity of sol-gel films can probably be ascribed to their great porosity determining an

increase of the contact area between the active film and the organic component to be destroyed.

Nevertheless it should be considered that only a small fraction of our film is constituted of active titanium cluster, while the great part is a SiO_2 like or mixed SiO_2-TiO_2 inert matrix. Moreover, the great advantage of this film is the absence of a thermal annealing, by this way they can be spin-coated even on thermally instable substrates.

Incident intensity $x10^{18}$ photon/cm^2/min	Rate, *Ri* $x10^{13}$ mol./cm^2/min	FQE[a] $x10^{-4}$ mol./photon	Fraction of light absorbed, *f*[b]	QY[c] $x10^{-2}$
1.11	2.05	0.18	0.138	0.013

[a] FQE (δ) calculated as δ = rate of stearic acid destruction (molecules removed/cm^2)/incident light intensity (photons cm^{-2}).

[b] Fraction of light absorbed (f) calculated using $f = (1–10^{-Abs(\lambda)})$ for the four main peak, from an analysis of the overlap of the UV-Vis spectra of the film, with that of the emission spectrum of the lamp (using the data in figure 12.1).

[c] QY (φ) calculated as $\varphi = \delta/f$.

Table 12.3 *Photocatalytic properties of our films.*

12.9 Photopatternig

Considering the preliminary measurements, where it comes out the evidence of film shrinkage of about 60 % after UV-exposition, this system has been tested for the realization of surface relief structure. To evaluate its potentiality towards the photo-patterning it has been exposed through a mask. The patterning tests have been performed with a Dupont Photomask, constitute of different structures, such as linear and ring gratings, showing periods in the range 40-150 µm. These tests have been performed by putting film samples at 3.5 cm distance from the LC5 UV source, by this way the light intensity is approximately 400 mW/cm^2 on the sample surface. The step duration is 600 seconds, four times longer than for the preliminary tests. This increase in the exposition time is necessary to compensate the strong absorption from the mask, evidenced in figure 12.11.

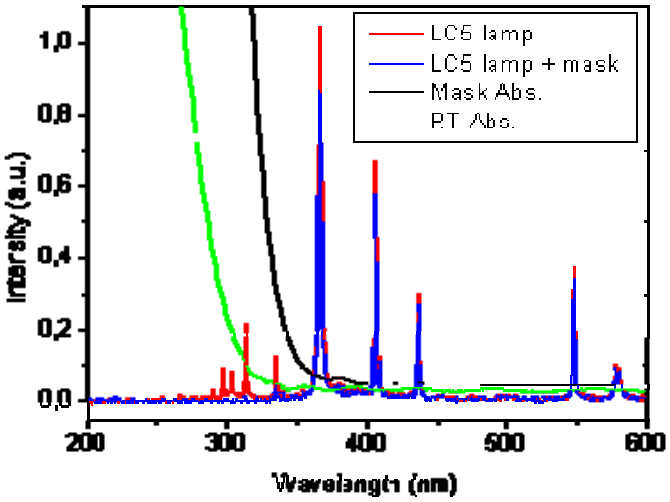

Figure 12.11 *Emission spectra of the LC5 lamp before (red line) and after (blue line) the photo mask. This latter absorb almost completely the lamp emission above 325 nm, where the photocatalytic sample absorbs. The absorption spectra of the mask (black line) and of the sample (red line) are also reported.*

A picture of the generated patterns is reported in Figure 12.12, together with the optical microscope magnified detail. The structures have been obtained with a four steps exposition of the sample.

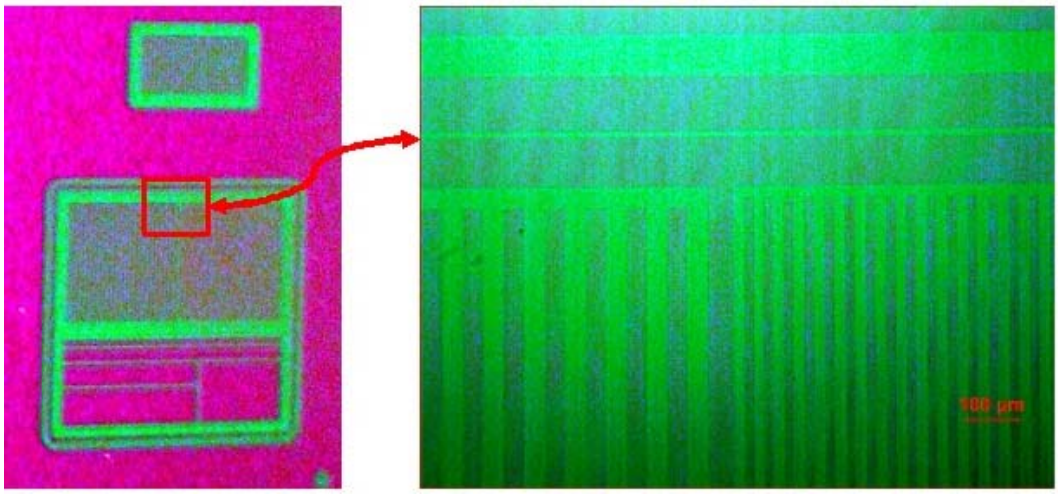

Figure 12 *Picture of a photo-induced structure, realized by UV irradiation through the mask (left). Optical microscope image of a magnified detail (right).*

The resulting surface modulation has been checked with AFM and profilometric measurements, reported in Figure 12.13 and 14 respectively. It is evident a peak-valley modulation of about 80-100 nm, with periods ranging from 40 to 100 µm.

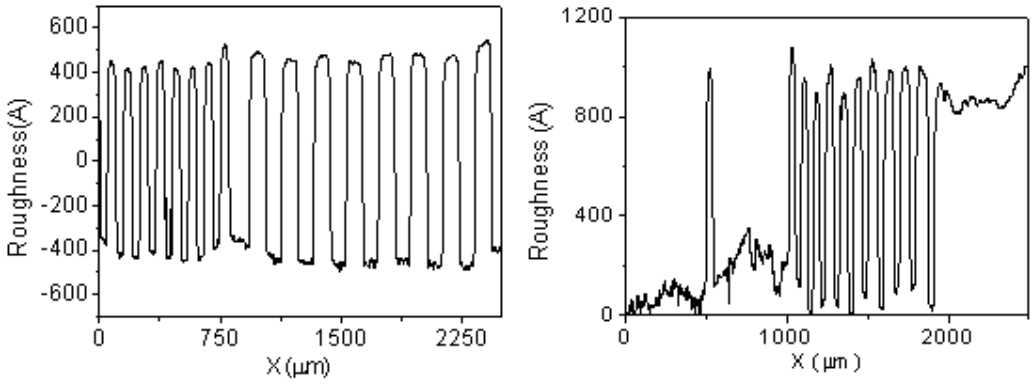

Figure 12.13 *Profile of two different gratings measured with a profilometer.*

This modulation has been achieved nevertheless the mask strongly absorbs the short wavelength components, lower than 350 nm, of the lamp, as clearly showed in Figure 12.11.

The use of the mask, placed between the UV-source and the sample, causes a decrease of the incident pump intensity to the ~40% of the pristine value. From the UV-Vis spectra it is clear that the cutting effect of the mask is almost complete below 3.54 eV, where the samples are more active toward photodecomposition. In spite of this set-up, it has been obtained shrinkage of about 10%: starting with films of 800 nm thickness, the final gratings show a depth of 80-100 nm.

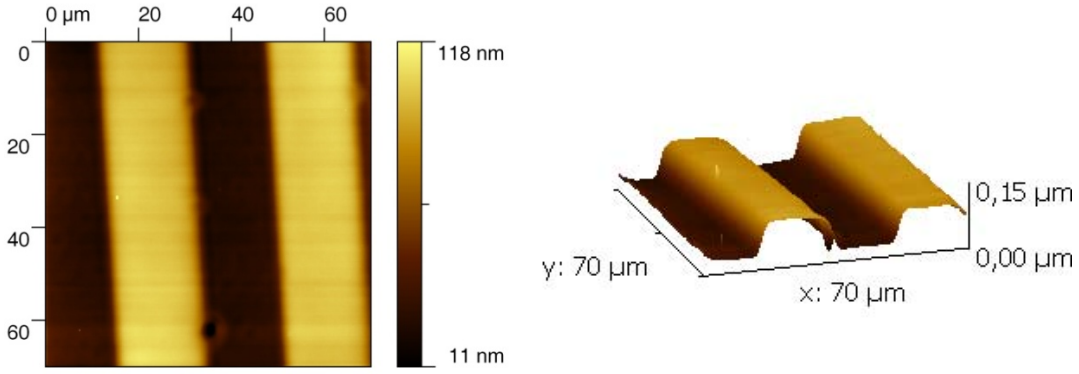

Figure 12.14 *AFM topography of the generated grating, with a period of about 40 µm, and 3D-AFM detail showing a modulation depth of 100 nm.*

12.10 Photopatterning with a quartz mask

To suppress the mask absorption limiting the performance of the patterning process, further tests have been performed by substituting the DuPont photo mask with one home-made replica realized on quartz. The photo-patterning parameters are exactly the same as before, except than the exposition time that can now be strongly decreased.

On figure 12.15 is reported the micro-IR spectra performed on the exposed and un-exposed area of a patterned sample, showing clearly the photo-induced decomposition of the organic component, along with the water release, according with (1).

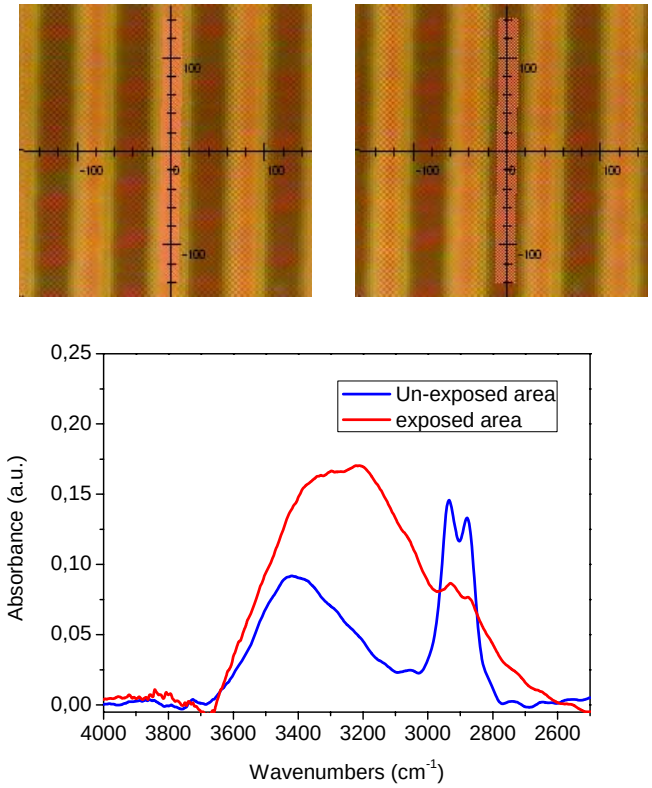

Figure 12.15 *Micro-IR spectra of the sample after the exposition with the UV-mask. The two image above show the sampled areas for the un-exposed spectrum (left) and for the exposed one (right). The organic component decomposition is clearly visible, together with the released water, according with equation 12.1.*

The realized structures have been monitored by means of SEM analysis, and the resulting images are reported in figure 12.16. 2D structures with dimension ranging from 20 to hundreds of micrometers have been obtained, the minimum resolution exploited being limited from the mask shape. These structures have been obtained irradiating a sample for four steps of 150 seconds, placing the UV-lamp at a distance of 3.5 cm from the sample.

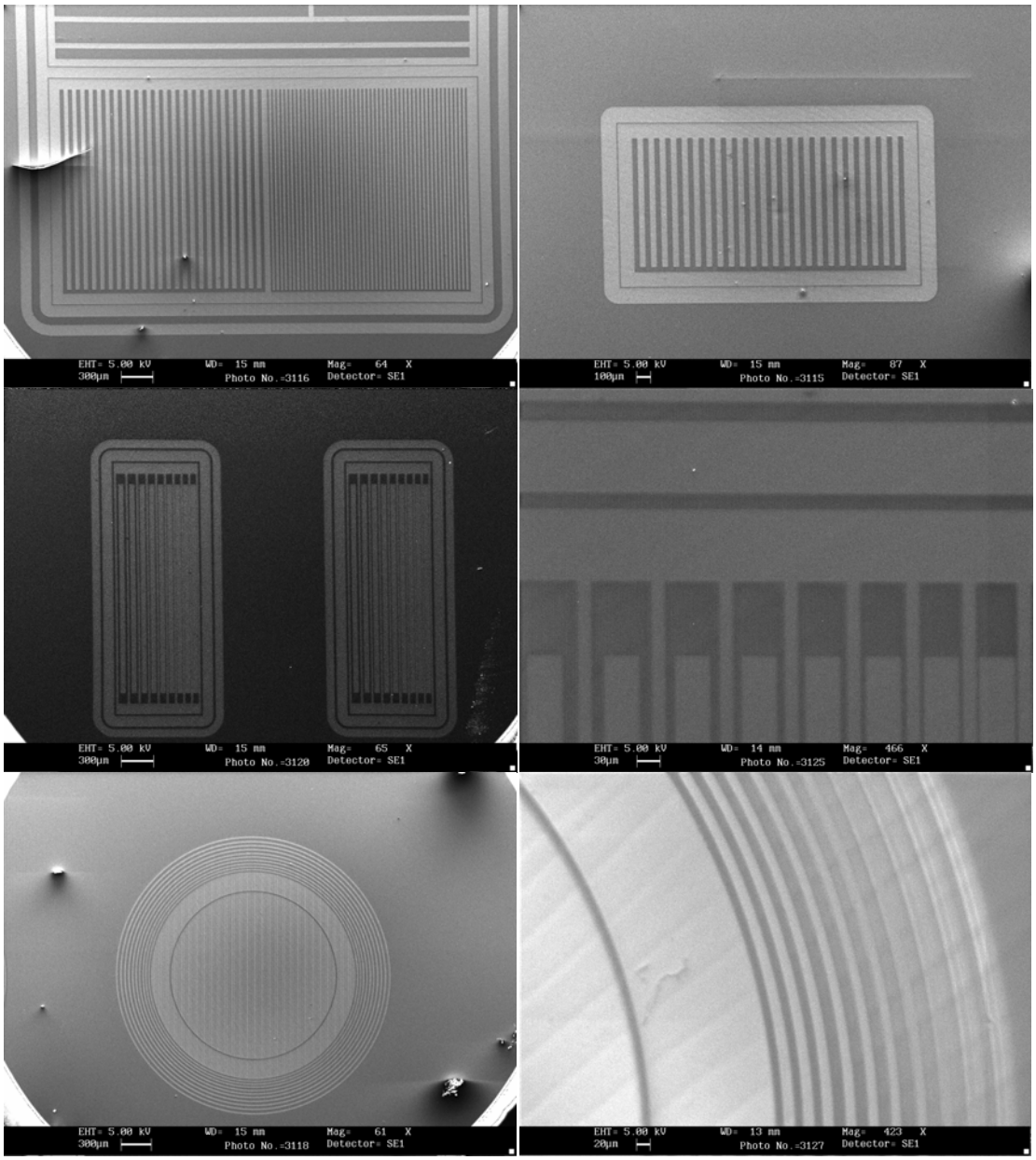

Figure 12.16 *Scanning electron microscopy of the pattern profile.*

12.11 Conclusion

We have reported the room temperature synthesis of hybrid SiO_2-TiO_2 sol-gel films with nanocrystalline TiO_2 clusters homogeneously dispersed inside the amorphous matrix. We have characterized the structure of these films and the UV induced changes. Moreover we have tested their photocatalytic activities using stearic acid as reference materials. This system seems to be really promising for future applications such as UV-treated inorganic films or photocatalytic coatings, to be deposited on thermally degradable substrates. We have also demonstrated the possibility to generate diffractive optical elements by irradiating a UV-sensitive hybrid sol-gel film, through an appropriate photo-mask. The induced decomposition of the organic components leads to a shrinkage of the film up to 60 % on the initial thickness, and

to the increase of the refractive index. To our knowledge, this is the first time that this effect has been exploited for the production of index contrast and surface modulation diffractive optical elements or waveguides.

REFERENCES

[1] A. Mills, S. LeHunte, J. Photochem. Phootobiol. A, 1997, 108, 1.

[2] B. Ohtani, Y. Ogawa, S. Nishimoto, J. Phys. Chem. B, 1997, 101, 3746.

[3] A. Scolan, C. Sanchez, Chem. Mater.,1998, 11, 3217; M. Lal, V. Chabra, P. Ayub, A. Maitra, J. Mater. Res., 1998, 13, 1249; M. Wu, G. Lin, D. Chen, G. Wang, D. He, S. Feng, R. Xu, Chem. Mater., 2002, 14, 1974; C.-C. Wang, J. Y. Ying, Chem. Mater., 1999, 11, 3113.

[4] K. H. Yoon, J. S. Noh, C. H. Kwon, M. Muhammed, Mater. Chem. and Phys., 2006, 95, 79.

[5] A. Fidalgo, L.M. Ilharco, J. Non-Cryst. Solids, 2001, 283, 144.

[6] T. Galo Cardenas, C. Ricardo Oliva, Mater. Res. Bul., 1998, 33, 1599.

[7] A.M. Seco, M.C. Gonçalves, R.M. Almeida, Mater. Sci. Eng. 2000 B76 193; R.M. Almeida, H.C. Vasconcelos, L.M. Ilharco, SPIE Proced. 1994, 2288, 678.

[8] X. Gao, I. E. Wachs, Catal. Today, 1999, 51, 233; A.Fidalgo, L. M. Ilharco, J. Non-Cryst. Solids, 2001 283 144; W. Que, X. Hu, Thin Solid Films, 2003, 436, 196.

[9] D. C. M. Dutoit, M.Schneider, A. Baiker, J. Catal., 1995, 153, 165 ; S. Klein, S. Thorimbert, W.F.Maier J. Catal., 1996, 163 476.

[10] Y. Sorek, R. Reisfeld, A.M. Weiss, Chem. Phys. Lett., 1995, 244, 371; O. Soppera, C. Croutxé-Barghorn, D. J. Lougnot, New J. Chem., 2001, 25, 1006.

[11] G. Brusatin, M. Guglielmi, P. Innocenzi, A. Martucci, G. Battaglin, S. Pelli, G. Righini, J. Non-Cryst. Solids, 1997, 220, 202.

[12] Y. Sorek, R. Reisfeld, A.M. Weiss, Chem. Phys. Lett., 1996, 244, 371.

FINAL REMARKS

In this thesis we have exploited the properties of two-dimensional periodic dielectric media, photonic crystals (PC) and distributed feedback (DFB) gratings, to confine photons inside cavities of wavelength scale dimension. Optical microcavities are key component allowing to obtain compact low threshold laser devices.

The first part of the thesis, from Chapter 1 to Chapter 5, deals with the study of PCs waveguide heterostructures, realized on InP semiconductor, engineered for lasing emission at 1.55 μm.
We proposed, studied theoretically, and demonstrated a small mode volume, photon confinement scheme in an active microcavity. We achieved efficient spatial optical confinement using a local effective index modulation in a W1 PC waveguide supporting a low group velocity mode at the edge of the first Brillouin zone.
The first two chapters are necessary to introduce the basic principles of semiconductor lasers and photonic crystals, whose comprehension is mandatory to understand the device operation's principles.
An intense computational work, described in Chapter 3, has been done for the theoretical investigation of the device. Firstly we have calculated the band diagram for the photonic crystal waveguide, to extract the slow waveguided modes frequencies. The electromagnetic field distribution inside the microcavity has been calculated with a FDTD software, extracting important device parameters, as the modal volume and the quality factor. Finally we have explained the physics of the confinement through a simple model, based on the envelope formalism.

In Chapter 5 we have presented our experimental results obtained with available technologies, as electron beam lithography and reactive ion etching, whose working principles are illustrated in Chapter 4.

With a two-step lithography process, we have realized manifold structures, with slightly different period or hole radius, or with different cavity dimension.

These structures have been characterized with an optical set-up, obtaining reproducible results in agreement with the theoretical predictions.

Laser emission has been obtained, at room temperature, with an estimated effective threshold of about 0.5 mW.

The simple and reproducible production process, together with the robustness and mechanical stability of the device, make this type of low threshold lasers good candidates for either surface-emitting or coupled-to-waveguide laser devices. Moreover the high Purcell Factor of 250 for the 3 μm wide PMMA strip could lead to applications in the field of integrated quantum photonics.

The introduction to non-linear optics, in Chapter 6, is necessary to introduce the reader to the second subjects of the thesis: the research of a device for the up-conversion lasing, discussed in Chapters 7-11.

Up-conversion lasing represents an alternative approach to blue-green light generation using infrared sources. In upconversion lasers, the energy from two or more pump photons is combined to excite the lasing transition; thus the pump wavelength can be longer than the lasing wavelength.

Chapter 7 contains the description of the optical set-up prepared for the characterization of the active medium for up-conversion, both in solution or inside solid-state samples. The operating principles of the IR ultrafast laser source employed for the two-photon pumping of the samples are also presented.

Using these facilities, we have investigated the emission properties of both organic push-pull molecule and II-VI semiconductors quantum dots (QD). Solid state samples have been prepared by dispersing these species inside sol-gel matrices, engineered to optimize their emission properties. The sol-gel synthesis and the characterization of the obtained films is described in Chapter 9.

The optical characterization demonstrates that semiconductors QDs are the most promising candidate for solid state device because of their high photostability.

The amplified spontaneous emission (ASE) of QDs/ZrO_2 films has been measured using the variable strip length method.

These QDs show two-photon gain values of more than 100 cm^{-1} and uncommonly high room temperature temporal stability, with up to 70% of the original ASE intensity retained after 1 hour of illumination (about $3.6x10^6$ pulses).

In order to exploit these systems for the up-converted laser device, we have worked on the design and the experimental realization of a DFB grating, with rectangular symmetry, realized on a sol-gel substrate.

The band diagram calculation gives the modes frequencies associated to the high symmetry point Γ_1. This point is particularly interesting as it provides both the feedback in the grating plane, required for lasing, and the laser mode extraction perpendicular to the grating surface.

Grating has been experimentally obtained with e-beam lithography, placing the frequency of the Γ_1 point on the maximum gain frequency of our QDs.

The grating has been directly defined using a sol-gel film sensible to the e-beam exposition. QDs/ZrO_2 film of desired thickness has been deposited above the grating, and the obtained device has been characterized. Unfortunately we have not succeeded in measuring up-converted laser emission in our structure. Other improved device geometries have been studied theoretically in such a way to lower the lasing threshold. The experimental realization of such structures will allow reaching our purpose: the realization of a solid-state compact device for visible up-converted laser emission.

Ringraziamenti

Ed infine eccoci ai ringraziamenti. Per primi voglio ringraziare il Professore Renato Bozio per l'appoggio scientifico e umano che ha sempre saputo darmi. Sono molto grato a Raffaella, per il tempo che mi ha dedicato nel corso di questi anni, in tesi prima e poi durante il dottorato. Ringrazio inoltre Camilla, Giovanna e Gioia per il per il prezioso aiuto. Mi ringraziano Ilaria, Eleonora, Ida, Roberto e Tode e l'amico di Tode per l'onore di condividere l'ufficio dottorandi con il sottoscritto.

Ringrazio inoltre tutte le persone che hanno collaborato durante lo svolgimento del mio lavoro, come Cinzia Sada, Nicola Argiolas, il Prof. Filippo Romanato, Mauro Prasciolu e tanti altri, senza i quali tutto questo lavoro non sarebbe stato possibile.

Per lo splendido periodo trascorso a Lione ringrazio Xavier e Christian, che mi hanno accolto e introdotto al magico mondo dei cristalli fotonici, e i dottorandi Patrick, Lydie, Fabian and Frederic per l'aiuto e la compagnia.

Ma più di tutti questa tesi è dedicata ai miei genitori che mi hanno sempre sostenuto e incoraggiato, e che anche adesso mi sopportano, speriamo per poco tempo ancora. E poi a mia sorella, ai miei nonni che sono sempre molto buoni con me e tutti gli zii, zie, cugini e cugine che compongono la mia famiglia.

Ringrazio poi i miei due migliori amici, Andrea e Toni, sulla cui amicizia so di poter sempre e comunque contare. Una dedica va anche alla Chicca, compagna mitica di serate mitiche, delle quali preservo uno splendido ricordo.

Un pensiero lo dedico a tutte le persone che mi hanno affiancato in questi tre anni, donandomi momenti di vera felicità.

Infine questa tesi la dedico alla mia musa ispiratrice, a mon petit raton, alla mia principessa, a una donna che mi ama alla follia e che per me si getterebbe tra le

fiamme, che ha abusato di me in un raro momento di ebbrezza, e che se riesco a trovarmi un lavoro magari riusciamo pure ad andare a vivere assieme, Laura!!!